# MODELLING THE NUCLEOPHILICITY OF METAL COMPLEXES

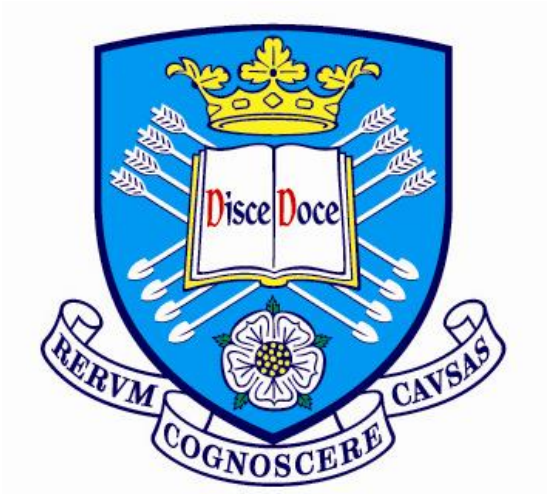


**Christopher M. Parks**

A Thesis Submitted for the Degree of Doctor of Philosophy

Department of Chemistry

University of Sheffield

October 2015

# Summary

This thesis describes a joint computational and experimental investigation into the reactivity of nucleophilic metal complexes with particular emphasis placed on using computational methods to predict reactivity.

A general introduction into nucleophilic reactivity is detailed in **Chapter 1**. Examples of how nucleophilic metal complexes are employed in stoichiometric and catalytic reactions are presented. Methodologies for rationalising the electronic and steric effects of ligands on the reactivity of metal complexes are also described.

In **Chapter 2** the nucleophilicity of anionic 18-electron metal carbonyl complexes ($[M(CO)_n]^-$ and $[CpM(CO)_n]^-$) towards iodomethane is investigated computationally using density functional theory. The methodology used in the remainder of this thesis is presented and the most appropriate basis set is identified. Transition state structures are optimised and a correlation between calculated barrier heights and experimental rate constants is established. The methodology is also applied to a series of phosphine containing Mn complexes, $[Mn(CO)_4L]^-$ for comparison with $[Mn(CO)_5]^-$. The effect of phosphine conformation on the calculated barrier height is discussed.

**Chapter 3** presents computational investigations on the nucleophilicity of neutral 18-electron iridium complexes, [CpIr(CO)(L)] and [Cp*Ir(CO)(L)], towards iodomethane. Detailed analysis of the effect of conformation of the phosphine ligand is presented for L = $PMe_3$ and L=$PEt_3$. The reactivity of the Cp* complexes is correctly computed in accordance with experiments to be higher than the corresponding Cp complexes.

Several series of neutral square-planar 16-electron complexes are analysed individually as well as collectively in **Chapter 4**. The effect of varying the phosphine ligand L is probed in iridium(I) Vaska-type complexes, $[IrCl(CO)(L)_2]$ as well as the rhodium(I) complexes [Rh(acac)(CO)(L)] and some Pt(II) systems. The effect of varying the alkyl/aryl ligand R in $[Pt(bpy)R_2]$ complexes is also investigated.

The results from the preceding chapters are analysed collectively in **Chapter 5**, along with data for a number of other complexes. The correlation of computed barrier heights and transition state geometries with experimental rate constants is discussed.

**Chapter 6** investigates reactivity from the opposite viewpoint, changing the electrophile, while keeping the nucleophile unchanged. In particular, it concerns investigations into a cobalt complex, $[Co(dmg)_2(PMe_3)]^-$ , a model for vitamin $B_{12}$, reacting with various alkyl chlorides.

**Chapter 7** discusses an experimental study of the reactivity of some [Rh(acac)(CO)(L)] complexes with iodomethane. The effect of changing the phosphine, L, on the oxidative addition and subsequent isomerisation steps is presented. Particularly high reactivity is found for complexes with *ortho*-anisyl-containing ligands ($L = PPh_n(o\text{-}An)_{3-n}$). DFT studies reveal that the $S_N2$ transition state is stabilised by interaction of an *ortho*-methoxy substituent with the Rh centre or with the incoming MeI molecule, the latter giving the lowest energy barrier for reaction.

The reactivity of some iridium iodocarbonyl complexes bearing xantphos-type ligands is investigated in **Chapter 8**. An Ir(I) dicarbonyl, $[IrI(CO)_2(xantphos)]$ is shown to react with MeI with loss of CO to give monocarbonyl Ir(III) methyl species. Attempted synthesis of an Ir(I) iodocarbonyl complex of *o*-tol-xantphos leads to two isomers of an iridium(III) hydride resulting from C-H activation of an *ortho*-methyl substituent. The C-H activation is shown to be reversible on abstraction of iodide to give an Ir(I) cation, $[Ir(CO)(o\text{-tol-xantphos})]^+$. An analogous complex $[Ir(CO)(^t\text{Bu-xantphos})]^+$ is shown to undergo reversible oxidative addition of $H_2$.

**Chapter 9** includes general conclusions and future work.

**Chapter 10** gives full details of the procedures employed for both the computational and experimental investigations.

# Acknowledgements

I am grateful to my supervisors Tony Haynes and Anthony Meijer for their support and guidance over the last four years and in particular to Mike Ward and Richard Jackson for the opportunity to undertake both the PhD and subsequent teaching work.

Thanks go to past and present members of the Haynes group, Dean Cocker, Dave Griffin and Stephen Repper for making the PhD as enjoyable as possible

Many thanks to past and present members of the Meijer group, Ben Irving, Jason Loader, Theo Keane and Benedict Hazel for educating me in the ways of computational chemistry and ensuring me that DFT does not stand for definitely flexible theory!

I would also like to thank the staff in the department for their friendship and support over the course of the PhD: Harry Adams for tireless help with solving crystals, Sue Bradshaw and Brian Taylor for running unusual NMR spectra and all of the stores team for unending teasing and light hearted comedy. Thanks also go to the Finance team for putting up with persistent nagging when payments went missing!

Thanks also go to my parents for supporting me through what has been a challenging time.

## Abbreviations

### General

| | |
|---|---|
| atm | atmosphere |
| COD | 1,5-cyclooctadiene |
| Cp | cyclopentadienyl |
| Cp* | pentamethylcyclopentadienyl |
| DCM | dichloromethane |
| Et | ethyl |
| $^{i}$Pr | iso-propyl |
| Me | methyl |
| *o*-tol | ortho-tolyl |
| Ph | phenyl |
| $^{t}$Bu | tertiary-butyl |
| THF | tetrahydrofuran |
| X | halogen |

### Spectroscopy

| | |
|---|---|
| IR | infrared |
| ν | stretching frequency |
| ν(CO) | carbonyl stretching frequency |
| Hz | hertz |
| J | coupling constant |
| s | singlet |
| d | doublet |
| dd | doublet of doublets |
| t | triplet |
| m | multiplet |

## Ligands

| | |
|---|---|
| xantphos | 4,5-bis(diphenylphosphino)-9,9-dimethylxanthene |
| $^{i}$Pr-xantphos | 4,5-bis(di-isopropylphosphino)-9,9-dimethylxanthene |
| $^{t}$Bu-xantphos | 4,5-bis(di-*tert*-butylphosphino)-9,9-dimethylxanthene |
| *o*-tol-xantphos | 4,5-bis(di-*o*-tol-butylphosphino)-9,9-dimethylxanthene |
| nixantphos | 4,6-bis(diphenylphosphino)phenoxazine |
| acac | acetylacetonate |
| PPN | $(PPh_3)_2N^+$ |
| bpy | bypyridine |
| ppy | 2- phenylpyridine |
| tpy | 2-(p-tolyl)pyridine |
| bhq | benzo[h]quinolone |
| dppe | 1,2-bis(diphenylphosphino)ethane |
| dppmS | bis(diphenylphosphino)methane sulphide |
| dppmSe | bis(diphenylphosphino)methane selenide |
| dppmo | 1,2-bis(diphenylphosphine)methane monooxide |

## Computational Chemistry

| | |
|---|---|
| DFT | density functional theory |
| PCM | polarisable continuum model |
| QM | Quantum Mechanics |
| HF | Hartree-Fock theory |
| SCF | Self consistent field theory |

# Contents

# CHAPTER 1

# Introduction

*"The answer is in the question"*

- Bobble head Einstein.

## 1.1 Reactivity

Chemical reactions involve one set of substances undergoing a transformation to form another set of substances as shown in **Scheme 1.1.** Those present at the start of a reaction are known collectively as reactants or reagents which interact to form products.

$$\mathbf{A + B} \longrightarrow \mathbf{C + D}$$

**Scheme 1.1:** Generalised reaction scheme showing formation of products **(C** and **D)** from reactants **(A** and **B).**

**Figure 1.1** shows a representation of a simple one step reaction profile where the reactants (**A** and **B**) form products (**C** and **D**) via a transition state **(TS).** If the products are at a lower enthalpy compared to the reactants the reaction is considered to be exothermic and if the products are at a higher energy it is said to be endothermic.

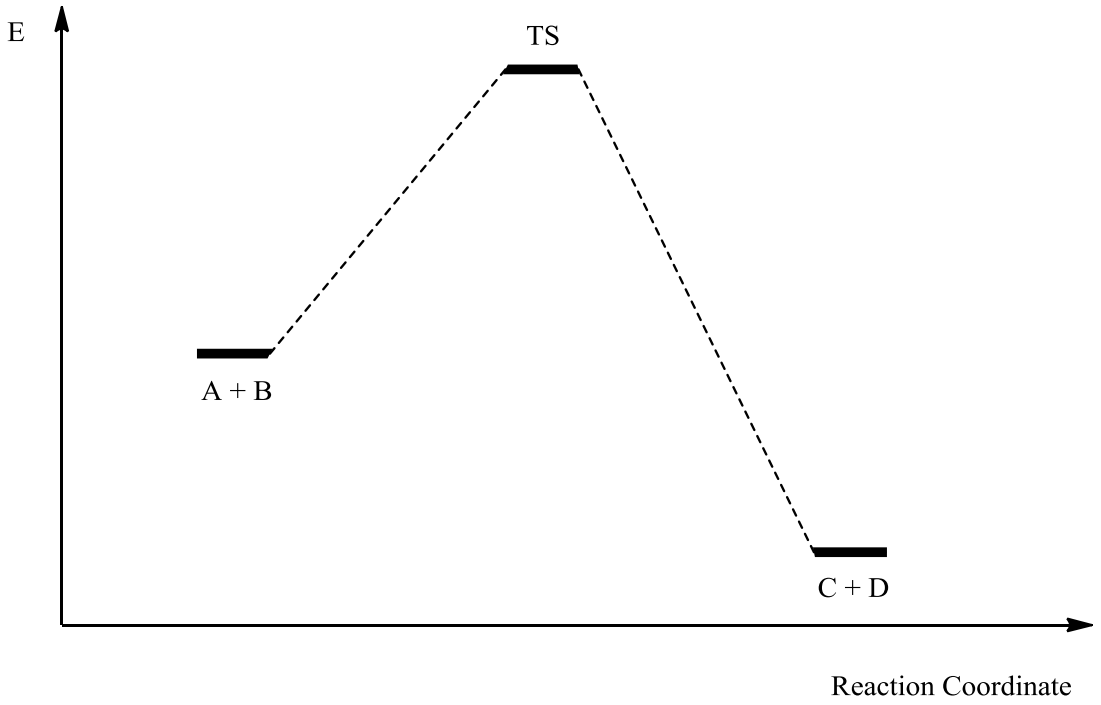


**Figure 1.1:** Reaction profile for the reaction of reactants (**A** and **B**) to form products (**C** and **D**) via a transition state.

Most chemical reactions can be rationalised by the movement of electrons from electron rich sources (nucleophiles) to electron deficient sources (electrophiles). Generally, a reaction is less likely to occur if the levels of electron density on the reactants are similar.

Being able to quantify the strength of nucleophiles has been the subject of many studies as far back as the 1920's when Brönsted and Pederson described the relationship between basicity and nucleophilicity. Further work by Swain and Scott attempted to formulate a scale of nucleophilicity based on a simple equation (**Equation 1.1**)[1] The rate constant ($k$) for the reaction of a nucleophile with an organic substrate was normalised against the reaction of the organic substrate with water ($k_0$). The substrate constant $s$ is a measure of the susceptibility of the substrate to undergo a reaction (defined as 1 for methyl bromide) and $n$ is the nucleophilic constant.

$$log_{10}\left(\frac{k}{k_0}\right) = sn \qquad \textbf{(1.1)}$$

A number of similar equations have been proposed (for example by Edwards and Ritchie) in an attempt to describe the nucleophilicity of molecules.[2,3] However, this approach only works for a certain subset of molecules.

## 1.2 Experimental studies on $S_N2$ reactions

Much of the early work on nucleophilicity and more generally $S_N2$ reactions was carried out by Hughes and Ingold in the 1930's. They were the first to establish that halide anions ($X^-$) undergo bimolecular $S_N2$ reactions with alkyl halides (RY) according to **Scheme 1.2**.

$$X^- + RY \longrightarrow RX + Y^-$$

**Scheme 1.2:** Generalised $S_N2$ reaction.

The $S_N2$ reaction is first order in both $X^-$ and RY and second order overall. Such a reaction involves an inversion of the stereochemistry as shown in **Figure 1.2.**

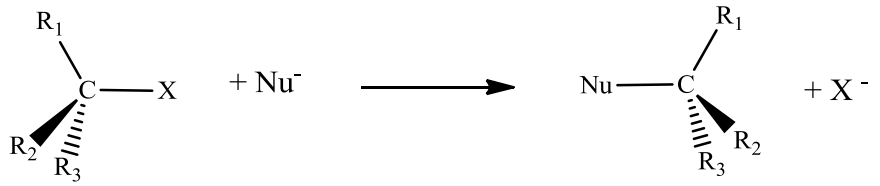


**Figure 1.2:** Reaction of $R_1R_2R_3CX$ with $Nu^-$ highlighting the inversion of stereochemistry. (Walden inversion)

Since Hughes' pioneering work, a large amount of experimental work has been undertaken on simple reactions of halide ions with alkyl halides which can act as models for larger systems.[4-23] Factors such as the solvent polarity, nature of nucleophile, leaving group and the nature of the R groups on the alkyl halide can combine to affect the nature and rate of these reactions.

These reactions are ionic in nature and are ideally suited to being studied using mass spectrometry. Olmstead and Brauman[19] investigated gas-phase $S_N2$ reactions and deduced that the rate of reaction is determined by the attractive nature of the ion and the molecule and whether the transition state collapses back to reactants or has enough energy to form products.

## 1.3 Experimental studies on nucleophilic metal complexes

A number of studies are present in the literature where the reaction of nucleophilic metal complexes with various electrophiles is probed, with particular attention paid to how changes in the spectator ligands affect the overall complex nucleophilicity. It is the reaction with alkyl halides, particularly iodomethane which is most relevant to this study.

Some of the earliest studies on nucleophilic metal complexes were carried out by Dessy and subsequently collated and expanded upon by Pearson et al..[24,25] They investigated

the reaction of various anionic 18-electron complexes bearing carbonyl ligands with iodomethane. **Figure 1.3** shows how these complexes react with iodomethane using $[CpFe(CO)_2]^-$ as an example. The metal acts as a nucleophile and attacks the carbon of iodomethane to form a metal-carbon bond.

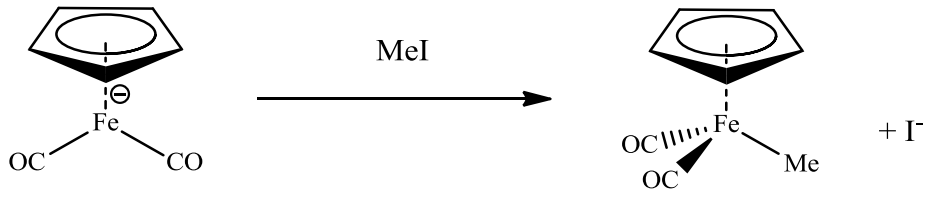


**Figure 1.3:** Reaction of $[CpFe(CO)_2]^-$ with a MeI.

**Table 1.1** shows a selection of complexes that were investigated and their respective rate constants, which span eight orders of magnitude. The highly nucleophilic nature of some of the complexes precluded the use of a single solvent and electrophile. EtBr was used in place of MeI for the iron and nickel complexes and a rate constant for the reaction with MeI was estimated based upon analogies with other systems.[24,25] Whilst this does not give an absolute value of the rate constant, it was concluded that the order of magnitude and the relative order of reactivity across the complexes was correct. Computational modelling of these systems will be discussed in **Chapter 2.**

| **Complex** | $k_2$ / $M^{-1}s^{-1}$ [a] |
|---|---|
| $[Co(CO)_4]^-$ | 0.044 |
| $[CpCr(CO)_3]^-$ | 0.075 |
| $[CpMo(CO)_3]^-$ | 1.5 |
| $[CpW(CO)_3]^-$ | 2.4 |
| $[Mn(CO)_5]^-$ | 7.1 |
| $[CpNi(CO)]^-$ | 22000 |
| $[CpFe(CO)_2]_-$ | 2800000 |

a – error values not reported.

**Table 1.1**: Selected metal carbonyl complexes and their respective rate constants for the reaction with iodomethane in THF at 25 °C. [24,25]

Another important class of complexes are 16-electron square-planar complexes. **Figure 1.4** shows the structure of Vaska's complex, $[IrCl(CO)(PPh_3)_2]$ which was first isolated in 1961 and readily undergoes oxidative addition reactions.[26] Although the name Vaska's complex refers specifically to the complex containing triphenylphosphine, the name is now typically used to refer to any complex of the general form $[IrX(CO)(L)_2]$.

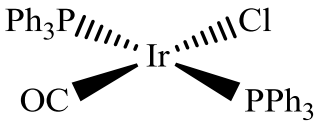


**Figure 1.4:** Structure of Vaska's complex, $[IrCl(CO)(PPh_3)_2]$.

Square-planar $d^8$ metal complexes such as these react with MeI in a two-step mechanism according to **Scheme 1.3.** Initially, attack of the metal nucleophile on MeI liberates an iodide ion which is then free to coordinate to the metal complex at an available site – typically *trans* to the methyl group. The formal oxidation state of the metal increases by two, as does the number of coordinated ligands.

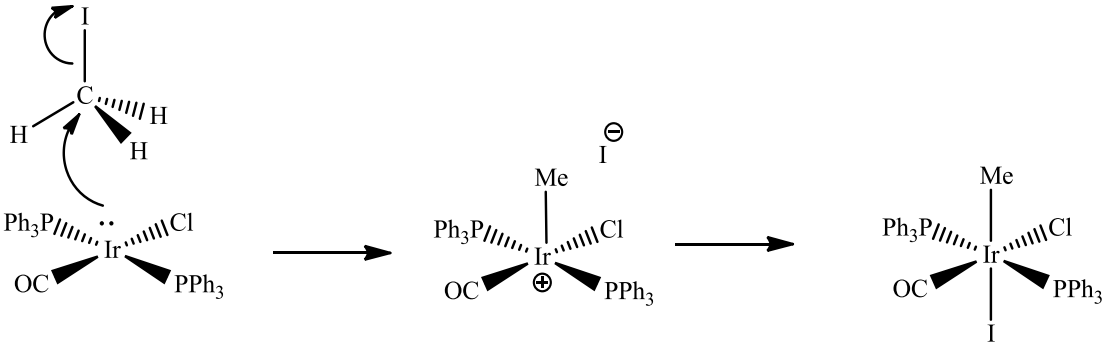


**Scheme 1.3:** Reaction of Vaska's complex with iodomethane.

In 1993 Wilson et al. investigated the reactivity of a number of Vaska-type complexes towards iodomethane.[27] **Table 1.2** shows that the reactivities span three orders of magnitude. In general, complexes bearing small predominantly alkyl phosphines ($PEt_3$, $PMe_2Ph$ for example) are the most nucleophilic whereas complexes bearing bulky phosphines such as $P^iPr_3$ and $PCy_3$ have the smallest rate constants despite being more

electron donating. The lower reactivity of these complexes is attributed to steric crowding of the metal.

| L | $10^3.k_2$ / $M^{-1}s^{-1}$ [a] |
|---|---|
| $P(4\text{-}MeOC_6H_4)_3$ | 25.3 |
| $PEt_3$ | 23 |
| $PMePh_2$ | 17.7 |
| $PPh_3$ | 3.5 |
| $PCy_3$ | 0.31 |
| $P^iPr_3$ | 0.19 |
| $P^tBuPh_2$ | 0.18 |

a – error values not reported.

**Table 1.2:** Selected rate constants for the reaction of $[IrCl(CO)(L)_2]$ with iodomethane in benzene at 25 °C. [27]

Experimental studies have not been limited to how changing the phosphine affects the reactivity. Kubota et al. studied a range of modified Vaska complexes with variation of the halide / pseudohalide.[28] The effect of replacing the phosphine by an analogous arsine ligand was also shown to increase the nucleophilicity of the metal complex.

| X | $10^3.k_2$ / $M^{-1}s^{-1}$ [a] |
|---|---|
| F | 20 |
| Cl | 3.5 |
| Br | 1.6 |
| I | 0.9 |
| $N_3$ | 3.6 |
| NCO | 1.1 |
| NCS | 0.2 |

a – error values not reported.

**Table 1.3:** Selected rate constants for the reaction of $[IrX(CO)(PPh_3)_2]$ with iodomethane in $CH_2Cl_2$.[28]

**Table 1.3** shows the reactivity of the halide complexes with iodomethane increases (F >>Cl > Br >I) which is in contrast to the reactions with hydrogen and oxygen and other electrophiles where the trend is reversed.[29,30] Similar observations were recorded for the pseudo halides ($NCO^-$ and $NCS^-$).

Whilst Vaska complexes are perhaps the most well studied 16-electron square-planar complexes, there are many experimental studies on oxidative addition to platinum complexes. The most relevant series of complexes from a recent review by Rendina that summarises the reactivity of platinum complexes bearing nitrogen donor ligands with alkyl halides are discussed here.[31]

**Figure 1.5** shows the structure of a series of platinum complexes bearing a bypyridyl ligand (bpy), which were investigated by Jawad et al..[32] These complexes react quickly with iodomethane due to a relatively unhindered and more nucleophilic metal centre and their rate constants span three orders of magnitude on variation of R.

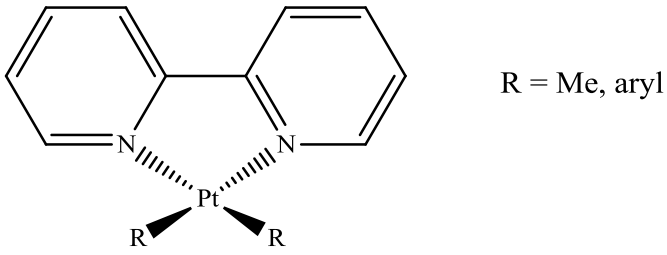


**Figure 1.5:** Structure of $[Pt(R)_2(bpy)]$

More recently, the reactivity of rhodium complexes bearing acetylacetonate ligands (**Figure 1.6**) towards iodomethane has been studied by Conradie et al. and Roodt et al..[33,34]

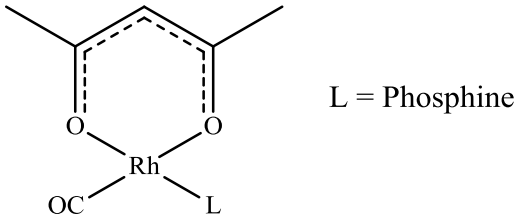


**Figure 1.6:** Structure of [Rh(acac)(CO)L]

Sequential replacement of phenyl with cyclohexyl rings in triphenyl phosphine created a more nucleophilic metal centre as evidenced by a lower carbonyl stretching frequency. However, the reactivity of these complexes towards iodomethane did not follow the expected trend of reactivity which was attributed to the steric properties of the ligands. Further tuning of the nucleophilicity of these complexes could be achieved by changing both the β-diketonate substituents and the phosphine ligand. Phosphite ligands[35,36] reduced the rate of reaction towards alkyl halides whereas modification of the acac ligand to feature either ferrocenyl or phenyl groups increased their reactivity. Further experimental investigations into these complexes will be discussed in **Chapter 4**.

Some of the most nucleophilic metal complexes known contain cobalt centres. **Figure 1.7** shows the structure of an anionic cobalt complex with dimethylgloximate (dmg) ligands. The reactivity of this complex with a series of alkyl chlorides was investigated as a model for vitamin $B_{12}$.[37,38]

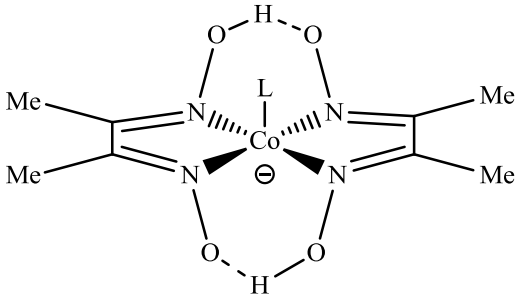


L = $P^nBu_3$ , $SMe_2$, Pyridine

**Figure 1.7:** Structure of $[Co(dmg)_2L]$

The most sterically hindered alkyl chlorides such as $^iPrCl$ reacted slowly with the metal complex. The reactivity could be enhanced significantly by the addition of an electronegative atom next to the reactive carbon.

Cobaloxime complexes are well known to form adducts with various Lewis bases (L in **Figure 1.7**), which mimics vitamin $B_{12}$ where a benzimidazole sugar likely coordinates to the metal centre. Upon addition of a Lewis base, the character of the $3d_z^2$ orbital, which is responsible for reaction with electrophiles can be affected.

## 1.4 Applications of nucleophilic transition-metal complexes

Nucleophilic metal complexes such as those in **Section 1.2** have found various applications most typically in synthesis, catalysis and in biologicial systems. The ability of the complexes to undergo changes in both oxidation state and coordination number allows them to fulfil a number of important roles.

The chemistry of $[CpFe(CO)_2]^-$ was the subject of a recent review by Theys et al. and covered literature from 1994 to 2009.[39] Two further reviews cover literature prior to 1994.[40,41] Whilst the complex has no widespread commercial uses, it has been extensively studied due to the ease with which it reacts with electrophiles such as alkyl and aryl halides, silyl triflates, epoxides and aldehydes.

Insertion of a carbonyl into organic substrates can often be facilitated by using a carbonyl containing metal nucleophile. One such example is the very reactive $d^8$ complex, $[Fe(CO)_4]^{2-}$ which is known as Collman's reagent and was first isolated in the 1970's.[42] This dianionic complex is often termed a "super nucleophile" due to its extremely high nucleophilicity and can potentially undergo subsequent reactions with electrophiles. This leads to an unstable intermediate which undergoes fast reductive elimination to form a coupled organic product. A high degree of functionalization can be imparted on the organic product by changing the organic electrophiles – acid chlorides can be converted to aldehydes and alkyl chlorides to carboxylic acids. This process is summarised in **Scheme 1.4.**


**Scheme 1.4:** Use of Collman's reagent in synthesis.

Another well-known carbonyl containing complex, $[Co(CO)_4]^-$, derived from $[Co_2(CO)_8]$ acts as a nucleophile in the displacement reaction with alkyl halides to generate alkylcobalt complexes. Subsequent migratory insertion forms an acyl species which undergoes reactions with hydroxides and alkoxides to form carboxylic acids and

esters. **Scheme 1.5** shows a further example of how $[Co(CO)_4]^-$ can be employed in the carbonylation of three membered rings. The proposed cycle involves four stages: activation of a substrate by a Lewis acid (**1**), the $S_N2$ attack on the substrate by $[Co(CO)_4]^-$ (**2**), CO insertion (**3**) and product release with catalyst regeneration (**4**).

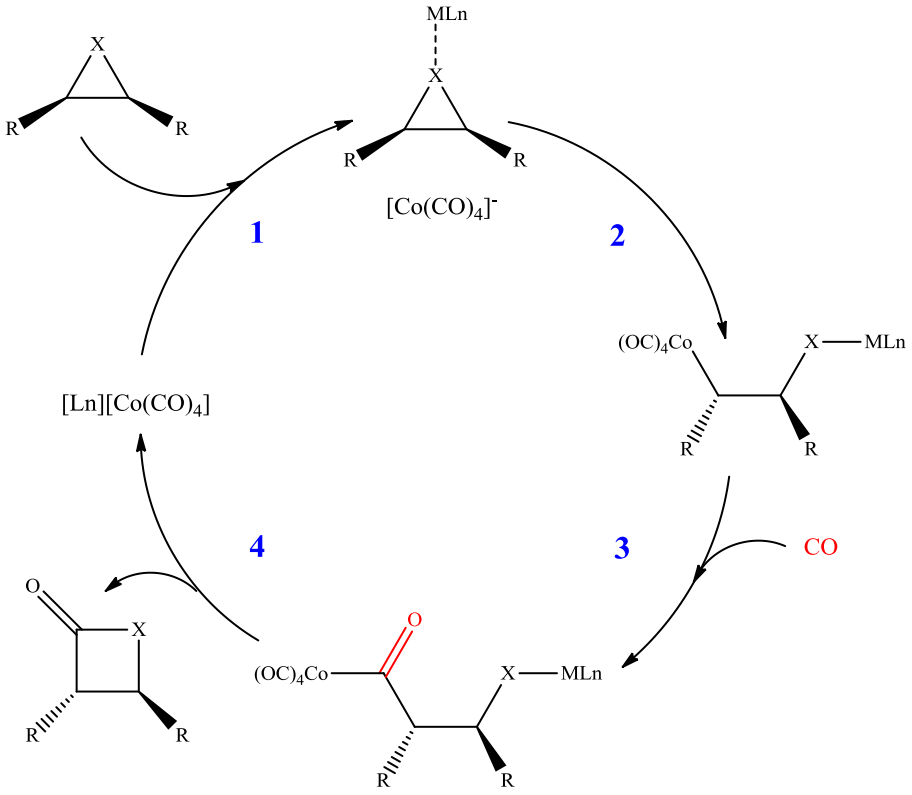


**Scheme 1.5:** Proposed catalytic cycle for the carbonylation of three membered rings using $[Co(CO)_4]^-$ (X = O, NR. $L_nM$ = Lewis acid)

$[Co(CO)_4]^-$ has also been used as a catalyst for methanol carbonylation where carbon monoxide and methanol are converted into acetic acid.[43] It was developed in 1965 by BASF and was the first catalytic process for producing acetic acid. There were a number of issues with the process including but not limited to high temperatures, high catalyst loading, high CO pressures and poor selectivity.

The necessity to improve this catalytic process led to the development of perhaps one of the most famous nucleophilic metal complexes, $[RhI_2(CO)_2]^-$. This complex was developed in the 1960's by scientists at Monsanto company and catalyses the carbonylation of methanol to acetic acid according to **Scheme 1.6.** Much milder

conditions are employed than the cobalt catalysed process and greater selectivity is found with respect to methanol.

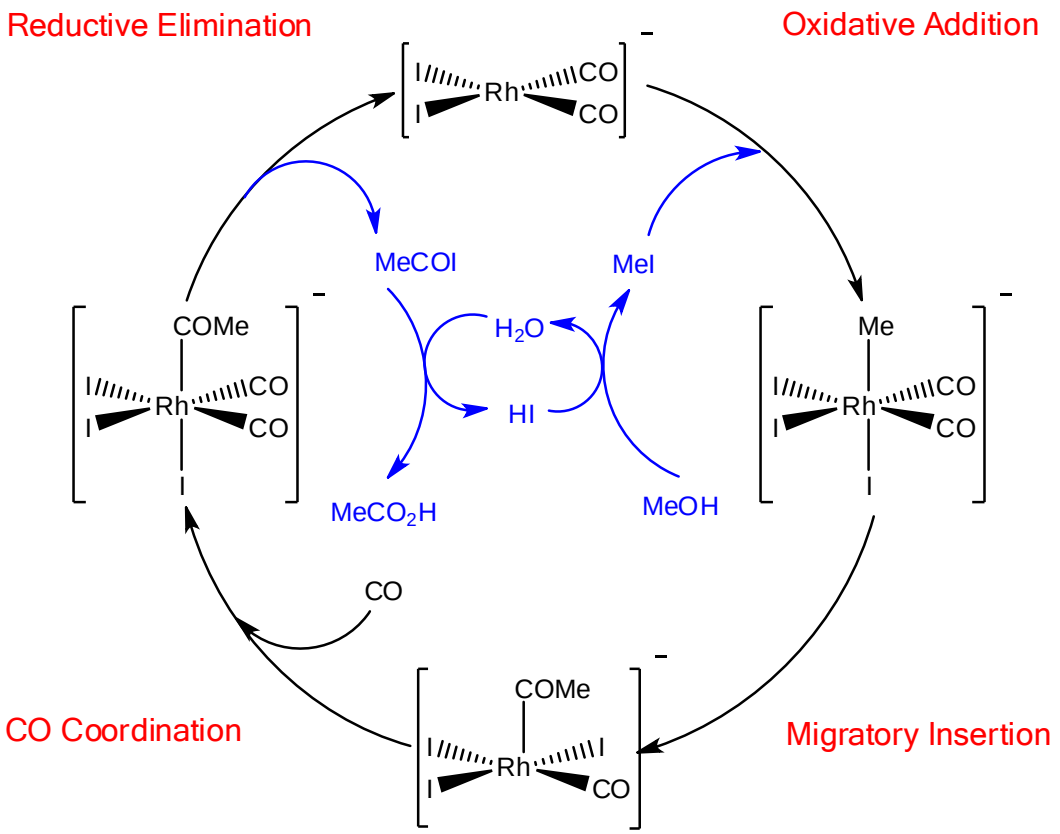


**Scheme 1.6:** Catalytic cycle for the formation of acetic acid.

The first step in the catalytic cycle is the most relevant to the current study. It involves the oxidative addition of iodomethane with $[RhI_2(CO)_2]^-$ acting as a nucleophile to form an octahedral complex. This is the rate determining step in the cycle and a great deal of research has been invested on how the rate of this step can be enhanced by incorporating phosphine ligands.

A comprehensive review of how changing the ligands affects the rate of reaction was published by Thomas et al.[44] Further details on the effect of phosphines on reactivity will be discussed in **Chapter 4**. Cole-Hamilton found that the rate of reaction towards iodomethane was 57 times faster at 298 K for a phosphine modified complex. $[RhI(CO)(PEt_3)_2]$.[45] However, such a complex was of little practical use industrially as

the complex degraded in under 10 minutes to form a combination of methylated phosphine, oxidised phosphine and $[RhI_2(CO)_2]^-$.

$[IrI_2(CO)_2]^-$ is a related complex and is a catalyst used in the Cativa process for the carbonylation of methanol to acetic acid. In contrast to the Monsanto process, where oxidative addition of iodomethane is the rate determining step, the analogous reaction of $[IrI_2(CO)_2]^-$ *ca.* 100 times faster and carbonylation of the resulting Ir(III) methyl species is rate determining in the catalytic cycle.[46]

## 1.5 Factors affecting nucleophilicity

Many factors can combine to affect the nucleophilicity of a substance and in some cases can even affect the nature of the mechanism. Bunnett postulated that there could be as many as 17 factors that can contribute to a substance's nucleophilicity though it is unlikely for all to be relevant for a single reaction.[47] Of these, the most relevant factors for this study are the effects of solvent and ligand electronic and steric effects.

There has been very little systematic investigation into how the solvent affects the reactivity of metal complexes towards alkyl halides. Shrauzer et al investigated the reactivity of $[Co(dmgH)_2(PBu_3)]^-$ with MeCl in various solvents and found there wasn't a large solvent effect. However, the solvents chosen (water, methanol, ethanol and propanol) all have very similar dielectric constants so the observations are not unexpected. Hart-Davis showed that the rate of reaction of $[CpM(CO)(PPh_3)]$ (M = Co, Rh, Ir) with iodomethane is dependent on the solvent as summarised in **Table 1.4**.[48] Similarly Jawad et al. showed that the rate of reaction of $[PtPh_2(bpy)]$ with iodomethane varies by up to fifteen times in going from the least to most polar solvent.[32]

| Solvent | Dielectric constant | $k_{rel}$ / $M^{-1}s^{-1}$ |
|---|---|---|
| THF | 7.4 | 0.2 |
| Acetone | 20.7 | 0.9 |
| $CH_2Cl_2$ | 9.08 | 1.0 |
| MeCN | 36.0 | 2.5 |

**Table 1.4:** Relative rate constants for the reaction of $[CpCo(CO)(PPh_3)]$ with iodomethane. [48]

The choice of counter-ion can also affect the nucleophilicity of metal complexes. **Table 1.5** shows that the rate of reaction of $X[Mn(CO)_5]$ (X = cationic counterion) with iodomethane in acetonitrile can vary by an order of magnitude due solely to the change in counterion.

| X | $k_{rel}$ / $M^{-1}s^{-1}$ [a] |
|---|---|
| PPN | 1.5 |
| Na | 0.66 |
| Li | 0.64 |

a – error values not reported.

**Table 1.5:** Rate constants for the reaction of $X[Mn(CO)_5]$ with iodomethane in acetonitrile.

The enhanced reaction rates for ion-pair complexes compared to separated ions was postulated to be due to a highly ordered transition state as shown in **Figure 1.8**. However, an alternative explanation is simply based upon the size of the cation. Small cations such as lithium and sodium can coordinate close to the anionic centre and physically get in the way of incoming electrophiles. The much larger PPN cation has a much more diffuse charge and cannot get as close to the anion as lithium and sodium.

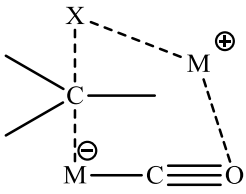


X = halide,
$M^+$ = cation

**Figure 1.8:** Proposed stabilisation of the transition state in ion-pair complexes.

Further studies looking into the effect of the counter-ion have been reported for $[CpFe(CO)_2]^-$, $[Co(CO)_4]^-$,[49] $[Mn(CO)L_4]^-$ (L = CO, $PR_3$), $[CpMo(CO)_3]^-$ and $[CpW(CO)_3]^-$.[50,51]

## 1.6 Quantifying ligand effects

One of the most prevalent methods of affecting the reactivity of a metal complex is through the choice of the attached ligand. To this end, a number of methodologies have been developed to explain and rationalise experimental observations with the aim of being able to predict the reactivity of new complexes.

Tolman's parameters are perhaps one of the earliest and still most widely applied methods of quantifying the properties of phosphines. The electronic properties of a phosphine ligand can be characterised by Tolman's electronic parameter, (ν) based on the carbonyl stretching frequency of a series of phosphine containing nickel complexes of the general formula, $[Ni(CO)_3L]$.[52,53] **Table 1.6** shows the experimental values for a selection of ligands. A correlation was observed between the ν(CO) and the electronic donating ability of the phosphine in question with the complexes containing the most donating phosphines exhibiting the lowest carbonyl stretching frequencies. ($P^tBu_3$ for example)

| **L** | ν(CO) / $cm^{-1}$ |
|---|---|
| $P(ptol)_3$ | 2066 |
| $P(o\text{-tol})_3$ | 2066 |
| $PMe_3$ | 2064 |
| $PEt_3$ | 2061 |
| $P^tBu_3$ | 2056 |

**Table 1.6:** ν(CO) for selected $[Ni(CO)_3L]$ complexes.[53]

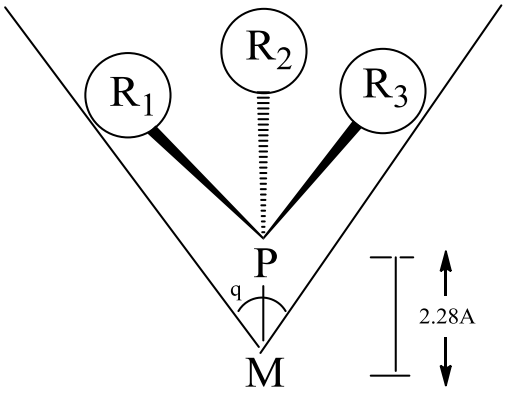


**Figure 1.9:** Representation of the Tolman cone angle, (θ) for a metal phosphine complex.

The steric bulk of the ligand was characterised by Tolman using another parameter, the *cone angle*. This is described as the angle which envelops all of the ligand and its substituents taken from a point 2.28 Å from the ligand. **Figure 1.9** shows a representation of the Tolman cone angle. The concept of both the electronic and steric parameters proposed by Tolman are useful for rationalising experimental observations and for predicting the reactivity of new complexes.

Tolman's electronic parameter is derived from IR spectroscopic data but other methods do exist to rationalise the basicity of phosphine ligands using other parameters. In a series of papers by Bodner, the $^{13}C$ and $^{31}P$ chemical shifts along with the C-P and M-P coupling constants were analysed to determine the donor and acceptor properties of the ligands.[54-65] The $pK_a$ of protinated phosphines ($HPR_3$)[66,67] and the heat of protonation of M-$PR_3$ complexes[68-76] have also been probed.

A more sophisticated method to rationalise ligand effects is the Quantitative Analysis of Ligand Effects (QALE) method which was developed by Giering and Prock.[27] It is a multiparameter correlation method that graphically compares the physical and chemical properties of complexes to the properties of their ligands. By conducting a QALE analysis on a series of complexes, the nature of the reactivity of similar complexes can be inferred.

A QALE analysis is dependent on several parameters:

- the σ electron donating power of the ligand
- the Tolman cone angle
- $E_{ar}$ – a secondary electronic affect which is also known as the aryl effect
- the π–acceptor capacity of the ligand
- "i" a parameter describing the number of hydrogens in the ligand.

The QALE methodology was applied to the series of $[IrCl(CO)(L)_2]$ complexes discussed in **Section 1.2**. Good agreements were found between the QALE stereoelectronic parameters and the experimental rate constants.

To date, over 109 analyses have been performed and collated on the QALE website, making it a useful resource.[27,77-86] In comparison to using only Tolman's parameters to rationalise experimental outcomes, QALE has proven apt at being able to separate the Tolman electronic parameter into σ-donor strength and π-acceptor strength ($\chi_d$ and $\pi_p$ respectively) of a particular ligand. Perhaps the greatest drawback of QALE is the reliance on experimental data. In order to perform a QALE analysis, detailed and extensively studied experimental systems are needed which precludes its use for new ligands for which no experimental data is available.

In 2006, Fey et al. published preliminary work investigating a series of monodentate phosphine ligands with a view to compiling a prototype ligand knowledge base (LKB).[87] This method is purely computational and its principal aim is to create a database on phosphine ligands (initially) and metal-phosphine complexes, which is sufficiently robust to allow prediction of the behaviour of new complexes.[88-91]

To construct the initial LKB, a number of parameters were selected which fulfilled the requirements of being derived from simple geometry optimisations or a single mathematical operation. Such requirements were necessary to ensure calculations could be fully automated so that a large amount of data could be generated in a short space of time. The descriptors that were selected were:

- Frontier molecular orbital energies on the free ligands
- Ligand proton affinities

- Adduct binding energies
- Two parameters to describe steric bulk – the S'4 parameter and a newly developed $He_8$ parameter

To illustrate the applicability and robustness of the computational calculations, the parameters in the LKB were applied to three systems for which extensive data is available – the Tolman electronic parameter for the $A_1$ frequency in $[Ni(CO)_3L]$ complexes, the Rh-P distance in square-planar $[RhCl(CO)(L)_2]$ complexes and $\Delta H$ / kcal $mol^{-1}$ for the reaction of $[RhCl(CO)_2]_2$ and 4L (L = phosphine). In each case, a good linear fit was found between experimental and computational data. More recent development of the LKB has extended similar methodology to diphosphine and carbene ligands and their corresponding complexes.[89]

The same drawback is present for the LKB as for QALE analysis – the necessity of a body of experimental data which is used to calibrate and refine the computational model. Such requirements has precluded the applicability of both QALE and LKB in designing new catalysts.

## 1.7 Computational Chemistry

Chemistry began as a science based solely on experiments in the laboratory. It was not until the 19th century with the advent of physical chemistry where a relationship was established between mathematics, chemistry and physics which facilitated the explanation of chemical experiments both quantitatively and qualitatively. With the advent of chemical kinetics and thermodynamics, the outcome of a reaction could be postulated before being undertaken experimentally. However, both kinetics and thermodynamics are concerned with processes on the macroscopic scale. At the end of the 19th century, it became clear that classical mechanics broke down at the sub-molecular level.

In the first quarter of the 20th century, the situation was improved by the establishment of quantum mechanics. In 1927, how hydrogen forms a chemical bond quantitatively was approached quantum mechanically by Heitler and Fritz.[92] This opened up a new

area of chemistry – quantum chemistry where approximate solutions to the Schrodinger equation for large systems were sought as opposed to exact solutions for hydrogenic systems.

Since this landmark development, quantum chemistry has enjoyed a number of other major developments. In 1930, Fock developed the Hartree equations which utilised Slater determinants in order to meet the *Pauli Exlcusion Principle*.[93] Twenty years later, the concept of Linear Combination of Atomic Orbitals (LCAO) was developed in order to solve the Hartree-Fock equation analytically.[94] More recently, more accurate methodologies to evaluate the energy of molecules have been developed such as density functional theory.

In the remainder of this chapter, a brief introduction into the key areas of computational chemistry will be undertaken.

### 1.7.1 The Schrödinger equation

Erwin Schrödinger derived the fundamental equation in quantum mechanics called the Time-dependent Schrödinger equation, given in **Equation 1.2.** In this equation $\widehat{H}$ is the Hamiltonian, which is a differential operator representing the total energy of the system. $\psi$ is the wavefunction, which depends on the space-spin coordinates of all particles. The square of the wavefunction, $\psi^2$, represents the probability distribution of the particles contained within a molecule. (This is typically referred to as the Copenhagen or Born interpretation of Quantum Mechanics).

$$\widehat{H}\psi = ih\frac{\vartheta\varphi}{\vartheta t} \qquad (\mathbf{1.2})$$

By assuming that the Hamiltonian is time-independent, the energy of a molecular system composed of *N* particles can be determined by the time independent Schrödinger equation. (TISE) as given in **Equation 1.3**.

$$\widehat{H}\psi(\vec{x}_1 \dots \vec{x}_N) = E\psi(\vec{x}_1 \dots \vec{x}_N) \qquad (\mathbf{1.3})$$

where $\hat{H}$ is the Hamiltonian operator, $x$ is the space-spin coordinate of particle, i and $E$ is the energy. The molecular Hamiltonian is given by **Equation 1.4.**

$$\hat{H} = \sum_{i=1}^{N} \frac{h^2}{2m_i} \nabla_i^2 - \sum_{i=1}^{N} \sum_{j-1,J>i}^{N} \frac{q_i \times q_j}{4\pi\epsilon |r_i - r_j|} \qquad (\mathbf{1.4})$$

The first term of **Equation 1.4** deals with the kinetic energy of the nucleus and electron. The second term is concerned with the columbic interactions between the charged particles.

The Schrödinger equation is only exactly solvable for a limited number of cases such as the hydrogen atom or hydrogen-like cations such as $He^+$. Thus a number of assumptions and simplifications are applied to **Equation 1.4** in order to ensure it is (approximately) solvable for more complicated systems.

One of these approximations is the *Born-Oppenheimer approximation*, which takes advantage of the fact that electrons are so much smaller than nuclei and thus adjust their position instantly in response to nuclear movement.[95] The TISE for a multi-electron molecule is given in **Equation 1.5.**

$$\hat{H}_T \psi_T = E_T \psi_T \quad where\, \psi_T = \psi_T(\boldsymbol{r}, \boldsymbol{R}) \qquad (\mathbf{1.5})$$

$\hat{H}_T$ is the total Hamiltonian which operates on the nuclei and electrons and $\psi_T$ is the total wavefunction for the entire system. $\boldsymbol{R}$ and $\boldsymbol{r}$ are the space-spin coordinates of all electrons and nuclei in the system, respectively. The Hamiltonian contains kinetic energy operators (both nuclear and electronic) and the potential operator. (**Equation 1.6**)

$$\hat{H}_T = \hat{T}_N + \hat{T}_e + V(\boldsymbol{r}, \boldsymbol{R}) \qquad (\mathbf{1.6})$$

$$where: \hat{T}_N = -\frac{1}{2}\sum_{\mu}\frac{1}{M_\mu}\nabla_\mu^2 \qquad (\mathbf{1.7})$$

$$and \quad \hat{T}_e = -\frac{1}{2}\sum_{i}\nabla_i^2 \qquad (\mathbf{1.8})$$

$$\hat{V}(r,R) = V_{NN} + V_{Ne} + V_{ee} = \sum_{\mu<v}\frac{Z_\mu z_v}{r_{\mu i}} - \sum_{\mu}\sum_{i}\frac{Z_\mu}{r_{\mu i}} + \sum_{i<j}\frac{1}{r_{ij}} \qquad (\mathbf{1.9})$$

The $\hat{T}_N$ term deals with the nuclear kinetic energy and $\hat{T}_e$ is the sum of all electron kinetic energy. $\hat{V}(\boldsymbol{r},\boldsymbol{R})$ is the potential energy of thee molecule in question and contains nucleus-nucleus repulsion energy ($V_{NN}$), nucleus-electron attraction energy ($V_{Ne}$) and finally electron-electron repulsion energy ($V_{ee}$).

As noted above, nuclei are much heavier than electrons and thus the nuclei can be considered as stationary with respect to the electrons. This allows the position of the nucleus to be fixed and allows for the total molecular wavefunction to be separated into two parts – the nuclear and electron wavefunction as shown in **Equation 1.10,** which can each be solved separately.

$$\psi_T(\boldsymbol{r},\boldsymbol{R}) = \phi(R)\psi(\boldsymbol{r},\boldsymbol{R}) \qquad (\mathbf{1.10})$$

where $\psi_T$ is the total wavefunction and $\phi(\boldsymbol{R})$ and $\psi(\boldsymbol{r},\boldsymbol{R})$ are the nuclear and electronic wavefunction respectively.

### 1.7.2 Orbital approximation

For a many electron atom, the wavefunction is a very complicated function of the coordinates of every electron and can be written as $\psi(r_1, r_2, \ldots)$ where $r$ is the vector from the nucleus to the electron. The orbital approximation simplifies this somewhat by writing the wavefunction as a product of $N$ single electron wavefunctions. Such

methodology is advantageous as single-electron wavefunctions can be calculated from the Schrodinger equation whereas wavefunctions for more than one electron cannot.

The wavefunction for an *N*-electron molecule is written according to **Equation 1.11.**

$$\psi(r_1, r_2, \dots N) = \psi(r_1)\,\psi(r_2)\dots \qquad (\mathbf{1.11})$$

The single electron wavefunctions in molecules are called molecular orbitals (MOs) and can be constructed from a linear combination of atomic orbitals (LCAO) as discussed in **Section 1.7.4.**

### 1.7.3 Identical particles and Slater determinants

The electrons in an atom or molecule all have identical mass and charge and hence make up an identical particle system. Exchanging the coordinates of two electrons in space results in no observable change whereas in classical mechanics two objects with identical velocity and mass can be distinguished by differing spatial coordinates. The electrons can therefore be considered identical and as the exchange does not lead to an observable result. The probability density also must not change. (**Equation 1.12a**)

$$|\psi(\overrightarrow{q_1}, \overrightarrow{q_2}, \dots \overrightarrow{q_a}, \overrightarrow{q_b}, \dots)|^2 = |\psi(\overrightarrow{q_1}, \overrightarrow{q_2}, \dots \overrightarrow{q_b}, \overrightarrow{q_a}, \dots)|^2 \qquad (\mathbf{1.12}\boldsymbol{a})$$

In order to satisfy this, exchanging the position of two electrons must either result in the same wavefunction or a change in the sign of the total wavefunction. (**Equations 1.12b** and **1.12c)**

$$\psi(\overrightarrow{q_1}, \overrightarrow{q_2}, \dots \overrightarrow{q_a}, \overrightarrow{q_b}, \dots) = \psi(\overrightarrow{q_1}, \overrightarrow{q_2}, \dots \overrightarrow{q_b}, \overrightarrow{q_a}, \dots) \qquad (\mathbf{1.12}\boldsymbol{b})$$

$$\psi(\overrightarrow{q_1}, \overrightarrow{q_2}, \dots \overrightarrow{q_a}, \overrightarrow{q_b}, \dots) = -\psi(\overrightarrow{q_1}, \overrightarrow{q_2}, \dots \overrightarrow{q_b}, \overrightarrow{q_a}, \dots) \qquad (\mathbf{1.12}\boldsymbol{c})$$

Any particle with a half integer spin, known as fermions, satisfies criterion **1.12c** and hence electrons are fermions. Bosons such as the oxygen molecule satisfy **1.12b.** As a consequence of **1.12c** two fermions cannot occupy the same quantum state which is known as the *Pauli Exclusion Principle*.

In order to satisfy the *Pauli Exclusion Principle*, Slater postulated that a determinant could be used to describe the wavefunction. An example Slater determinant for a two-electron system is shown in **Equation 1.13**.

$$\varphi = \frac{1}{\sqrt{2!}} \begin{vmatrix} \psi_1(1)\alpha(1) & \psi_1(1)\beta(1) \\ \psi_1(2)\alpha(2) & \psi_1(2)\beta(2) \end{vmatrix} \quad \textbf{(1.13)}$$

where $\frac{1}{\sqrt{2!}}$ is the normalisation factor and $\psi$ is the spatial orbital and α and β are spin functions.

Exchanging any two rows of the determinant results in a sign change whereas two identical rows leads to a vanishing of the determinant. Therefore, a Slater determinant satisfies the *Pauli Exclusion Principle*.

### 1.7.4 Linear Combination of Atomic Orbitals (LCAO)

The previous equations require the wave function to be written as a product of one-electron orbitals, the orbital approximation. A linear combination of atomic orbitals can be combined in order to generate molecular orbitals (MOs) as in **Equation 1.14.** This methodology was first used by Pauling for $H_2^+$ and was further developed by Leonard-Jones in 1929 and is known as the LCAO method.[96]

$$\phi = \sum_{i-1}^{N} a_i \psi_i \quad \textbf{(1.14)}$$

*where*: $N$ is the number of functions, $\psi_i$ is the basis set and $a_i$ is the coefficient associated with the basis set

### 1.7.5 Variational Principle

The variational principle is key to computational methods for approximating solutions to the Schrodinger equation. It is represented by the following equation:

$$E = \frac{\int \psi^* H \psi \, d\tau}{\int \psi^* \psi d\tau} \geq E_0 \qquad (\mathbf{1.15})$$

This shows that for any trial wavefunction, the energy associated with it is always greater than the energy of the ground state wavefunction. The implication is that if the energy is calculated variationally, then the lower the energy, the better the trial wavefunction. Such methodology of calculating the energy of a system allows the exact ground state energy to be approached.

## 1.8 Hartree Fock Theory

Hartree Fock theory was developed in the late 1920's by Hartree and remains a cornerstone of modern quantum chemistry. The original method developed by Hartee was called the self-consistent field (SCF) method and found the best atomic orbitals by solving the Schrodinger equation. This methodology was improved by Fock and Slater to include electron exchange, which is known as Hartree-Fock theory.

In its original formulation, the theory makes the assumption that the wave function of a system can be described by one Slater determinant consisting of spin orbitals each representing one electron. Moreover, the 2-electron electron-electron repulsion is replaced by an effective 1-electron operator. The variation principle is invoked and the coefficients of the atomic orbitals can be iteratively optimised until the lowest energy of the system is reached. The energy of the molecular system and the wavefunction corresponding to this energy are approximate.

$$\hat{F}(x_1)\psi_i = \varepsilon_i \psi_i(x_1) \qquad \mathbf{(1.16)}$$

$$\hat{F}(x_1) = \hat{H}^{core}(x_1) + \sum_{j=1}^{n} [2\hat{J}_j(x_1) - \hat{K}_j(x_1)] \qquad (\mathbf{1.17})$$

where $\hat{F}$ is the Fock operator, $\psi$ is a spatial orbital, $\varepsilon_i$ is the energy of the orbital, $\hat{J}_j$ is the coulombic operator, $K_j$ is the exchange operator and $\hat{H}^{core}$ is the Hamiltonian

$$\hat{H}^{core}(x_1) = -\frac{1}{2}\nabla_1^2 - \sum_{\alpha} \frac{Z_\alpha}{r_{1\alpha}} \qquad (\mathbf{1.18})$$

The Hamiltonian is composed of the kinetic energy of the electron and the potential energy caused by the attraction of the electron to the nucleus. $\hat{J}_j$ deals with the interaction of electron 1 and 2. (**Equation 1.19**)

$$\hat{J}_j\psi_i(x_1) = \psi_i(x_1) \iint \psi_j^*(x_2) \left(\frac{1}{r_{12}}\right) \psi_1(x_2) d\tau_2 \qquad \mathbf{(1.19)}$$

The final operator, $K_j$ arises from the fact that due to the Pauli exclusion priniciple, electrons which have the same spin cannot occupy the same quantum state

$$\hat{K}_j\psi_i(x_1) = \psi_i(x_1) \int \psi_j^*(x_2) \left(\frac{1}{r_{12}}\right) \psi_i(x_2) d\tau_2 \qquad \mathbf{(1.20)}$$

The overall electronic energy obtained using the Hartree Fock method is given by **Equation 1.21.**

$$E_{HF} = 2\sum_{i=1}^{n} \epsilon_i - \sum_{i=1}^{n}\sum_{j=1}^{n} (2J_{ij} - K_{ij}) \qquad \mathbf{(1.21)}$$

where $\varepsilon_i$ is the spatial orbital.

An initial guess of the coefficient matrix, combined with diagonalizing the Fock matrix leads to the energy matrix. Once the coefficient matrix is obtained, the result can be put into the next iteration process until the convergence criteria is met. This methodology of optimisation is often referred to as Self-Consistent-Field Theory.

## 1.9 Basis sets

The Hartree-Fock equations require molecular orbitals (MOs) to be constructed from a linear combination of atomic orbitals (AOs). Recently, a great deal of effort has been focussed into constructing basis functions in order to construct these MOs. One of the earliest types of basis functions are called Slater Type Orbitals (STOs) which result from the accurate solution to the Schrödinger equation for a hydrogenic atom. These orbitals correctly have a cusp at the nucleus and correctly decay exponentially as *r* increases. (**Figure 1.10)**

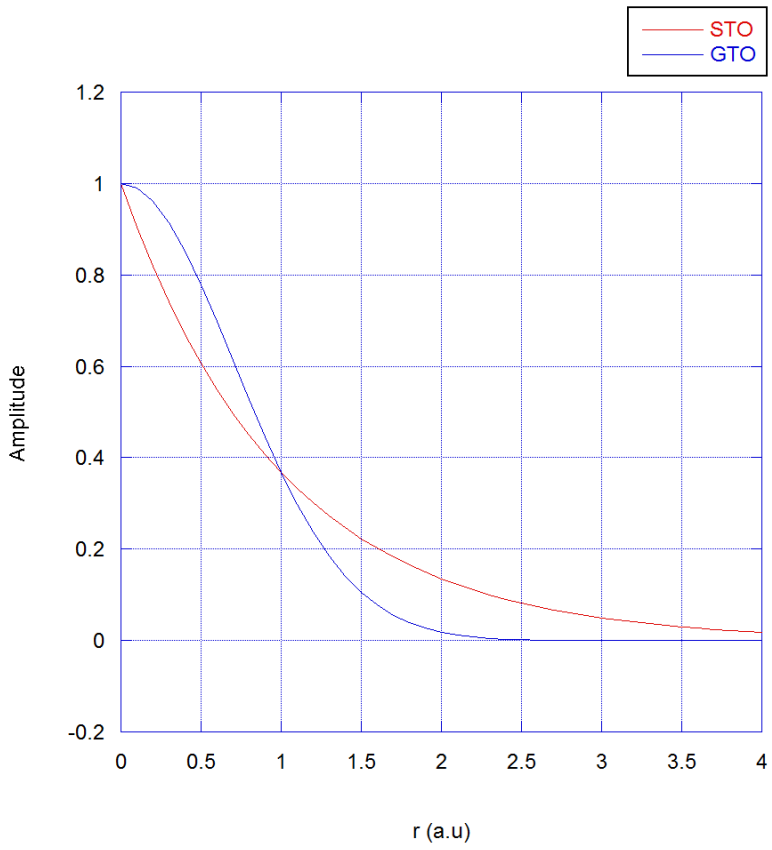


**Figure 1.10:** Illustration of GTOs (blue) and STOs (red)

One of the major issues with STOs is that their integrals are difficult and time consuming to evaluate and hence their usage has gradually diminished.

$$STO = Nr^{n-1}e^{-\varsigma r}Y_l^m(\vartheta, \phi) \quad \textbf{(1.22)}$$

Gaussian type orbitals (GTOs) were first developed by Pople *et al* to attempt to overcome this issue. These orbitals are represented by **Equation 1.23** in Cartesian coordinates.

$$GTO = Nx^i y^j z^k e^{-ar^2} \quad \textbf{(1.23)}$$

The sum of the exponents, *i, j* and *k* in **Equation 1.23** indicates the type of the orbital. A sum of zero is an s-type orbital and a sum of one indicates a p type orbital. The main difference between GTOs and STOs is the radial distance in the exponential factor is now squared and hence $r^2 = x^2 + y^2 + z^2$. Integration of GTOs is significantly quicker as integration of STOs, since the product of two Gaussians is another Gaussian and since the resulting integral is an incomplete error function, which can be evaluated efficiently. As a result, most (though not all) electronic structure programmes use GTOs

However, whilst GTOs are easier to integrate, they do have their problems. As evidenced in **Figure 1.10,** they do not have the correct cusp at the nucleus ($r = 0$) and the orbital value decreases too rapidly with increasing *r*. Such limitations must be addressed in order to justify the use of such orbitals over STOs.

Contracted Gaussian type orbitals (cGTOs) were developed in order to combine the efficiency of GTOs and the accuracy of STOs. The formula for these orbitals is given in **Equation 1.24.**

$$\varphi(CGTO) = \sum_{n=1}^{n} c_i \phi_i(pGTO) \quad \textbf{(1.24)}$$

where $\varphi(CGTO)$ is the contracted Gaussian-type orbital, $\phi_i(pGTO)$ is the primitive Gaussian function and $c_i$ is the weight of $\phi_i(pGTO)$ in the contraction.

The first term describes the weighting and *n* is the number of Gaussian primitives. Initially, *n* = 3 was shown to be the best compromise between accuracy and computational expense. This became known as a minimal basis set (STO-3G) – essentially the minimum description to achieve reasonable results.[97] However, these basis sets only have one CGTO for each atomic orbital and often do not predict the correct geometry. In order to increase the accuracy of calculations, the basis set can be further improved by the use of split valence sets.

### 1.9.1 Split Valence Basis Sets

The poor performance of minimal basis sets led to the development of new ways to construct basis sets. One methodology to attempt to improve the poor performance was to use split valence basis sets where the orbitals are split into two sets – the inner and valence electrons. The advantage of this approach is it allows the electrons to respond to any changes in bonding. The general representation for these orbitals is given in **Equation 1.25.**

X-YZg **(1.25)**

*where* X is the number of Gaussian Primitives on the inner electrons and Y and Z are the Gaussians of the valence electrons. Some examples of such basis sets are 3-21G, 6-31G and 6-311G. [97-101]

The applicability of split basis sets was further extended by Dunning et. al. Basis sets called correlation consistent basis sets are more complicated than those introduced by Pople and are more computationally expensive. Some examples are cc-pVDZ, cc-pVTZ, cc-pVQZ.[102-104]

### 1.9.2 Polarisation functions

Occasionally, split valence basis sets fail to give the correct structure as in the structure of aniline where the geometry is predicted to be flat for 3-21G basis set which is

incorrect. Polarisation functions are added to the basis set, which are basis functions with higher angular momentum (ie – p orbitals are added to hydrogen atoms and d orbitals are added to second row elements such as carbon nitrogen and oxygen. Two common examples of these basis sets are 6-31G(d,p) and 6-311G(d,p) which will feature in this thesis. Dunning's basis sets include polarisation functions in their original definition.

### 1.9.3 Diffuse functions

Some molecules that contain a lone pair of electrons, that are anionic or that are in the excited state can require the usage of diffuse functions. The level of electron density should generally decrease rapidly outside of the bonding region but for these cases, the electron density is distributed over a larger area and does not decay as rapidly. In the Pople basis sets, diffuse functions are denoted with a plus symbol. Two plus symbols in succession denote that diffuse functions are added to both heavy and light atoms. In the Dunning basis sets, the use of the prefix aug- denotes that diffuse functions are to be used. eg. 6-31++G and aug-cc-pvdz.[99,102]

### 1.9.4 Effective core potentials (ECPs)

The inner electrons of heavy atoms are largely unaffected by any chemical bonding. Moreover, the all-electron basis sets are impractical for heavy elements such as transition metals due to the prohibitive computational cost, which scales to the fourth power. . In addition, in particular for the second and third row of the transition metals, relativistic effects start to become important. To address these issues, effective-core potential basis sets were developed. There are two general methods here – model potential and pseudo potential. For the pseudo potential the core electrons are replaced with an artificial potential which contains relativistic effects. This reduces computational cost and gives a better description of inner electrons compared with the model potential. Any interactions between the core electrons and the valence electrons are ignored. Two of the most commonly used effective core potentials are LANL2DZ and SDD. [105,106 105,106 105,106 105,106 105,106 105,106 105,106 105,106 105,106]

## 1.10 Density Functional Theory (DFT)

Density functional theory has been employed in solid state physics since the 1970s as a method for evaluating the energy of many electron systems. It was not adopted in calculations in quantum chemistry until the 1990s when the approximations employed in the theory were better refined. DFT tends to be fast and gives qualitatively correct results. Whilst there are still issues associated with the methodology, it has emerged as one of the most commonly used methods in quantum chemistry. The methodology relies on the premise that the ground state energy of a molecule can be determined using the electron density, which is a function of the spatial coordinates. As the electron density is mathematically simple, a relationship between the electron density and the energy of a system would be advantageous if one were to exist.

In 1964, Hohenberg and Kohn showed that the ground state of a N-electron system is determined by the distribution of the electron density. This observation is now known as the first *Hohenberg-Kohn theorem*.[107,108]

The proposed theorem can be proven using a theoretical argument. Let us define two systems with different potentials, $V_1(r)$ and $V_2(r)$ with Hamiltonians for each system defined by **Equations 1.26** and **1.27**.

$$\hat{H}_1 = \hat{T} + \sum i\, V_1(\vec{r_i}) + \sum_{i<j} \frac{1}{r_{ij}} \qquad (\mathbf{1.26})$$

$$\hat{H}_2 = \hat{T} + \sum i\, V_2(\vec{r_i}) + \sum_{i<j} \frac{1}{r_{ij}} \qquad (\mathbf{1.27})$$

The use of the variation principle allows for the derivation of **Equations 1.28** and **1.29** where $\psi_1$ and $\psi_2$ are the eigenfunctions of $\hat{H}_1$ and $\hat{H}_2$ respectively.

$$E_1 = \langle \psi_1 | \hat{H}_1 | \psi_1 \rangle < \langle \psi_2 | \hat{H}_1 | \psi_2 \rangle \qquad (\mathbf{1.28})$$

$$E_2 = \langle \psi_2 | \hat{H}_2 | \psi_2 \rangle < \langle \psi_1 | \hat{H}_2 | \psi_1 \rangle \quad (\mathbf{1.29})$$

The right hand side of **Equations 1.28 and 1.29** can be rewritten according to **Equations 1.30 and 1.31.**

$$\langle \psi_2 | \hat{H}_1 | \psi_2 \rangle = \langle \psi_2 | \hat{H}_1 - \hat{H}_2 | \psi_2 \rangle + \langle \psi_2 | \hat{H}_2 | \psi_2 \rangle = \int \rho_2(\vec{r}) [V_i(\vec{r}) - V_2(\vec{r})] + E_2$$

**(1.30)**

$$\langle \psi_1 | \hat{H}_2 | \psi_1 \rangle = \langle \psi_1 | \hat{H}_2 - \hat{H}_1 | \psi_1 \rangle + \langle \psi_2 | \hat{H}_2 | \psi_2 \rangle = \int \rho_1(\vec{r}) [V_2(\vec{r}) - V_1(\vec{r})] + E_1$$

**(1.31)**

**Equations 1.30** and **1.31** can be combined into one expression to give **Equation 1.32.**

$$E_1 + E_2 < E_1 + E_2 + \int \rho_1(\vec{r}) [V_2(\vec{r}) - V_1(\vec{r})] + \int \rho_2(\vec{r}) [V_1(\vec{r}) - V_2(\vec{r})]$$

**(1.32)**

$$E_1 + E_2 < E_1 + E_2 \quad \textbf{(1.33)}$$

If $\rho_1$ and $\rho_2$ are identical, the final two integral terms in **Equation 1.32** vanish and a contradiction is reached in **Equation 1.33.** Therefore, $\rho_1$ and $\rho_2$ cannot be equal to one another and hence this proves that the electron density is unique for different external potentials. The ground state DFT energy is therefore given by **Equation 1.34.**

$$E_0[\rho] = T[\rho] + E_{ee}[\rho] + \int \rho(\vec{r}) V(\vec{r}) d\vec{r} \quad (\mathbf{1.34})$$

where $T[\rho]$ is the kinetic energy functional, $E_{ee}$ is the electron-electron repulsion and $\int \rho(\vec{r}) V(\vec{r}) d\vec{r}$ is the external potential term.

### 1.10.1 Kohn-Sham Equation

In 1965, HF-like orbitals were introduced into DFT in order to work out the kinetic energy of an artificial system of non-interacting particles.

$$T_{ref} = \langle T[\rho_0] \rangle_{ref} = -\sum_{i-1}^{n} \left\langle \psi_i^{KS} \middle| \frac{1}{2}\nabla^2 \middle| \psi_i^{KS} \right\rangle \quad (\mathbf{1.35})$$

where $\psi^{KS}$ is the Kohn-sham orbital.

The electron-electron repulsion and electron-nucleus attraction can be simulated classically according to **Equations 1.36** and **1.37** respectively.

$$V_{ee}^{ref} = \langle v_{ee}[\rho_0] \rangle_{ref} = J[\rho_0] = \iint \frac{\rho_0(\vec{r}_1)\rho_0(\vec{r}_2)}{r_{12}} d\vec{r}_1 d\vec{r}_2 \quad (\mathbf{1.36})$$

$$V_{en} = \int \rho_0(\vec{r}) V(\vec{r}) d\vec{r} = -\sum_A^{\cdot} Z_A \int \frac{\rho_0(\vec{r}_1)}{|\vec{r}_1 - \vec{r}_A|} d\vec{r}_1 \quad (\mathbf{1.37})$$

The replacement of the terms, $T[\rho]$ *and* $E_{ee}[\rho]$ in **equation 1.34** with $T_{\text{ref}}$ and $T[\rho]$ leads to a new formula for the ground state energy of a molecule.

$$E_0 = \langle T[\rho_0] \rangle_{ref} + J[\rho_0] + \int \rho_0(\vec{r}) V(\vec{r})\, d\vec{r} + \Delta\langle T[\rho_0] \rangle + \Delta\langle V_{ee}[\rho_0] \rangle \quad \mathbf{(1.38)}$$

The first three terms in **Equation 1.38** can be solved exactly and the remaining terms are simply the difference between a real and an imaginary reference system. The final two terms can be combined into a new term, known as the exchange correlation, denoted by $E_{\text{XC}}$.

$$E_{XC}[\rho_0] = \Delta\langle T[\rho_0] \rangle + \Delta\langle V_{ee}[\rho_0] \rangle \quad \mathbf{(1.39)}$$

The final equation for calculating ground state energies is given in **Equation 2.41.**

$$E_0 = \langle T[\rho_0] \rangle_{ref} + J[\rho_0] + \int \rho_0(\vec{\boldsymbol{r}}) V(\vec{\boldsymbol{r}})\, d\vec{\boldsymbol{r}} + E_{xc}[\rho_0]$$

$$= \sum_{i=1}^{n} \left\langle \psi_i^{KS} \middle| \frac{1}{2}\nabla^2 \middle| \psi_i^{KS} \right\rangle + \iint \frac{\rho_0(\vec{r}_1)\rho_0(\vec{r}_2)}{r_{12}} d\vec{r}_1 d\vec{r}_2 + \int \rho_0(\vec{r}) V(\vec{r}) d\vec{r} + E_{XC}[\rho_0]$$

**(1.40)**

The first term is concerned with the expectation value. The second term is the electron electron coulombic repulsion energy. The third term is the coulombic attraction energy. The final term, $E_{XC}[\rho_0]$, is the hardest term to evaluate due to the exact formulation of this term being unknown. Modern approaches to DFT focus on finding good approximations for this term.

## 1.10.2 Exchange Correlation functionals

There are currently five different types of exchange correlation functional in common usage. These are:

- Local Density Approximation (LDA)
- Local Spin Density Approximation (LSDA)
- The generalised gradient approach (GGA)
- Meta-GGA
- Hybrid GGA

### 1.10.2.1 Local density approximation (LDA) and Local Spin density approximation (LSDA)

The LDA is the simplest approach to approximate the exchange correlation. In this case it can be calculated from the Thomas-Fermi gas model.[109,110] It is based on the fact that the exchange functional at any point in space is dependent on the local density at that point – which gives rise to the name of this functional.

The LDA is a very crude method and was originally met with scepticism from the community as its performance for systems which were not as homogeneous as gas systems was questionable. However, due to cancellation of errors, the functional still performs reasonably.

The local spin density approximation is a modified version of LDA which allows for spin polarisation. The local densities of $\alpha$ and $\beta$ spin electrons are not equal and hence the LDA is modified to allow for this spin polarisation. The LSDA functional is equivalent to the LDA functional for any system where the electrons are securely paired but has the advantage that it can handle systems which contain one or more unpaired electrons (such as radical systems) . An example of an LSDA functional would be VWN (Vosko, Wilk and Nusair)[111]

Both the LDA and LDSA are not typically employed anymore in quantum chemistry where the electron density distribution in molecules is not as homogeneous as in gases. They have been superseded by other methods such as gradient functionals.

### 1.10.2.2 Generalised gradient approach (GGA)

True molecular systems are more complicated than a simple homogenous electron gas. Therefore for a real system the $E_{XC}[\rho_0]$ functional cannot be simply approximated using the LDA or LSDA approach. The gradient of the electron density also has to be taken into account which gives rise to the generalised gradient approach (GGA). Two of the most well-known functionals include Becke's B88 functional and Perdew and Wang's PW91 functional.[112,113] GGA functionals yield ground state bond distances with an accuracy of 1.5 pm and binding energies within around 20 $kJmol^{-1}$.

### 1.10.2.3 Meta – GGA and Hybrid GGA

Basic GGA only includes the first derivative of the electron density. In meta-GGA the second derivative of the electron density (the Laplacian) is taken into account. The $E_{XC}$ functional can be treated as a functional of the Laplacian of the density, the kinetic

energy density or the electron density. Some meta-GGA functionals include TPSS, VSXC and the Minnesota functionals.

Hybrid GGA formulates the exchange correlation functional by combining a GGA functional with exact exchange energy from HF. The most popular hybrid GGA is the B3LYP functional which includes exchange correlation functionals and adjustable fitting parameters.

One of the greatest challenges for computational chemists is how to appropriately describe *Van der Waals* interactions, which are critical particularly in modelling proteins and supramolecular systems. These interactions are often not modelled well using DFT as it is a non-local interaction. Efforts have been made by Grimme in order to address such problems by including a semi-empirical dispersion potential to the DFT energy.[114,115]

## 1.11 Solvation

Historically, *ab-initio* calculations were carried out in the gas phase which simplified the system of interest. However, it is necessary to take solvent into account in order to accurately model reaction conditions. In the gas phase, many reactions are predicted to be endothermic and should not progress yet in solution phase, they proceed readily. Two methodologies have been developed in order to address this issue. The first is the explicit or microsolvation model and the second one is the implicit or continuum model.[116-120]

### 1.11.1 Explicit model

The explicit solvent model is one in which solvent molecules are directly included in the calculations and either covalently or hydrogen bond to the molecule of interest. It is significantly better than gas phase models as it attempts to simulate real environment of the molecules studied. However, there are limitations to this approach – where should the molecules be placed and how many are required in order to construct an accurate

model? Typically, this approach only models one solvation shell which in some cases is not sufficient. The addition of more solvent molecules considerably increases the computational cost of the calculations and issues can be encountered with convergence. Where there is a specific solvent – molecule interaction (such as coordinated acetonitrile) then the explicit model must be used. However, in other cases, more approximate methods can be employed.

### 1.11.2 Onsager model

Perhaps the simplest model to account for solvent in Gaussian is the Onsager model where a spherical cavity is generated and the solute is placed in the centre of the cavity. The cavity is surrounded by a continuous medium of dielectric constant. Any present dipole in the molecule induces a dipole in the solvent medium.

### 1.11.3 PCM method

The implicit model also called the Polarizable Continuum Model treats solvent effects differently. A cavity is created by a series of overlapping spheres centred on the atoms in a medium and then places the solute in this cavity. The free energy change for this reaction is given by **Equation 1.41.**

$$\boldsymbol{G_{sol} = G_{es} + G_{dr} + G_{cav}} \qquad \textbf{(1.41)}$$

where $G_{es}$ is the free energy change caused by electrostatic interaction between solvent and solute, $G_{dr}$ is the dispersion repulsion interaction between solute-solvent and solvent-solvent and $G_{cav}$ is the cost in terms of free energy of creating a cavity in the continuum medium.

A recent paper by Ward and Meijer successfully modelled a series of reactions using the PCM method with explicit inclusion of solvents.[121] Where there is a specific solvent – molecule interaction (such as coordination) then the explicit model must be used. This is not expected to be the case here as the majority of the solvents employed are non-

coordinating. Thus, the PCM method is employed throughout this thesis to model solvent effects.

## 1.12 Computational studies on $S_N2$ reactions

Much effort has been put in the reaction of $X^- + CH_3Y$, which is often used as a model for larger, more complicated systems.[122-132] If both X and Y are halogens, then the dominant mechanism is $S_N2$ nucleophilic substitution as shown in **Scheme 1.7.**

$$X^- + CH_3Y \longrightarrow CH_3X + Y^-$$

**Scheme 1.7:** Generalised $S_N2$ reaction

Computational studies on these reactions have focussed on both symmetrical reactions (where X and Y are the same) and non-symmetrical reactions (where X and Y are different halide ions). The reaction of chloride ions with MeCl and MeBr has been shown to occur via three mechanisms, with formation of products via an ordered pre-reaction complex being the most favourable.

These computational studies confirmed that $S_N2$ reactions of anionic halides with alkyl halides (where the halides are the same) occur via a double-well potential as shown in **Figure 1.11**. The nucleophile, $X^-$ reacts with RY and displaces $Y^-$ in a single reaction step. There is a central barrier, separated by pre- and post- reaction complexes. This is often termed a Walden-inversion reaction and was first observed experimentally in 1896 by Paul Walden who showed that an enantiomerically pure compound could be converted to the alternative enantiomer and back again through an $S_N2$ attack of hydroxide.[133]

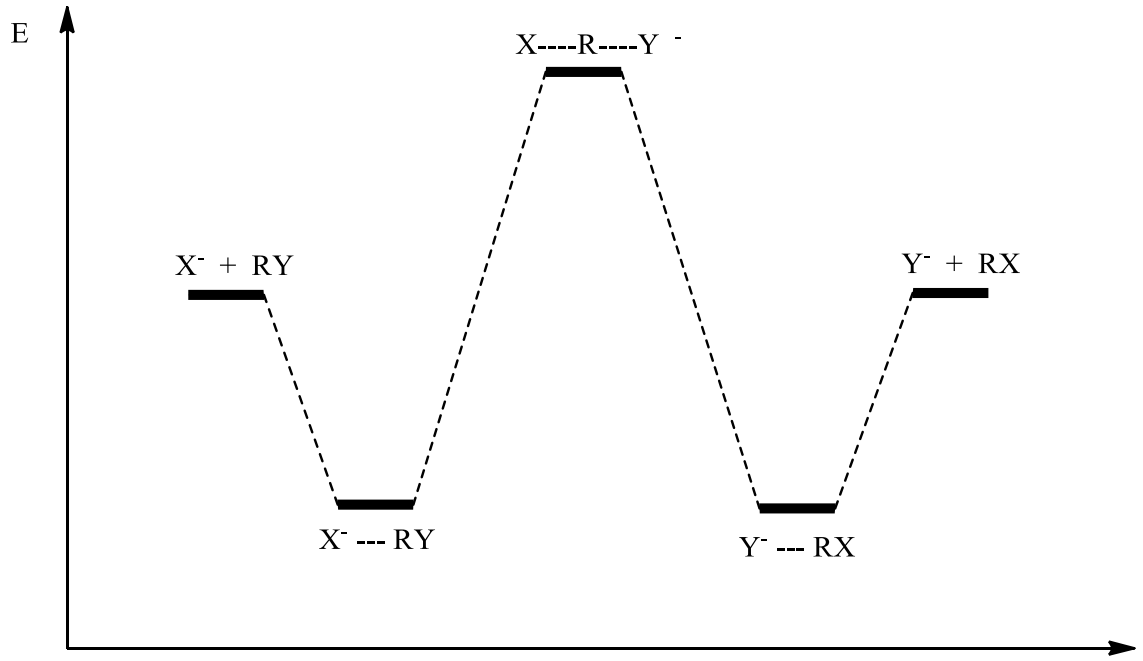


**Figure 1.11:** Schematic of a Walden Inversion Reaction for a symmetrical nucleophilic reaction.

### 1.12.1 Computational studies on nucleophilic metal complexes

The reactivity of nucleophilic metal complexes with alkyl halides has received some attention in computational studies, particularly for the complex $[RhI_2(CO)_2]^-$ and variants where one iodide and one carbonyl ligand are replaced with phosphines. In 1996, the geometries of two distinct transition states were optimised using HF theory as shown in **Figure 1.12**.[134] Iodomethane can approach the complex linearly as in **a** where the Rh-C-I angle is approximately linear or in a side-on fashion as in **b** where the Rh-C-I angle deviates significantly from 180°, which was the first report of a transition state structure for this type of system. Note that structure **a** is more stable than structure **b**.

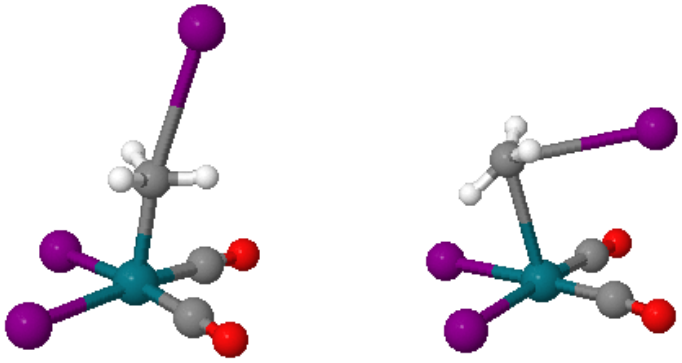

**(a)** **(b)**

**Figure 1.12:** Optimised structures (RHF, LANL1DZ basis) of linear **(a)** and bent **(b)** transition states for the reaction of $[Rh(CO)_2I_2]^-$ and MeI.[134] Figure reproduced from reference 122.

The complete catalytic cycle for the reaction of $[Rh(CO)_2I_2]^-$ and MeI was investigated independently using DFT by Kinnunen and Laasonen and Ivanova et al.[135-137] The oxidative addition of iodomethane to both *cis*-$[Rh(CO)_2I_2]^-$ and *trans*-$[Rh(CO)_2I_2]^-$ was investigated and the reaction with *trans*-$[Rh(CO)_2I_2]^-$ was found to be the most energetically favourable. The oxidative addition step was further examined by Cheong et al. who took solvent into account in the calculations.[138] The calculated barrier height for the reaction (19.3 kcal $mol^{-1}$) was in good agreement with the experimental value (20.9 kcal $mol^{-1}$).

Kinnunen et al. also investigated the complexes *cis*- and *trans*-$[Rh(CO)_2X_2]^+$ (X = $PI_3$, $PBr_3$, $PCl_3$, $PF_3$ and $P^tBu_3$) with a view to establish whether the rate of oxidative addition of iodomethane could be enhanced by changing the phosphine.[139] The addition to the *trans* complex was either equally or more favourable than addition to the *cis* isomer. For X = $PCl_3$ and $PBr_3$ the activation barriers were lower than those for $[Rh(CO)_2I_2]^-$. The complex bearing the most nucleophilic phosphine, $P^tBu_3$ had the highest activation barriers attributed to the steric bulk of the ligand.

A DFT study by Felix et al. investigated $[Rh(CO)_2I_2]^-$, $[RhI(CO)(PEt_3)_2]$ and $[Rh_2Cl_2(CO)_2(spanphos)]$ where spanphos is a bridging diphosphine ligand.[140] Initially three different transition state structures for $[Rh(CO)_2I_2]^-$, shown in **Figure 1.13,** were optimised in solution phase and in agreement with Griffin et al., the linear transition

state was found to be the most energetically favourable. However the geometrical parameters of the transition state showed some notable differences from the gas-phase HF study, in particular the Rh-$CH_3$ and C-I distances

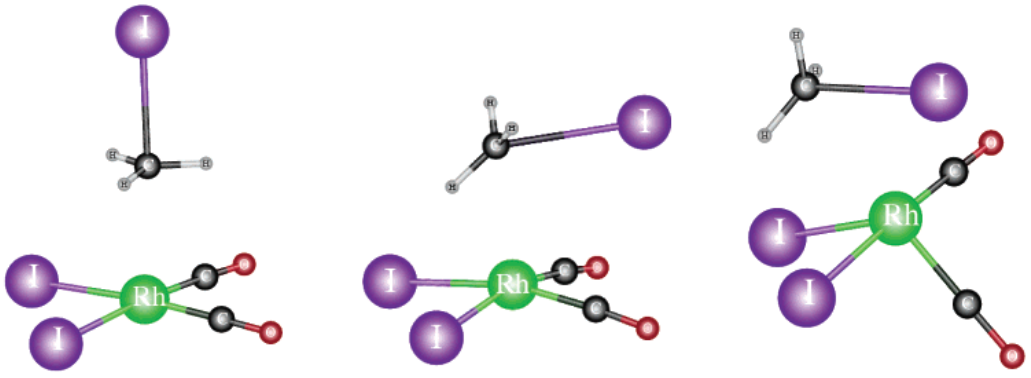


**(a)** **(b)** **(c)**

**Figure 1.13:** Optimised structures of linear **(a)**, bent **(b)** and front **(c)** transition states for the reaction of $[Rh(CO)_2I_2]^-$ and MeI.[140] Figure reproduced from reference 128.

The complex $[RhI(CO)(PEt_3)_2]$ reported by Cole-Hamilton was modelled by $[RhI(CO)(PH_3)_2]$ and $[Rh_2Cl_2(CO)_2(spanphos)]$ by $[Rh_2Cl_2(PH_3)_2(CO)_2]$. For the dimeric complex, reaction of iodomethane with only one rhodium centre was considered which is consistent with the experimental findings. For both systems, a linear $S_N2$ transition state was optimised **(Figure 1.14)**.

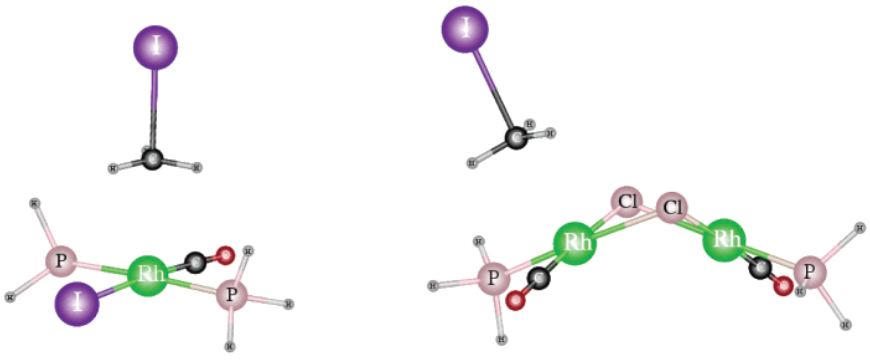


**(a)** **(b)**

**Figure 1.14:** Optimised transition state structures for the reaction of $[RhI(CO)(PH_3)_2]$ **(a)** and $[Rh_2Cl_2(PH_3)_2(CO)_2]$ **(b)** with MeI.[140] Figure reproduced from reference 126.

A number of other phosphine modified complexes have also been investigated computationally. **Figure 1.15** shows the structures of three complexes bearing chelating phosphines whose reactivity towards iodomethane was investigated by Haynes et al. [RhI(CO)(dppms)] was of particular interest as it showed enhanced reactivity towards iodomethane when compared to $[RhI_2(CO)_2]^-$ (8 times faster) but also exhibited a fast migratory CO insertion.[141] $[Rh(CO)(xantphos)]^+$ was shown to catalyse the carbonylation of methanol in the presence of a source of iodide.[142] Computational investigations by both Cavallo and Haynes on [RhI(CO)(dppms)] confirmed a lower barrier height for the oxidative addition reaction and also showed that the enhanced rate of migratory insertion could be due to steric crowding of the octahedral complex which is alleviated after insertion.[143]

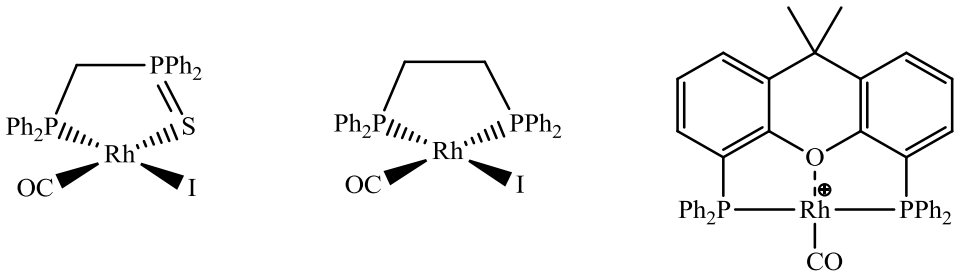


**Figure 1.15:** Structures of [RhI(CO)dppms], [RhI(CO)dppe] and $[Rh(CO)(xantphos)]^+$.

[Rh(β-diketonate)(CO)L] complexes, as shown in **Figure 1.16,** have been the subject of a number of papers and a comprehensive review by Conradie.[144] The influence of the R and R' groups in the β-diketonate ligand $(RCOCHCOR')^-$ on the reactivity of the rhodium complexes towards oxidative addition was investigated computationally. The reactivity was determined to be largely dependent on the energy of the HOMO which strongly resembles a metal $d_z^2$ orbital. A linear relationship between this energy and the experimental rate constant for the reaction with iodomethane showed that this methodology could be used to indicate the reactivity of other complexes.

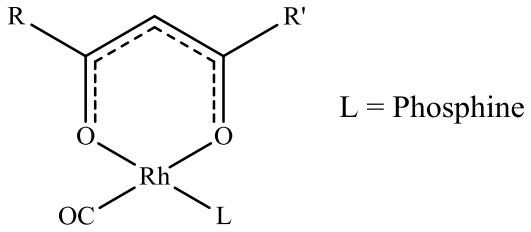


**Figure 1.16:** Structure of [Rh(β-diketonate)(CO)L]

Such methodology was further explored in a recent paper by Hashemi et al. where the series of platinum complexes from **Section 1.2** were computationally investigated. A very good linear relationship between the experimental rate constant ($k_2$) and the reactant HOMO energies was established.[145]

## 1.13 Computational parameters

With so many different basis sets and functionals available to the modern computational chemist, it can be difficult to identify the most appropriate. Recent papers have benchmarked a variety of functionals in terms of computational time and how accurately they model geometries. The B3LYP functional has been selected for use herein as it performs well for organometallic complexes and allows for comparisons to be made with work previously undertaken in the group.[112,113,146]

Multiple basis sets will be used throughout the thesis: SDD[106], 6-311G(d,p),[100,147] cc-pVDZ[102] and a mixed basis set consisting of SDD on the central metal and 6-311G(d,p) on all other atoms (denoted as Mixed Basis).

## 1.14 Thesis aims

A number of computational studies of the nucleophilic reactivity of metal complexes have been reported in the literature, as described above. However, there has been no systematic investigation covering a range of systems. In this project, the principal aim was to apply DFT methods to model the $S_N2$ reactions of several classes of metal nucleophiles in order to establish how computed parameters correlate with experimental rate constants. Since there is quite a large body of experimental data available for the

reactions of metal complexes with iodomethane, this provides an ideal opportunity to test the applicability of computational methods for these systems. Location of transition state structures allows barrier heights to be calculated for comparison with experimental rate data. It is also of interest whether other computed parameters show correlations with observed reactivity, for example transition state geometrical data (such as M–C and C–X distances) and reactant HOMO energies or ν(CO) frequencies. The classes of metal complex targeted were (i) 18-electron anions (e.g. $[M(CO)_n]^-$, $[CpM(CO)_n]^-$); (ii) neutral 18-electron species (e.g. [CpIr(CO)L]); (iii) 16-electron square planar complexes (e.g. $[IrCl(CO)L_2]$, [Rh(acac)(CO)L], $[Pt(bpy)R_2]$). These examples span a wide range of reactivity and enable the modelling of the effects of changing both the metal and the ligands to be tested. The effect of phosphine ligands is a particular focus of the investigation, along with the role of solvent.

As well as modelling existing literature data, another aim was to supplement this by carrying out experimental studies to generate additional reactivity data. To this end, kinetic studies have been conducted on the oxidative addition reactions of a number of complexes from the [Rh(acac)(CO)L] family. Of particular interest were complexes containing phosphines with *ortho*-anisyl substituents, due to the enhanced reactivity displayed by these systems. The origin of this high nucleophilicity was also probed computationally.

A further aim of the experimental work was to explore the reactivity of iridium carbonyl complexes containing xantphos-type diphosphine ligands, with different steric and electronic properties, as illustrated in **Figure 1.17**. This resulted in the observation of some interesting transformations which were probed spectroscopically and using DFT.

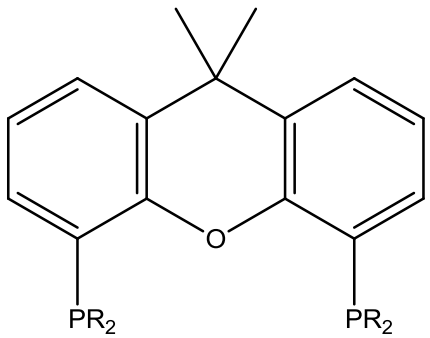


R = *o*tol, $^t$Bu, Ph

**Figure 1.17:** General ligand structure of xantphos-type ligands.

## 1.15 References


(1) Swain, C. G.; Scott, C. B. *J. Am. Chem. Soc.* **1953**, *75*, 141.

(2) Edwards, J. O. *J. Am. Chem. Soc.*, **1954**, *76*, 1540.

(3) Edwards, J. O. *J. Am. Chem. Soc.* **1956**, *78*.

(4) Bach, R. D.; Dmitrenko, O.; Thorpe, C. *J. Org. Chem.*, **2008**, *73*, 12.

(5) Bachrach, S. M.; Pereverzev, A. *Org. Biomol. Chem.*, **2005**, *3*, 2095.

(6) Bento, A. P.; Bickelhaupt, F. M. *J. Org. Chem.*, **2007**, *72*, 2201.

(7) Bickelhaupt, F. M.; Buisman, G. J. H.; de Koning, L. J.; Nibbering, N. M. M.; Baerends, E. J. *J. Am. Chem. Soc.*, **1995**, *117*, 9889.

(8) Chandrasekhar, J.; Smith, S. F.; Jorgensen, W. L. *J. Am. Chem. Soc.*, **1985**, *107*, 154.

(9) Deng, L.; Branchadell, V.; Ziegler, T. *J. Am. Chem. Soc.*, **1994**, *116*, 10645.

(10) Glukhovtsev, M. N.; Pross, A.; Radom, L. *J. Am. Chem. Soc.*, **1995**, *117*, 2024.

(11) Graul, S. T.; Bowers, M. T. *J. Am. Chem. Soc.*, **1991**, *113*, 9696.

(12) Gronert, S. *Acc. Chem. Res.*, **2003**, *36*, 848.

(13) Harder, S.; Streitwieser, A.; Petty, J. T.; Schleyer, P. v. R. *J. Am. Chem. Soc.*, **1995**, *117*, 3253.

(14) Laerdahl, J. K.; Uggerud, E. *Int. J. Mass Spectrom.*, **2002**, *214*, 277.

(15) Lee, I.; Kim, C. K.; Sohn, C. K.; Li, H. G.; Lee, H. W. *J. Phys. Chem.*, **2002**, *106*, 1081.

(16) Li, C.; Ross, P.; Szulejko, J. E.; McMahon, T. B. *J. Am. Chem. Soc.*, **1996**, *118*, 9360.

(17) Nibbering, N. M. M. *Acc. Chem. Res.* **1990**, *23*, 279.

(18) Norton, S. H.; Bachrach, S. M.; Hayes, J. M. *J Org. Chem.*, **2005,** , *70*, 5896.

(19) Olmstead, W. N.; Brauman, J. I. *J. Am. Chem. Soc.*, **1977**, *99*, 4219.

(20) van Bochove, M. A.; Bickelhaupt, F. M. *Eur. J. Org. Chem.* **2008**, 649.

(21) van Bochove, M. A.; Swart, M.; Bickelhaupt, F. M. *J. Am. Chem. Soc.* **2006**, *128*, 10738.

(22) Vayner, G.; Houk, K. N.; Jorgensen, W. L.; Brauman, J. I. *J. Am. Chem. Soc.* **2004**, *12*, 9054.

(23) Viggiano, A. A.; Morris, R. A.; Paschkewitz, J. S.; Paulson, J. F. *J. Am. Chem. Soc.* **1992**, *114*, 10477.

(24) Dessy, R. E.; Pohl, R. L.; King, R. B. *J. Am. Chem. Soc.*, **1966**, *88*, 5121.

(25) Pearson, R. G.; Figdore, P. E. *J. Am. Chem. Soc.*, **1980**, *102*, 1541.

(26) Vaska, L.; DiLuzio, J. W. *J. Am. Chem. Soc.* **1961**, *83*, 2784.

(27) Wilson, M. R.; Woska, D. C.; Prock, A.; Giering, W. P. *Organometallics*, **1993**, *12*, 1742.

(28) Kubota, M.; Kiefer, G. W.; Ishikawa, R. M.; Bencala, K. E. *Inorg.Chim. Acta.*, **1973**, *7*, 195.

(29) Vaska, L. *Acc. Chem. Res.*, **1968**, *1*, 335.

(30) Chock, P. B.; Halpern, J. *J. Am. Chem. Soc.*, **1966**, *88*, 3511.

(31) Rendina, L. M.; Puddephatt, R. J. *Chem. Rev.* **1997**, *97*, 1735.

(32) Jawad, J. K.; Al-Obaidy, F. N. K.; Hammud, J. A.; Al-Azab, F. *Organomet. Chem.*, **2000**, *599*, 166.

(33) Brink, A.; Roodt, A.; Steyl, G.; Visser, H. G. *Dalton Trans.*, **2010**, *39*, 5572.

(34) Conradie, J.; Conradie, M. M. *Dalton Trans.*, **2011**, 8226.

(35) Conradie, M. M.; Erasmus, J. J. C.; Conradie, J. *Polyhedron*, **2011**, *30*, 2345.

(36) Conradie, J.; Erasmus, J. J. C. *Cent. Eur. J. Chem.*, **2012** *10*, 256.

(37) Schrauzer, G. N.; Deutch, E. *J. Am. Chem. Soc.*, **1969**, *91*, 12.

(38) Schrauzer, G. N.; Deutch, E.; Windgassen, R. J. *J. Am. Chem. Soc.*, **1968**, *90*, 2441.

(39) Theys, R. D.; Dudley, M. E.; Hossain, M. M. *Coord. Chem. Rev.*, **2009**, *253*, 180.

(40) Rosenblum, M.; Bucheister, A.; Chang, T. C. T.; Cohen, M.; Marsi, M.; Samuels, S. B.; Scheck, D.; Sofen, N.; Watkins, J. C. *Pure Appl. Chem.*, **1984**, *56* 129.

(41) Ma, H.; Yang, B. *Huaxue Tongbao*, **1993**, 5.

(42) Cooke, M. P. *J. Am. Chem. Soc.*, **1970**, *92*, 6080.

(43) Hohenschutz, H.; Von Kutepow, N.; Himmele, W. *Hydrocarbon Processing*, **1966**, *45*, 141.

(44) Thomas, C. M.; Suss-Fink, G. *Coord. Chem. Rev.*, **2003**, *243*, 125.

(45) Rankin, J.; Poole, A. D.; Benyei, A. C.; Cole-Hamilton, D. J. *Chem. Commun.*, **1997**, 1835.

(46) Ellis, P. R.; Pearson, J. M.; Haynes, A.; Adams, H.; A., B. N.; Maitlis, P. M. *Organometallics*, **1994**, *13*, 3215

(47) Bunnett, J. F. *Annu. Rev. Phys. Chem.*, **1963**, *14*, 271.

(48) Hart-Davis, A. J.; Graham, W. A. G. *Inorg. Chem.*, **1970**, *9*, 2658.

(49) Moro, A.; Foa, M.; Cassar, L. *J. Organomet. Chem.*, **1980**, *185*, 79.

(50) Darensbourg, M. Y.; Darensbourg, D. J.; Burns, D.; Drew, D. A. *J. Am. Chem. Soc.*, **1976**, *98*, 3127.

(51) Darensbourg, M. Y.; Jimenez, P.; Sackett, J. R. *J. Organomet. Chem.*, **1980**, *202*, C68.

(52) Tolman, C. A. *Chem. Rev.*, **1977** *77*, 313.

(53) Tolman, C. A. *J. Am. Chem. Soc.*, **1970**, *92*, 2953.

(54) Bodner, G. M.; Todd, L. J. *Inorg Chem.*, **1974**, *13*, 360.

(55) Bodner, G. M.; Gagnon, C.; Whittern, D. N. *J. Organomet. Chem.*, **1983**, *243*, 305.

(56) Bodner, G. M.; May, M. P.; McKinney, L. E. *Inorg Chem.*, **1980**, *19*, 1951.

(57) Bodner, G. M. *Inorg Chem.*, **1975**, *14*, 1932.

(58) Bodner, G. M.; Kahl, S. B.; Bork, K.; Storhoff, B. N.; Wuller, J. E.; Todd, L. J. *Inorg Chem.*, **1973**, *12*, 1071.

(59) Bodner, G. M.; Todd, L. J. *Inorg Chem.*, **1974**, *13*, 1335.

(60) Bodner, G. M. *Inorg Chem.*, **1975**, *14*.

(61) Mann, B. E. *J. Chem. Soc., Perkin Trans.*, **1972**, *2*, 80.

(62) Lauterbur, P. C.; King, R. B. *J. Am. Chem. Soc.*, **1965**, *87*, 3266.

(63) Bodner, G. M.; Gaul, M. *J. Organomet. Chem.*, **1975**, *101*, 63.

(64) McFarlane, W. *Proc. R. Soc. A.*, **1968**, *306*, 185.

(65) Gansow, O. A.; Kimura, B. Y. *Chem. Commun.*, **1970**, 1621.

(66) P.B. Kisanga; J.G. Verkade; Schwesinger, R. *J. Org. Chem.*, **2000**, *65*, 5341.

(67) Allman, T.; Goel, R. G. *Can. J. Chem.*, **1982**, *60* 716.

(68) Angelici, R. J. *Acc. Chem. Res.*, **1988**, *28*, 51.

(69) Sowa Jr., J. R.; Angelici, R. J. *Inorg. Chem.*, **1991**, *30*, 3534.

(70) Sowa Jr., J. R.; Zanotti, V.; Angelici, R. J. *Inorg. Chem.*, **1991**, *30*, 4110.

(71) Sowa Jr., J. R.; Zanotti, V.; Angelici, R. J. *Inorg Chem.*, **1993**, *32*, 848.

(72) Sowa Jr., J. R.; Zanotti, V.; Facchin, G.; Angelici, R. J. *J. Am. Chem. Soc.*, **1991**, *113*, 9185.

(73) Sowa Jr., J. R.; Zanozzi, V.; Facchin, G.; Angelici, R. J. *J. Am. Chem. Soc.*, **1982**, *114*, 160.

(74) Rottink, M. K.; Angelici, R. J. *J. Am. Chem. Soc.*, **1993**, *115*.

(75) Sowa Jr., J. R.; Bonamo, J. B.; Zanotti, V. *Inorg. Chem.*, **1992**, *31*, 1370.

(76) Bush, R. C.; Angelici, R. J. *Inorg. Chem.*, **1988**, *27*, 681.

(77) Clarke, M. L.; Cole-Hamilton, D. J.; Slawin, A. M. Z.; Woollins, J. D. J. C. S. *Cherm. Commun.*, **2000,**, 2065.

(78) Eriks, E.; Liu, H.-Y.; Prock, A.; Giering, W. P. *Inorg. Chem.*, **1989**, *28*, 1759.

(79) Golovin, M. N.; Rahman, M. M.; Belmonte, J. E.; Giering, W. P. *Organometallics*, **1985**, *4*, 1981.

(80) Rahman, M. M.; Liu, H.-Y.; Eriks, K.; Prock, A.; Giering, W. P. *Organometallics*, **1989**, *8*, 1.

(81) Rahman, M. M.; Liu, H.-Y.; Prock, A.; Giering, W. P. *Organometallics*, **1987**, *6*, 650.

(82) Smith, J. M.; Coville, N. J. *Organometallics*, **2001**, *20*, 1210.

(83) Bartholomew, J.; Fernandez, A. L.; Lorsbach, B. A.; Wilson, M. R.; Prock, A.; Giering, W. P. *Organometallics*, **1996**, *15*, 295.

(84) Fernandez, A. L.; Reyes, C.; Prock, A.; Giering, W. P. *Perkin Trans.*, **2000**, *1033*.

(85) Liu, H.-Y.; Eriks, E.; Prock, A.; Giering, W. P. *Organometallics*, **1990**, *9*, 1758.

(86) Smith, J. M.; Coville, N. J.; Cook, L. M.; Boeyens, J. C. A. *Organometallics*, **2000**, *19*, 5273.

(87) Fey, N.; Tsipis, A. C.; Harris, S. E.; Harvey, J. N.; Orpen, A. G.; Mansson, R. A. *Chem. Eur. J.*, **2006**, *12*, 291.

(88) Jover, J.; Fey, N.; Harvey, J. N.; Lloyd-Jones, G. C.; Orpen, A. G.; Owen-Smith, G. J. J.; Murray, P.; Hose, D. R. J.; Osborne, R.; Purdie, M. *Organometallics*, **2010**, *29*, 6245.

(89) Jover, J.; Fey, N.; Harvey, J. N.; Lloyd-Jones, G. C.; Orpen, A. G.; Owen-Smith, G. J. J.; Murray, P.; Hose, D. R. J.; Osborne, R.; Purdie, M. *Organometallics*, **2012**, *31*, 5302.

(90) Fey, N.; Orpen, A. G.; Harvey, J. N. *Coord. Chem. Rev.*, **2009**, *253*, 704.

(91) Fey, N.; Haddow, M. F.; Harvey, J. N.; McMullin, C. L.; Orpen, A. G. *Dalton Trans.*, **2009**, 8183.

(92) Heitler, W.; London, F. *Zeit. fur. Phys.*, **1927**, *44*, 455.

(93) Fock, V. A. *Z. Phys.* **1930**, *61*, 126.

(94) Roothaan, C. C. J. *Rev. Mod. Phys.*, **1951**, *23*, 69.

(95) Born, M.; Oppenheimer, R. *Ann. Phys.*, **1927** *389*, 457.

(96) Lennard-Jones, J. E. *Trans. Faraday. Soc.* **1929**, *25*, 668.

(97) Hehre, W., J, . *J. Chem. Phys.*, **1969**, *51*, 2657.

(98) Binkley, J. S. *J. Am. Chem. Soc.*, **1980**, *102*, 939.

(99) Ditchfield, R.; Hehre, W., J,; ; Pople, J. A. *J. Chem. Phys.*, **1971**, *54*, 724.

(100) McLean, A. D. *J. Chem. Phys.* **1980**, *72*, 5639.

(101) Raghavachari, K.; Binkley, J. S.; Seeger, R.; Pople, J. A. *J. Chem. Phys.* **1980** *72*, 650.

(102) Dunning Jr, T. H. *J. Chem. Phys.*, **1989**, *90*, 1007.

(103) Kendall, R. A.; Dunning Jr, T. H.; Harrison, R. J. *J. Chem. Phys.* **1992,** , *96*, 6796.

(104) Woon, D. E.; Dunning Jr, T. H. *J. Chem. Phys.* **1993**, *98*, 1358.

(105) Hay, P. J.; Wadt, W. R. *J. Chem. Phys.* **1985**, *11*, 793.

(106) Dolg, M. *Theor. Comput. Chem.*, **2002** *11*, 793.

(107) Hohenberg, P.; Kohn, W. *Phys. Rev.* **1964, 1**, *36*, B86.

(108) Kohn, W.; Sham, L. J. *Phys. Rev.* **1965**, *140(4A), A1133*.

(109) Fermi, E. *Rend. Accad. Naz. Lincei.* . **1927**, *6*, 602.

(110) Thomas, L. H. *Proc. Carmbridge. Phil. Roy. Soc* **1927**, *23(5)*, 542.

(111) Vosko, S. H.; Wilk, L., ;; Nusair, M. *Can. J. Chem.*, **1980**, *58*, 1200.

(112) Perdew, P.; Cbevary, J. A.; Vosko, S. H.; Jackson, K. A.; Rederson, M. R.; Singh, D. J.; Fiolhais, C. *Phys. Rev. B.* **1992** *37* . 785.

(113) Lee, C.; Yang, W.; Parr, R. G. *Phys. Rev. B.* **1988**, *37* 785.

(114) Grimme, S. *J. Comput. Chem.* . **2004**, *25*, 1463.

(115) Grimme, S. *J. Comput. Chem.*. **2006,**, *27*, 1787.

(116) Canses, E.; Mennucci, B.; Tomasi, J. *J. Chem. Phys.*, **1997**, *107*, 3032.

(117) Miertus, S.; Tomasi, J. *J. Chem. Phys.*, **1955**, *23*, 1833.

(118) Mulliken, R. S. *J. Chem. Phys.* **1982**, *3*, 214.

(119) Tomasi, J.; Mennucci, B.; Camm, R. *Chem. Rev.* **2005**, *105*, 2999.

(120) Tomasi, J.; Persisco, M. *Chem. Rev.* **1994**, *94*, 2027.

(121) Wragg, A. B.; Derossi, S.; Easun, T. L.; George, M. W.; Sun, X. Z.; Hartl, F.; Shelton, A. H.; Meijer, A. J. H. M.; Ward, M. D. *Dalton Trans.* **2012**, *41*, 10354.

(122) Manikandan, P.; Zhang, J.; Hase, W. L. *J. Phys. Chem. A*, **2012**, *116*, 3061.

(123) Mikosch, J.; Trippel, S.; Eichhorn, C.; Otto, R.; Lourderaj, U.; Zhang, J. X.; Hase, W. L.; Weidemüller; M.; Wester, R. *Science* **2008**, *319*, 183.

(124) Vande Linde, S. R.; Hase, W. L. *J. Am. Chem. Soc.*, **1989**, *111*, 2349.

(125) Vande Linde, S. R.; Hase, W. L. n. *J. Phys. Chem.* **1990**, *94*, 6148.

(126) Mann, D. J.; Hase, W. L. *J. Phys. Chem. A* **1998**, *10*, 6208.

(127) Hase, W. L. *Science*, **1994**, *266*, 998.

(128) Wang, Y.; Hase, W. L.; Wang, H. *J. Chem. Phys.*, **2003**, *118*, 2688.

(129) Mikosch, J.; Zhang, J.; Trippel, S.; Eichhorn, C.; Otto, R.; Sun, R.; de Jong, W. A.; Weidemüller, M.; Hase, W. L.; Wester, R. *J. Am. Chem. Soc.*, **2013**, *135*, 4250.

(130) Xie, J.; Sun, R.; Siebert, M. R.; Otto, R.; Wester, R.; Hase, W. L. *J. Phys. Chem. A*, **2013**, *117*, 7162.

(131) Xie, J.; Kohale, S. C.; Hase, W. L.; Ard, S. G.; Melko, J. J.; Shuman, N. S.; Viggiano, A. *J. Phys. Chem. A* **2013**, *117*, 14019.

(132) Otto, R.; Xie, J.; Brox, J.; Trippel, S.; Stei, M.; Best, T.; Siebert, M. R.; Hase, W. L.; Wester, R. *Direct Dynamics Faraday Discuss*, **2012**, *157*, 41.

(133) Walden, P. *Eur. J. Org. Chem.* **1896**, *29*, 133.

(134) Griffin, T. R.; Cook, D. B.; Haynes, A.; Pearson, J. M.; Monti, D.; Morris, G. E. *J. Am. Chem. Soc.*, **1996**, *118*, 3029

(135) Kinnunen, T.; Laasonen, K. *Journal of Molecular Structure (Theochem)*, **2000**, *540*, 910.

(136) Kinnunen, T.; Laasonen, K. *Journal of Molecular Structure (Theochem)*, **2001**, *542*, 272.

(137) Ivanova, E. A.; Gisdakis, P.; Nasluzov, V. A.; Rubailo, A. I.; Rosch, N. *Organometallics*, **2001**, *20*, 1161.

(138) Cheong, M.; Ziegler, T. *Organometallics*, **2005**, *24*, 3053.

(139) Kinnunen, T.; Laasonen, K. *Journal of Organometallic Chemistry* **2003**, *665*, 150.

(140) Feliz , M.; Freixa , Z.; van Leeuwen , P. W. M. N.; Bo, C. *Organometallics*, **2005**, *24* 5718.

(141) Gonsalvi, L.; Adams, H.; Sunley, G. J.; Ditzel, E.; Haynes, A. *J. Am. Chem. Soc.*, **2002**, *124*, 13597

(142) Williams, G. L.; Parks, C. M.; Smith, C. R.; Adams, H.; Haynes, A.; Meijer, A. J. H. M.; Sunley, G. J.; Gaemers, S. *Organometallics*, **2011**, *30*, 6166.

(143) Cavallo, L.; Sola, M. *J. Am. Chem. Soc.*, **2001**, *123*, 12294.

(144) Conradie, J. *Dalton Trans.*, **2015**, *44*, 1503.

(145) Hashemi, M. *J. Organomet. Chem.*, **2015**, *776*, 77.

(146) Becke, A. D. *Phys. Rev.*, **1988**, *38*.

(147) Krishnan, R.; Binkley, J. S.; Seeger, R.; Pople, J. A. *J. Chem. Phys.*, **1980**, *72*, 650.

# CHAPTER 2

# Modelling nucleophilicity of anionic 18-electron metal complexes

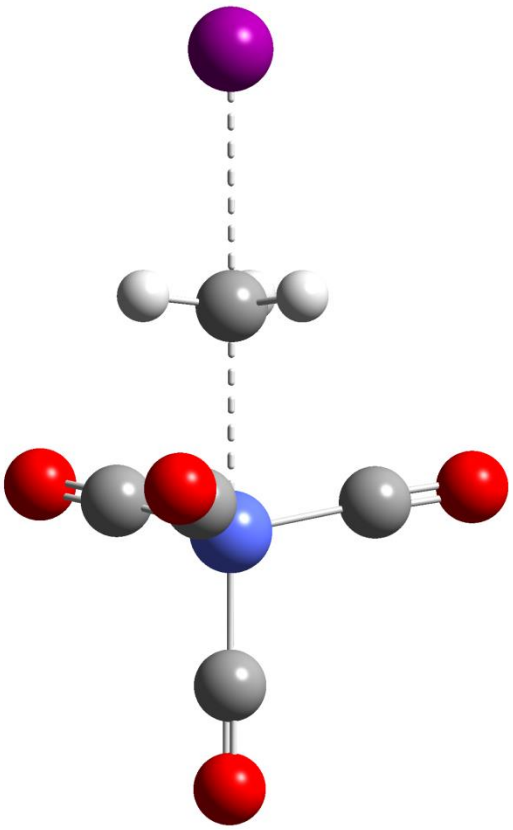

## 2.1 Introduction

The concept of nucleophilicity plays a central role in organic chemical reactions. It has received less attention in inorganic chemistry, where metal carbonyl complexes are perhaps the most well studied. Some complexes such as $[V(CO)_6]^-$ are poor nucleophiles with a nucleophilicity similar to water.[1] On the other hand, others such as $[CpFe(CO)_2]^-$ are highly nucleophilic.[2-4] Cobaloxime nucleophiles, which are model complexes for vitamin $B_{12}$[5,6] and Ni-porphryin complexes are some of the most powerful nucleophiles in the literature.[7] The structures of these anions are shown in **Figure 2.1.**

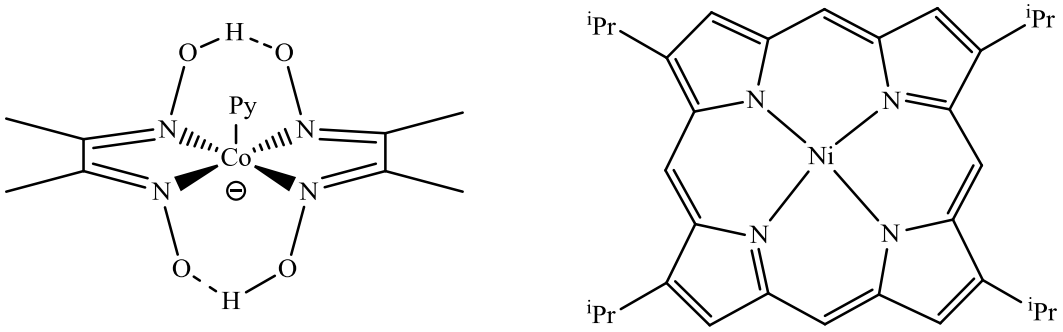


**Figure 2.1:** Example structures of cobaloxime and Ni-porphyrin complexes.

In this study, an important goal is to determine which, if any, computed parameters show a good relationship with experimental rate constants with a view of both explaining experimental observations and predicting the behaviour of novel complexes. In order to do this, a small, well described system was initially needed. Such prerequisites were necessary to allow a number of basis sets and computational methods to be investigated within a suitable time frame. **Figure 2.2** shows the structures of a series of metal complexes investigated by Dessy et al. and Pearson et al. and discussed in **Chapter 1** which are ideally suited for this purpose.[2,4] They are all mono-anionic metal complexes bearing carbonyl ligands and are small and computationally inexpensive to investigate. Perhaps most importantly, their reactivities towards iodomethane span several orders of magnitude.

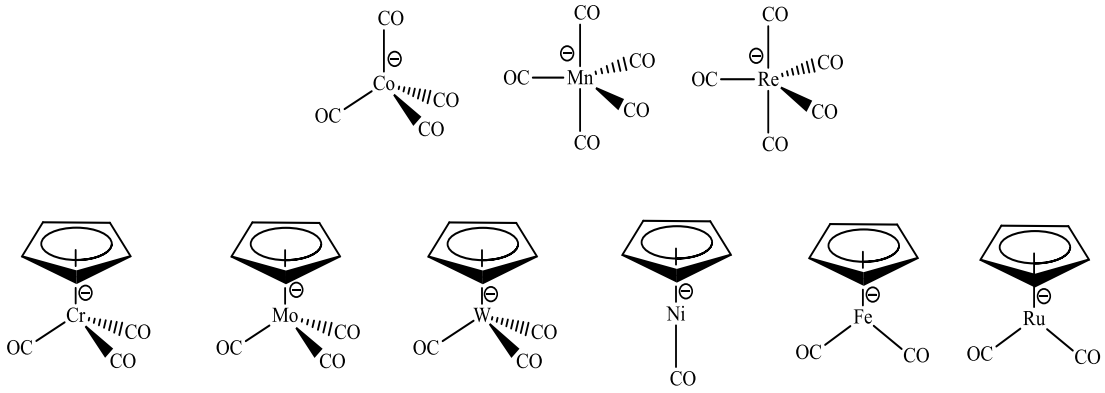


**Figure 2.2:** A series of anionic 18-electron metal carbonyl complexes

The nucleophilicity of the complexes in **Figure 2.2** was quantified through reactions with alkyl halides. These complexes each have 18-electrons and react with iodomethane according to **Scheme 2.1.** The metal complex reacts as a nucleophile towards the carbon atom of iodomethane through an $S_N2$ transition state, which subsequently liberates an iodide ion.

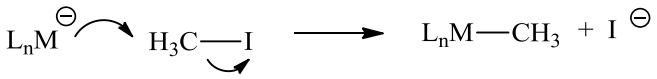


**Scheme 2.1:** General reaction of a metal nucleophile with iodomethane.

It is noted that the experimental data was subject to a number of assumptions which are summarised along with their experimental rate constants in **Table 2.1.** The rate constants for the reaction of these complexes with iodomethane span eight orders of magnitude. Here, $[Co(CO)_4]^-$ is the least nucleophilic and $[CpFe(CO)_2]^-$ is the most nucleophilic anion.

| Complex | $k$ [b]/ $M^{-1}s^{-1}$ | log ($k$ /$M^{-1}s^{-1}$) |
|---|---|---|
| $[Co(CO)_4]^-$ | 0.0437 | -1.36 |
| $[CpCr(CO)_3]^-$ | 0.075 | -1.12 |
| $[CpMo(CO)_3]^-$ | 1.5 | 0.176 |
| $[CpW(CO)_3]^-$ | 2.4 | 0.380 |
| $[Mn(CO)_5]^-$ | 7.4 | 0.869 |
| $[Re(CO)_5]^-$ | 1000 [a] | 3.00 |
| $[CpNi(CO)]^-$ | 220000 [a] | 5.34 |
| $[CpRu(CO)_2]^-$ | 300000 [a] | 5.48 |
| $[CpFe(CO)_2]^-$ | 2800000 [a] | 6.45 |

a - data estimated from experimental data for reaction of complex with EtBr in DME

b – error values not reported.

**Table 2.1:** Experimental rate constants for reaction of a series of anionic metal carbonyls with iodomethane.[2,4] (THF, 25 °C)

In this chapter, a number of different parameters will be investigated for comparison with experimental rate constants. The calculated barrier height, defined as the energy difference between the separated reactants and the transition state, the energy of the HOMO of the reactant complex and the carbon-iodide (C-I) and carbon-metal (C-M) bond lengths in the transition state were selected for analysis. A number of basis sets will also be investigated to deduce which affords the best results in an acceptable time frame. The effect of the solvent on the nature of the transition state will also be probed.

## 2.2 Modelling nucleophilicity using DFT

The symmetric reaction of a chloride or iodide ion with MeCl or MeI respectively in the gas-phase is often used as a benchmark for these studies. A significant number of experimental[8-13] and theoretical studies have been reported for these reactions.[14-22] The reaction of iodide and iodomethane was initially investigated in this study to illustrate the reaction profile. The energy profile for the reaction of iodide with iodomethane is shown in **Figure 2.3** in the gas-phase and the solution phase. The potential energy surface is characterised by two minima associated with the reactant and product ion-

dipole structures, which interconvert through a transition state resulting from attack of the iodide ion at the carbon centre.

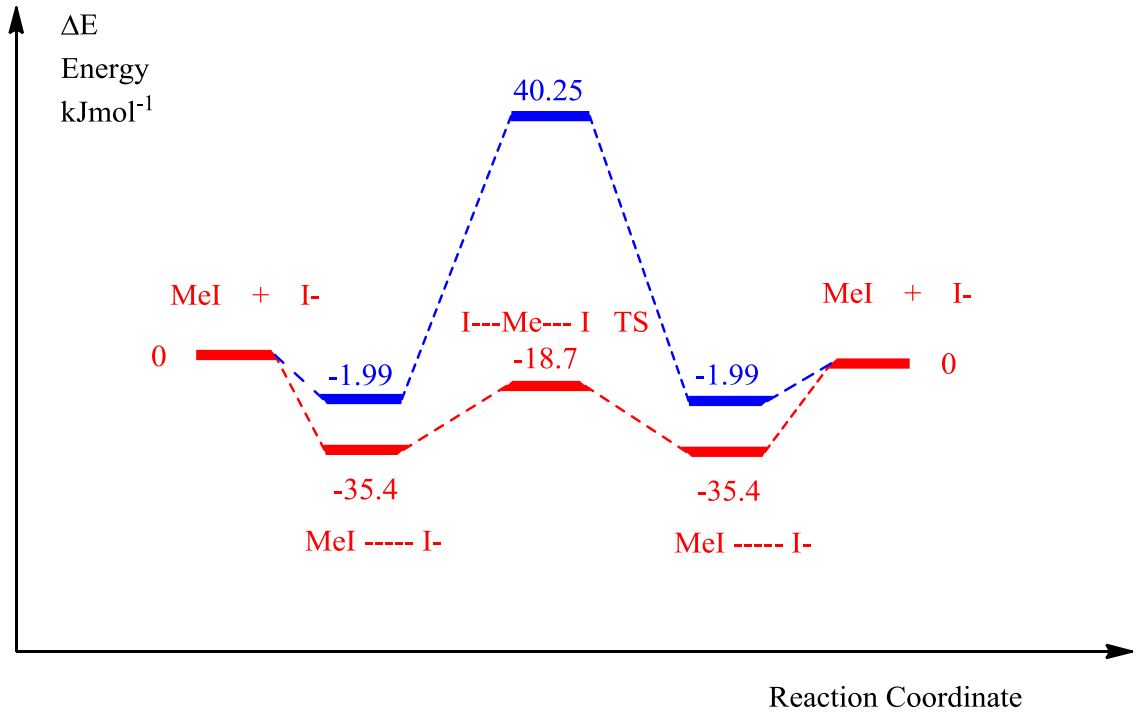


**Figure 2.3:** Energy profile (ΔE) for the reaction of iodide ion with iodomethane. (DFT-B3LYP/SDD Gas (red) and THF (blue))

Inclusion of solvent in the calculations raises the barrier height of the reaction. The reactants, products and both ion-dipole complexes are solvated more strongly than the transition state. In each of these, the anionic charge is localised on an iodide and thus strongly solvated whereas in the transition state it is more delocalised.

A representation of the gas-phase transition state is shown in **Figure 2.4**. The C-I distances in the gas-phase (2.77 Å) are almost identical to those in solvent phase (2.76 Å) The I-C-H angles for both transition states were all 90°.

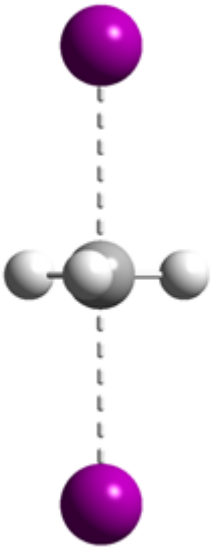

**Figure 2.4:** Optimised transition state for the reaction of iodomethane and iodide ion. (DFT-B3LYP/SDD Gas)

### 2.2.1 $[Co(CO)_4]^-$

$[Co(CO)_4]^-$ was the smallest complex in the series and so was investigated first. To construct a reaction energy profile it was necessary to optimise the structures of several species as illustrated in **Figure 2.5.** These are the separated reactants (**I**), the reactant ion-dipole complex (**II**), the transition state (**III**), the product ion-dipole complex (**IV**) and the separated products (**V**).

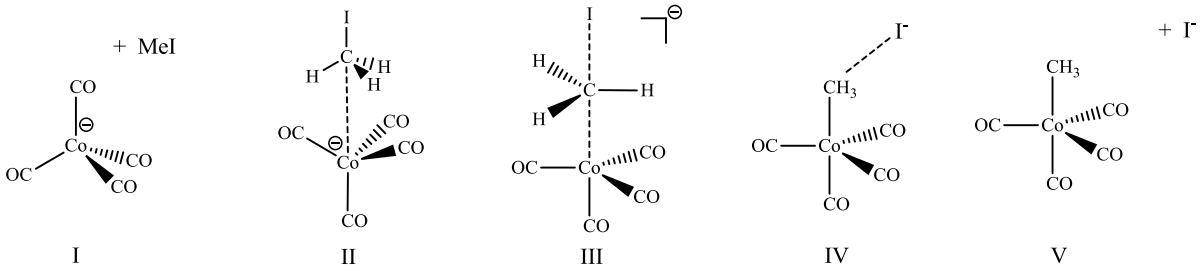


**Figure 2.5:** Structures optimised for the reaction of $[Co(CO)_4]^-$ with MeI to construct a reaction energy profile

The effect of solvent was investigated by repeating optimisations using solvents with a wide range of dielectric constants. The effect of different basis sets was also probed. **Figure 2.6** shows the structure of the transition state which was initially optimised in the gas-phase.

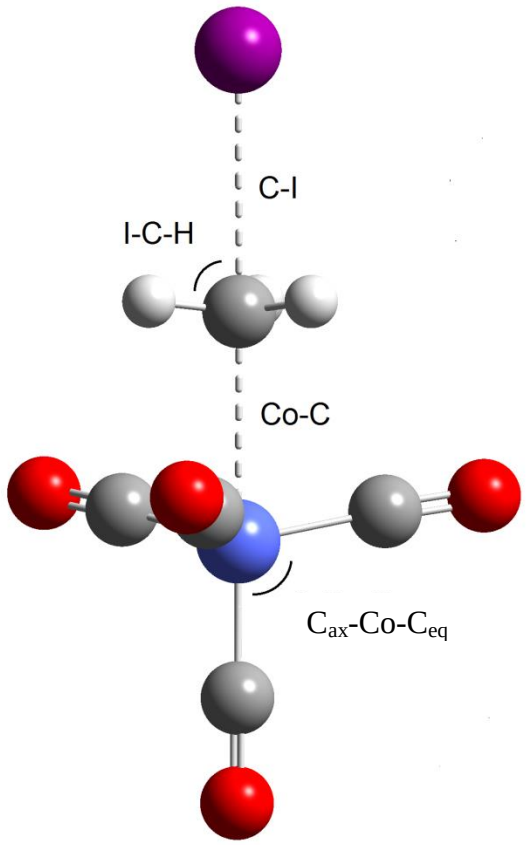


**Figure 2.6:** Optimised transition state for the reaction between $[Co(CO)_4]^-$ and iodomethane. (DFT-B3LYP/SDD – gas-phase)

The reactant complex adopts a regular tetrahedral geometry around the metal centre with C-Co-C angles of 109.5°. In the transition state, the average $C_{ax}$-Co-$C_{eq}$ angle is 101.14° and the geometry around the cobalt atom is approximately trigonal bypyramidal. The C-I distance has lengthened from 2.20 Å in the reactant to 2.95 Å in the transition state. Iodomethane is approximately tetrahedral with I-C-H angles of 107.27° but in the transition state the I-C-H bond angles are 84°. The transition state can therefore be described as quite "late" as it more closely resembles the product structure rather than the reactant structure.

To probe how the solvent affects the properties of the transition state a number of solvents were selected with dielectric constants ranging from ε = 1.92 (heptane) to 80.1 (water). Transition states were optimised with inclusion of solvent using Gaussian's default PCM model. DFT computed geometric data is given in **Table 2.2.**

| Solvent | ε | C-I / Å | C-Co / Å | Average $C_{ax}$-Co-$C_{eq}$ angle / ° | Average I-C-H angle/ ° |
|---|---|---|---|---|---|
| Gas | 1 | 2.94 | 2.59 | 101.14 | 83.95 |
| Heptane | 1.92 | 2.87 | 2.67 | 101.61 | 86.79 |
| Toluene | 2.38 | 2.82 | 2.69 | 101.77 | 87.10 |
| THF | 7.58 | 2.80 | 2.74 | 102.18 | 89.230 |
| DCM | 8.53 | 2.80 | 2.74 | 102.33 | 89.310 |
| Acetone | 20.70 | 2.79 | 2.76 | 102.35 | 89.76 |
| MeOH | 24.55 | 2.78 | 2.76 | 102.37 | 89.85 |
| MeCN | 32.50 | 2.78 | 2.76 | 102.37 | 89.86 |
| $H_2O$ | 80.10 | 2.78 | 2.760 | 102.35 | 90.24 |

**Table 2.2:** Geometric data for $[Co(CO)_4]^-$ and MeI transition state (DFT-B3LYP/SDD solvent as listed)

**Table 2.2** clearly shows that the transition state structure is affected by the solvent polarity. As the dielectric constant increases, the C-I distance decreases and the C-Co distance increases – the transition state gradually becoming earlier and more "reactant like". The largest change is observed between gas-phase and heptane where the C-I distance decreases by 0.0784 Å. A change of 0.0856 Å is observed between heptane and water. Similar changes were observed for the angles. The I-C-H angles for the gas-phase transition state are all close to 84 ° but become larger as the dielectric constant increases.

The effect of the basis set on the structure of the transition state was also investigated in the gas-phase. Selected transition state distances and angles are given in **Table 2.3**.

| Basis set | C-I / Å | C-Co / Å | Average $C_{ax}$-Co-$C_{eq}$ angle / ° | Average I-C-H angle / ° |
|---|---|---|---|---|
| **SDD** | 2.95 | 2.59 | 101.14 | 83.96 |
| **6-311G(d,p)** | 2.95 | 2.59 | 101.04 | 83.95 |
| **cc-pVDZ** | 2.91 | 2.59 | 101.30 | 83.56 |
| **cc-pVTZ** | 2.90 | 2.59 | 100.97 | 85.98 |
| **Mixed** | 2.85 | 2.66 | 101.57 | 86.49 |

**Table 2.3:** Geometric data for $[Co(CO)_4]^-$ and MeI transition state (DFT-B3LYP/ Gas, basis set as listed)

Across the basis sets investigated, a small difference of 1° was observed in the C-Co-C and 3° for the I-C-H angles. A small change from 2.95 Å to 2.91 Å was observed in the C-I distance in changing from SDD to cc-pVTZ respectively. The largest change in distance from SDD was for the mixed basis whose transition state is earlier as characterised by a short C-I distance. Overall, the choice of basis set has an effect on the nature of the transition state but the effect is not as large as the effect of solvent.

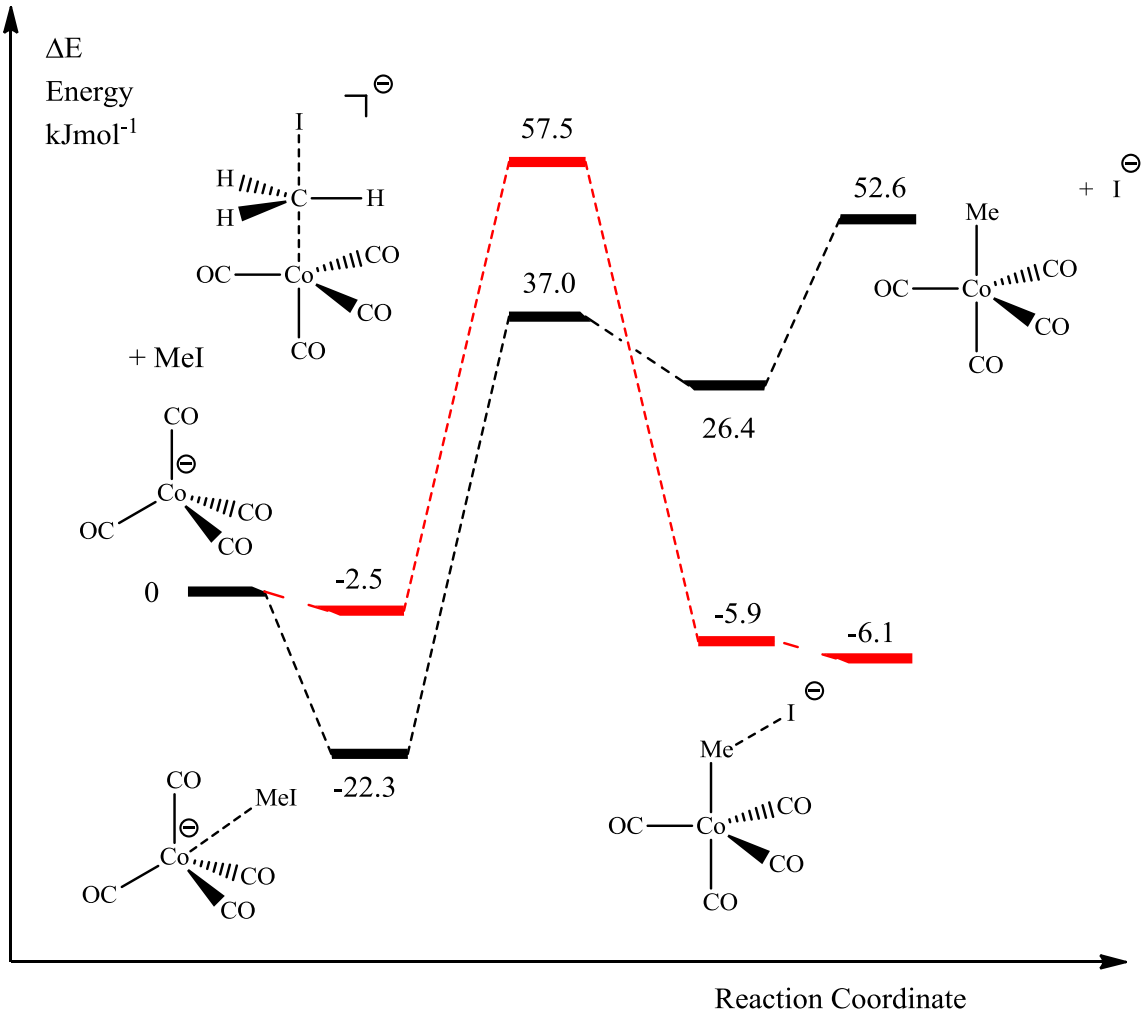


**Figure 2.7:** Energy profile (ΔE) for the reaction of $[Co(CO)_4]^-$ with iodomethane. (DFT-B3LYP/SDD – Gas (black) and THF (red))

**Figure 2.7** shows an energy profile for the reaction of $[Co(CO)_4]^-$ with iodomethane**.** The reactant ion-dipole complex is at a lower energy than the separated reactants. The iodomethane molecule adopts an eclipsed conformation with respect to the carbonyl ligands of $[Co(CO)_4]^-$ in this species, presumably due to weak hydrogen bonds between the hydrogen atoms on iodomethane and the oxygen atoms of the carbonyl ligands. This structure is shown in **Figure 2.8**. In the transition state, the C-H bonds of iodomethane are staggered with respect to the carbonyl ligands of the cobalt complex.

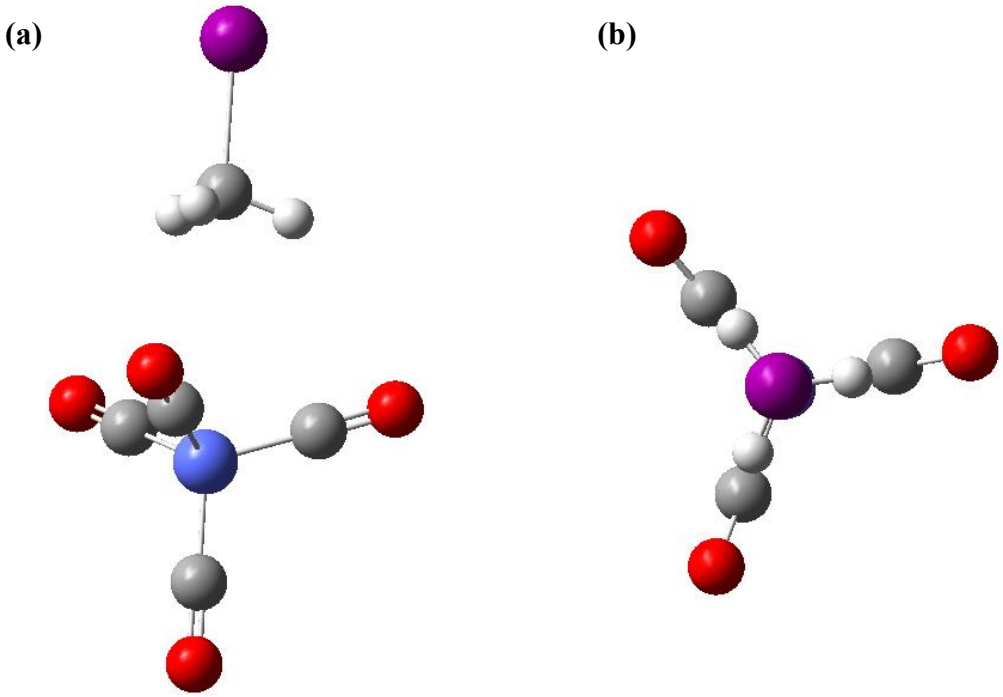


**Figure 2.8:** Two views of iodomethane – $[Co(CO)_4]^-$ reactant ion dipole complex, **(a)** side view and **(b)** along I-C-Co axis. (DFT-B3LYP/SDD – gas-phase)

The energy of the $S_N2$ transition state is 37 kJ $mol^{-1}$ higher than the separated reactants. The overall substitution reaction in the gas-phase to give separated $[Co(CO)_4Me]$ and $I^-$ is endothermic by around 53 kJ $mol^{-1}$.

Since the reaction kinetics were studied experimentally in THF, a corresponding energy profile was constructed using THF as the solvent (**Figure 2.7**) From this figure it is clear that the inclusion of solvent has a large effect on the profile. Moreover, it correctly predicts the reaction to be exothermic. The products are solvated more strongly than the reactants because iodide is a smaller anion than the cobalt complex. The barrier height to the reaction with iodomethane is higher than for the gas-phase calculation. This is because the transition state is less strongly solvated than the reactant complex since the negative charge becomes more dispersed.

### 2.2.2 $[M(CO)_5]^-$ (M = Mn, Re)

The complexes $[Mn(CO)_5]^-$ and $[Re(CO)_5]^-$ contain transition-metals from the same group of the periodic table, which allows for the investigation of the effect of the metal on the nucleophilicity of the complex with all other parameters kept the same. Each reactant complex adopts a trigonal bypyramidal geometry. The transition states for the reactions of both complexes with iodomethane are shown in **Figure 2.9**.

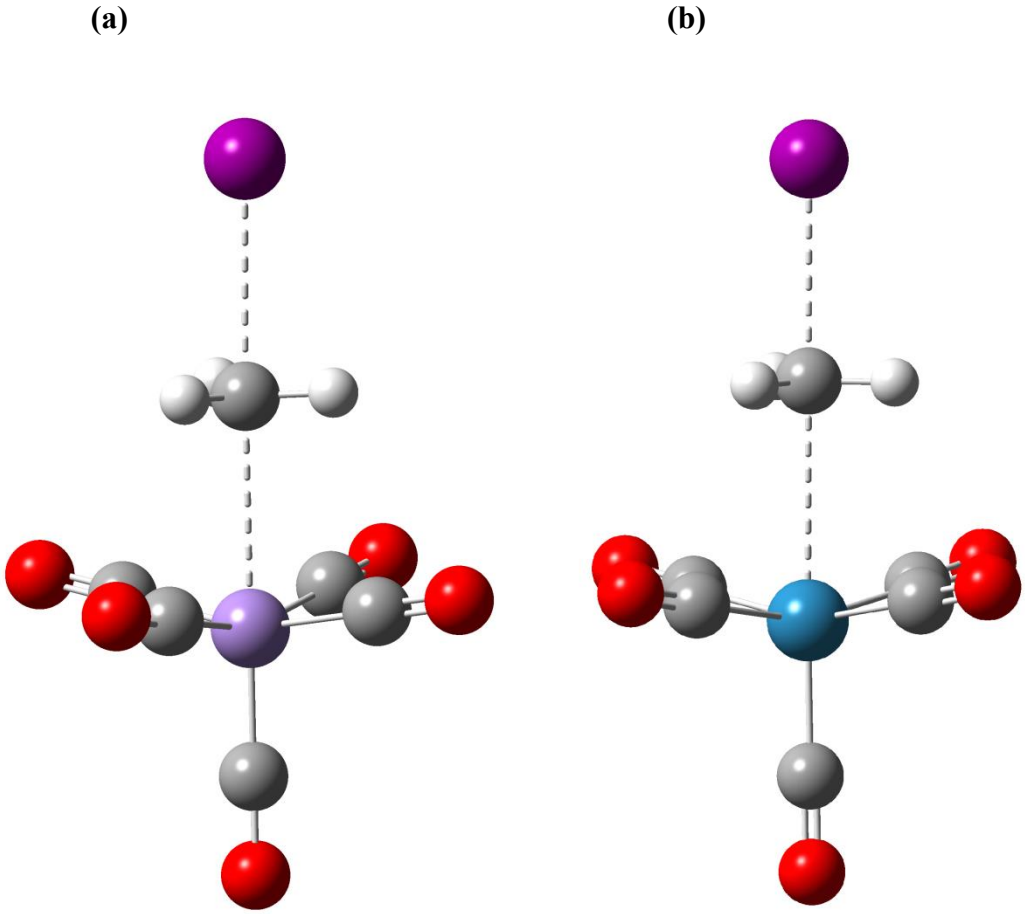


**Figure 2.9:** Optimised transition states for the reactions of $[Mn(CO)_5]^-$ **(a)** and $[Re(CO)_5]^-$ **(b)** with iodomethane (DFT-B3LYP/SDD – gas-phase)

In the transition state, the forming C-M bond bisects two equatorial carbonyl ligands. The transition state has an approximately square-based pyramidal geometry at the metal. The C-I distance increases from 2.21 Å in iodomethane to 2.85 Å and 2.76 Å in the transition state for $[Mn(CO)_5]^-$ and $[Re(CO)_5]^-$ respectively. The C-M distance is 2.79 Å

and 2.97 Å for $[Mn(CO)_5]^-$ and $[Re(CO)_5]^-$ respectively. $[Re(CO)_5]^-$ has an earlier transition state when compared to $[Mn(CO)_5]^-$ as expected for a more nucleophilic complex.

Energy profiles where solvent has been included for the reaction of $[Mn(CO)_5]^-$ and $[Re(CO)_5]^-$ with iodomethane are shown in **Figure 2.10**. As for $[Co(CO)_4]^-$ the reactant ion-dipole complex is at a lower energy than the separated reactants. The energy of the transition state is 21.8 and 36.7 kJ $mol^{-1}$ higher than the separated reactants for $[Re(CO)_5]^-$ and $[Mn(CO)_5]^-$ respectively. Both barriers are lower than that for $[Co(CO)_4]^-$ (57.5 kJ $mol^{-1}$), which is consistent with the more reactive nature of the group VII reactants. The barrier height is lower for rhenium than for manganese which is consistent with the experimental reactivity in **Table 2.1**.

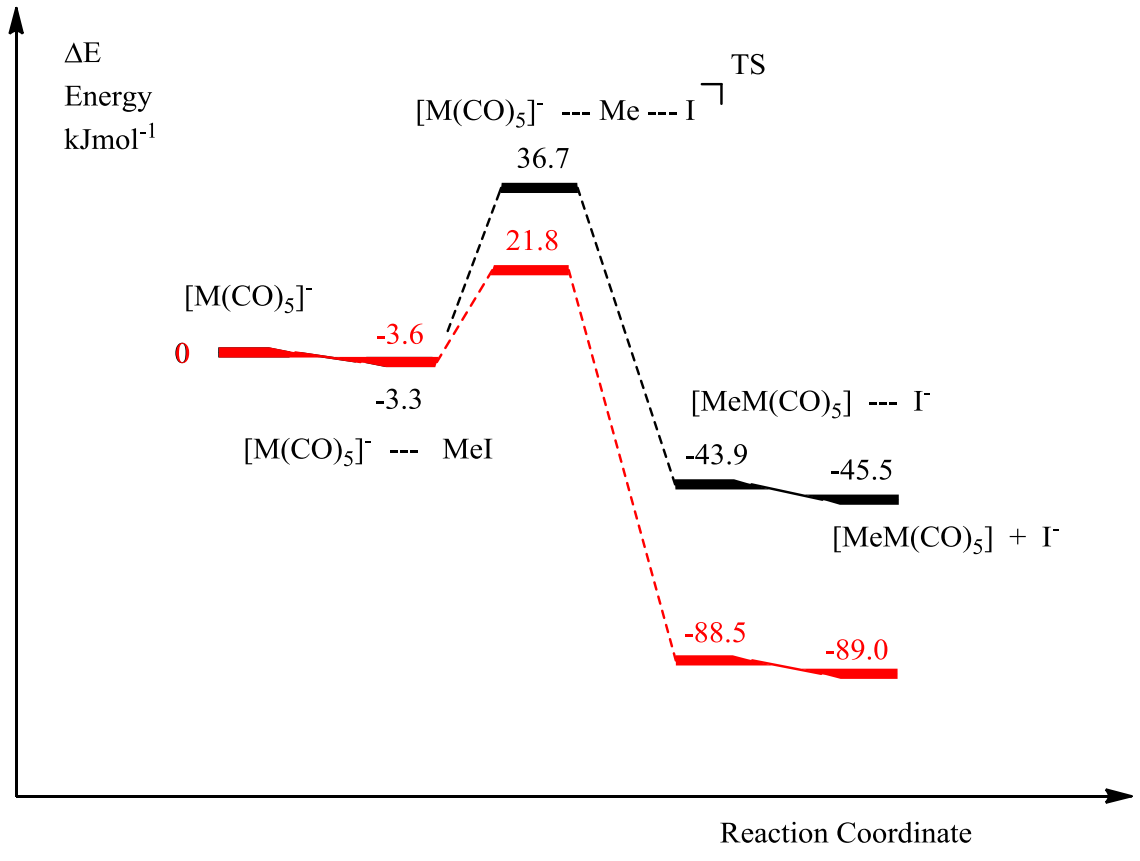


**Figure 2.10:** Energy profile (ΔE) for the reactions of $[Mn(CO)_5]^-$ (black) and $[Re(CO)_5]^-$ (red) with iodomethane (DFT-B3LYP/SDD - THF)

### 2.2.3 $[CpM(CO)_3]^-$ (M = Cr, Mo,W)

The group VI tricarbonyl complexes differ structurally from those already investigated. The reactants adopt a piano stool geometry due to the presence of a cyclopentadienyl ligand. **Figure 2.11** shows the solution phase reaction profiles for $[CpM(CO)_3]^-$ (M = Cr, Mo, W) which are similar to that for $[Mn(CO)_5]^-$.

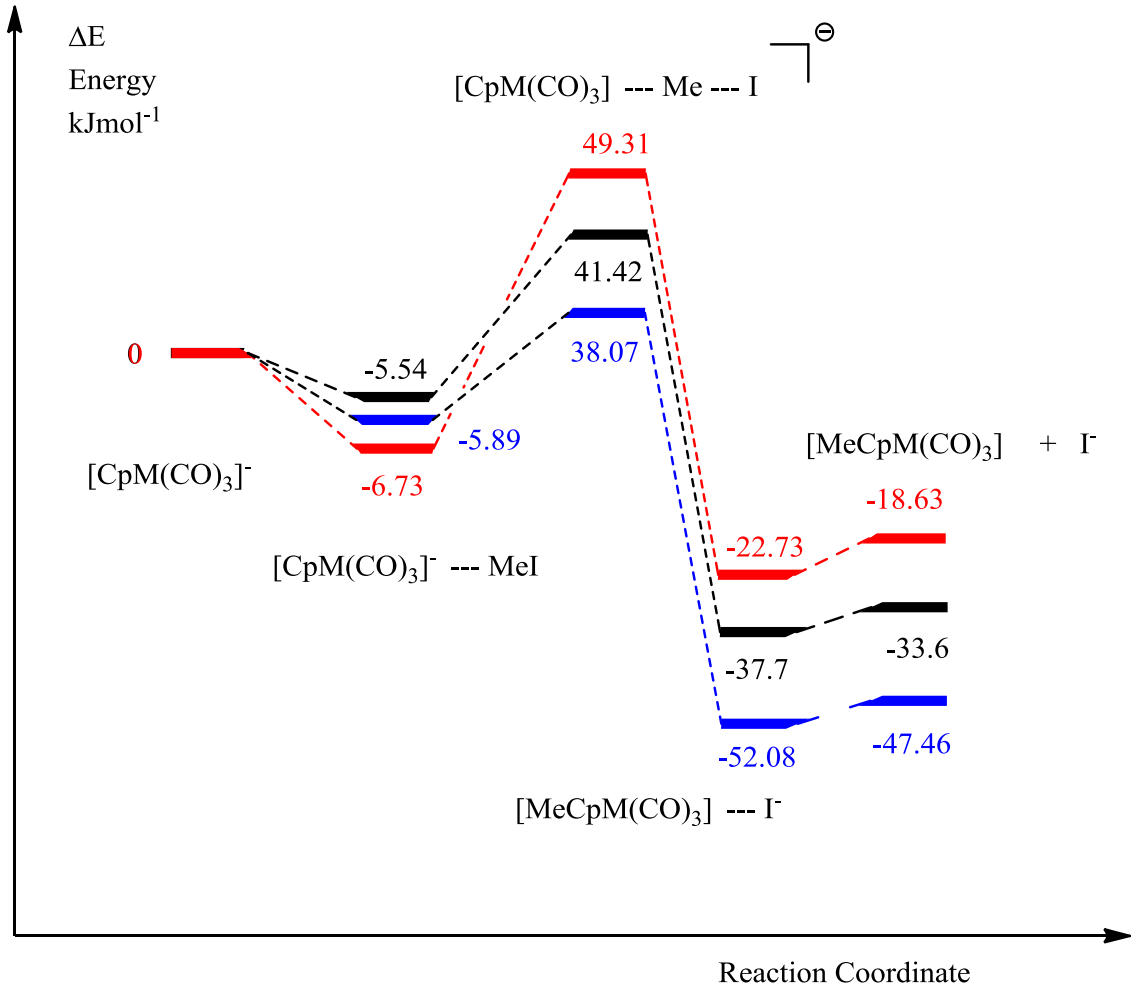


**Figure 2.11:** Energy profiles (ΔE) for the reaction of $[CpM(CO)_3]^-$ with iodomethane (M = Cr (red), Mo (black), W (blue)) (DFT-B3LYP/SDD - THF)

Optimised structures of $[CpCr(CO)_3]^-$ and the $S_N2$ transition state for its reaction with iodomethane are shown in **Figure 2.12.** This shows that the transition state structures are somewhat different than those for $[Co(CO)_4]^-$ and $[Mn(CO)_5]^-$. The M-C-I angle is 174 ° compared to 180 ° for $[Co(CO)_4]^-$. This deviation from linearity is due to the

presence of the cyclopentadienyl ligand. As in the transition state for $[Co(CO)_4]^-$, the C-I distance is longer than in free iodomethane and the geometry around the $CH_3$ unit is close to planar.

The C-I distances are 2.91, 2.84 and 2.80 Å for M = Cr, Mo and W respectively. The corresponding C-M distances are 2.84, 2.91 and 2.94 Å respectively. Thus, the transition state becomes progressively earlier as the nucleophilicity of the complex increases.

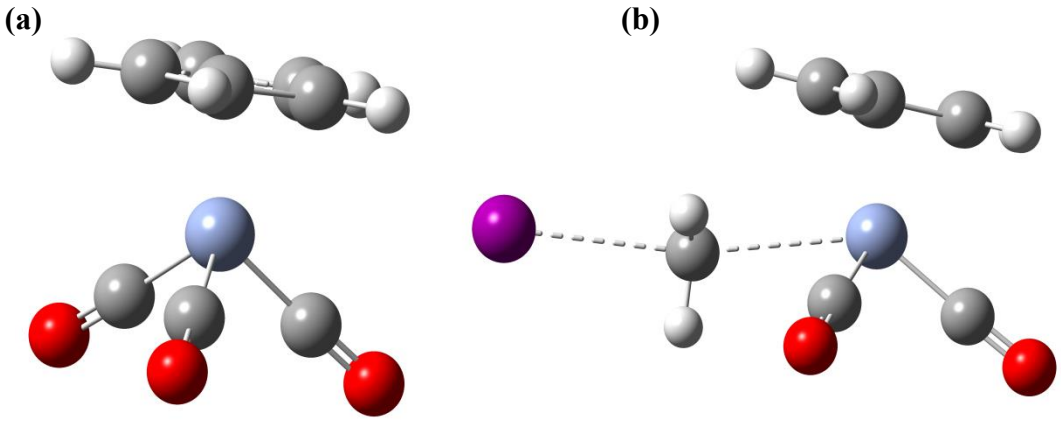


**Figure 2.12:** Optimised geometries of **(a)** $[CpCr(CO)_3]^-$ and **(b)** the transition state for the reaction with iodomethane (DFT-B3LYP/SDD – gas-phase)

## 2.2.4 $[CpFe(CO)_2]^-$

The most reactive anionic complex investigated by Dessy and Pearson was $[CpFe(CO)_2]^-$. It is prepared by cleavage of $[Cp_2Fe_2(CO)_4]$ typically using sodium amalgam and is often termed a "super nucleophile" due to its high nucleophilicity.[23] The anion is a useful precursor since it is readily alkylated and acylated using the appropriate electrophile.[24]

The structure of the reactant and transition state is shown in **Figure 2.13**. The C-I distance increases from 2.20 Å in free iodomethane to 2.53 Å in the transition state, which is the shortest such distance calculated thus far. The C-M distance is 3.00 Å, which is the longest distance observed and the I-C-M bond angle is 170°. Hence, the

transition state for the reaction of $[CpFe(CO)_2]^-$ is notably earlier in character than the nucleophiles discussed earlier.

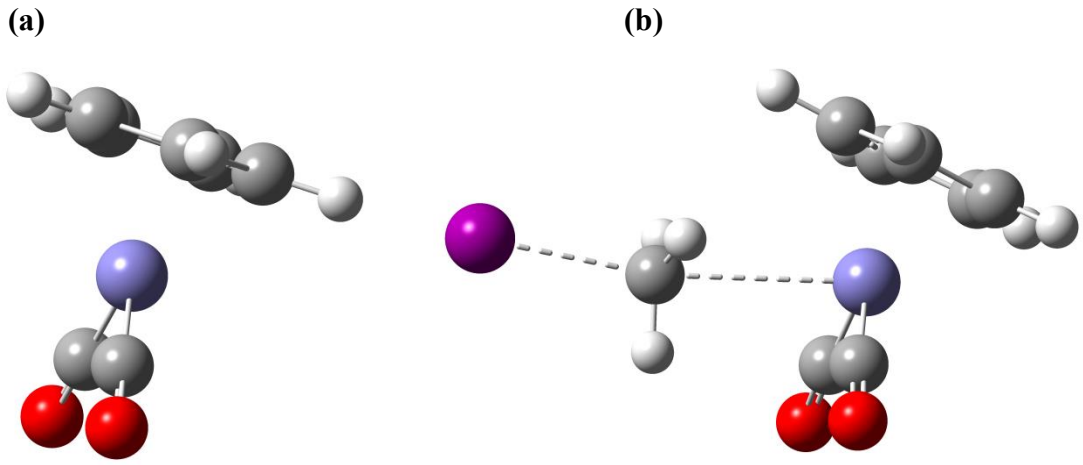


**Figure 2.13:** Optimised geometries of **(a)** $[CpFe(CO)_2]^-$ and **(b)** the transition state for the reaction with iodomethane (DFT-B3LYP/SDD – gas-phase)

Furthermore, the high nucleophilicity of the complex is reflected in the reaction energy profiles as shown in **Figure 2.14**. The gas-phase and solution phase profiles are both exothermic for $[CpFe(CO)_2]^-$ in contrast to what was observed for $[Co(CO)_4]^-$ where only the solution phase profile was exothermic. The reactant ion-dipole complex is at a lower energy than the separated reactants as is the product ion-dipole complex and the separated products. When solvation effects are taken into account, the transition state energy is 6.9 kJ $mol^{-1}$ higher than the separated reactants, representing a lower barrier than for the systems discussed above.

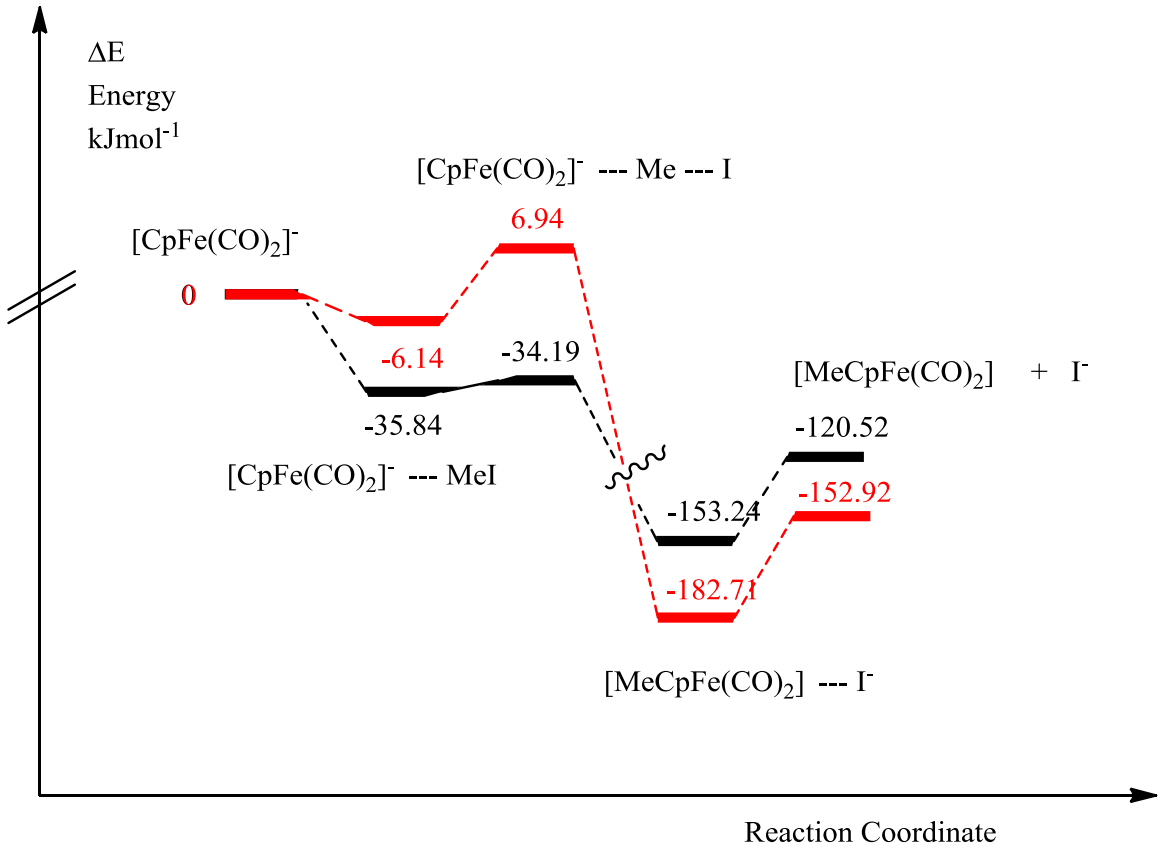


**Figure 2.14:** Energy profile (ΔE) for the reaction of $[CpFe(CO)_2]^-$ with iodomethane. Gas-phase (black) and THF (red) (DFT-B3LYP/SDD)

### 2.2.5 $[CpNi(CO)]^-$

The final complex investigated in this series was $[CpNi(CO)]^-$, which experimentally was found to be highly nucleophilic. The structure of the reactant and transition state is shown in **Figure 2.15.** This complex contains only one carbonyl ligand and hence is less sterically hindered than those in **Sections 2.2.4** and **2.2.5.** The reaction profiles for the reaction of $[CpNi(CO)]^-$ with iodomethane are shown in **Figure 2.16.** The reaction is exothermic in both gas and solution phase as was observed for $[CpFe(CO)_2]^-$.

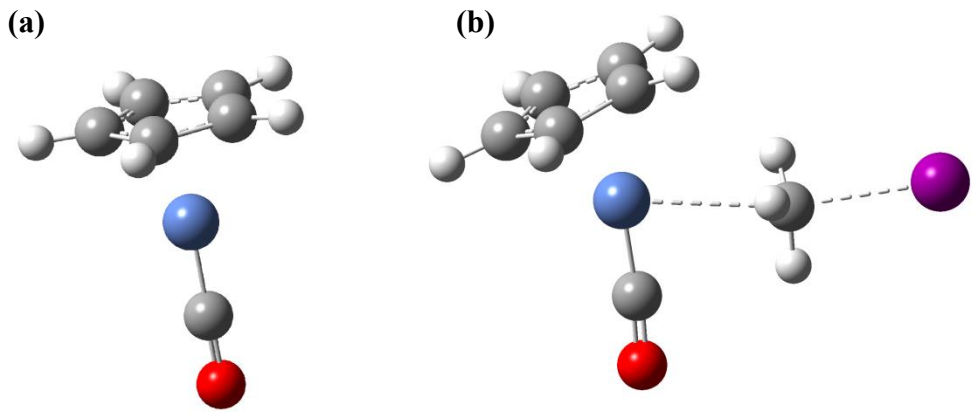


**Figure 2.15:** Optimised geometries of $[CpNi(CO)]^-$ **(a)** and the transition state **(b)** for the reaction with iodomethane (DFT-B3LYP/SDD – gas-phase)

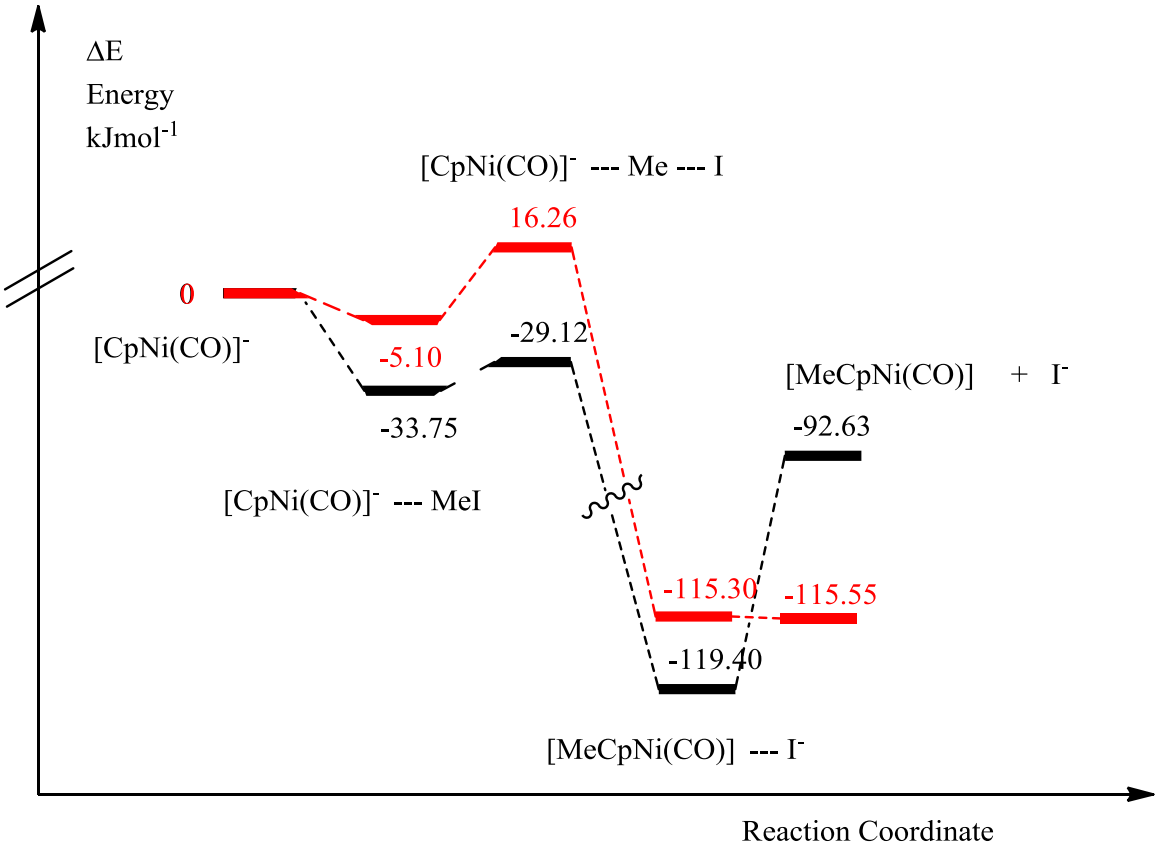


**Figure 2.16:** Energy profile (ΔE) for the reaction of $[CpNi(CO)]^-$ with iodomethane. Gas-phase (black) and THF (red) (DFT-B3LYP/SDD)

## 2.3 Comparison of computational and experimental data

### 2.3.1 Barrier heights

Reaction profiles were generated for each complex in turn using different basis sets. The basis sets investigated were SDD both in gas-phase and with solvent inclusion, 6-311G(d,p) where appropriate, cc-pVDZ and a mixed system consisting of SDD on the metal and 6-311G(d,p) on all other atoms. For each profile, the barrier height for the reaction with iodomethane was calculated as the energy of the transition state relative to the two separated reactants. The experimental rate constants, along with the calculated energy barriers are given in **Table 2.4.**

| Complex | log ($k$ / $M^{-1}s^{-1}$) (THF) | $\Delta E^{\ddagger}$ barrier heights / kJ $mol^{-1}$ | | | | | |
|---|---|---|---|---|---|---|---|
| | | SDD | SDD (THF) | cc-pVDZ | Mixed | Mixed (THF) | 6-311G(d,p) |
| $[Co(CO)_4]^-$ | -1.36 | 36.97 | 57.46 | 30.50 | 21.90 | 46.99 | 9.18 |
| $[CpCr(CO)_3]^-$ | -1.12 | 28.03 | 49.30 | 21.05 | 17.35 | 39.85 | 13.24 |
| $[CpMo(CO)_3]^-$ | 0.18 | 18.58 | 41.42 | 13.98 | 11.70 | 35.25 | * |
| $[CpW(CO)_3]^-$ | 0.38 | 13.60 | 38.07 | 9.09 | 6.99 | 32.10 | * |
| $[Mn(CO)_5]^-$ | 0.87 | 19.46 | 36.72 | 11.56 | 3.88 | 26.48 | -9.81 |
| $[Re(CO)_5]^-$ | 3.00 | 1.65 | 21.84 | -4.05 | -7.97 | 16.65 | * |
| $[CpNi(CO)]^-$ | 5.34 | -29.12 | 16.26 | -23.80 | -27.24 | 17.43 | - |
| $[CpRu(CO)_2]^-$ | 5.48 | -33.98 | 6.93 | - | -33.57 | 8.72 | * |
| $[CpFe(CO)_2]^-$ | 6.45 | -34.19 | 6.94 | -32.04 | -36.3 | 5.24 | -45.36 |

*Basis set not available for complexes with these metals

**Table 2.4:** Experimental rate constants and computed $\Delta E^{\ddagger}$ barrier heights for the reaction of anionic 18-electron metal complexes with iodomethane. (gas-phase unless stated)

**Figure 2.17** shows a plot of the calculated barrier against the experimental rate constants. There is a clear correlation for all basis sets investigated. The best correlation ($R^2$ = 0.99) was for gas-phase calculations using the mixed basis set

consisting of SDD on the metal centre and 6-311G(d,p) on the remaining atoms. Surprisingly, the lowest correlation ($R^2$ = 0.92) was observed for the calculations using the same basis set with the PCM solvation method (THF).

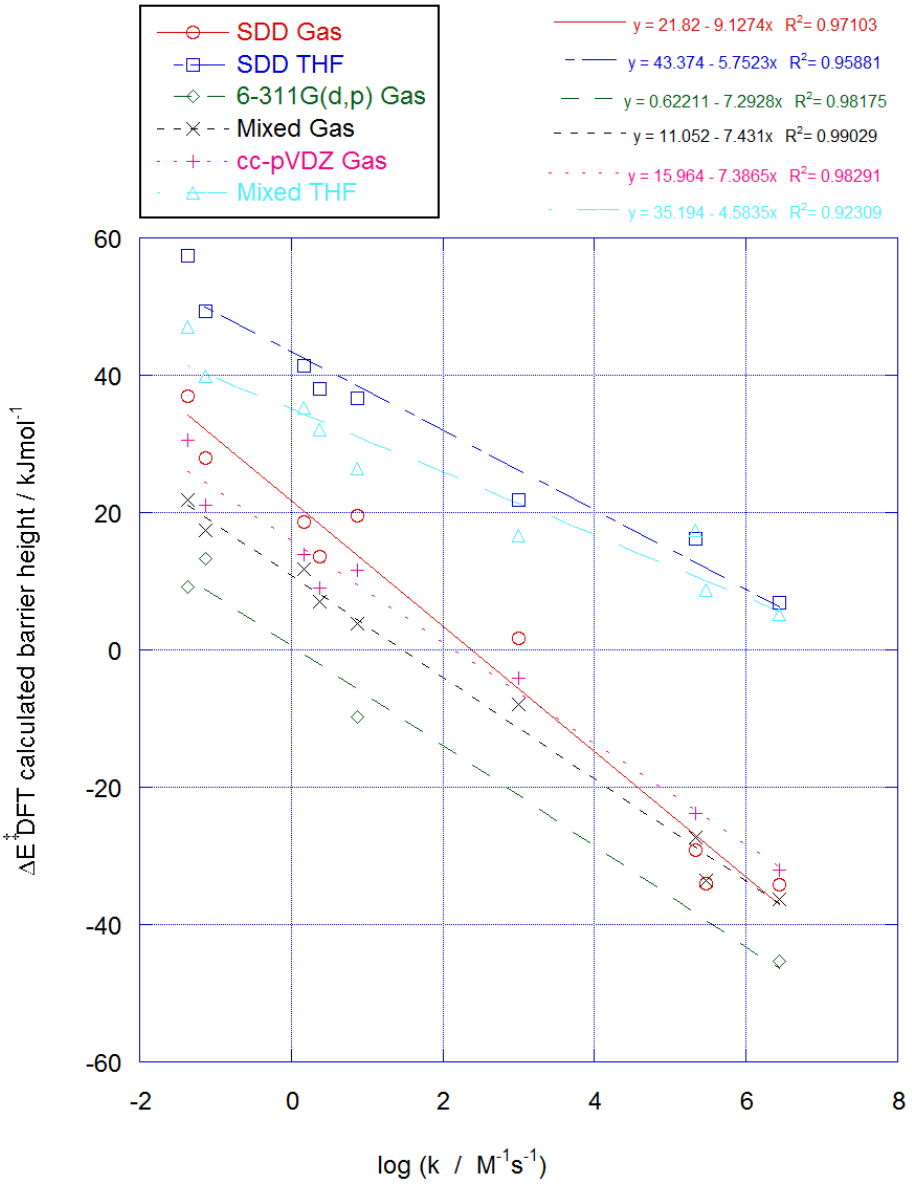


**Figure 2.17:** Plots of calculated barrier height ($\Delta E^{\ddagger}$) against experimental log *k* (THF, 25 °C) for the reaction of metal carbonyl complexes with iodomethane. Basis sets, linear fit equations and $R^2$ values given in key

Further comparisons can be made between the experimental rate constants and the DFT computed barrier heights. **Figure 2.18** shows plots of $\Delta E^{\ddagger}$, $\Delta H^{\ddagger}$ and $\Delta G^{\ddagger}$ against log *k* where the $R^2$ values were 0.97, 0.98 and 0.99 respectively.

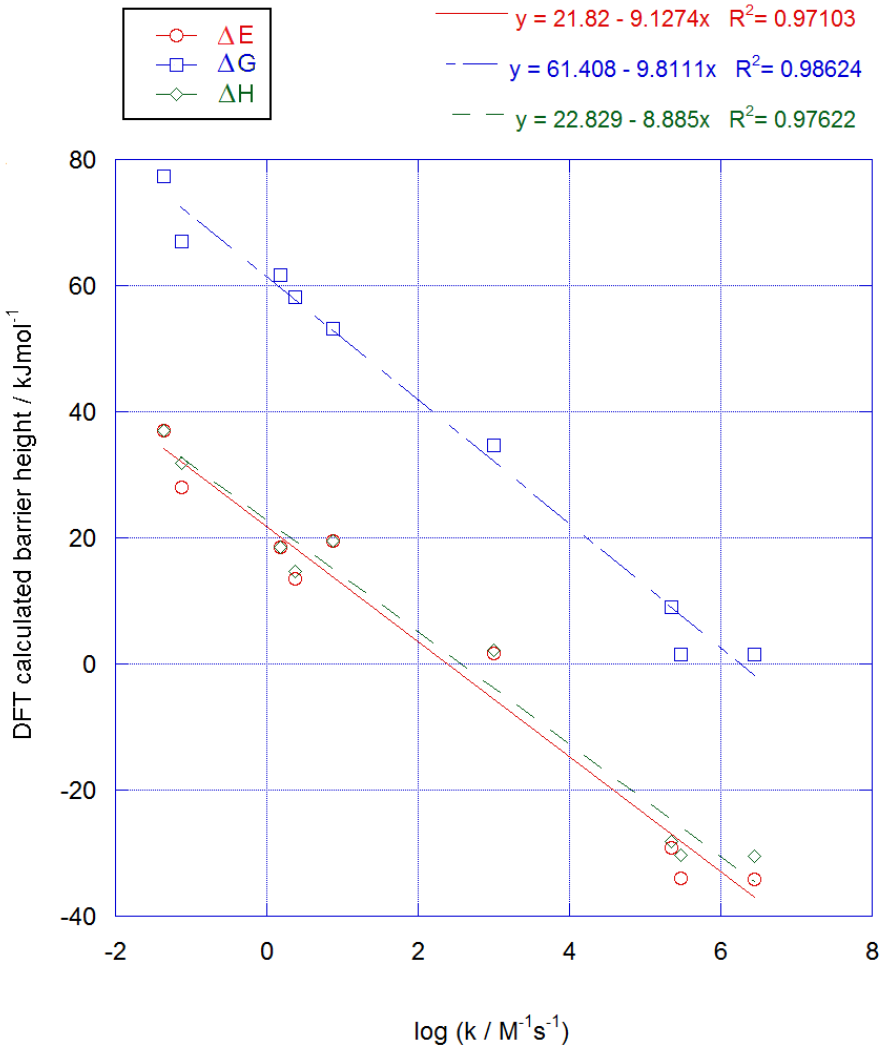


**Figure 2.18:** Plots of $\Delta E^{\ddagger}$, $\Delta G^{\ddagger}$ and $\Delta H^{\ddagger}$ barrier height against log *k* (THF, 25 °C) (DFT-B3LYP/SDD - GAS) Basis sets, trend line equations and $R^2$ values given in key

There is very little difference in the linearity of the plots with similar $R^2$ values for each parameter. The values of $\Delta E^{\ddagger}$ and $\Delta H^{\ddagger}$ are very similar whereas the values for $\Delta G^{\ddagger}$ are generally 30-40 kJ $mol^{-1}$ larger due to the entropic contributions in an associative bimolecular reaction. As $\Delta G^{\ddagger}$ is directly related to experimental rate constants by the Eyring equation, a comparison between the calculated and experimental $\Delta G^{\ddagger}$ values can be made. The experimental $\Delta G^{\ddagger}$ value is calculated from the rate constant according to **Equation 2.1** and a plot of the $\Delta G^{\ddagger}$ values is shown in **Figure 2.19** for three selected computational methods.

$$\Delta G^{\neq}_{exp} = -RTLn\left(\frac{kh}{k_bT}\right) \qquad \textbf{Equation 3.1}$$

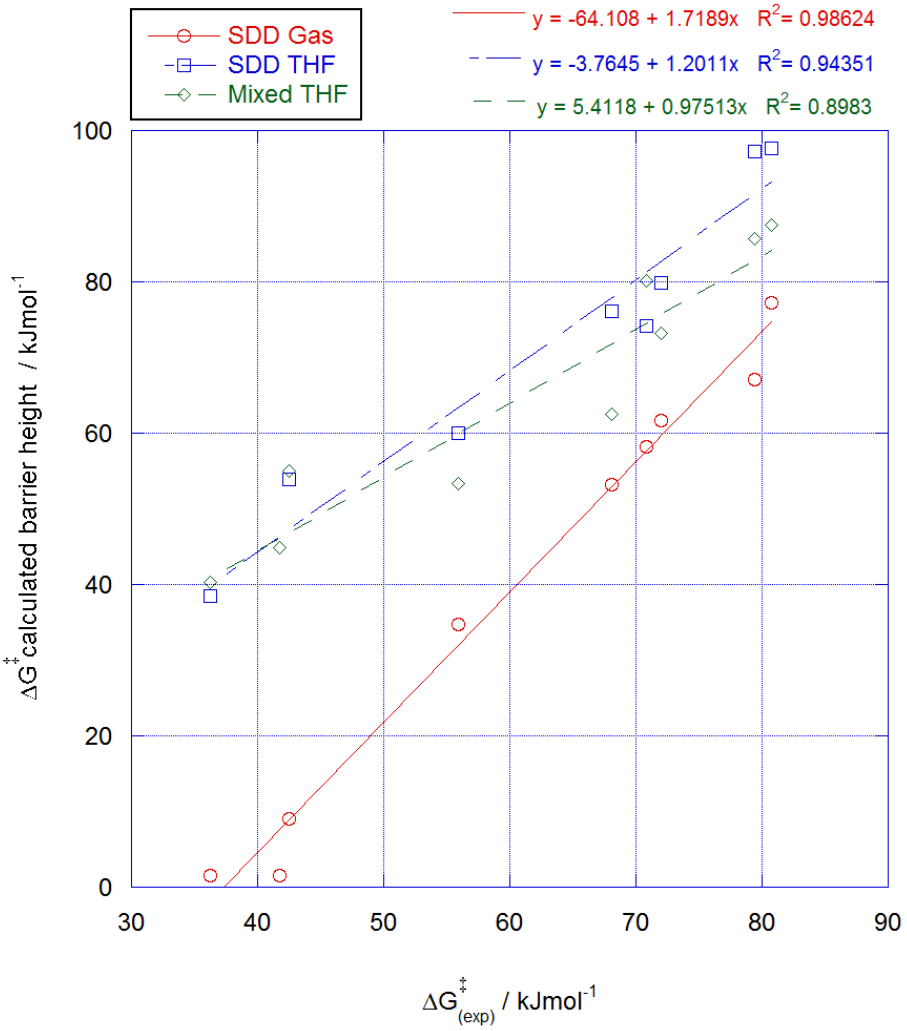


**Figure 2.19:** Plot of computed versus experimental $\Delta G^{\ddagger}$ values for the reaction of metal carbonyl complexes with iodomethane (DFT-B3LYP) Basis sets, trend line equations and $R^2$ values given in key.

Reasonable correlations were observed for each computational method. The worst correlation was observed for the mixed basis data where the $R^2$ value was 0.90. Both of the data sets with THF solvent modelled by the PCM method give reasonable predictions of the absolute $\Delta G^{\ddagger}$ values, with the mixed basis generally giving a result within 6 kJ $mol^{-1}$ of experiment. The gas-phase calculations systematically predict smaller $\Delta G^{\ddagger}$ values than observed experimentally especially for the more reactive

nucleophiles. This results in a significant negative intercept for the gas-phase plot whereas the solution phase plots have intercepts close to the origin.

### 2.3.2 Transition state geometries

In addition to the calculated barrier height, it was of interest to see whether other properties of the optimised transition state correlate with the experimental rate constant. To explore this, the C-I and C-M distances were plotted against log *k*. **Figure 2.20** shows a plot of the C-I distance against experimental rate constant. A good correlation was observed for all basis sets such that as the reactivity of the complex increases, C-I distance at the transition state shortens.

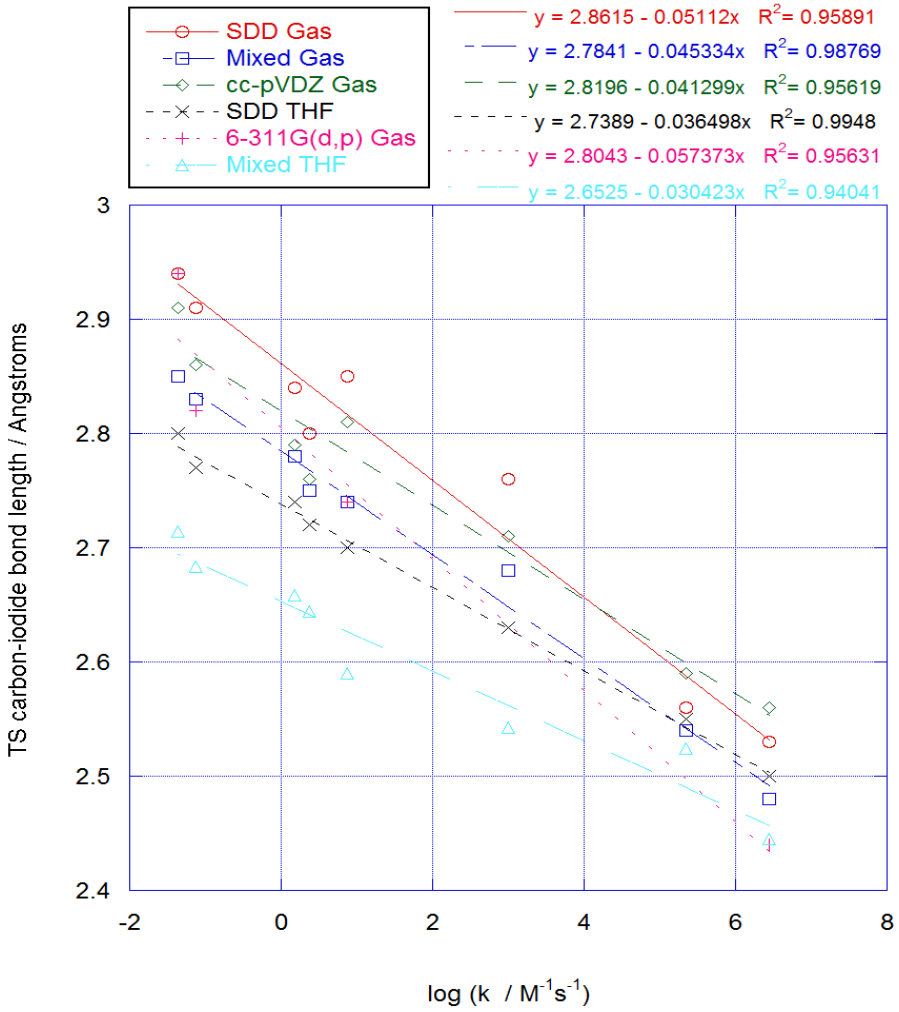


**Figure 2.20:** Plot of transition state C-I distance against experimental log *k* (THF, 25 °C) for the reaction of metal carbonyl complexes with MeI. Basis sets, trend line equations and $R^2$ values given in key.

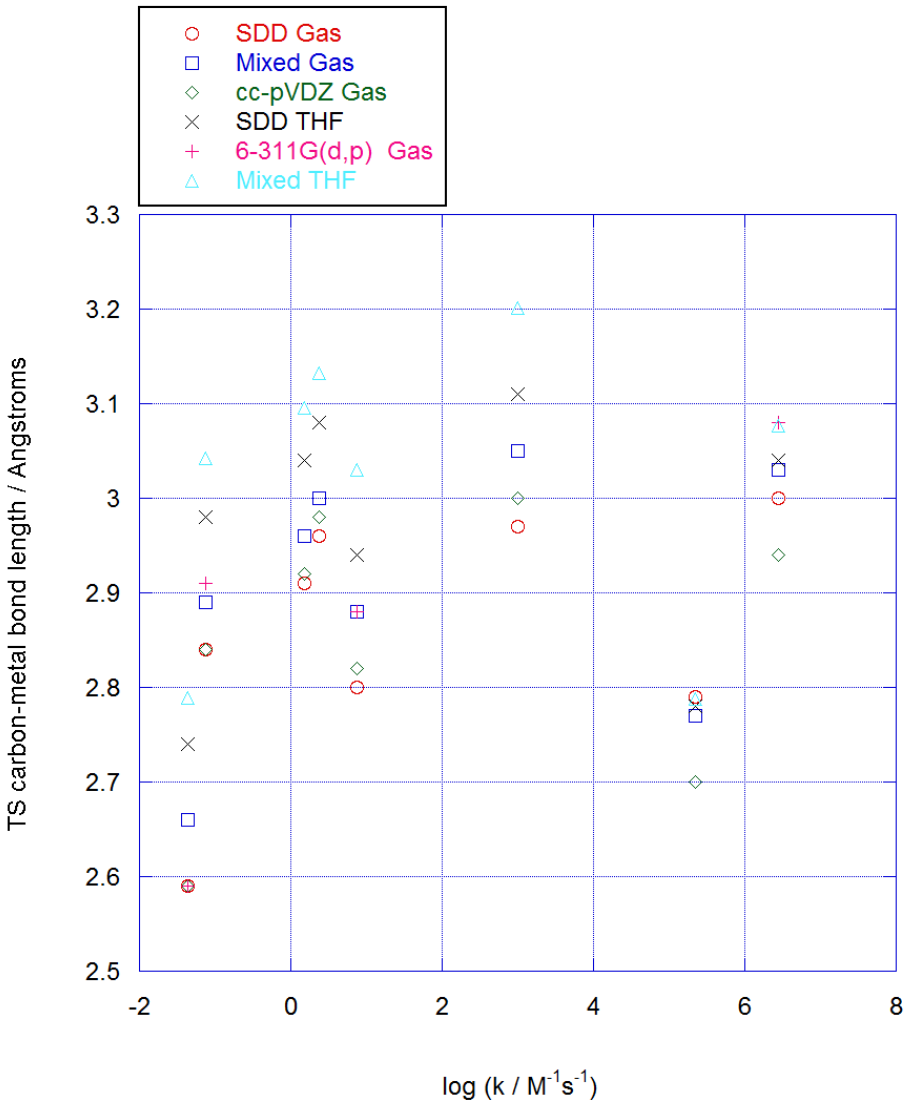


**Figure 2.21** Plot of transition state C-M distance against experimental log *k* (THF, 25 °C) for the reaction of metal carbonyl complexes with MeI.

**Figure 2.21** shows a plot of the C-M distance against experimental rate constants, which in contrast shows no obvious correlation. This is likely due to each complex having a different central metal with a different radius. In addition, some of the complexes contain only carbonyl ligands whereas others contain both carbonyls and cyclopentadienyl rings. This change in steric environment could potentially affect the nature of the transition state by restricting how close the metal can approach the iodomethane. Further plots were drawn to discern whether any relationship could be observed for complexes bearing similar steric environments, complexes bearing metals from the same row of the periodic table and complexes bearing metals from the same

group of the periodic table. However, whilst in some cases the correlations improved marginally, they were still not at a level where experimental reactivity could be predicted with confidence.

## 2.4 Investigations into $[Mn(CO)_4L]^-$ complexes

The reactivities of a series of manganese complexes bearing phosphine ligands was investigated experimentally by Lai et al.[3] These were of particular interest as their structures are related to the $[Mn(CO)_5]^-$ complex that was investigated in **Section 2.2.3**, with one of the carbonyl ligands replaced with a phosphine ligand. Experimentally, the phosphine bearing complexes react faster than $[Mn(CO)_5]^-$ with iodomethane due to the increased electron density on the metal from the phosphine ligand. However for $[Mn(CO)_4(P(OPh)_3)]^-$ the experimental rate constant is lower than for $[Mn(CO)_5]^-$. This behaviour is expected since phosphites are more electron withdrawing than phosphines which decreases the overall nucleophilicity of the complex.

Since the geometry around the metal centre is trigonal bypyramidal there are two possible isomers for $[Mn(CO)_4L]^-$ with the phosphine in either the axial or the equatorial position as shown in **Figure 2.22.**


**Figure 2.22:** Two possible reactant geometries of $[Mn(CO)_4L]^-$

All structures found in the Cambridge Crystallographic Database (CCD) show that the phosphine is located in the axial position in the solid state. However, the solid state structure is not always a true representation of the structure in solution so both potential isomers were optimised for a model complex bearing $PMe_3$, which was chosen for computational ease. The complexes were optimised using the SDD basis set and MeCN as the solvent. Both structures converged to the same isomer with the $PMe_3$ ligand in

the axial position in agreement with the CCD structure so it was this structure that was investigated for the remaining complexes.

In the reaction of $[Mn(CO)_5]^-$ with iodomethane an octahedral complex is formed where only one orientation of the ligands is possible. Replacing a carbonyl with a phosphine ligand leads to two potential product isomers where the methyl group can be either *trans* or *cis* to the phosphine. Transition states leading to both these products were found and are shown in **Figure 2.23.**

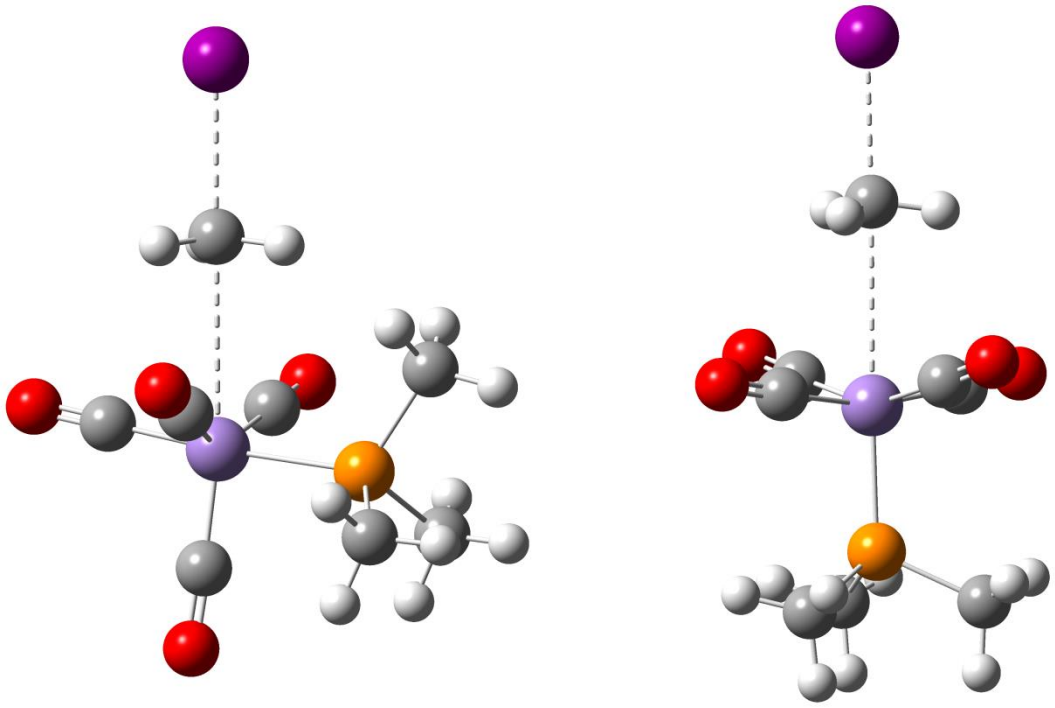

**Figure 2.23:** Optimised transition states for reaction of $[Mn(CO)_4L]^-$ with iodomethane to form *cis* and *trans* product isomers. (DFT-B3LYP/SDD - MeCN)

The remaining species necessary to construct an energy profile were optimised for both isomers. The energy profiles in **Figure 2.24** show the reaction to give the *cis* isomer of $[Mn(CO)_4L]^-$ is favoured both kinetically and thermodynamically. The transition state leading to the *cis*- isomer is 22 kJ $mol^{-1}$ lower in energy. The *cis*-product is also more stable than the *trans*- product by 15 kJ $mol^{-1}$. The *trans*-isomer is less stable as it has two ligands with strong *trans*-influence *trans* to one another.

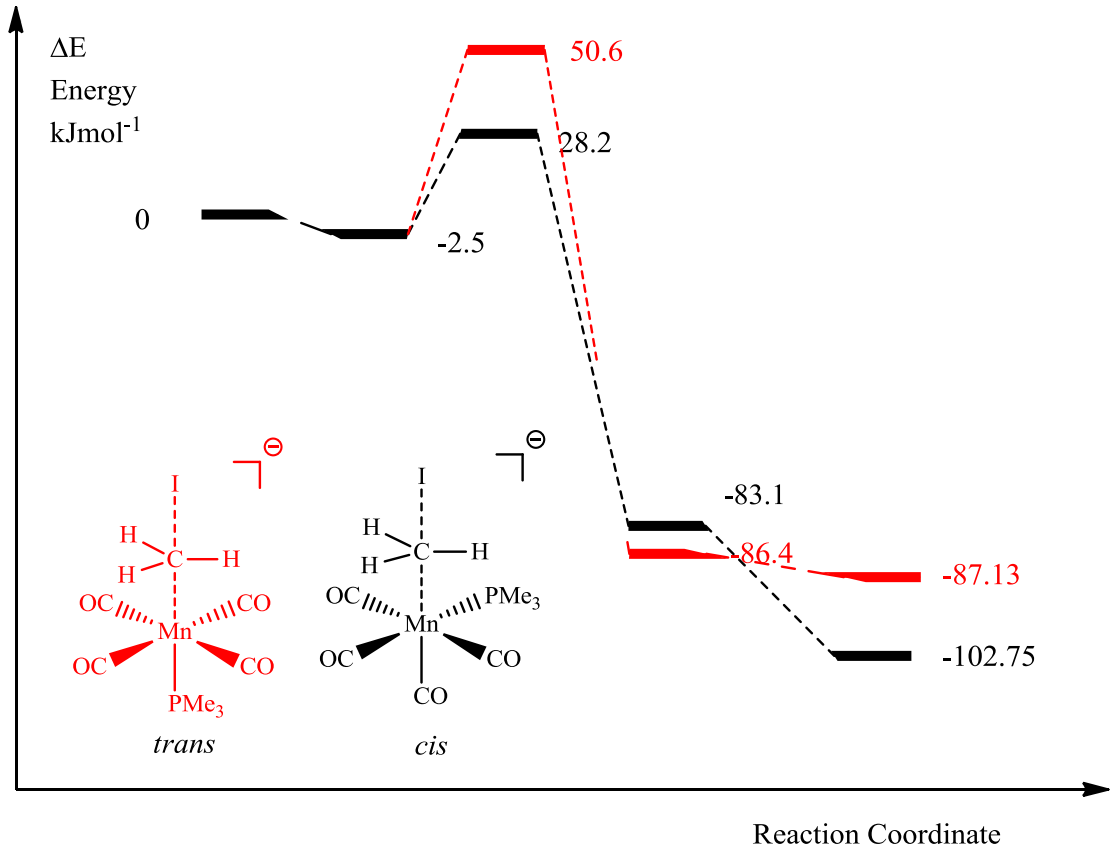


**Figure 2.24:** Energy profile (ΔE) for the reaction of $[Mn(CO)_4L]^-$ and MeI. L = $PMe_3$ (DFT-B3LYP/SDD - MeCN) (Not to scale)

### 2.4.1 Barrier heights

Analogous reaction profiles were constructed for the series of complexes bearing different ligands using three computational methods. The calculated barrier heights and experimental data are given in **Table 2.5.**

| L | log ($k$ / $M^{-1}s^{-1}$) | $\Delta H^{\ddagger}$ Barrier heights / kJ $mol^{-1}$ | | |
|---|---|---|---|---|
| | | SDD Gas | SDD MeCN | Mixed MeCN |
| $PBu_3$ | 1.95 | -0.94 | 28.41 | 22.48 |
| $PEt_3$ | 1.79 | -0.96 | 29.11 | 22.69 |
| $PPh_2Me$ | 1.28 | 13.07 | 33.25 | 30.26 |
| $PPh_3$ | 0.89 | 8.00 | 32.69 | 25.91 |
| $P(OPh)_3$ | 0.28 | 17.68 | 37.80 | 34.93 |

**Table 2.5:** DFT computed $\Delta H^{\ddagger}$ barrier heights and experimental data for $[Mn(CO)_4L]^-$ complexes. (DFT-B3LYP/basis sets as listed)

A plot of the calculated barrier height ($\Delta H^{\ddagger}$) against log $k$ is shown in **Figure 2.25.** Similar correlations were observed for all three methods investigated, with the mixed basis set having the best $R^2$ value ($R^2 = 0.984$).

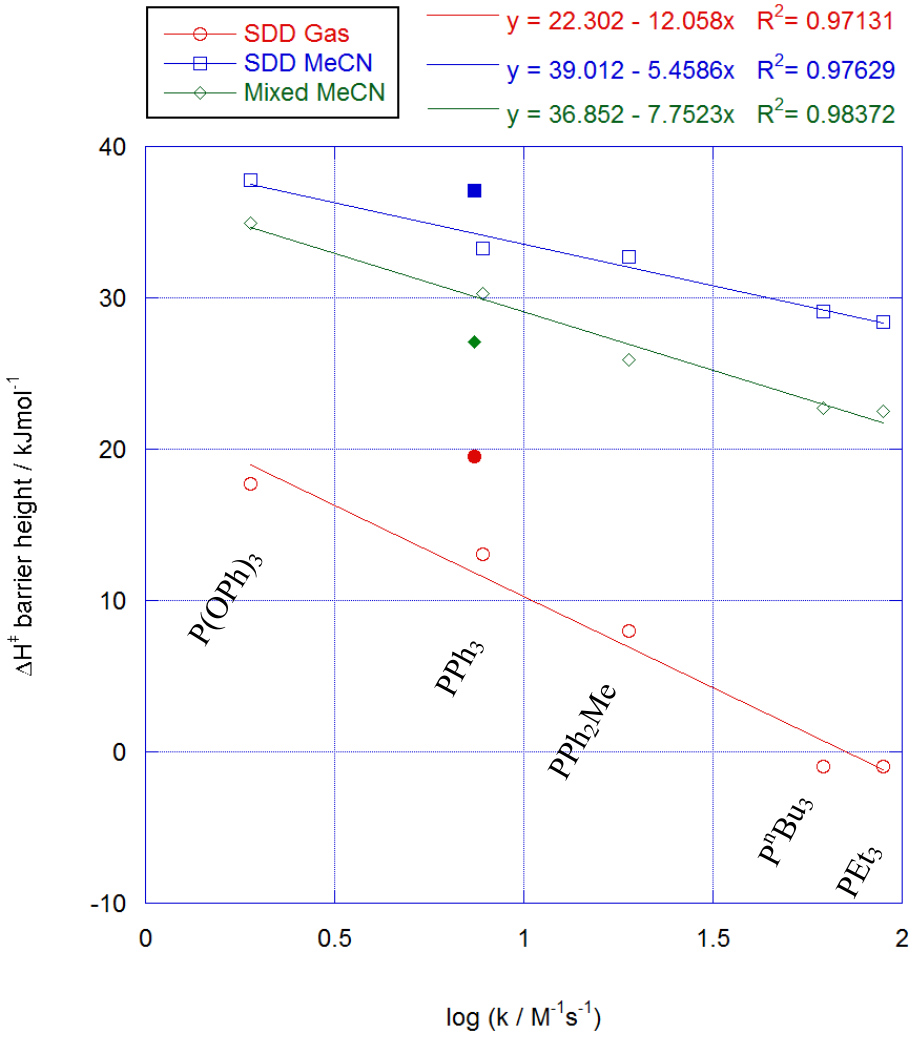


**Figure 2.25:** Plots of computed barrier height ($\Delta H^{\ddagger}$) against log *k* (MeCN, 25 °C) for reaction of $[Mn(CO)_4L]^-$ with MeI. Basis sets, linear fit equations and $R^2$ values given in key. $[Mn(CO)_5]^-$ points shown for reference in solid colour.

**Figure 2.26** shows a plot of calculated barrier heights ($\Delta E^{\ddagger}$, $\Delta H^{\ddagger}$ and $\Delta G^{\ddagger}$) versus experimental rate constant. As seen with the simpler complexes the values of $\Delta G^{\ddagger}$ are generally 40 kJ $mol^{-1}$ higher than the corresponding $\Delta H^{\ddagger}$ and $\Delta E^{\ddagger}$ values which are very similar. Computed $\Delta G^{\ddagger}$ values tend to be overestimated in reactions occurring in solution phase where the number of molecules changes since the entropy value is overestimated. This was discussed in detail by Houk.[22] Martin et al proposed a methodology where the Gibbs energy could be corrected simply by carrying out

optimisations with a pressure correction. We have not tested this yet, so as a consequence of these issues, for the remainder of this work, values of $\Delta H^{\ddagger}$ will be compared with experimental rate constants.

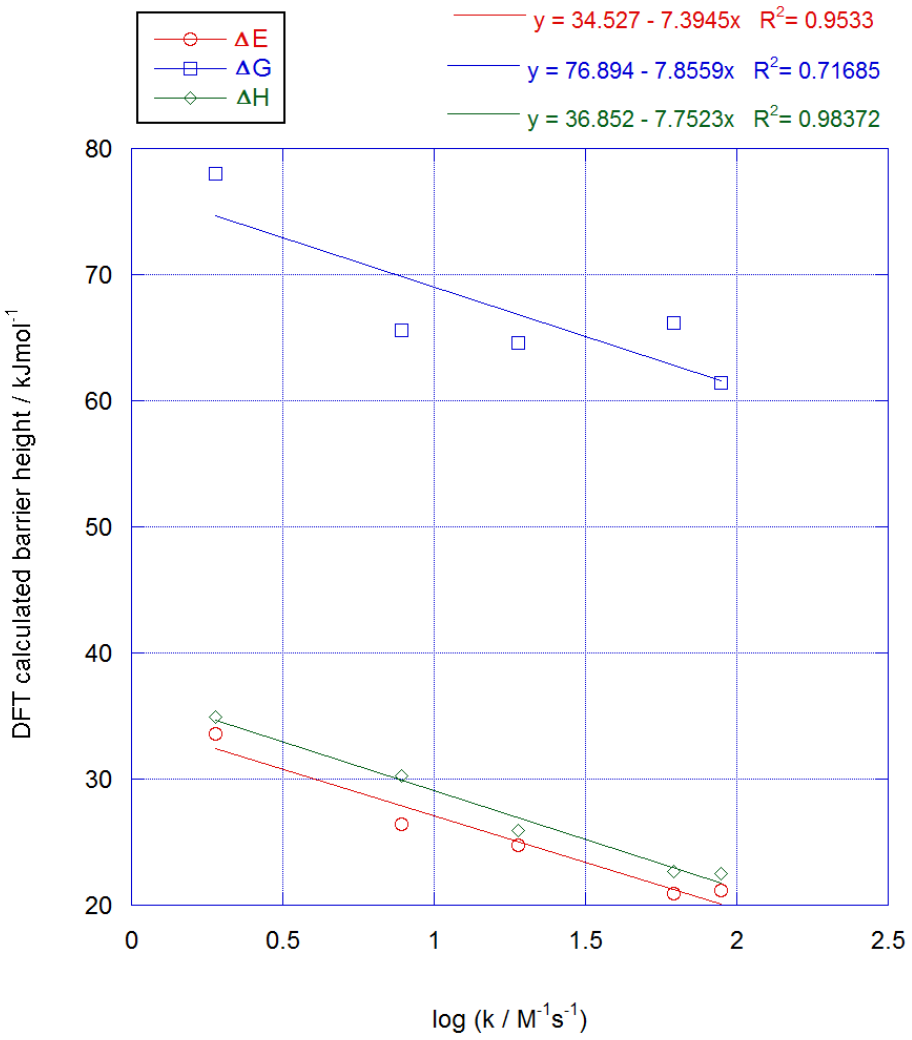


**Figure 2.26:** Plots of $\Delta E^{\ddagger}$, $\Delta G^{\ddagger}$ and $\Delta H^{\ddagger}$ barrier height against log *k* (MeCN, 25 °C) (DFT-B3LYP/ Mixed basis) Linear fit equations and $R^2$ values given in key

## 2.4.2 Transition state geometries

A relationship was established in **Section 2.3.2** between the transition state C-I distance and experimental rate constant. The comparison of the C-M distance and experimental rate constant showed no appreciable correlation. Similar trends were probed for the $[Mn(CO)_4L]^-$ complexes to investigate whether better correlations are observed.

**Figures 2.27** and **2.28** show plots of the C-I and C-Mn distances versus experimental rate constants respectively.

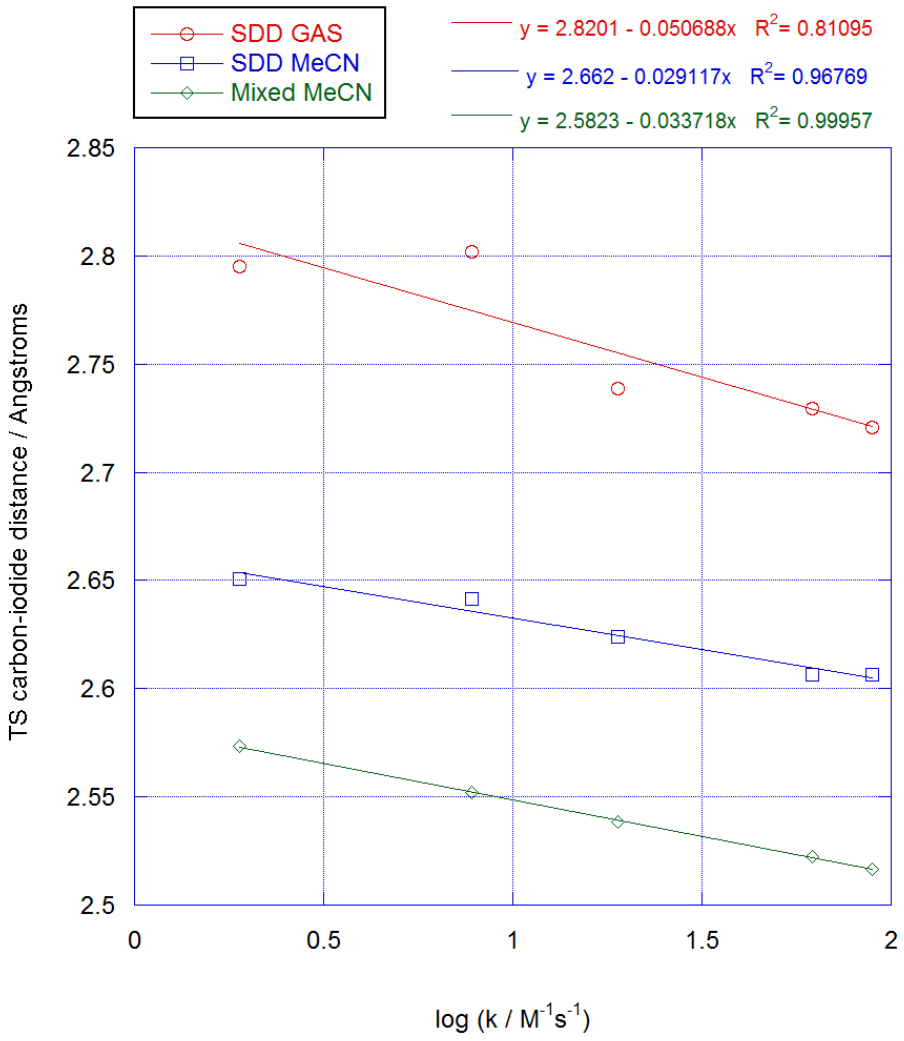


**Figure 2.27:** Plots of transition state C-I distance against experimental log *k* (MeCN, 25 °C) for reactions of $[Mn(CO)_4L]^-$ complexes with MeI. Basis sets, linear fit equations and $R^2$ values given in key.

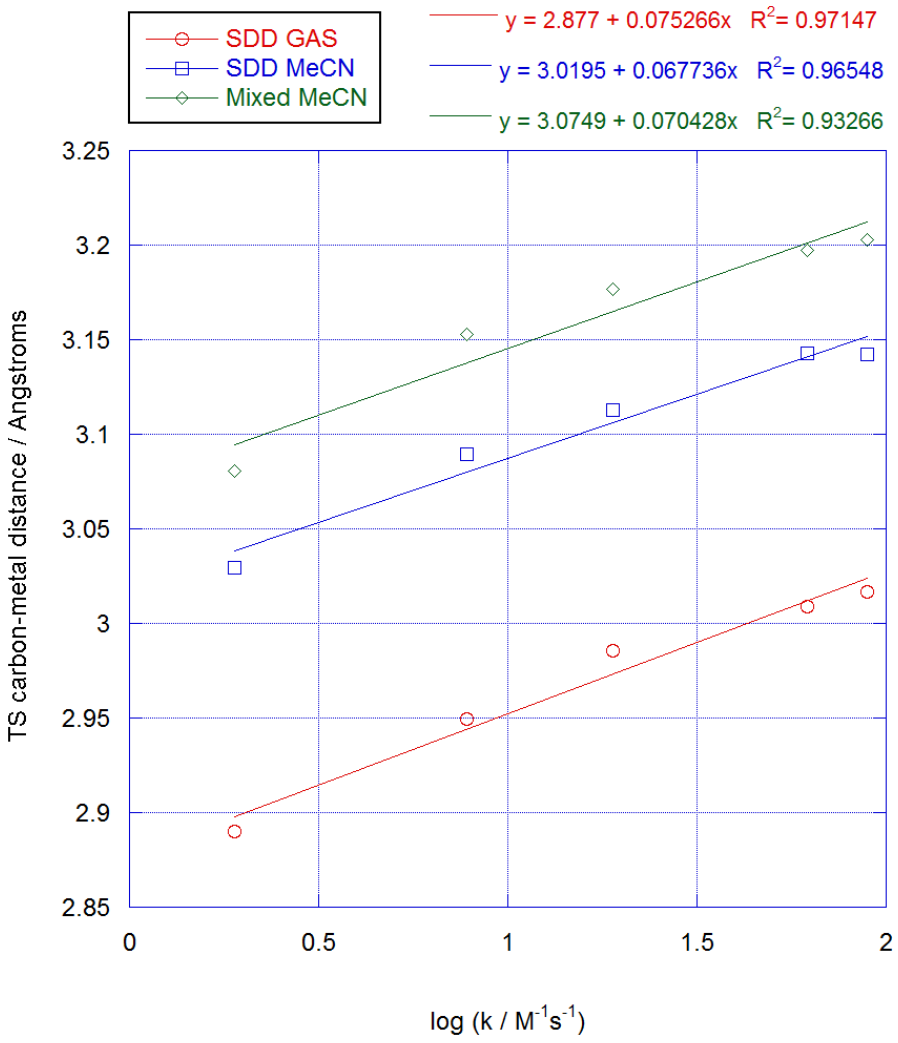


**Figure 2.28:** Plots of transition state C-Mn distance against experimental log *k* (MeCN, 25 °C) for reactions of $[Mn(CO)_4L]^-$ complexes with MeI. Basis sets, linear fit equations and $R^2$ values given in key.

A correlation was established between the transition state C-I and C-M distances and experimental rate constants. As the nucleophilicity of the metal complex increases, the C-I distance decreases and the C-M distance increases. The stronger nucleophiles have earlier transition states. Interestingly, the C-M distance shows a better correlation to the experimental rate constant than for the more diverse series of complexes in S**ection 2.2.2.1**, which is presumably because this series contains the same metal.

### 2.4.3 Reactant HOMO energies

Computationally, the reactivity of a metal complex is largely determined by the frontier orbital energies of the reactants. Frontier orbital theory (FMO theory) simplifies complex reactivity to the energies of the HOMO of one reactant and the LUMO of the other reactant. If the HOMO energy is indeed a good probe of experimental reactivity, it would allow for a rapid prediction of the experimental rate without having to optimise the transition states. Two views of the HOMO of $[Mn(CO)_4(PMe_3)]^-$ are shown in **Figure 2.29.**

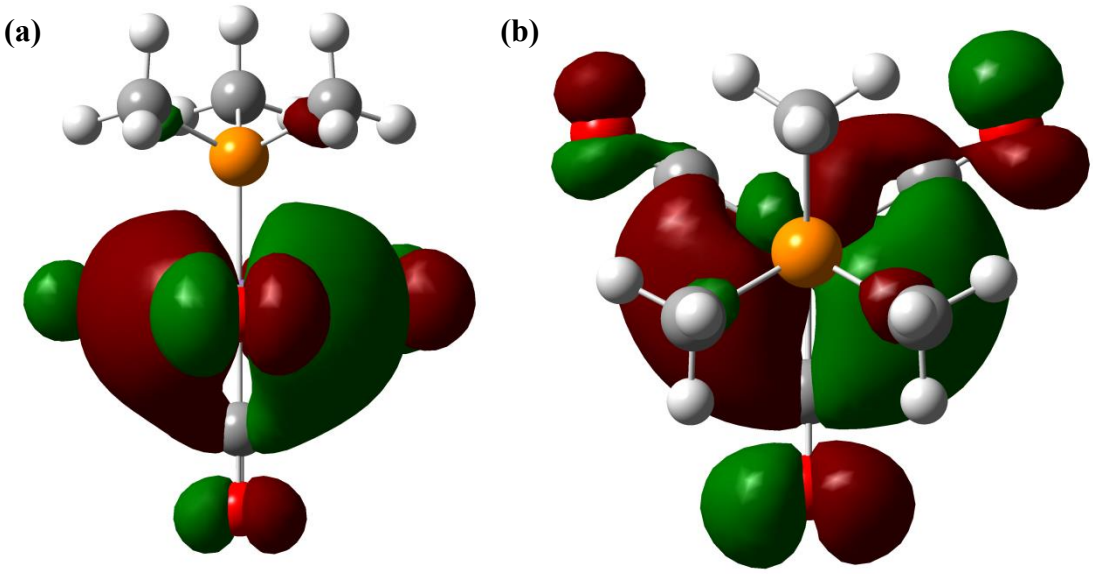


**Figure 2.29:** Two views of the HOMO of $[Mn(CO)_4(PMe_3)]^-$. (DFT-B3LYP/SDD) **(a)** Along equatorial CO-Mn bond. **(b)** Along $PMe_3$-Mn-CO axis.

The HOMO has major lobes between the equatorial carbonyl ligands which are in the correct orientation to react with iodomethane approaching in the equatorial plane, resulting in the transition state leading to *cis*- $[Mn(CO)_4(PMe_3)Me]$.

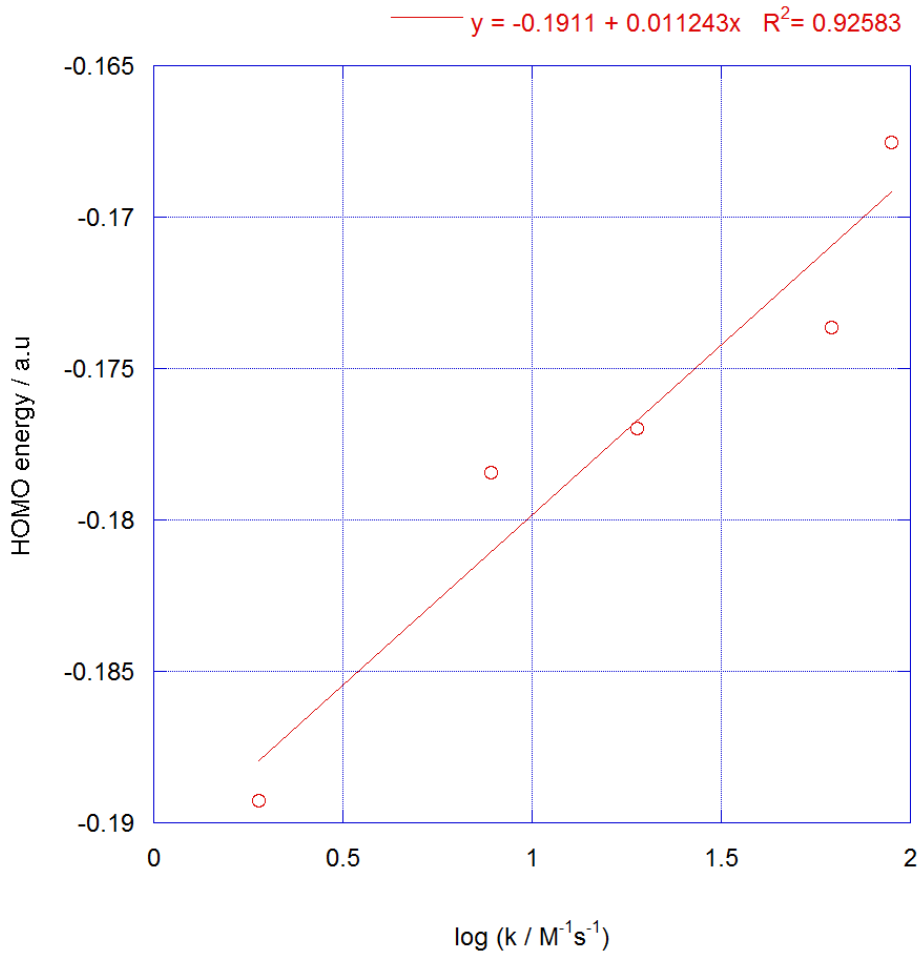


**Figure 2.30:** Plot of DFT calculated HOMO energy against experimental log *k* (MeCN, 25 °C).

**Figure 2.30** shows a plot of the calculated HOMO energy against log *k*. A reasonable correlation was found with a $R^2$ value of 0.93 suggesting that the HOMO energy may indeed be a reasonable predictor of experimental reactivity.

## 2.5 General Conclusions

A number of anionic metal complexes have been investigated to determine which computed parameters show best correlation with experimental rate constants, with the aim of both understanding experimental reactivity and predicting the nucleophilicity of novel complexes.

The effect of both solvent and the basis set on the nature of the transition state has been probed for $[Co(CO)_4]^-$. The solvent has the greater effect, with higher dielectric constants giving rise to earlier transition states. A significant effect on transition state geometry was observed on moving from gas-phase calculations to solution phase, modelled by the PCM method.

Inclusion of solvent in the calculations is crucial for accurate representation of energy profiles. Profiles for reactions in the gas-phase were generally endothermic whereas solution phase profiles were correctly predicted to be exothermic.

Calculated barrier heights show good correlations to experimental rates with marginally better correlations being observed for a mixed basis set with solvent inclusion. The higher nucleophilicity of some complexes is reflected in an earlier transition state. The transition state C-I distance shows a good correlation with experimental rate constants for the simple carbonyl complexes whereas the C-M distance shows a poorer correlation. This is attributed either to the varying steric bulk of the complexes or to the different atomic radii of different metal centres. Comparisons of computed parameters and experimental rate constants for multiple series of complexes will be further discussed in **Chapter 5.**

A series of substituted manganese complexes investigated for comparison with $[Mn(CO)_5]^-$ were found to be more nucleophilic in general due to having an electron donating phosphine. The only exception was the complex bearing a phosphite whose reactivity was less than $[Mn(CO)_5]^-$. Again, good correlations were found between the calculated $\Delta H^{\ddagger}$ and experimental log *k* values with similar $R^2$ values to those observed for the simple carbonyl complexes. The C-I transition state distance showed a good correlation with experimental rate constants. A correlation was also observed in this system for the TS Mn-C distances with the metal centre remaining constant.

The HOMO energies of the manganese complexes also show a good correlation with experimental rate constants, which may provide a simple and quick means of estimating experimental nucleophilicity for systems of comparable steric properties.

Whilst the gas-phase barrier heights show reasonable correlations with experimental rate data for all basis sets, both the SDD and mixed basis with solvent inclusion seem to be the most promising in terms of computational efficiency and correlations with experiments. Moreover they give the right overall reaction profile. For the systems of interest investigated in the following chapters, optimisations will be carried out using both SDD and the mixed basis set, both with inclusion of solvent. Comparisons between the transition state distances and experimental log *k* values will be undertaken, as will comparisons between the calculated and experimental $\Delta H^{\ddagger}$ values.

## 2.6 References


(1) Davison, A.; Ellis, J. E. *J. Organomet. Chem.* **1972**, *36*, 113.

(2) Dessy, R. E.; Pohl, R. L.; King, R. B. *J. Am. Chem. Soc.,* **1966**, *88*, 5121.

(3) Lai, C. K.; Feighery, W. G.; Zhen, Y.; Atwood, J. D. *Inorg. Chem.* **1989**, *28*, 3929.

(4) Pearson, R. G.; Figdore, P. E. *J. Am. Chem. Soc.,* **1980**, *102*, 1541.

(5) Schrauzer, G. N.; Deutsch, E. *J. Am. Chem. Soc.* **1968**, *90*, 2441.

(6) Schrauzer, G. N.; Deutsch, E. *J. Am. Chem. Soc.* **1969**, *91*, 3341.

(7) Stolzenberg, A. M.; Stershic, M. T. *J. Am. Chem. Soc.* **1988**, *110*, 5397.

(8) Bickelhaupt, F. M.; Buisman, G. J. H.; de Koning, L. J.; Nibbering, N. M. M.; Baerends, E. J. *J. Am. Chem. Soc.,* **1995**, *117*, 9889.

(9) DePuy, C. H.; Gronert, S.; Mulin, A.; Bierbaum, V. M. *J. Am. Chem. Soc.* **1990**, *112*, 8650.

(10) Gronert, S. *Chem. Rev.* **2001**, *101*, 329.

(11) Gronert, S. *Acc. Chem. Res.* **2003**, *38*, 848.

(12) Nibbering, N. M. M.; *Acc. Chem. Res.* **1990**, *23*, 279.

(13) Olmstead, W. N.; Brauman, J. I. *J. Am. Chem. Soc. **1977, 99, 4219.***

(14) Glukhovtsev, M. N.; Pross, A.; Radom, L. *J. Am. Chem. Soc.,* **1995**, *117*, 2024.

(15) Gonzales, J. M.; Allen, W. D.; Schaefer III, H. F. *J. Phys. Chem. A,* **2005**, 109, 10613.

(16) Grüning, M.; Gritsenko, O. V.; Baerends, E. J. *J. Phys. Chem. A* **2004**, *108*, 4459.

(17) Hase, W. L. *Science,* **1994**, *266*, 998.

(18) Lee, C.; Yang, W.; Parr, R. G. *Phys. Rev. B* **1988**, 37, 785-789.

(19) Okuno, Y. *Int. J. Quantum Chem* **1998**, *68*, 261.

(20) Schmatz, S.; Botschwina, P.; Hauschildt, J.; Schinke, R. *J. Chem. Phys.* **2001**, *114*, 5233.

(21) Tucker, S. C.; Truhlar, D. G. *J. Phys. Chem.* **1989**, *93*, 8138.

(22) Vayner, G.; Houk, K. N.; Jorgensen, W. L.; Brauman, J. I. *J. Am. Chem. Soc.* **2004**, *126*, 9054.

(23) Chang, T. C. T.; Rosenblum, M.; Simms, N. *Org. Synth.* **1988**, *8*, 479.

(24) King, B. *Accounts of Chemical Research* **1970**, *3*, 417.

# CHAPTER 3

# Modelling nucleophilicity of neutral 18-electron metal complexes

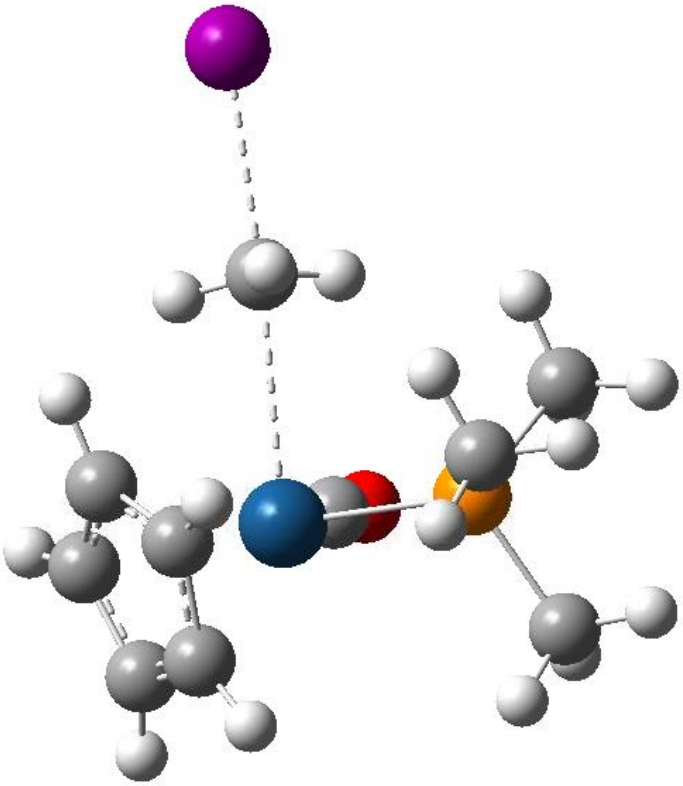

## 3.1 Introduction

The work described in **Chapter 2** explored a number of anionic 18-electron anionic complexes to investigate how the structure of the $S_N2$ transition state is affected by solvent and basis set and which computed parameters correlate best with experimental data. The calculated barrier heights and C-I distance showed a good correlation with experimental rate constants whereas the C-M distances in the transition state only correlated well with experimental reactivity when the central metal was kept constant and the steric environment was similar as was the case for $[Mn(CO)_4L]^-$. The calculated HOMO energies showed a reasonable correlation for complexes with comparable steric bulk.

Many of the complexes which are experimentally interesting contain phosphine ligands. The nucleophilicity of such complexes can be readily tuned by changing the phosphine. Unlike the simple anionic complexes investigated in **Section 2.2**, the complexes bearing phosphine ligands can potentially adopt a number of conformations which need to be investigated before an accurate barrier height can be determined, as was the case for the $[Mn(CO)_4L]^-$ complexes in **Section 2.4.**

Three series of phosphine-containing complexes were selected for investigation. The half-sandwich complexes [CpIr(CO)L] and [Cp*Ir(CO)(L)] (L = phosphine) investigated experimentally by Wang et al. are considered in this chapter.[1] Square-planar Vaska–type complexes, $[IrCl(CO)(PR_3)_2]$ [2] will be discussed in **Chapter 4**. Each series contains a larger number of complexes than the manganese series which only contained five complexes.[3]

Complexes bearing cyclopentadienyl (Cp) ligands have been extensively studied in the literature. A comprehensive review by Werner investigated the reaction of various substrates with group IX metal complexes.[4] Further work investigating the reaction of alkyl halides with $[CpM(CO)(PR_3)]$ (M = Co, Rh, Ir) was conducted by Hart-Davis.[5] The reaction was shown to form an ionic species, which is stable for the iridium complexes but rapidly undergoes migratory CO insertion and coordination of an halide to form a neutral acetyl species in the case of rhodium and cobalt. This reaction was

shown to be faster in more polar solvents, suggesting that the reaction proceeds through a polar transition state. Further studies have also focused on the use of chiral ligands.[6,7]

[CpIr(CO)L] complexes are 18-electron neutral complexes that react with iodomethane to form an ion-pair as shown in **Figure 3.1.**

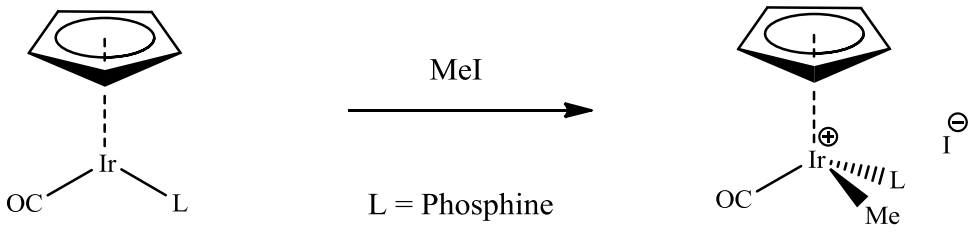


**Figure 3.1:** General reaction of [CpIr(CO)L] complexes with MeI

## 3.2 Computational results for [CpIr(CO)L] complexes

### 3.2.1 [CpIr(CO)($PMe_3$)]

The simplest complex in this series contains a $PMe_3$ ligand, which adopts conformations with a methyl group either eclipsed or staggered with respect to the carbonyl ligand as shown in **Figure 3.2**. The complex with the $PMe_3$ ligand in the eclipsed conformation **(1a)** was marginally higher in energy (1.19 kJ $mol^{-1}$) than with the ligands staggered **(1b).**

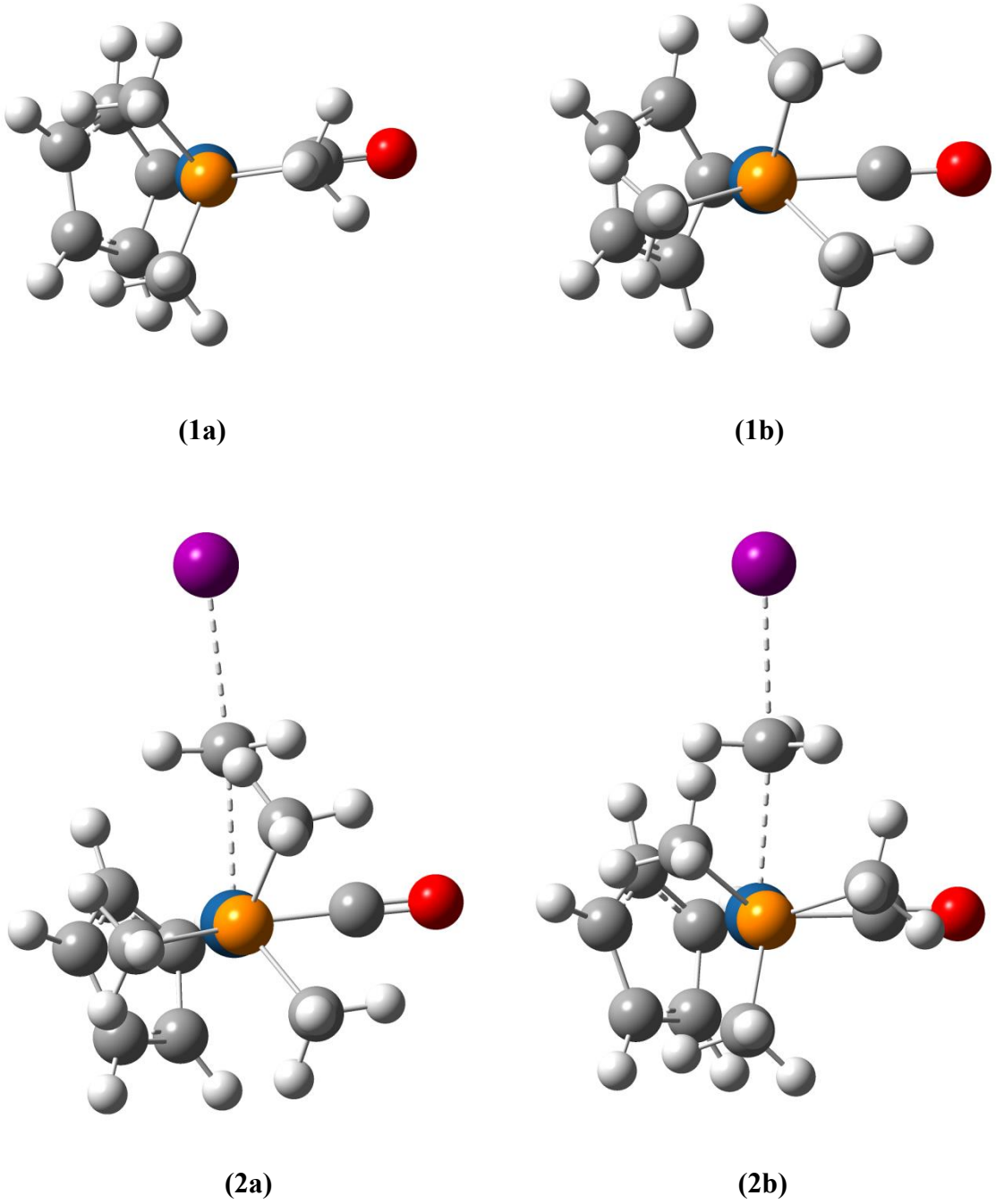

**(1a)** **(1b)**

**(2a)** **(2b)**

**Figure 3.2:** Optimised structures of two conformers of [CpIr(CO)($PMe_3$)], **1a** and **1b** and two transition states **2a** and **2b.** (DFT-B3LYP/SDD – gas-phase)

Transition states for the reaction with iodomethane were also optimised with the phosphine ligand in each of these conformations as shown in **Figure 3.2.** The two transition states only differ from one another by 2.03 kJ $mol^{-1}$ with the staggered conformation **(2a)** being the lower in energy. The C-I transition state distances are 2.78 Å for **2a** and 2.77 Å for **2b** and the C-M distances were 2.60 Å for **2a** and 2.61 Å for **2b**

showing that the conformation of the phosphine ligand in this case has little effect on the transition state structure or energy.

The calculated barrier heights are 58.44 and 59.28 kJ $mol^{-1}$ for the staggered and eclipsed complexes respectively, suggesting that both pathways are feasible and either reactant geometry could lead to product formation.

Energy profiles for the reaction of [CpIr(CO)($PMe_3$)] and iodomethane with and without inclusion of solvent are shown in **Figure 3.3.** Similarly to the anionic complexes discussed in **Chapter 2**, the profile is endothermic in the gas-phase but inclusion of solvent correctly predicts the reaction to be exothermic. In contrast to the anionic complexes, inclusion of solvent acts to lower the barrier with the polar transition state being more strongly solvated than the neutral reactants.

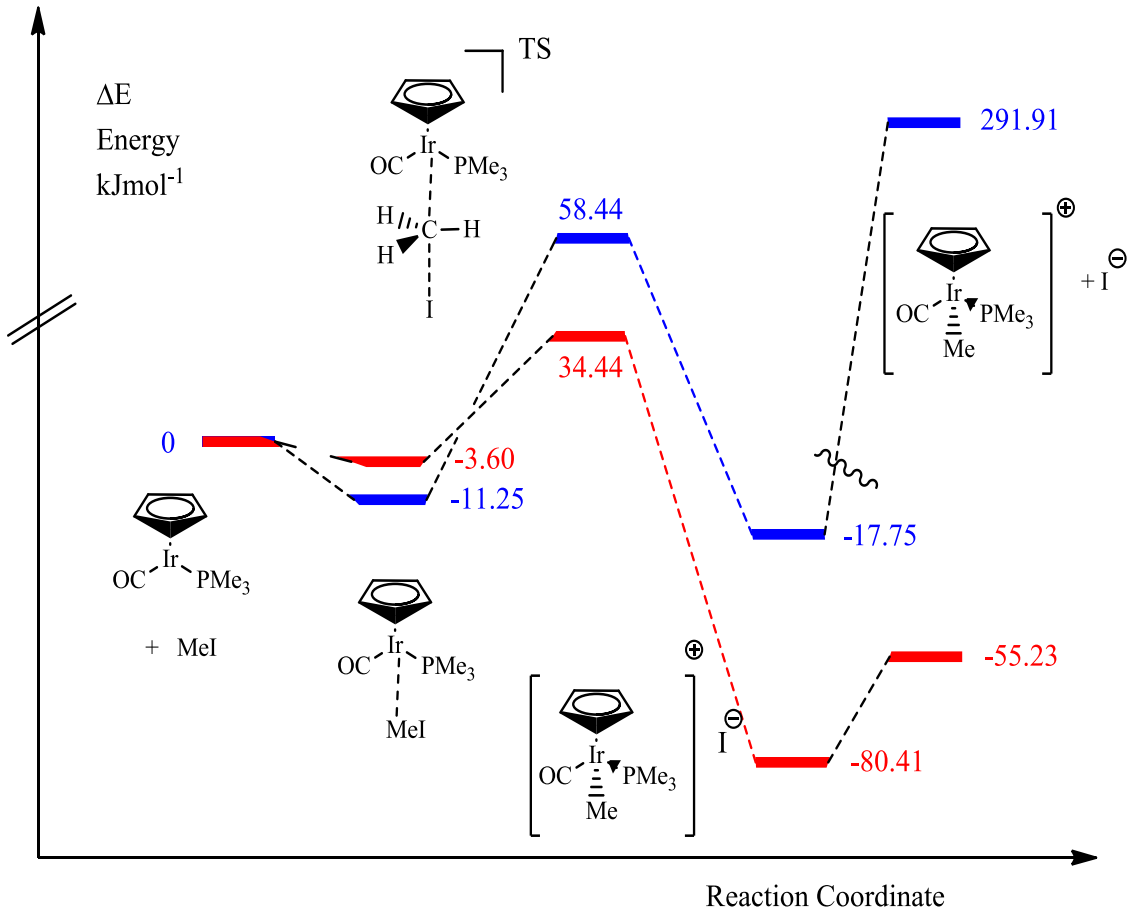


**Figure 3.3:** Energy profiles ($\Delta E^{\ddagger}$) for the reaction of [CpIr(CO)($PMe_3$)] with iodomethane in gas-phase (blue) and with inclusion of solvent (red) (DFT-B3LYP/SDD)

### 3.2.2 [CpIr(CO)($PEt_3$)]

The next complex investigated was [CpIr(CO)($PEt_3$)]. Due to the conformational flexibility of the ethyl groups on the $PEt_3$ ligand, a number of different configurations of the ligand are possible which could potentially affect the calculated barrier heights. Several different geometries were investigated for this complex. The structures of five optimised conformers are shown in **Figure 3.4** and their respective energies are in **Table 3.1.**

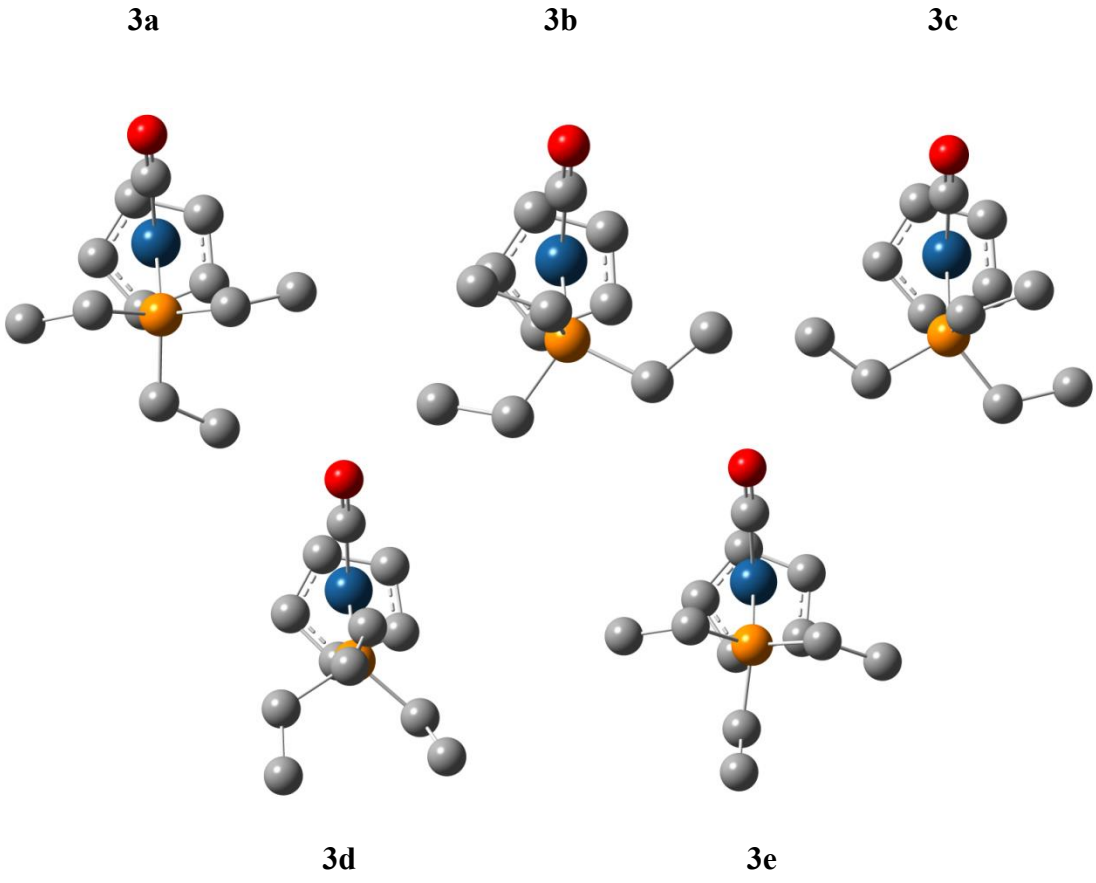


**Figure 3.4:** Five optimised geometries of [CpIr(CO)($PEt_3$)] (DFT-B3LYP/SDD – gas-phase) Hydrogen atoms omitted for clarity.

| Conformer | 3a | 3b | 3c | 3d | 3e |
|---|---|---|---|---|---|
| $E_{REL}$/ kJ mol$^{-1}$ | 24.90 | 3.97 | 4.01 | 27.60 | 0.00 |

**Table 3.1:** Relative energies of five conformers of [CpIr(CO)($PEt_3$)] (DFT-B3LYP/SDD – gas-phase)

Five different geometries were optimised for the complex [CpIr(CO)($PEt_3$)]. In the lowest energy conformer **3e** the $PEt_3$ ligand adopts a conformation close to that found in a crystal structure of [IrCl(CO)($PEt_3$)$_2$] and is 28 kJ mol$^{-1}$ lower in energy than **3d,** which was the least stable conformer. In **3e**, two of the ethyl groups are in the same plane and one is pointing perpendicular to the plane. Further views of **3e** and **3d** are shown in **Figure 3.5** and **Figure 3.6.** The higher energy of **3d** is attributed to the unfavourable steric interactions caused by all the ethyl fragments pointing towards each other.

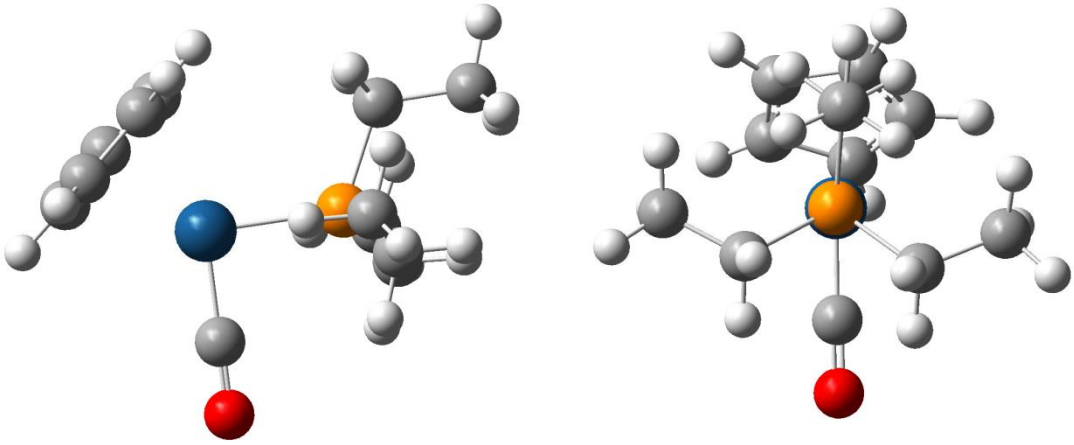

**Figure 3.5:** Two views of **3e.** (DFT-B3LYP/SDD – gas-phase)

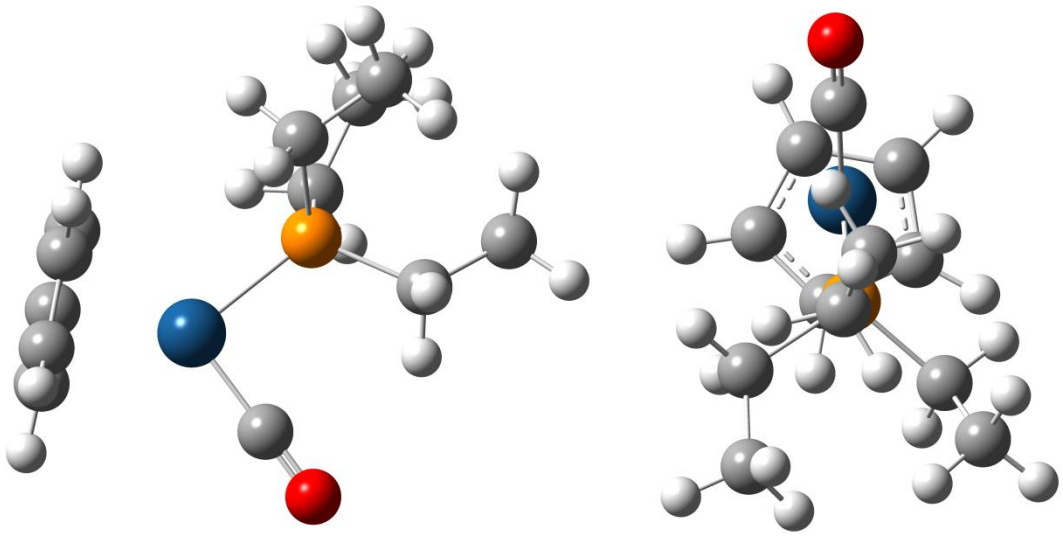

**Figure 3.6:** Two views of **3d.** (DFT-B3LYP/SDD – gas-phase)

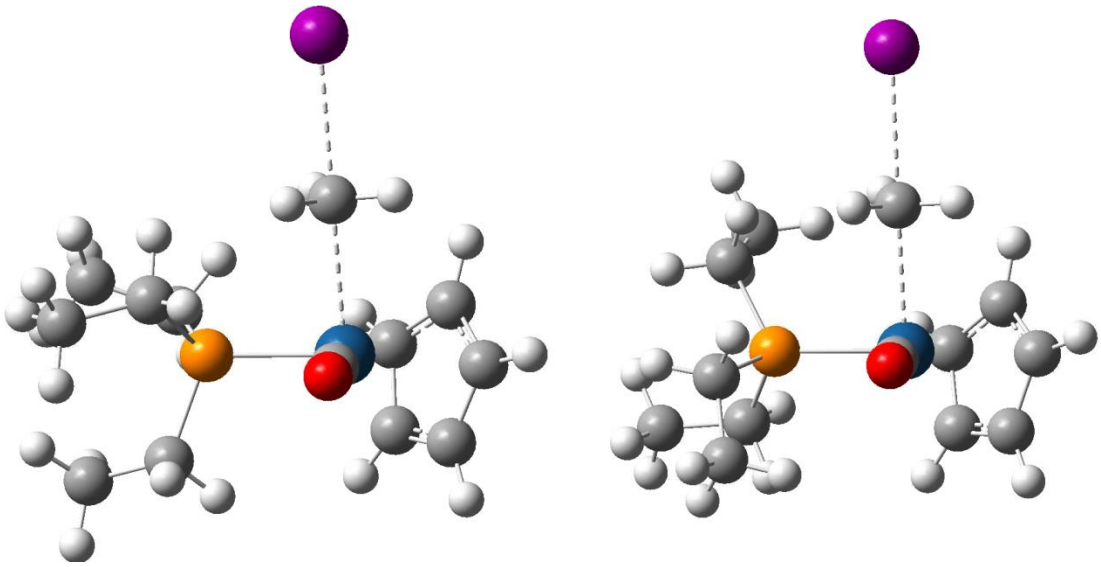

**4d** **4e**

**Figure 3.7:** Optimised transiton states for reaction of conformer **3d** and **3e** with iodomethane (DFT-B3LYP/SDD – gas-phase)

**Figure 3.7** shows the transition states for the reaction of conformers **3d** and **3e** with iodomethane**.** **4e** is more stable than **4d** by 18.03 kJ $mol^{-1}$ due to the reduced steric interaction of the ethyl groups which are no longer pointing towards each other. The C-M and C-I distances are very similar for both structures. For **4d** the C-I and C-M distances are 2.76 Å and 2.63 Å respectively whereas for **4e** these are 2.79 Å and 2.61

Å. The $\Delta H^{\ddagger}$ barrier height **3d** to **4d** is 54.22 kJ $mol^{-1}$ whereas the corresponding barrier height from **3e** to **4e** is 61.38 kJ $mol^{-1}$ (**Figure 3.8**). Whilst the transition **3e-4e** has a significantly higher barrier height, it is more than compensated by the enhanced stability of the reactants and transition state, making the transition **3e to 4d** unlikely.

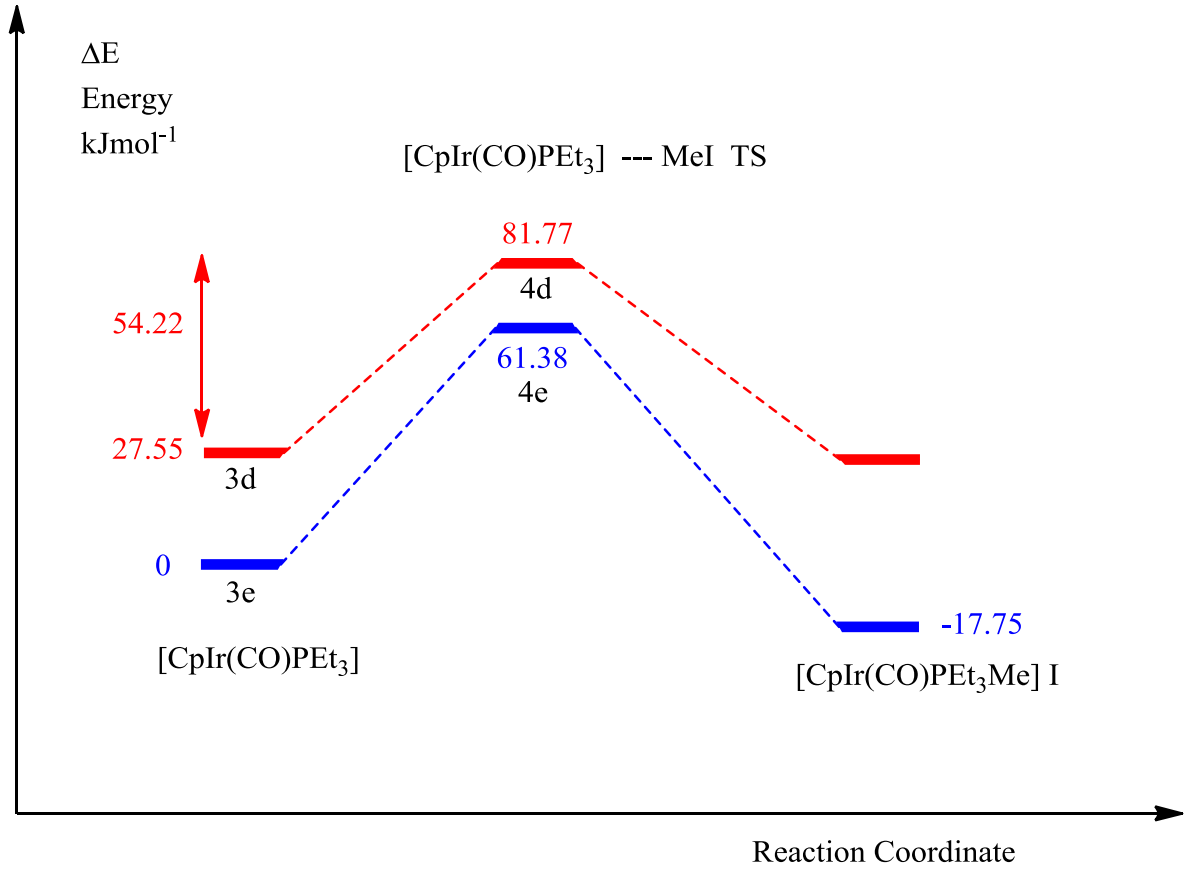


**Figure 3.8:** Energy profiles ($\Delta H^{\ddagger}$) for the reactions of two confomers of [CpIr(CO)($PEt_3$)] (**3d** (red) and **3e** (blue)) with iodomethane. (DFT-B3LYP/SDD – Gas)

The conformational analysis on [CpIr(CO)($PMe_3$)] and [CpIr(CO)($PEt_3$)] highlights the importance of locating the lowest energy reactamt conformer before any tranisiton state analysis is undertaken. Whilst the change in conformation had little effect on [CpIr(CO)($PMe_3$)], the increase in number of possible conformers for [CpIr(CO)($PEt_3$)] is significant for both the reactant and the transition state. Optimisation of transition states starting from high energy reactant conformers will lead to poor correlations with experimental data.

### 3.2.3 Complexes bearing other phosphines

Six of the complexes in the series contained tri-aryl phosphine ligands. The reactant geometries for these complexes were optimised using a crystal structure of $[CpIr(CO)(PPh_3)]$[8] as a starting point. The remaining complexes bearing aryl substituents were based upon modifications to this structure. The starting structure for $[CpIr(CO)PCy_3]$ was taken from a Vaska complex found in the crystal database. The chloride and one of the phosphine ligands were removed and a Cp ring was added to construct the appropriate reactant, which was subsequently optimised.

Initially, SDD gas-phase calculations were carried out, which are relatively fast. The optimised structures were all subsequently re-optimised using the SDD and the mixed basis set both with inclusion of solvent. The complexes investigated, their corresponding rate constants and $\Delta H^{\ddagger}$ barrier heights are shown in **Table 3.2.**

| | | **$\Delta H^{\ddagger}$ Barrier heights / kJ mol$^{-1}$** | | |
|---|---|---|---|---|
| **L** | **log ( $k$ / M$^{-1}$s$^{-1}$)** | **SDD Gas** | **SDD DCM** | **Mixed DCM** |
| $P(4\text{-}CF_3C_6H_4)_3$ | -2.82 | 84.61 | 52.14 | 56.28 |
| $P(4\text{-}ClC_6H_4)_3$ | -2.21 | 73.26 | 47.62 | 54.89 |
| $PCy_3$ | -2.09 | 80.17 | 52.42 | 59.04 |
| $P(4\text{-}FC_6H_4)_3$ | -1.96 | 75.54 | 50.78 | 55.28 |
| $PPh_3$ | -1.57 | 65.60 | 44.15 | 50.68 |
| $P(4\text{-}MeC_6H_4)_3$ | -1.16 | 60.81 | 42.03 | 49.08 |
| $P(4\text{-}MeOC_6H_4)_3$ | -1.14 | 60.35 | 42.82 | 48.52 |
| $PPh_2Me$ | -0.96 | 63.34 | 37.16 | 46.42 |
| $PPhMe_2$ | -0.62 | 62.18 | 37.68 | 44.59 |
| $PEt_3$ | -0.82 | 64.03 | 34.00 | 44.08 |
| $PMe_3$ | -0.34 | 60.09 | 36.09 | 42.11 |

**Table 3.2:** DFT calculated barrier heights and experimental rate constants ($CH_2Cl_2$, 25 °C) for reaction of [CpIr(CO)L] complexes with MeI.[1] Basis sets and solvents as listed.

### 3.2.4 Comparison of computed and experimental reactivity

Plots of calculated barrier height ($\Delta H^{\ddagger}$) against experimental log *k* are shown in **Figure 3.9.** The same general trends are apparent for this series as were observed for the anionic complexes in **Chapter 3.** The least nucleophilic complexes based upon experimental observations have the highest calculated barrier heights and *vice-versa.*

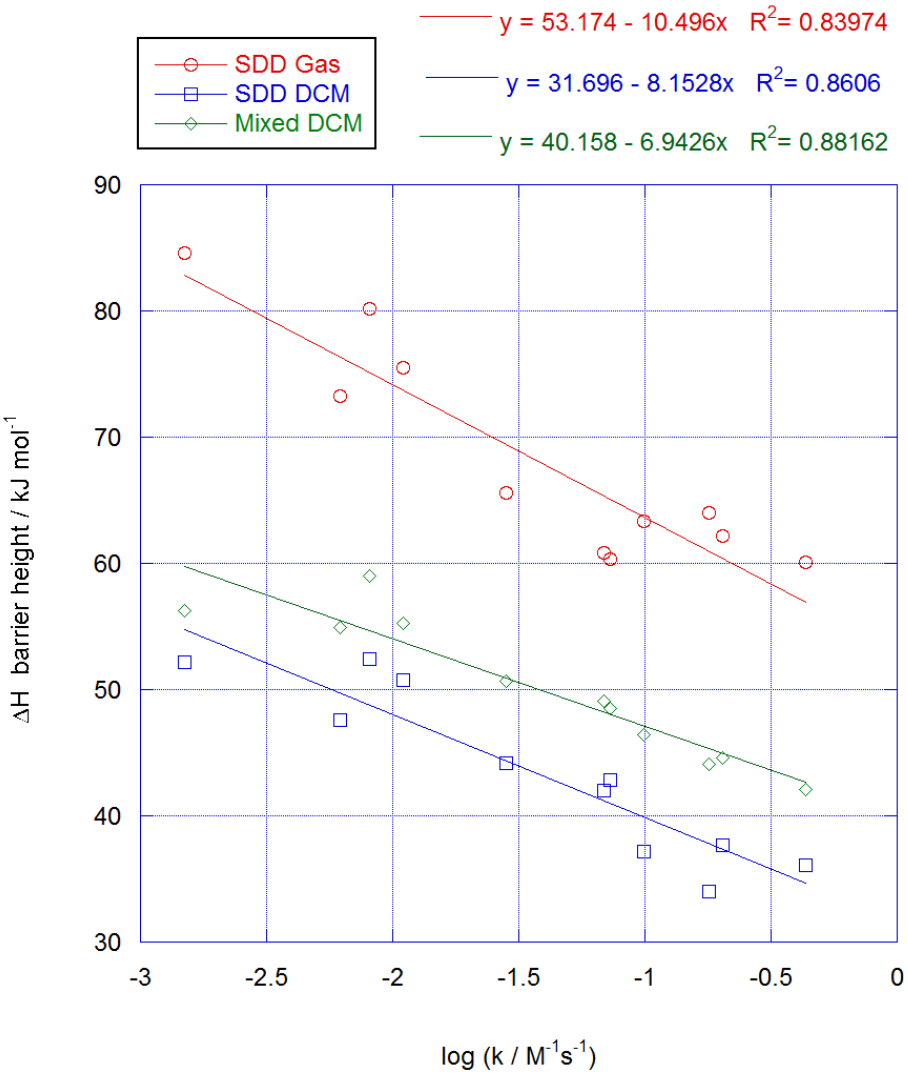


**Figure 3.9:** Plots of calculated $\Delta H^{\ddagger}$ barrier heights against log *k* ($CH_2Cl_2$, 25 °C) for the reaction of [CpIr(CO)L] complexes with iodomethane. Basis sets, linear fit equations and $R^2$ values given in key.

The correlations are not quite as good as for the anionic systems investigated in **Chapter 2**. Inclusion of solvent in the calculations results in a small improvement in the $R^2$ value. Moreover, inclusion of solvent is required for accurate representation of the

reaction since gas-phase profiles calculated for this system are endothermic whereas they become exothermic once solvent is taken into account.

### 3.2.5 Transition state geometries

Plots of the C-I and C-M distances in the transition state against experimental rate data for the [CpIr(CO)L] series are shown in **Figures 3.10 and 3.11.**

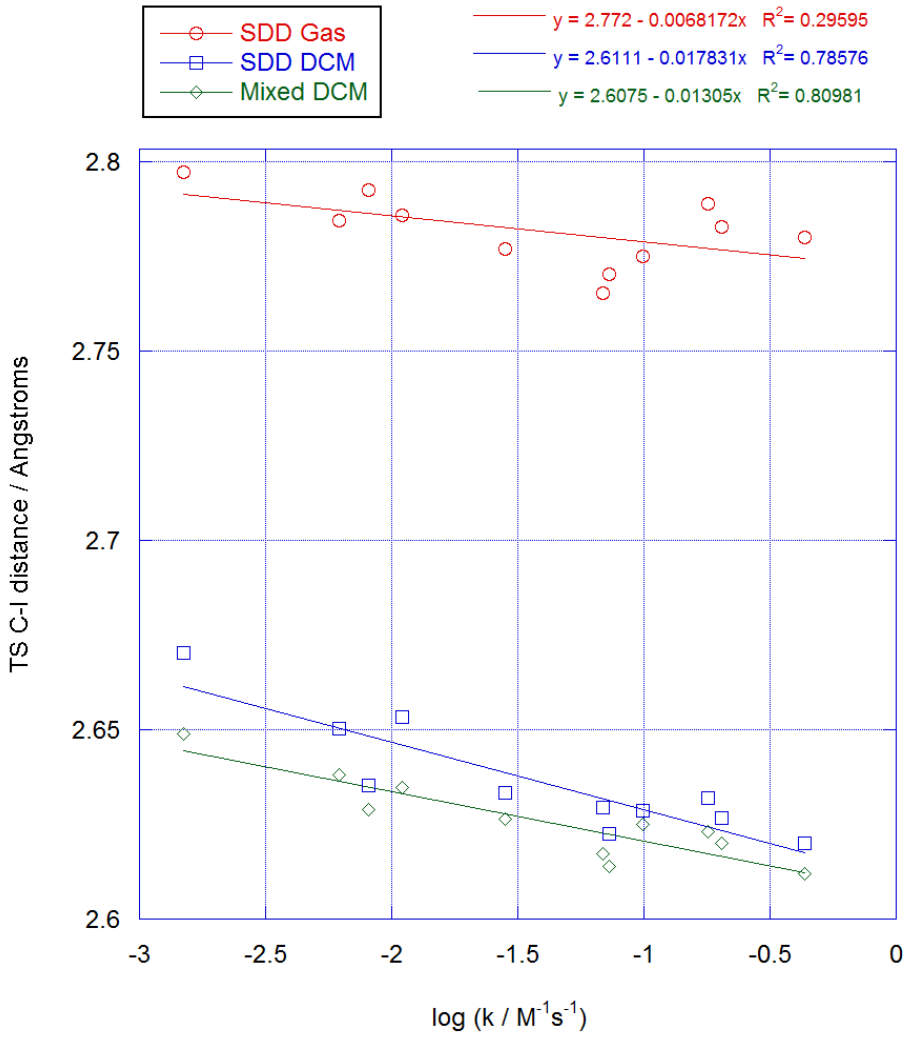


**Figure 3.10:** Plots of transition state C-I distances against experimental log *k* ($CH_2Cl_2$/ 25 $^oC$) for the reaction of [CpIr(CO)L] complexes with MeI. Basis sets, linear fit equations and $R^2$ values given in key.

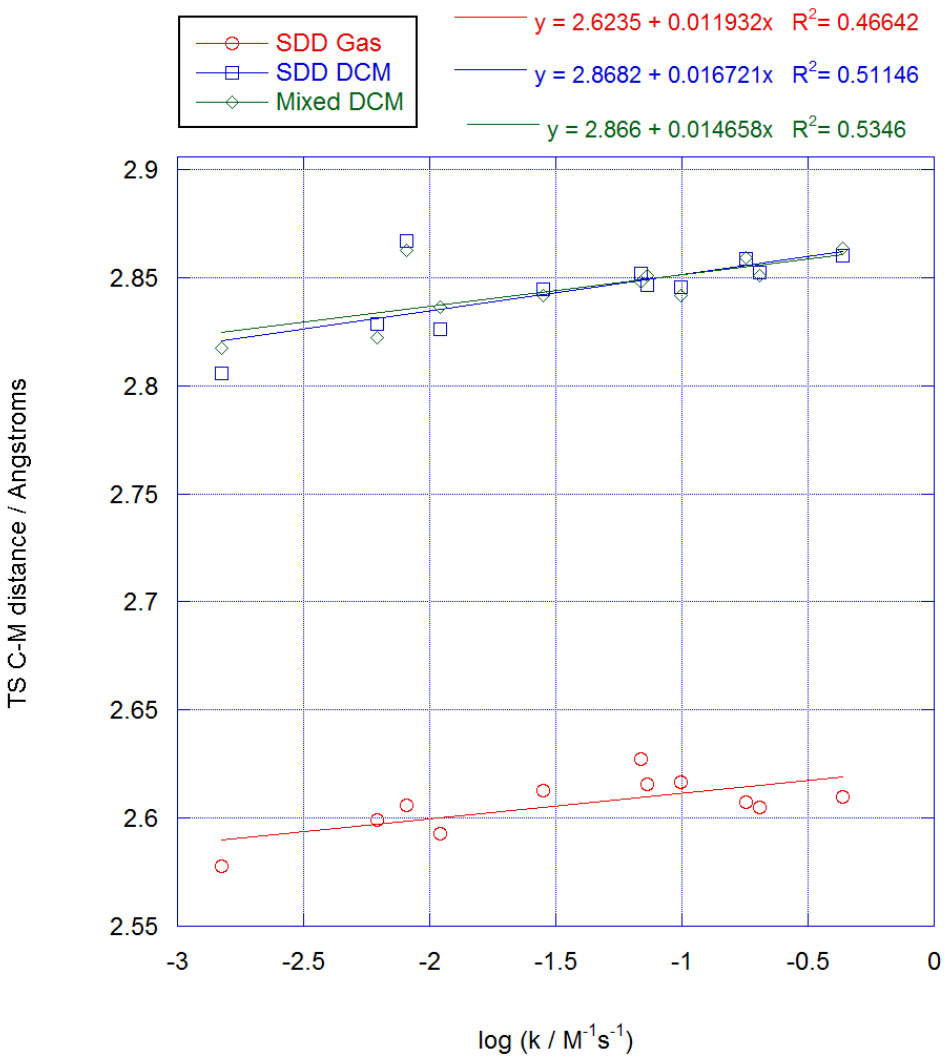


**Figure 3.11:** Plots of transition state C-Ir distances against experimental log *k* for the reaction of [CpIr(CO)L] complexes with MeI. Basis sets, linear fit equations and $R^2$ values given in key.

The trends for the [CpIr(CO)L] system are similar to those in **Chapter 2** for anionic complexes. The most reactive complexes have the earliest transition states. The C-I distance shows the greatest correlation with experimental rates. The complex bearing a $PCy_3$ ligand is an outlier for two of the setups used, with a longer C-M distance and shorter C-I distance than expected, suggesting that the complex should be more reactive than is observed experimentally.

### 3.2.6 Reactant HOMO energies

**Figure 3.12** shows that the HOMO for [CpIr(CO)($PMe_3$)] has its major lobes above and below the plane defined by the Ir-P-CO plane, with appropriate orientation to act as a donor towards iodomethane approaching perpendicular to this plane. Similar orbitals were observed for each complex in the series. A plot of the calculated HOMO energy against log *k* is shown in **Figure 3.13.**

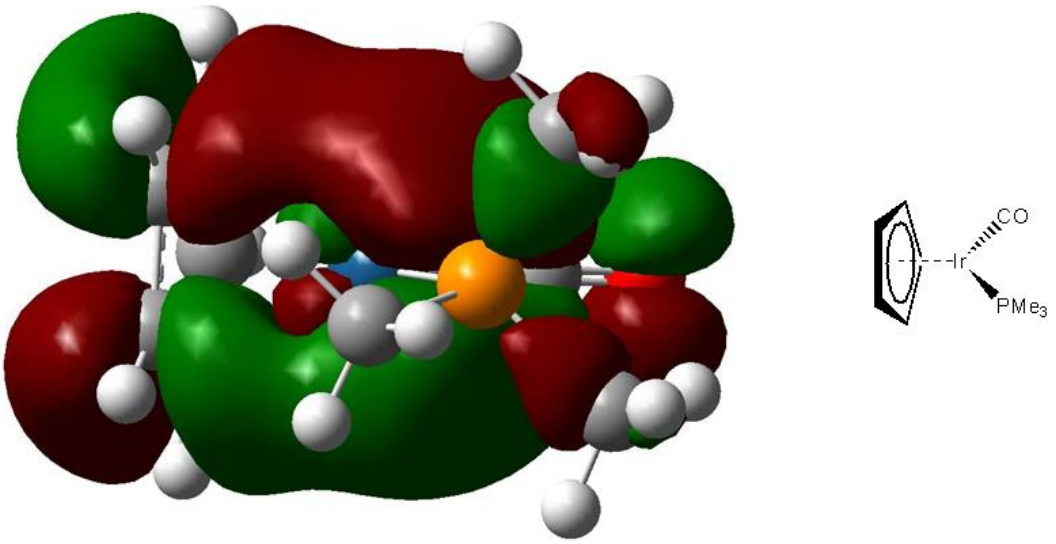


**Figure 3.12:** HOMO of [CpIr(CO)($PMe_3$)] (DFT-B3LYP/Mixed basis - DCM)

A good correlation was observed for the majority of the complexes investigated with a $R^2$ value of 0.83. The complex bearing $PCy_3$ is an outlier so is omitted from the fit. Based solely upon the DFT calculated HOMO energies, [CpIr(CO)($PCy_3$)] is predicted to be the most reactive complex in the series. Evidently the extreme steric bulk of the ligand reduces the reactivity of the complex by hindering the approach of iodomethane. For complexes lacking the extreme steric bulk, the reactant HOMO energy appears to be quite a good predictor of nucleophilicity towards MeI.

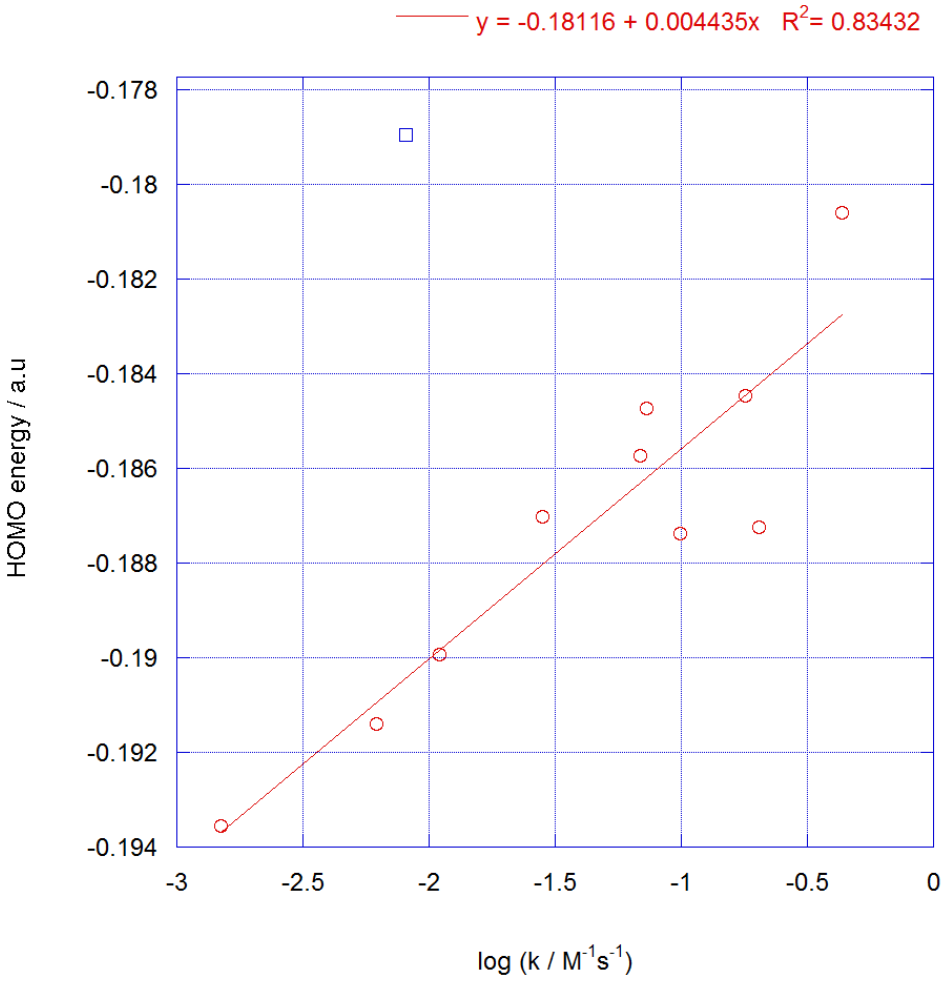


**Figure 3.13:** Plot of DFT calculated HOMO energy against log *k* ($CH_2Cl_2$, 25 °C). [CpIr(CO)($PCy_3$)] is excluded from the linear fit. (shown in blue) (DFT-B3LYP/Mixed basis - DCM)

### 3.2.7 Reactant vibrational frequencies

Each of the complexes in this series contains a carbonyl ligand. The carbonyl stretching frequency is easily measurable experimentally and is often used as an indicator of electron density on the metal centre which will affect nucleophilicity.

Comparisons between the calculated and experimental carbonyl stretching frequencies for metal complexes have been made in the literature. Kelly et al focused on a series of iridium NHC complexes with the general formula [$IrCl(CO)_2$(NHC)] which were chosen for their ease of synthesis.[9] The experimental carbonyl strtetching frequencies

were compared with Tolman's electronic parameter to quantify the electron density on the complex.[10]

Gusev investigated several series of metal carbonyl complexes using computational methods.[11] The series investigated were $[Ni(CO)_3L]$, $[IrCl(CO)_2L]$ and $[CpIr(CO)L]$. The experimental stretching frequency and carbon-oxygen bond distance were compared to the computational counterpart with a view to predict and explain experimental reactivity. Further investigations have also been carried out.[12-15]

Work carried out at the Univeristy of Sheffield as part of two fourth year projects by Clifton and Smith looked into a series of metal complexes and analysed the relationships between calculated and experimental carbonyl stretching frequencies.[16,17] This work has been extended in the present study to included data obtained using the mixed basis set and including solvent. Plots of the calculated ν(CO) against experimental ν(CO) are shown in **Figure 3.14** for the three computational methods employed.

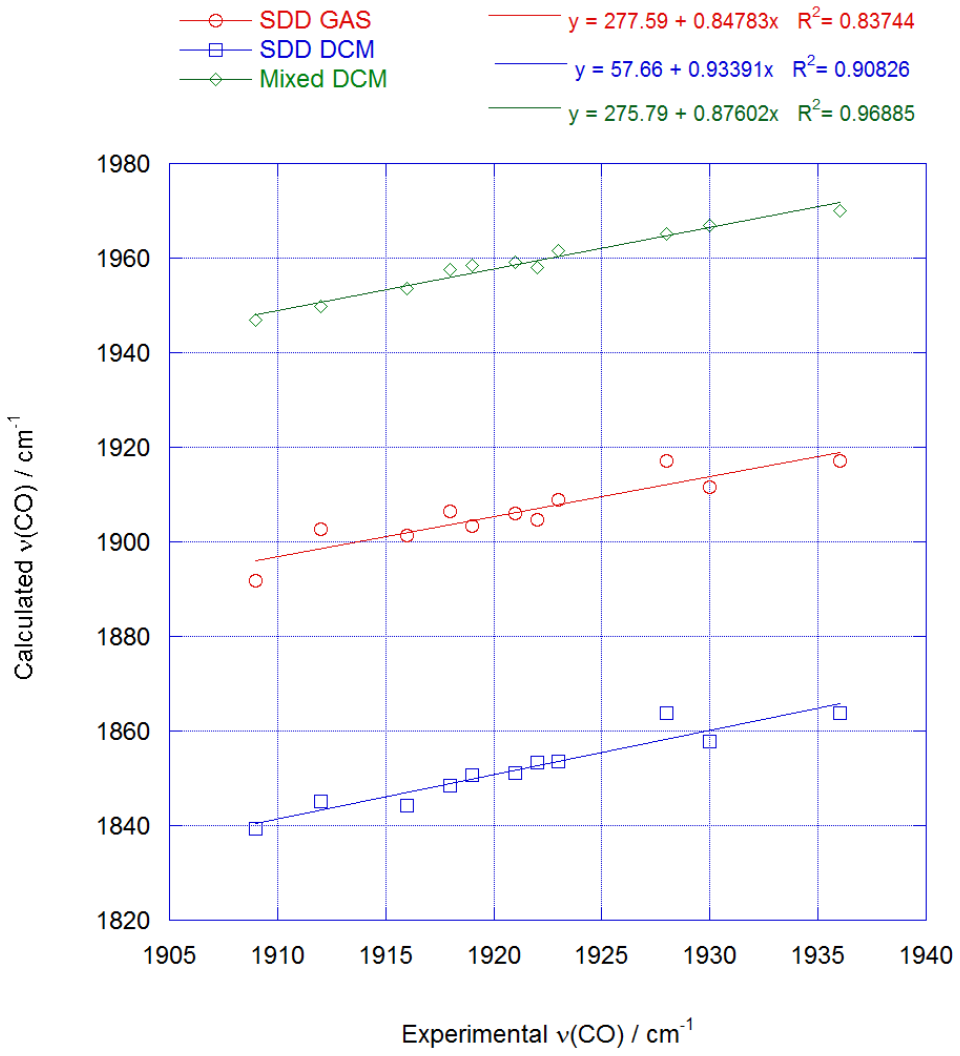


**Figure 3.14:** Plots of DFT calculated ν(CO) against experimental ν(CO) for [CpIr(CO)L] complexes. Basis sets, linear fit equations and $R^2$ values given in key.

A good correlation was observed for each of the three computational methods investigated with the best $R^2$ of 0.969 being observed for the mixed basis calculations with solvent included. Including solvent in the SDD calculations improves the correlation and gives ν(CO) values lower than those from gas-phase SDD calculations.

The carbonyl stretching frequency is a measure of the amount of electron density on the complex and thus can be used to make a prediction of reactivity. A plot of the calculated and experimental stretching frequencies against experimental rate constants

is shown in **Figure 3.15.** The $R^2$ values are reasonable for all computational methods investigated but are not quite as good as experimental values.

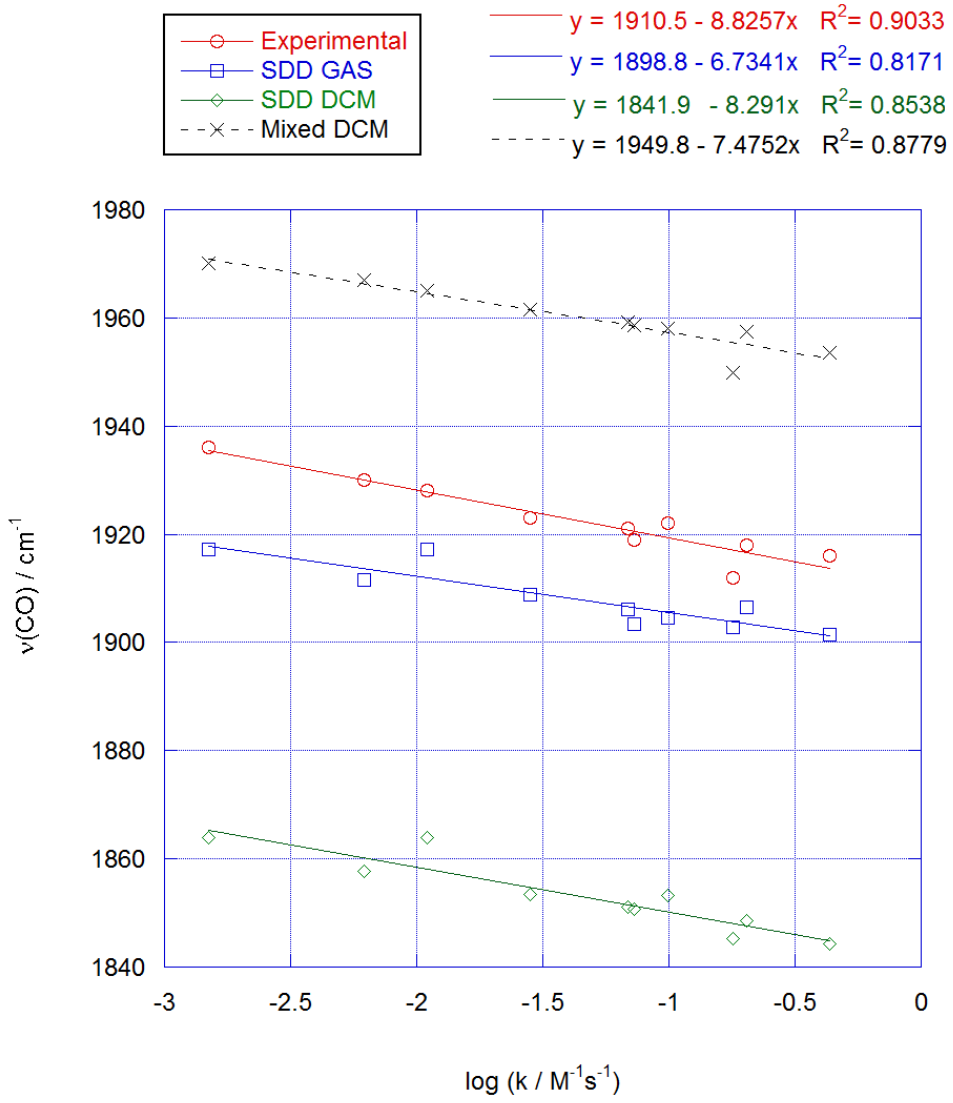


**Figure 3.15:** Plots of DFT calculated and experimental ν(CO) against experimental log *k* for [CpIr(CO)L] complexes. Basis sets, linear fit equations and $R^2$ values given in key.

## 3.3 [Cp*Ir(CO)L] complexes

### 3.3.1 Barrier heights and stretching frequencies

Wang et al. investigated an analogous series of complexes in which the Cp- ring was replaced with a pentamethylcyclopentadienyl ring (Cp*).[1] This ligand is known to be more electron donating and to impart greater nucleophilicity onto the metal centre despite its increased steric bulk. For the purposes of this work, the experimental data for the Cp and Cp* series are directly comparable as the kinetic analysis was undertaken in the same solvent. The complexes react with iodomethane according to **Figure 3.1.**

As before a conformational analysis was performed upon each reactant complex in order to identify the lowest energy conformer before transition states were optimised based upon this conformer. The complexes investigated, their respective experimental kinetic data and DFT calculated barrier heights are shown in **Table 3.3.** A plot of calculated barrier heights against experimental rate constants is shown in **Figure 3.16.**

| | | $\Delta H^{\ddagger}$ Barrier heights / kJ mol$^{-1}$ | | |
|---|---|---|---|---|
| **L** | **log ($k$ / M$^{-1}$s$^{-1}$)** | **SDD Gas** | **SDD DCM** | **Mixed DCM** |
| $P(4\text{-}CF_3C_6H_4)_3$ | -1.61 | 70.83 | 47.06 | 50.26 |
| $P(4\text{-}ClC_6H_4)_3$ | -0.92 | 61.68 | 40.82 | 51.35 |
| $PPh_3$ | 0.17 | 55.06 | 37.95 | 44.91 |
| $PPh_2Me$ | 0.53 | 48.12 | 31.22 | 37.90 |
| $PMe_3$ | 1.41 | 48.12 | 27.70 | 35.83 |

**Table 3.3:** DFT calculated barrier heights and experimental kinetic data (DCM, 25 °C) for reactions of [Cp*Ir(CO)L] complexes with iodomethane. Basis sets and solvents as listed.

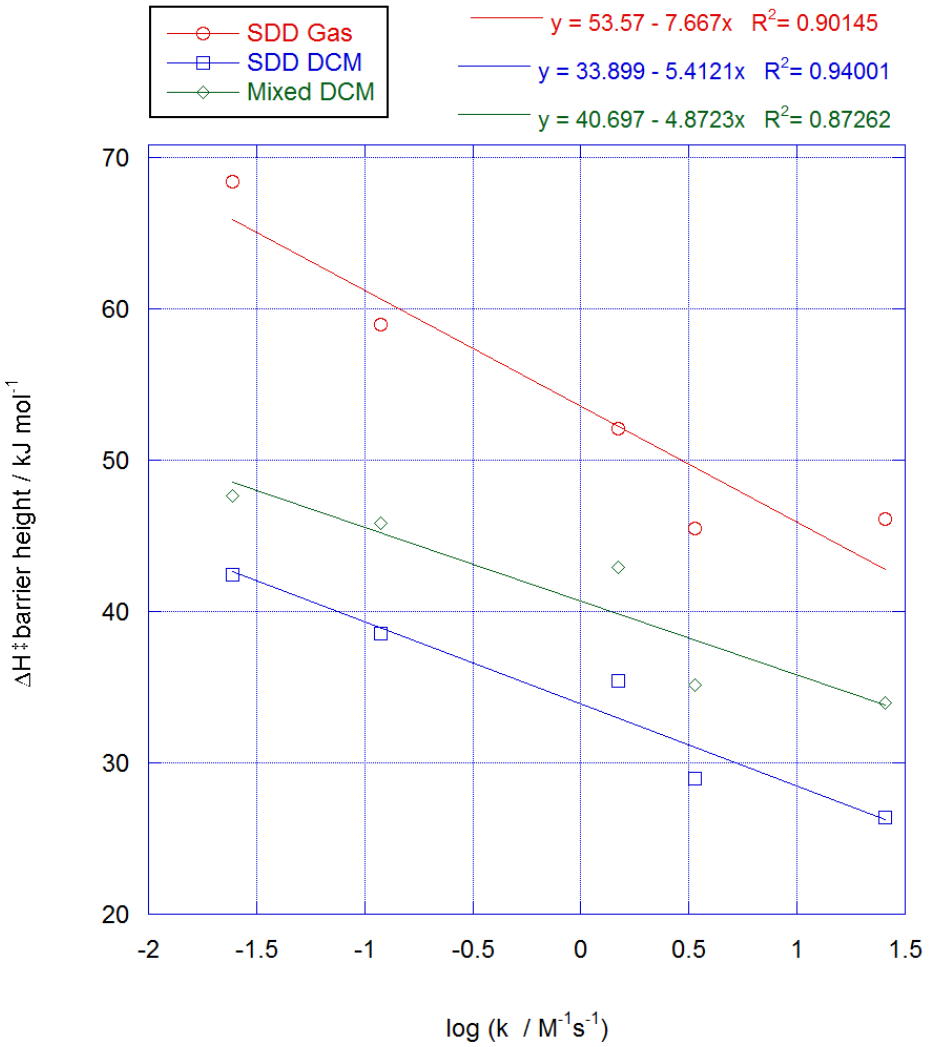


**Figure 3.16:** Plot of calculated barrier height ($\Delta H^{\ddagger}$) against log *k* for the reactions of [Cp*Ir(CO)L] complexes with MeI. Basis sets, linear fit equations and $R^2$ values given in key.

As for the Cp-system there is a clear relationship between the calculated barrier height ($\Delta H^{\ddagger}$) and experimental log *k* values. As the nucleophilicity of the complex increases, the barrier height decreases. Each of the three computational methods investigated showed the same relationship with the worst correlation being observed for mixed basis with solvent included where the $R^2$ value was 0.87.

### 3.3.2 Reactant HOMO energies and vibrational frequencies

**Figure 3.17** shows a plot of the calculated HOMO energy against log *k*. A better linear relationship was found for this system than for [CpIr(CO)L] ($R^2$ = 0.95 *cf* 0.83) which could be due to the [Cp*Ir(CO)L] complexes containing ligands with a similar steric bulk.

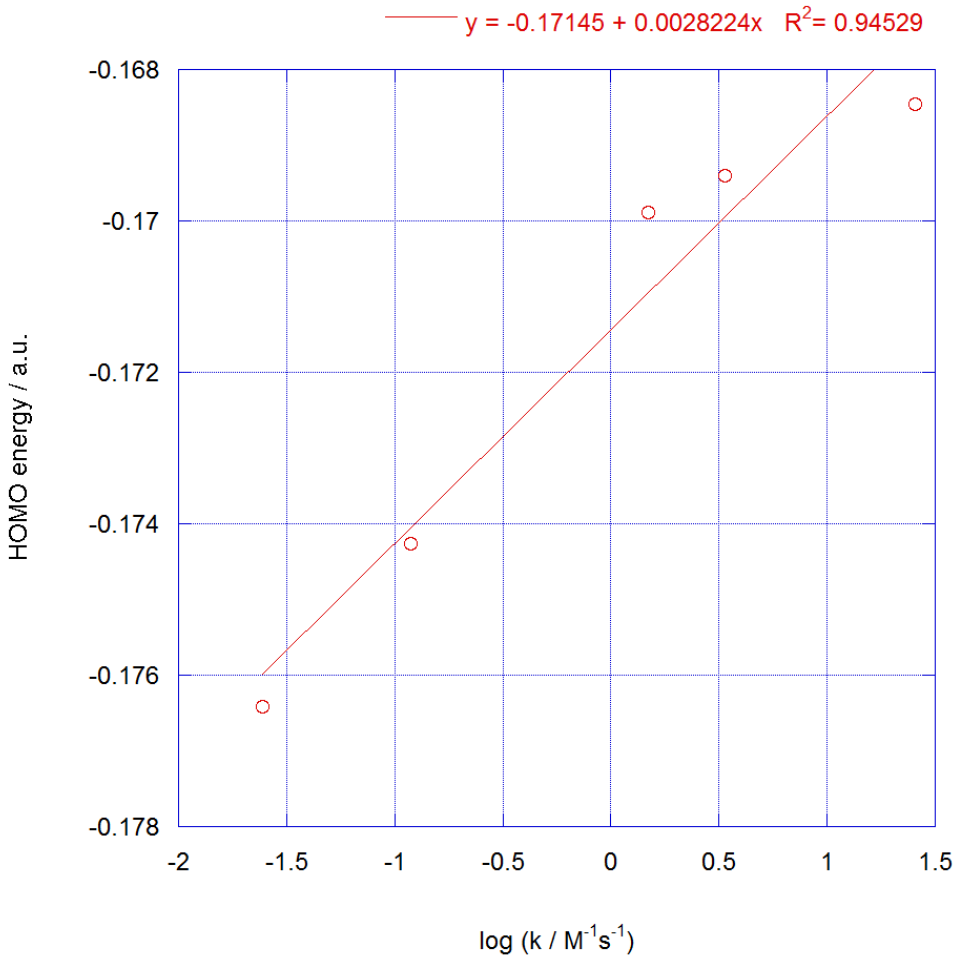


**Figure 3.17:** Plot of DFT calculated HOMO energy against log *k* ($CH_2Cl_2$, 25 °C). (DFT-B3LYP/Mixed basis - DCM)

**Figure 3.18** shows that the calculated carbonyl stretching frequencies also correlate well with experimental values for this series.

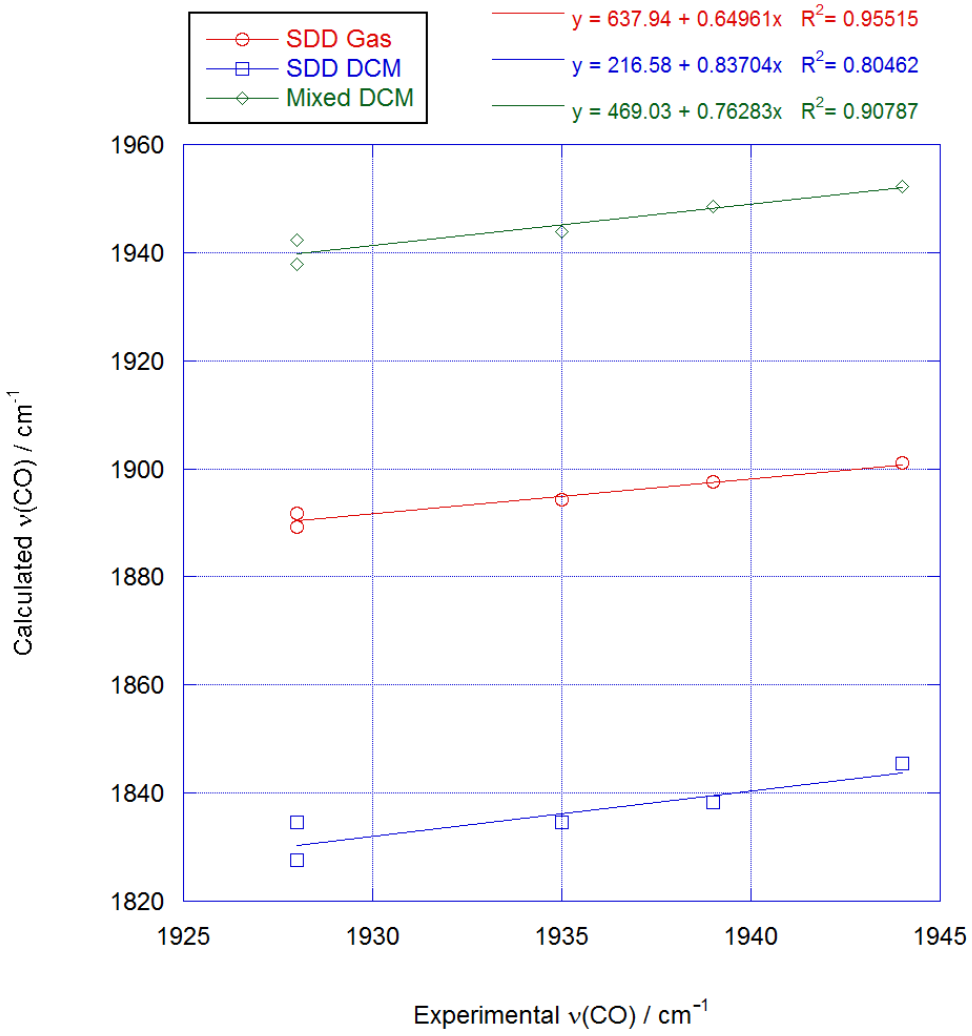


**Figure 3.18:** Plots of DFT calculated ν(CO) against experimental ν(CO) for [CpIr(CO)L] complexes. Basis sets, linear fit equations and $R^2$ values given in key.

### 3.3.3 Transition state geometries

Plots of calculated transition state C-M and C-I distances against experimental log *k* are shown in **Figure 3.19** and **Figure 3.20** and show a good correlation to experimental reactivity. In both cases the correlation is improved significantly with inclusion of solvent, with the best correlations obtained using the mixed basis set (with solvent).

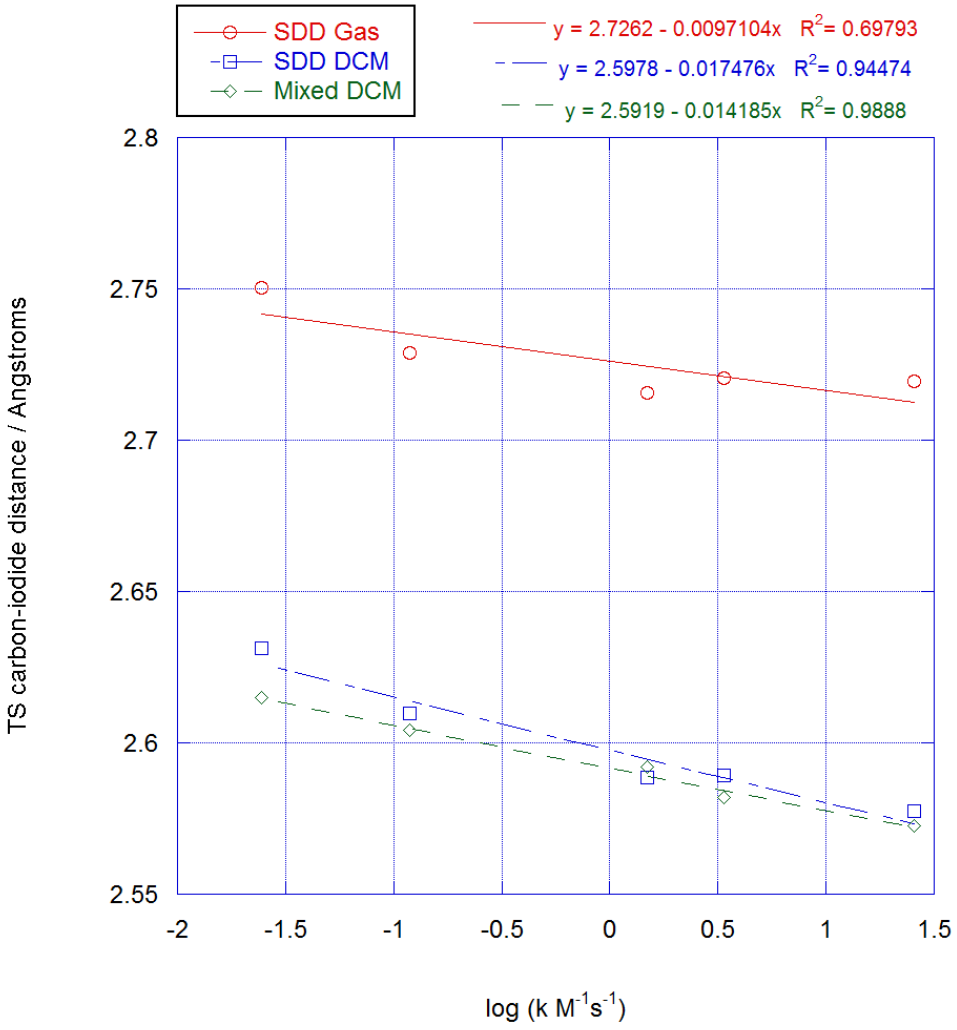


**Figure 3.19** Plot of transition state C-I distance against experimental log *k* for the reactions of [Cp*Ir(CO)L] complexes with MeI. Basis sets, linear fit equations and $R^2$ values given in key.

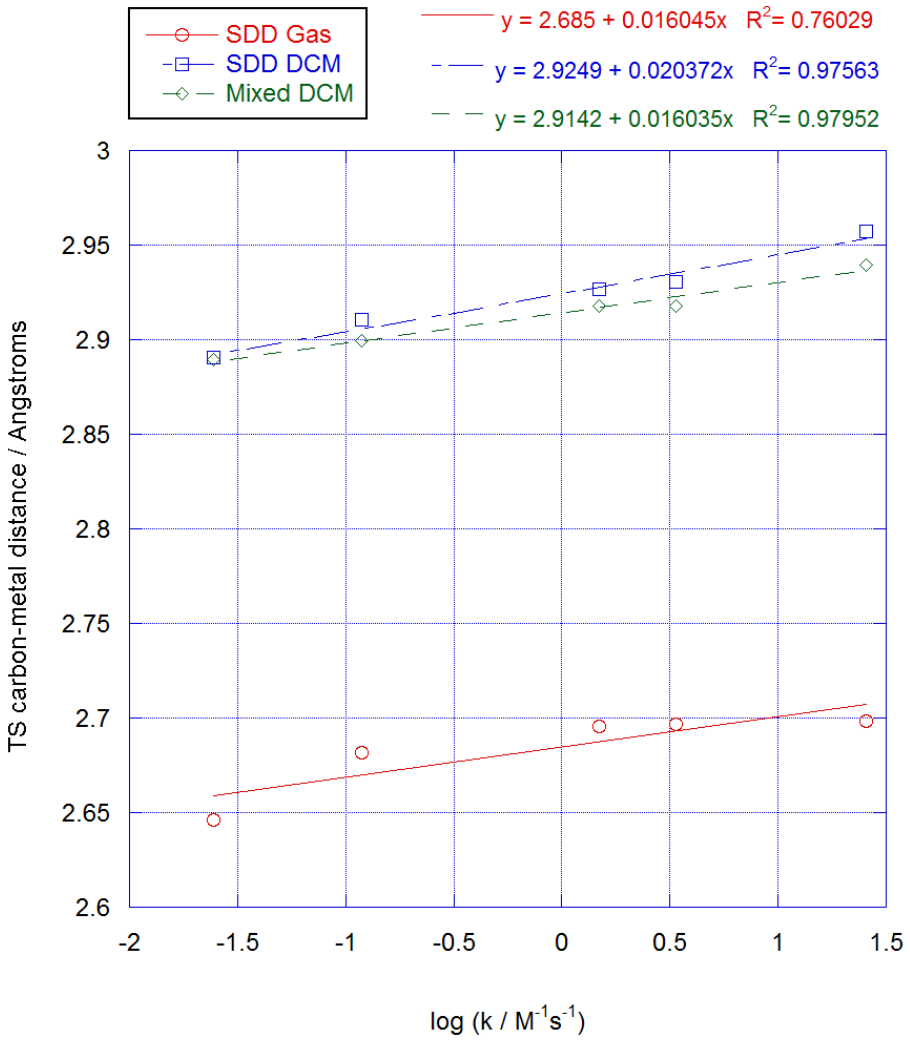


**Figure 3.20:** Plots of transition state C-M distance against experimental log *k* for the reactions of [Cp*Ir(CO)L] complexes with MeI.

As this series was investigated as an extension to the [CpIr(CO)L] system, the data can be analysed as one single series. **Figure 3.21** shows a plot of experimental reactivity against calculated barrier height for both systems.

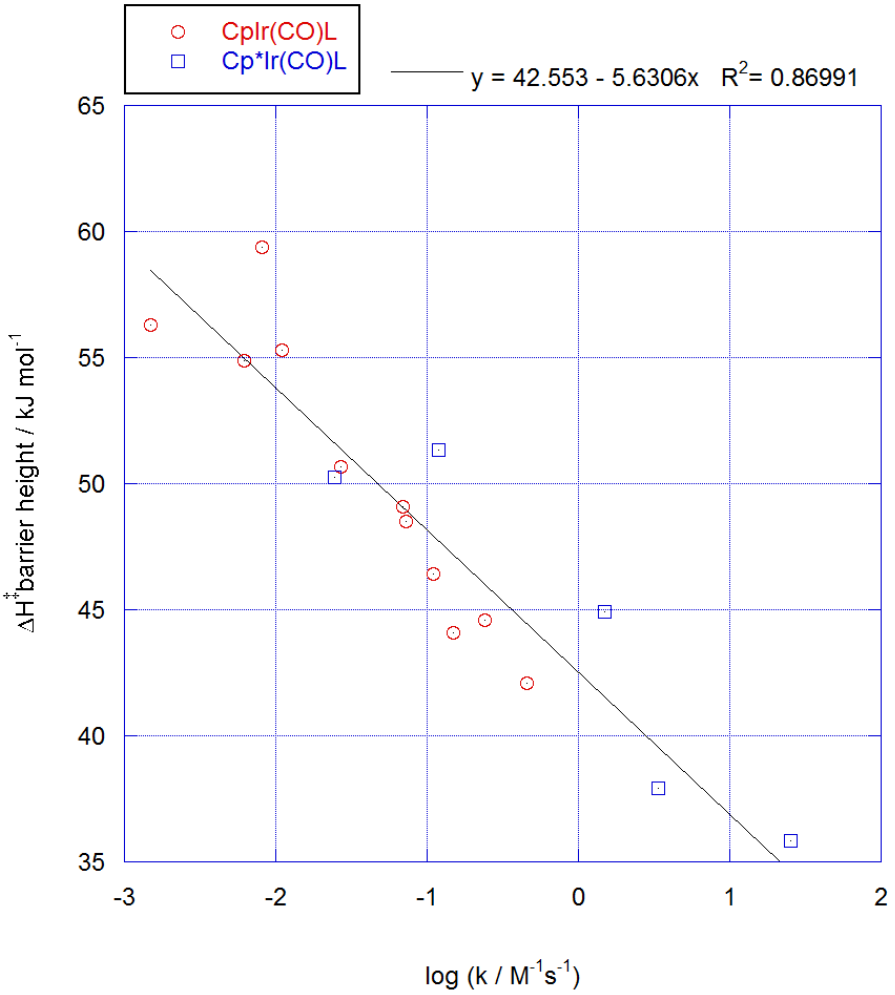


**Figure 3.21:** Plot of calculated barrier height ($\Delta H^{\ddagger}$) against experimental log *k* ($CH_2Cl_2$, 25 °C) for the reaction of [Cp*Ir(CO)L] and [CpIr(CO)L] complexes with MeI. (DFT-B3LYP/Mixed basis – $CH_2Cl_2$)

It is clear that the Cp* complexes follow the same general trend as the Cp complexes. The two series dovetail well with the most reactive Cp-complexes overlapping with the least reactive Cp*-complexes. Interestingly a better correlation is observed between the experimental $\Delta G^{\ddagger}$ and calculated $\Delta E^{\ddagger}$ values as shown in **Figure 3.22** where the complex bearing $PCy_3$ is the only significant outlier.

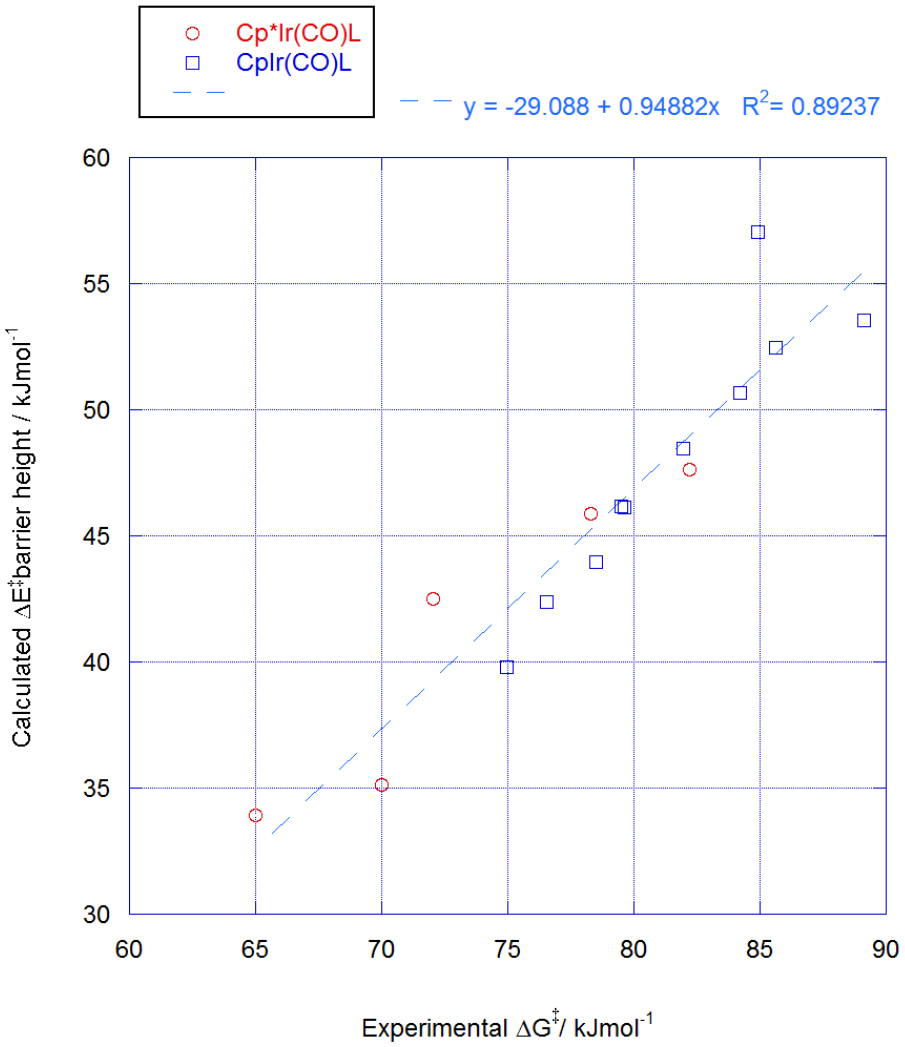


**Figure 3.22:** Plot of calculated $\Delta E^{\ddagger}$ against experimental $\Delta G^{\ddagger}$ barrier for the reactions of [Cp*Ir(CO)L] and [CpIr(CO)L] complexes with MeI. (DFT-B3LYP/Mixed basis – $CH_2Cl_2$)

Five ligands (L = $PMe_3$, $PPh_3$, $PPh_2Me$, $P(4\text{-}ClC_6H_4)_3$, $P(4\text{-}CF_3C_6H_4)_3$ ) are present in both series. A comparison of their rate constants and barrier heights ($\Delta\Delta H^{\ddagger}$) is given in **Table 3.4.** The replacement of a Cp with a Cp* ring results in a rate enhancement of between 16 and 59 times as a result of the increased nucleophilicity of the ligand. The enhanced reactivity is also mirrored in the difference in the barrier heights for the two systems ($\Delta\Delta H^{\ddagger}$) which range from 3.54 – 8.51.

| Ligand | $k_{Cp^*}/k_{Cp}$ | $\Delta\Delta H^{\ddagger}$ / kJ mol$^{-1}$ |
|---|---|---|
| $PMe_3$ | 58.6 | 6.28 |
| $PPh_3$ | 52.7 | 5.76 |
| $PPh_2Me$ | 34.0 | 8.51 |
| $P(4\text{-}ClC_6H_4)_3$ | 19.3 | 3.54 |
| $P(4\text{-}CF_3C_6H_4)_3$ | 16.3 | 6.02 |

**Table 3.4:** Ratio of rate constants and barrier height differences ($\Delta\Delta H^{\ddagger}$) for five [CpIr(CO)L] and [Cp*Ir(CO)L] complexes. (DFT-B3LYP/Mixed basis – $CH_2Cl_2$)

## 3.4 General conclusions

The reactivities of two series of neutral iridium complexes have been probed computationally. The effect of the phosphine conformation on the relative energies of the reactants and transition states has also been probed and found to be of key importance in locating the lowest energy structures. When the coordinated phosphine is $PMe_3$ the effect on the reactant and transition state energies is minimal. Replacing this ligand with $PEt_3$ significantly increases the number of possible reactant and transition state geometries with the difference between the lowest and highest reactant energy around 28 kJmol$^{-1}$.

DFT calculated barrier heights ($\Delta H^{\ddagger}$) show a good correlation to experimental rate constants for all methodologies investigated. Inclusion of solvent acts to lower the barrier height in contrast to the anionic complexes in **Chapter 2.** The C-I and C-M distances in the transition state correlate well with the experimental rate constants with the most reactive complexes having earlier transition states. DFT calculated stretching frequencies for the carbonyl ligand correlate well with experimental values but are subject to a systematic error which must be accounted for in order to predict an accurate experimental value.

Reactant HOMO energies correlate well with experimental rate constants providing that the steric bulk of the complexes is comparable. Where the steric environment around

the metal is markedly different, a poorer correlation is observed, as is the case for [CpIr(CO)($PCy_3$)].

Analysis of both systems simultaneously showed that a similar trend line was followed with the more nucleophilic Cp* complexes having the lowest calculated $\Delta H^{\ddagger}$. The higher observed reactivity of Cp* versus Cp complexes was correctly modelled by the computational methods.

## 3.5 References


(1) Wang, D.; Angelici, R. J. *Inorg. Chem.* **1996**, *35*, 1321.

(2) Wilson, M. R.; Liu, H.; Prock, A.; Giering, W. P. *Organometallics* **1993**, *19*, 2044.

(3) Lai, C. K.; Feighery, W. G.; Zhen, Y.; Atwood, J. D. *Inorg. Chem.* **1989**, *28*, 3929.

(4) Werner, H. *Angew. Chem. Int. Ed. Engl.,* **1983**, *22* 927.

(5) Hart-Davis, A. J.; Graham, W. A. G. *Inorg. Chem.* **1970**, *9*, 2658.

(6) Quinn, S.; Shaver, A. *J. Am. Chem. Soc.* **1982**, *104,* 1096.

(7) A. C. McConnell; P. J. Pogorzelec; A. M. Z. Slawin; G. L. Williams; P. I. P. Elliott; A. Haynes; A. C. Marr; Cole-Hamilton, D. J. *Dalton Trans.* **2006**, 91.

(8) Bennett, M. J.; L.;, P. J.; Tuggle, R. M. *Inorg. Chem.* **1974**, *13*, 2408.

(9) Kelly III, R. A; Clavier, H; Giudice, S; Scott, N. M; Stevens, E. D; Bordner, J; Samardjiev, I; Hoff, C. D; Cavallo, L; Nolan, S. P. *Organometallics,* **2008**, *27*, 202.

(10) Tolman, C. *A. Chem. Rev.* **1977**, *77*, 313.

(11) Gusev, G. D. *Organometallics* **2009**, *28*, 763.

(12) Grobbelaar, E.; Lötter, S.; Visser, H. G.; Conradie, J.; Purcell, W. *Inorg. Chim. Acta.,* **2009**, *362*, 3949.

(13) Perrin, L.; Clot, E.; Eisenstein, O.; Loch, J.; Crabtree, R. H. *Inorg. Chem.* **2001**, *40*, 5806.

(14) Tonner, R.; Frenking, G. *Organometallics* **2009**, *28*, 3901.

(15) Kuhl, O. *Coord. Chem. Rev.* **2005**, *249*, 693.

(16) Clifton, A. R. *4th Year Thesis,* **2009**.

(17) Smith, R. *4th Year Thesis,* **2008**.

# CHAPTER 4

# Modelling nucleophilicity of square-planar metal complexes

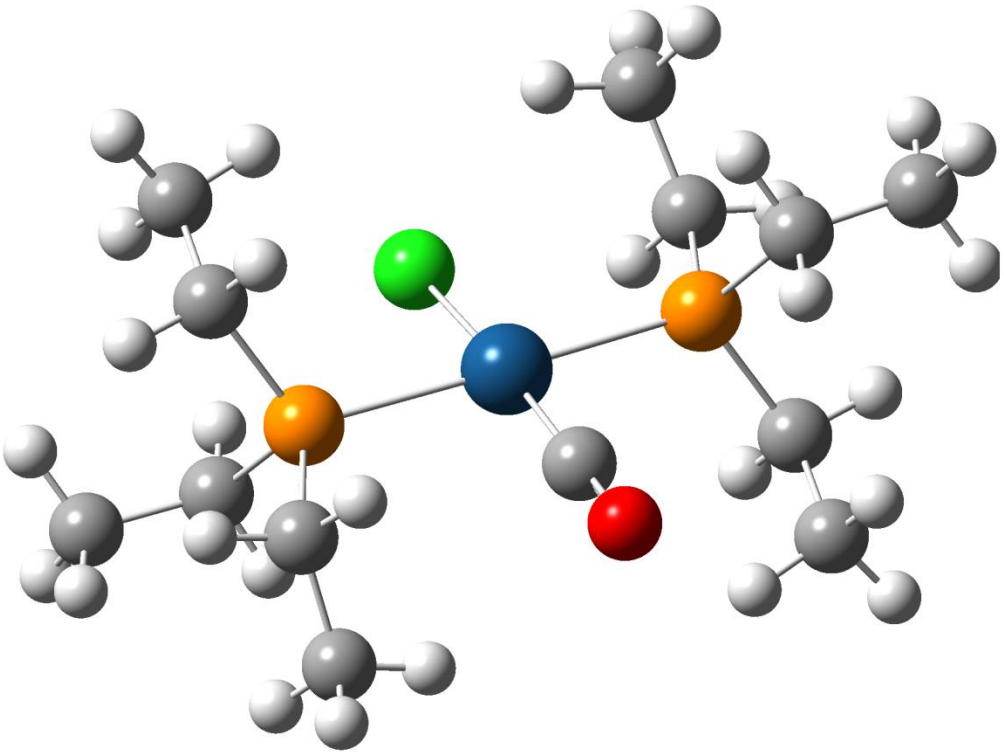

## 4.1 Introduction

In the preceding chapters, a number of 18-electron neutral and anionic metal complexes have been investigated. Another important class of molecules is 16-electron square-planar complexes of which Vaska-type complexes are an example. These complexes undergo oxidative addition of iodomethane according to **Scheme 4.1**. In contrast to the 18-electron complexes, the reaction with iodomethane proceeds through a two-step mechanism. The iodide ion liberated by the initial $S_N2$ reaction can coordinate to the cationic intermediate complex at an available site which is generally *trans* to the methyl group.

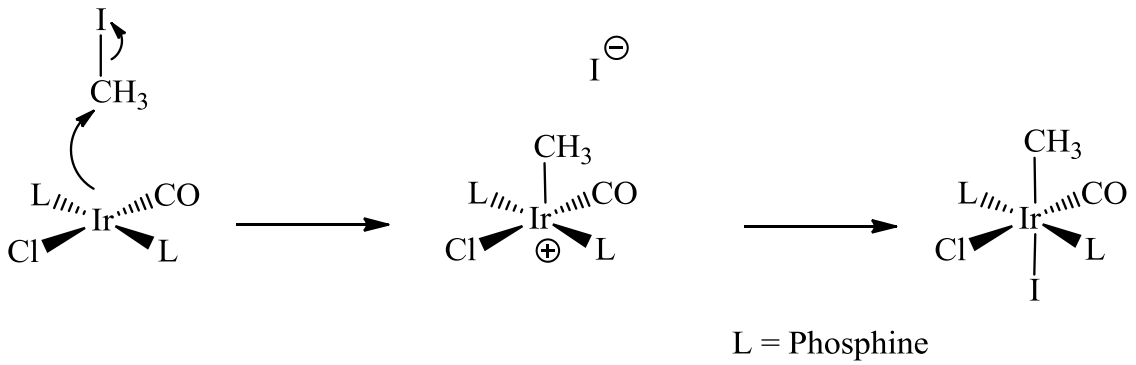


**Scheme 4.1:** Two step mechanism for reaction of Vaska-type complex with iodomethane

A number of theoretical studies have been conducted on the oxidative addition of alkyl halides to square planar metal complexes. Perhaps one of the most well-known examples is the Rh(I)-complex, $[Rh(CO)_2I_2]^-$ which catalyses the formation of acetic acid from carbon monoxide and methanol (called the Monsanto Process) according to **Scheme 4.2.**[1-5]

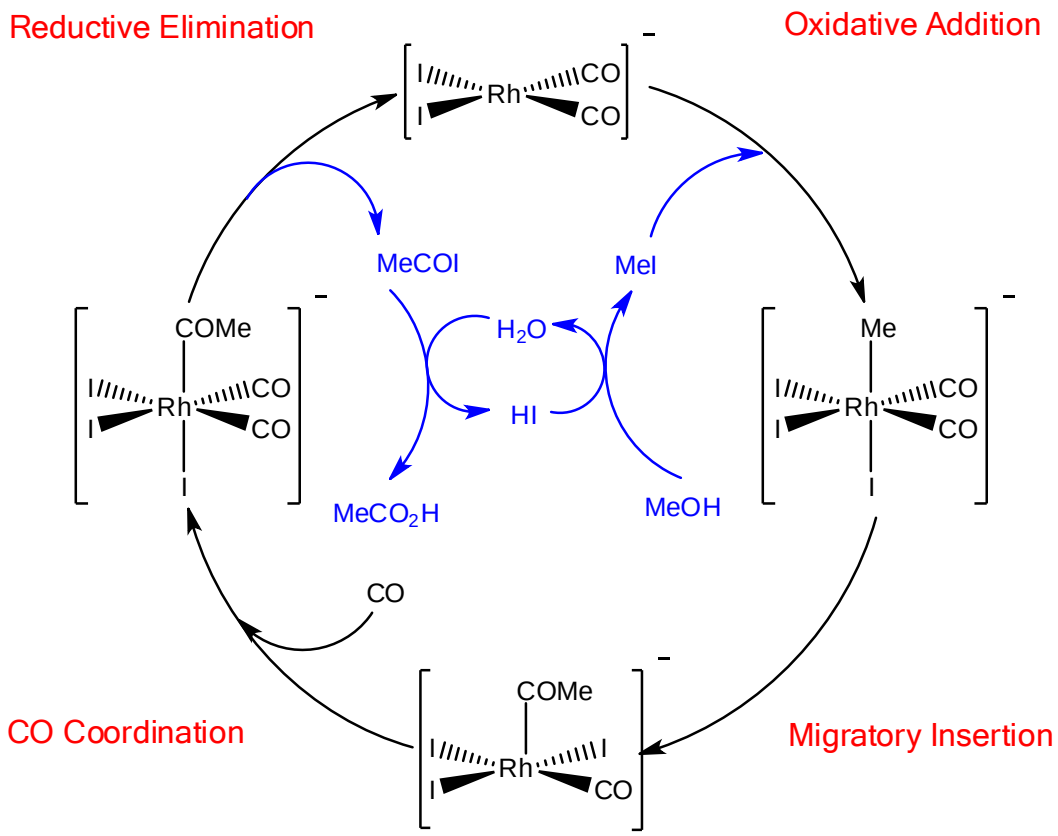


**Scheme 4.2:** Catalytic cycle for the formation of acetic acid.

In 1996, the nature of the transition state was probed by Griffin et al.[6] The geometries of two distinct transition states were optimised at the Hartree Fock (HF) level as shown in **Figure 4.1.** In the linear $S_N2$-like transition state iodomethane approaches the complex perpendicular to the coordination plane. The Rh-C-I angle deviates marginally from linearity. In the bent transition state, the iodomethane molecule approaches the complex in a side-on fashion. The Rh-C-I angle is bent towards the carbonyl ligands and results in inversion at the carbon centre. The $S_N2$-like transition state is more stable than the bent orientation which was the first confirmation of the transition state structure for this system.

Ivanova et al. and Kinnunen et al. both independently investigated the complete catalytic cycle for methanol carbonylation. Kinnunen and coworkers investigated the oxidative addition both to the experimentally observed *cis*-$[Rh(CO)_2I_2]^-$ and to *trans*-$[Rh(CO)_2I_2]^-$, which is not observed experimentally.[7-10] The oxidative addition to *trans*-

$[Rh(CO)_2I_2]^-$ was found to be energetically more favourable than to *cis*-$[Rh(CO)_2I_2]^-$. The cycle was later investigated with inclusion of solvent effects by Cheong et al. [11]

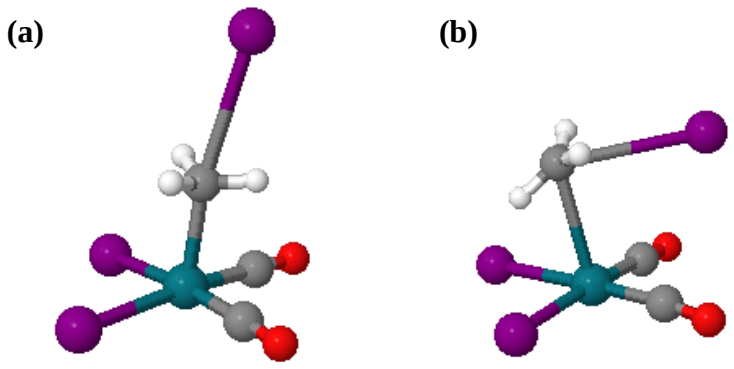


**Figure 4.1:** Optimised structures (RHF, LANL1DZ basis) of linear **(a)** and bent **(b)** transition states for the reaction of $[Rh(CO)_2I_2]^-$ and MeI.

In this chapter, the oxidative addition of iodomethane to a a range of Ir(I), Rh(I) and Pt(II) square-planar metal complexes is investigated. The effect of ligand orientation on the reactant and transition state energies is probed. The structures of these series are summarised in **Figure 4.2.**

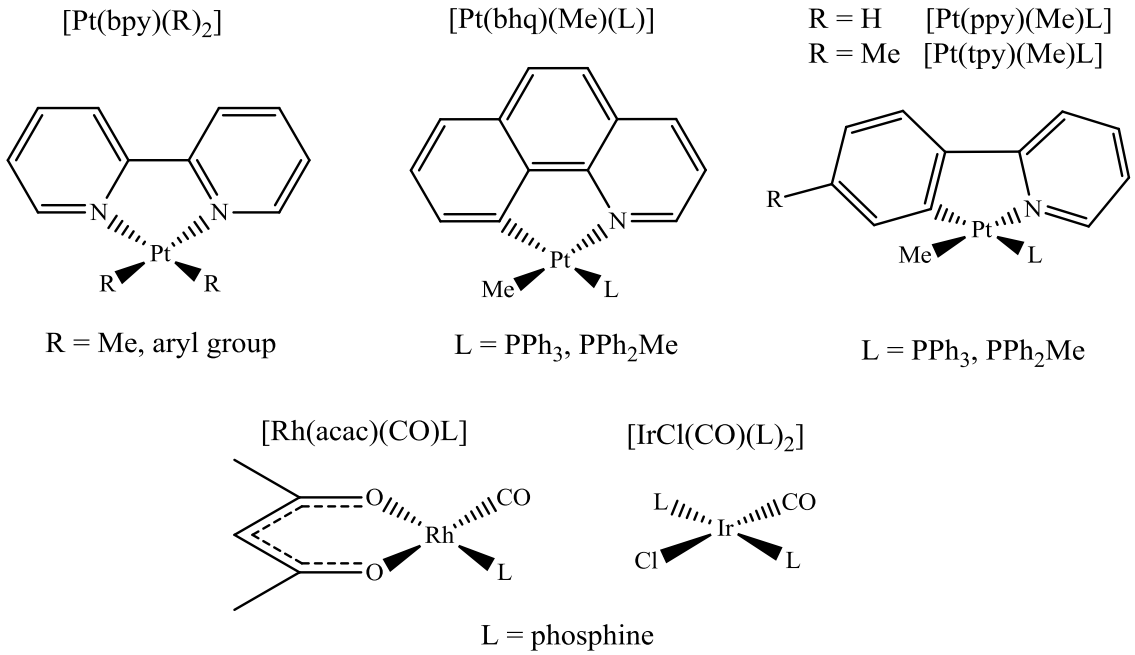


**Figure 4.2:** Structures of several series of Rh(I), Ir(I) and Pt(II) complexes.

Wilson et al., investigated the reactivities of a series of Ir(I) complexes towards a number of electrophiles.[12] Experimental kinetics were measured for the oxidative addition reactions with $H_2$, $O_2$, MeI and methyl tosylate. Data for the reactivity of fifteen complexes towards iodomethane constitutes an ideal series for computational investigation.

On the other hand, the platinum series [Pt(bpy)$(R)_2$] investigated by Jawad et al. is a good series to probe the electronic effects of various aryl substituents with little change to the steric environment of the complex.[13] A related platinum series, [PtX(Me)(L)] (X = ppy, bhq, tpy) is appropriate to investigate the effect on the calculated barrier height of varying the ligand, L.

A series of Rh(I) complexes, [Rh(acac)(CO)L] were investigated in our laboratory to expand on data already in the literature. The experimental studies on this system will be discussed in more detail in **Chapter 7.** Again, the effect of the ligand on the calculated barrier height will be investigated.

## 4.2 Results

### 4.2.1 Effect of solvent

The reaction energy profile for 16-electron square-planar complexes is more complicated than the profile for the 18-electron anionic complexes discussed in **Chapter 2.** These complexes react with iodomethane via a two-step process. Initially, the complex reacts with iodomethane *via* an $S_N2$ transition state which liberates an iodide ion. The iodide ion is then free to coordinate to the metal centre at an available site, normally *trans* to the methyl group. The structures necessary to construct a reaction profile are shown in **Figure 4.3** using the platinum series as an example.

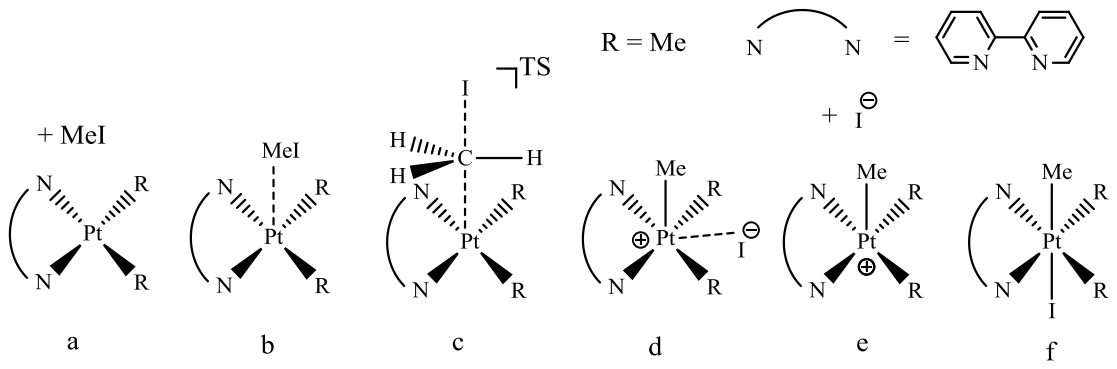


**Figure 4.3:** Geometries required to construct a reaction energy profile.

The requisite geometries were optimised for [(bpy)Pt($Me_2$)] using two methods (SDD, Gas-phase and SDD Acetone). The resulting energy profiles ($\Delta H$) are shown in **Figure 4.4.** The first step in the $S_N2$ reaction in the gas-phase is endoethermic. The separated ionic products (**e**) are significantly higher in energy than the reactants due to the energy required in separating ions in the gas-phase. The inclusion of solvent in the calculations acts to stabilise the polar transition state (**c**) and the separated ion species (**d** and **e**).

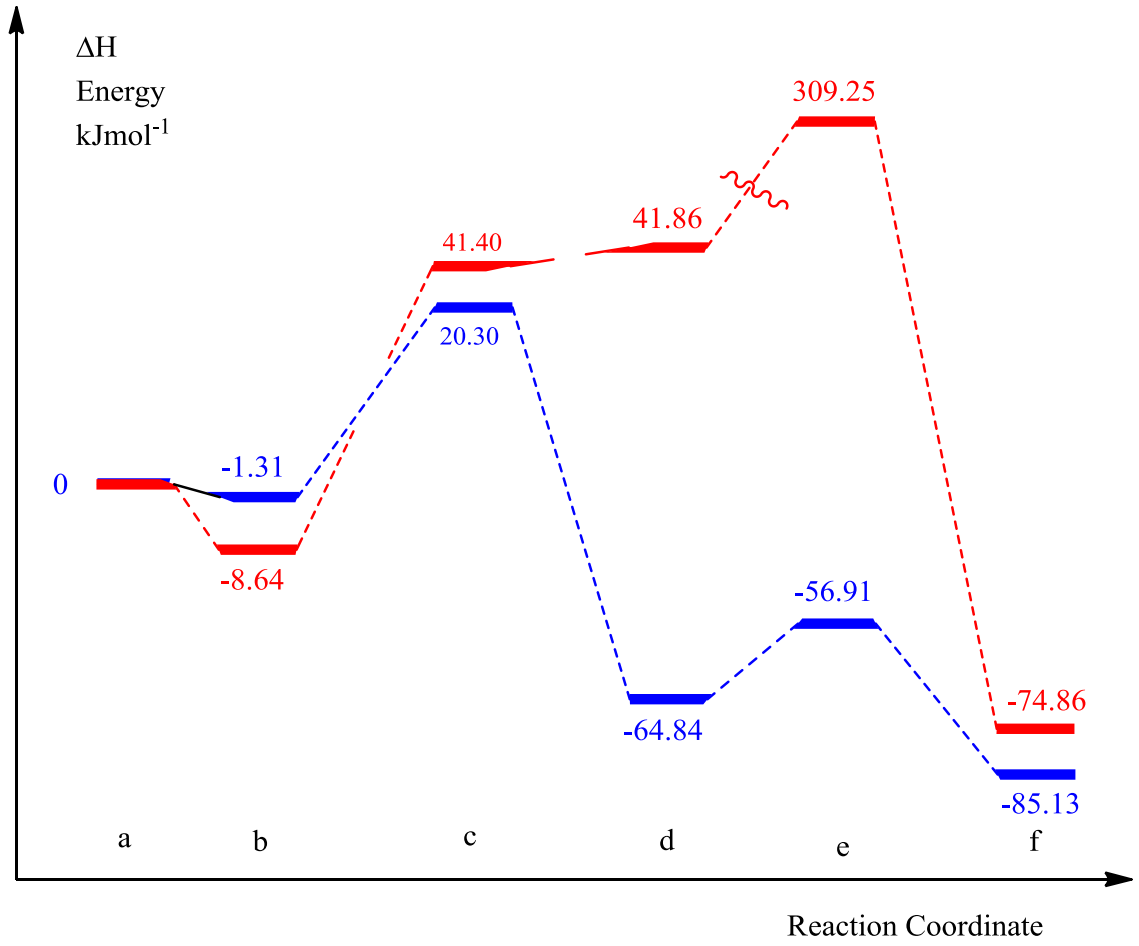


**Figure 4.4:** Energy profiles ($\Delta H^{\ddagger}$) for the reaction of [(bpy)Pt(Me)$_2$] with iodomethane in gas-phase (red) and with inclusion of solvent (blue) (DFT-B3LYP/SDD)

Initially, these complexes were investigated in the gas-phase for computational ease. However, location of the transition states in the gas-phase proved to be problematic for many of the square-planar complexes with minimal changes in the geometries resulting in the transition state collapsing to either the reactant or the product. Energy scans of the reaction coordinate were carried out in both the gas-phase and solution phase in order to locate the position of the transition state. **Figure 4.5** shows a representation of how the scan was constructed. The Pt-C-I angle was fixed at 180 ° and the Pt-I distance was also fixed. The methyl group was then systematically moved further from the platinum centre until it approached the iodide ion and the energy calculated at each step.

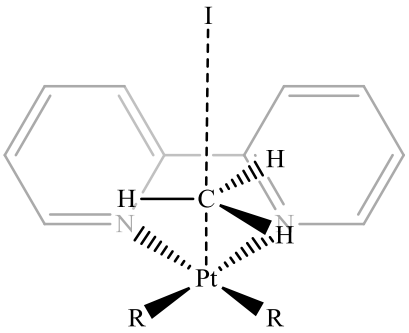


**Figure 4.5:** Illustration of the input geometry for the scans

The gas-phase profile in **Figure 4.6** shows no obvious maximum whereas when solvation effects are included there is a clear maximum corresponding to the transition state. In the gas-phase the ion-pair has very similar energy to the transition state whereas once solvent effects are taken into account the ion-pair is more strongly solvated than the transition state which creates the saddle point.

No gas-phase transition states were located for the Rh(I) complexes and only four of the eight were located for the platinum complexes. For the remainder of the analyses, mixed-basis optimisations were undertaken with inclusion of solvent to avoid issues with location of gas-phase transition states.

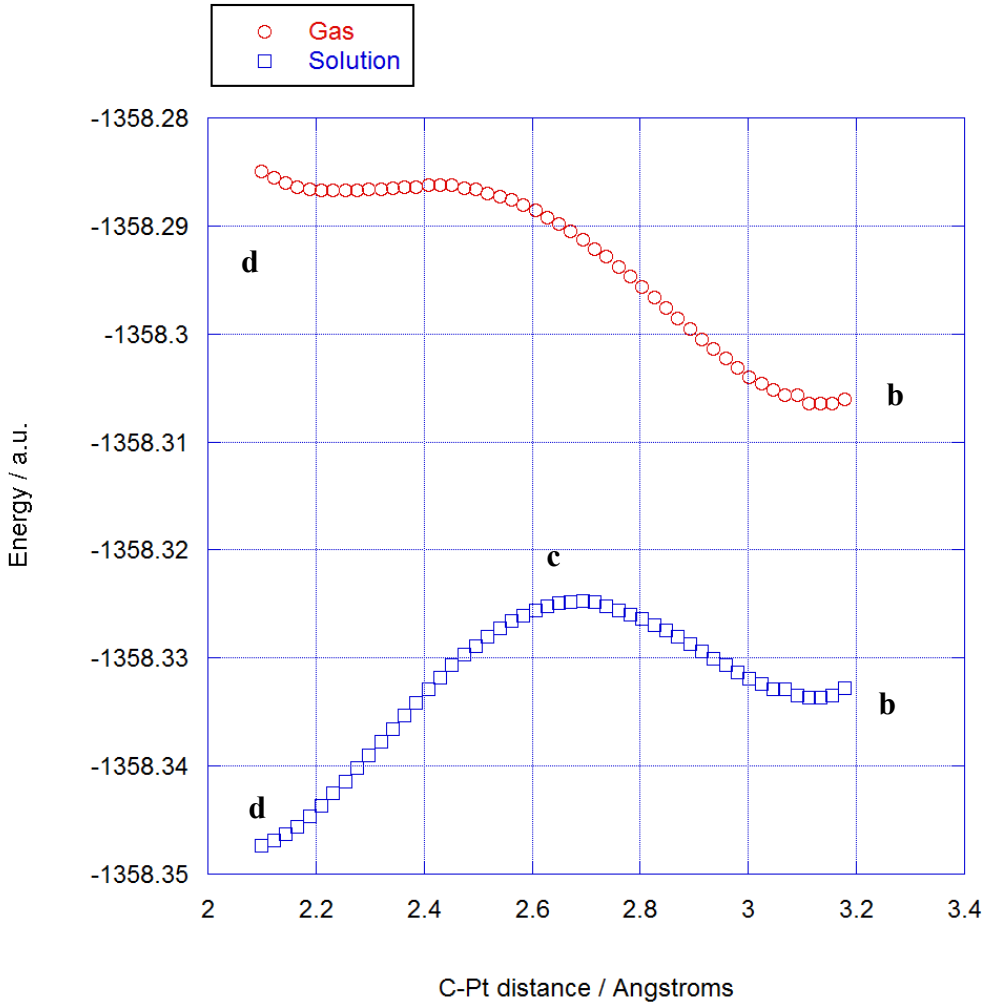


**Figure 4.6**: Solution phase (blue) versus gas-phase (red) energy scans (DFT-B3LYP/SDD) for approach of MeI to [Pt(bpy)$Me_2$]

### 4.2.2 Ligand conformation

The specific orientation of the phosphine ligand was shown to be critical for predicting an accurate barrier height. Before any barrier heights were calculated, the reactant geometries were probed by changing the orientation of the phosphine ligand to ensure that the lowest energy geometry had been correctly optimised. This process is illustrated below using [IrCl(CO)($PPhMe_2$)$_2$] as an example.

Two distinct reactant geometries were located for [IrCl(CO)($PPhMe_2$)$_2$]. **Figure 4.7** shows two optimised geometries for the complex. **1a** is the initial geometry investigated whilst **1b** is an alternative geometry formed by rotation of one of the phosphine ligands.

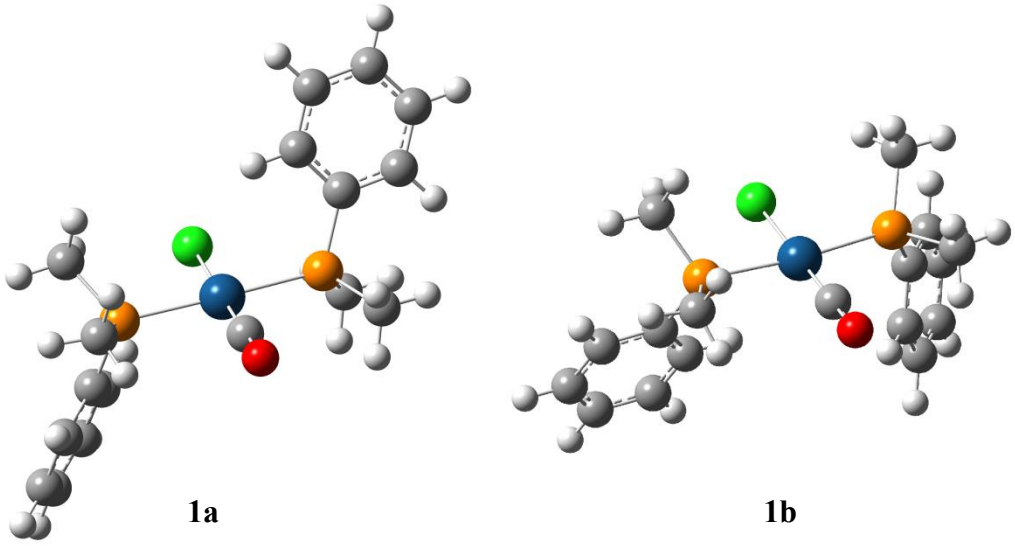


**Figure 4.7:** Two optimised geometries of [IrCl(CO)($PPhMe_2$)$_2$]. (DFT-B3LYP/SDD – mixed - Benzene)

**1a** has the phenyl groups on the ligand *anti* to one another which should reduce any unfavourable steric interactions that might arise from the phenyl groups being in close proximity. On the other hand, **1b** has the phenyl groups positioned on the same face of the metal which effectively creates an open face which would be more accessible for the approach of iodomethane. **1a** is more stable by 1.06 kJ $mol^{-1}$ so there is very little energetic difference between the two isomers. The unscaled carbonyl stretching frequencies are 1916.34 and 1913.79 $cm^{-1}$ for **1a** and **1b** respectively. Transition states were optimised based upon these two reactant geometries and are shown in **Figure 4.8.**

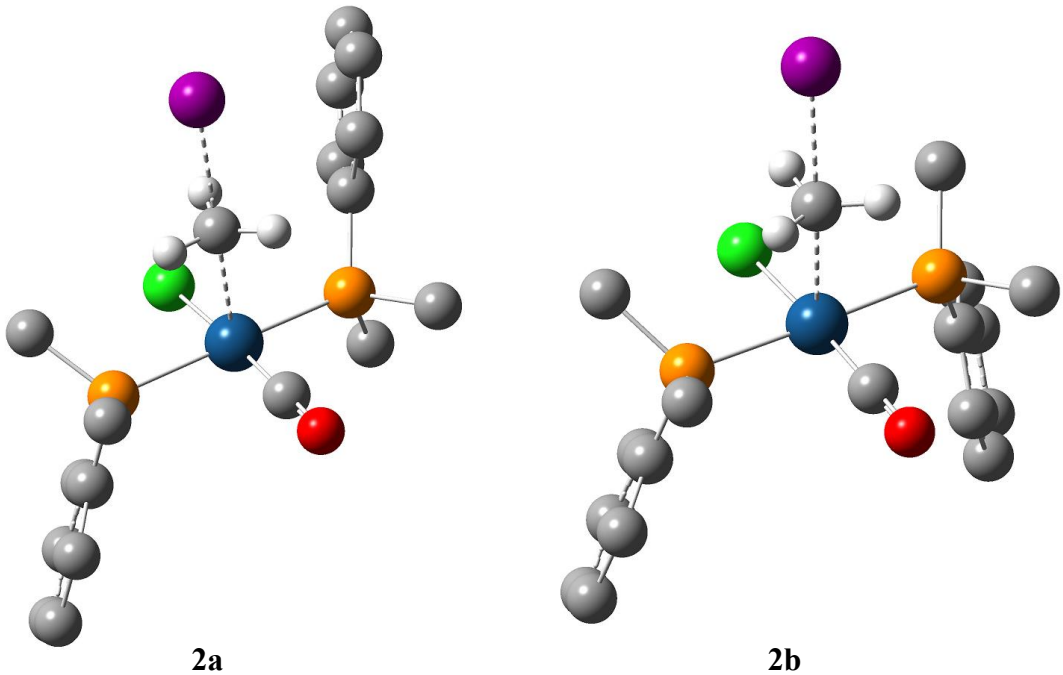

**2a** **2b**

**Figure 4.8:** Two optimised transition states for the reaction of $[IrCl(CO)(PPhMe_2)_2]$ with iodomethane. Hydrogen atoms removed for clarity. (DFT-B3LYP/SDD – gas-phase)

The two transition states have comparable structures in terms of the approaching iodomethane molecule. The C-Ir distances are 2.459 Å and 2.461 Å and the C-I distances are 2.777 Å and 2.767 Å – **2b** having a slightly earlier transition state. Energetically, **2b** is favoured by 3.64 kJ $mol^{-1}$ possibly due to a reduction in steric interactions between the phenyl groups and the incoming iodomethane molecule. The resulting energy profile is shown in **Figure 4.9.**

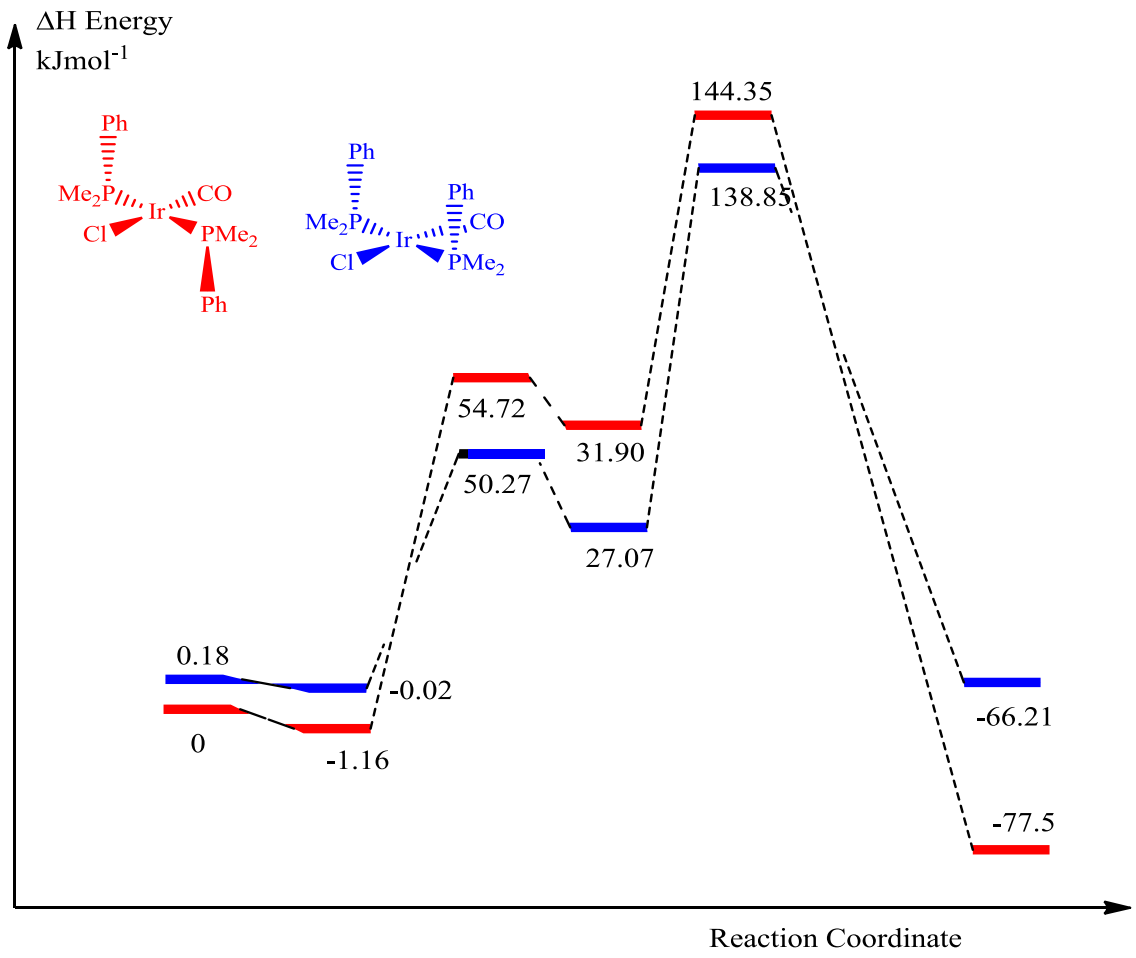


**Figure 4.9:** Reaction profile for the reaction of $[IrCl(CO)(PPhMe_2)_2]$ with MeI (DFT-B3LYP/SDD – gas-phase)

The reaction with iodomethane can potentially proceed from either reactant geometry which only differ in energy by 0.18 kJ $mol^{-1}$. However, it is more energetically favourable to undergo a change in geometry to the higher energy reactant which reacts with iodomethane via a lower energy transition state. The final octahedral product is most stable with the phenyl groups *anti* to one another and can be reached by rotation of the phosphine ligand in the product or in the cation prior to the coordination of iodide. The barrier height for this complex is calculated using the lowest energy reactant and transition state and it is this value which is used in further analyses. The remaining 16-electron square-planar complexes were subject to the same conformer analysis. Their respective experimental rate constants and DFT calculated barrier heights are shown in **Table 4.1.**

| [IrCl(CO)(L)$_2$] | | | [Rh(acac)(CO)L] | | |
|---|---|---|---|---|---|
| **L** | **log ($k$ / $M^{-1}s^{-1}$) (benzene)** | **$\Delta H^{\ddagger}$ Barrier height / kJ $mol^{-1}$** | **L** | **log ($k$ / $M^{-1}s^{-1}$) (DCM)** | **$\Delta H^{\ddagger}$ Barrier height / kJ $mol^{-1}$** |
| $PCy_2Ph$ | -5.70 | 90.76 | P(*o*-anisyl)$_3$ | 0.30 | 31.17 |
| P(4-$ClC_6H_4$)$_3$ | -4.84 | 75.14 | PPh(*o*-anisyl)$_2$ | 0.09 | 32.75 |
| P(4-$FC_6H_4$)$_3$ | -4.07 | 71.62 | $PPh_2$(*o*-anisyl) | -0.31 | 39.12 |
| $PPh_2{}^tBu$ | -3.75 | 68.52 | $PMe_3$ | -0.37 | 41.33 |
| $P^iPr_3$ | -3.72 | 93.71 | $PPhMe_2$ | -0.76 | 36.65 |
| $PCy_3$ | -3.51 | 78.59 | $PEt_3$ | -0.87 | 47.40 |
| $PPh_3$ | -2.44 | 62.58 | $PPhEt_2$ | -0.88 | 45.13 |
| $PCyPh_2$ | -2.31 | 58.94 | $PPh_2Me$ | -1.01 | 43.83 |
| $PPhEt_2$ | -1.94 | 56.66 | $PPh_2Et$ | -1.03 | 45.52 |
| P(4-$MeC_6H_4$)$_3$ | -1.88 | 58.04 | P(4-$MeC_6H_4$)$_3$ | -1.16 | 49.19 |
| $PPh_2Et$ | -1.87 | 49.02 | $PPh_3$ | -1.51 | 45.06 |
| $PPh_2Me$ | -1.75 | 51.54 | P(*p*-anisyl)$_3$ | -1.37 | 45.56 |
| $PEt_3$ | -1.64 | 57.34 | $PCy_3$ | -1.58 | 51.76 |
| P(*p*-anisyl)$_3$ | -1.60 | 55.14 | P(4-$ClC_6H_4$)$_3$ | -2.16 | 53.74 |
| $PPhMe_2$ | -1.30 | 50.26 | P(4-$FC_6H_4$)$_3$ | -2.24 | 51.40 |

| [Pt(bpy)(R)$_2$] | | | [PtX(Me)L] | | | |
|---|---|---|---|---|---|---|
| **R** | **log ($k$ / $M^{-1}s^{-1}$) (acetone)** | **$\Delta H^{\ddagger}$ Barrier height / kJ $mol^{-1}$** | **X** | **L** | **log ($k$ / $M^{-1}s^{-1}$) (chloroform)** | **$\Delta H^{\ddagger}$ Barrier height / kJ $mol^{-1}$** |
| Me | 1.67 | 33.25 | ppy | $PPh_3$ | -2.07 | 54.77 |
| *p*-anisyl | 0.15 | 42.08 | ppy | $PPh_2Me$ | -1.54 | 48.34 |
| *p*-tol | -0.08 | 46.31 | bhq | $PPh_3$ | -2.11 | 55.25 |
| *m*-anisyl | -0.39 | 44.02 | bhq | $PPh_2Me$ | -1.60 | 49.02 |
| Ph | -0.43 | 45.02 | tpy | $PPh_3$ | -1.90 | 53.81 |
| 4-$FC_6H_4$ | -1.10 | 50.09 | tpy | $PPh_2Me$ | -1.36 | 51.04 |
| 4-$ClC_6H_4$ | -1.16 | 49.86 | | | | |
| 2-$FC_6H_4$ | -1.40 | 48.87 | | | | |

**Table 4.1:** Table of DFT $\Delta H^{\ddagger}$ calculated barrier heights and experimental data for reactions of various square-planar metal complexes with iodomethane. (DFT-B3LYP Mixed basis with solvent)

**Figure 4.10** shows a plot of the calculated barrier height ($\Delta H^{\ddagger}$) against experimental log *k*. The $R^2$ value for all complexes analysed as one series is 0.83 and values for each individual series are good with the best correlation observed for the [(bpy)Pt$(R)_2$] complexes ($R^2 = 0.931$). The steric environment around the metal for the [(bpy)Pt$(R)_2$] series is very similar whereas the environment in the remaining systems, which all contain phosphine ligands, is varied. Where there is variation in the steric environment, the observed correlation is lower.

There is one major outlier in the [Rh(acac)(CO)L] series (L = $PPh_2Cy$). Further work on this system could potentially identify a lower energy transition state.

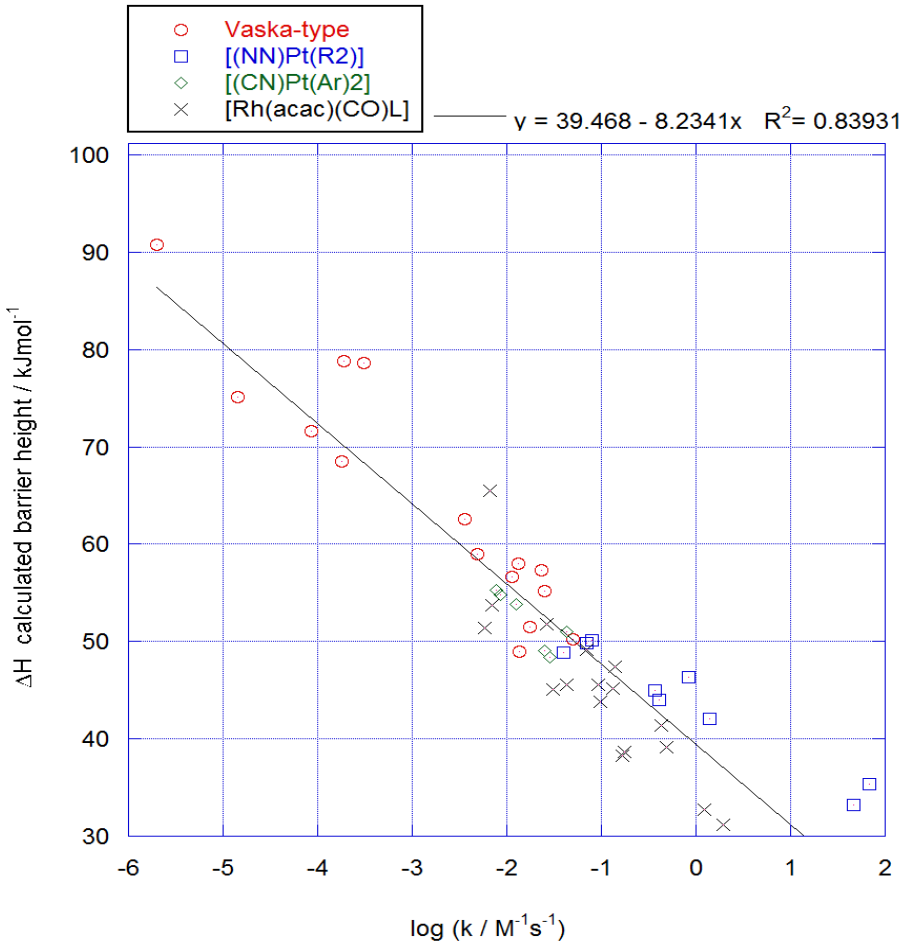


**Figure 4.10:** Plot of calculated barrier height ($\Delta H^{\ddagger}$) against experimental log *k* (25 °C) for the reaction of various square-planar complexes with MeI. (DFT-B3LYP / Mixed basis)

### 4.2.3 Transition state geometries

Plots of the transition state C-I distances against log *k* for all four series are shown in **Figures 4.11 and 4.12.** The corresponding C-M distances against log *k* plots are shown in **Figures 4.13 and 4.14.** The more reactive of the Vaska-type complexes in general have shorter C-I and longer C-Ir distances but a poor correlation is found overall. A better correlation is found for the [Rh(acac)(CO)L] series and the best correlation is found for the [(bpy)Pt($R_2$)] series where the $R^2$ value is 0.97. The good correlation for this series is attributed to the complexes each having an almost identical steric environment, which allows the electronic effect of the substituents to be probed without the steric environment complicating the analysis. The other three series each contain phosphine ligands and the lower observed correlations could be attributed to not having the correct ground state or transition state structure.

The transition state structures for three complexes in the [Rh(acac)(CO)(L)] series, which contain anisyl-modified phosphines are discussed in more detail in **Chapter 7.**

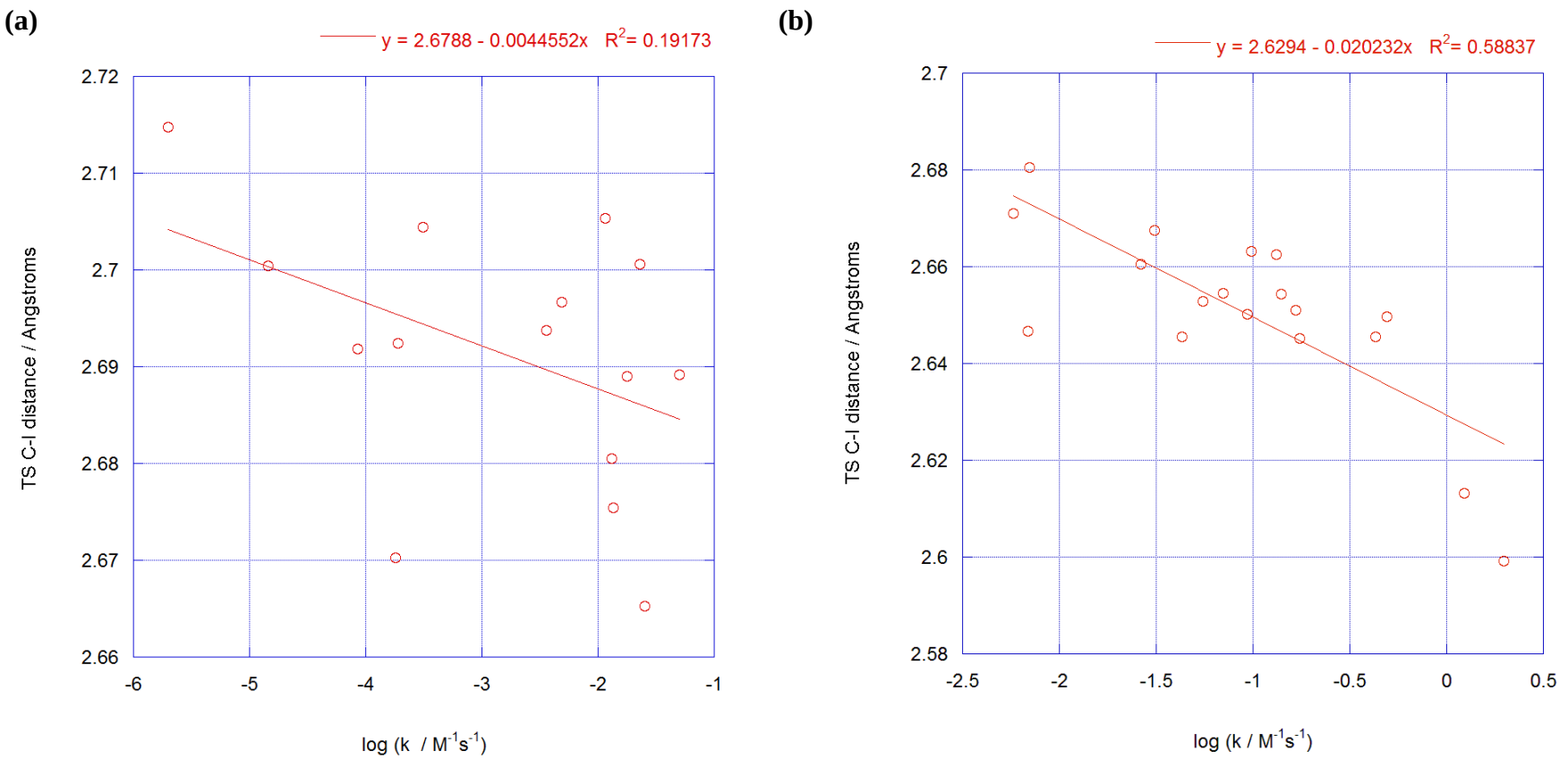


**Figure 4.11:** Plots of transition state C-I distance against experimental log *k* for the reaction of **(a)** [IrCl(CO)$(L)_2$] and **(b)** [Rh(acac)(CO)L] complexes with MeI (DFT-B3LYP / Mixed basis)

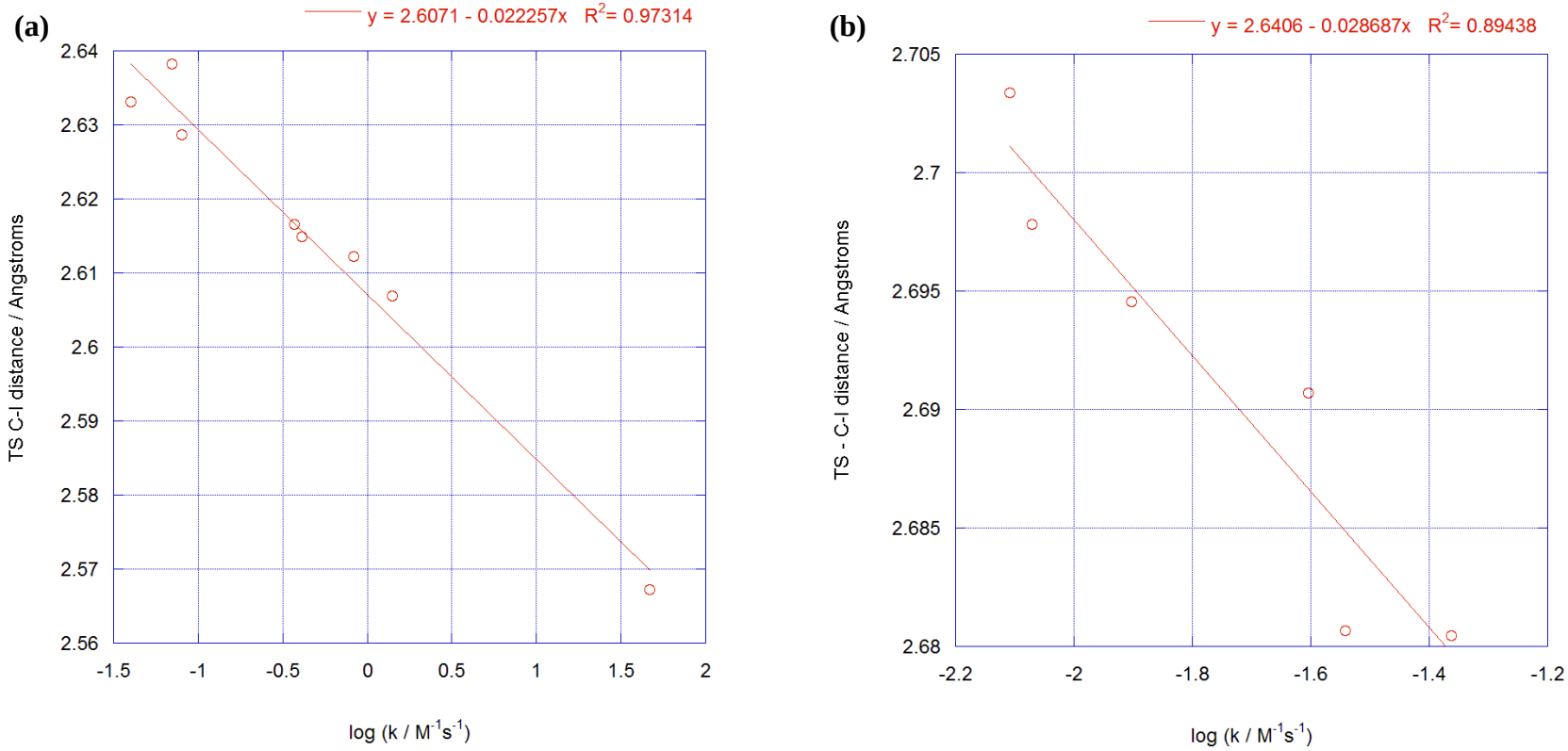


**Figure 4.12:** Plots of transition state C-I distance against experimental log *k* for the reaction of **(a)** [Pt(bpy)(R)$_2$] and **(b)** [PtX(Me)(L)] complexes with MeI (DFT-B3LYP / Mixed basis)

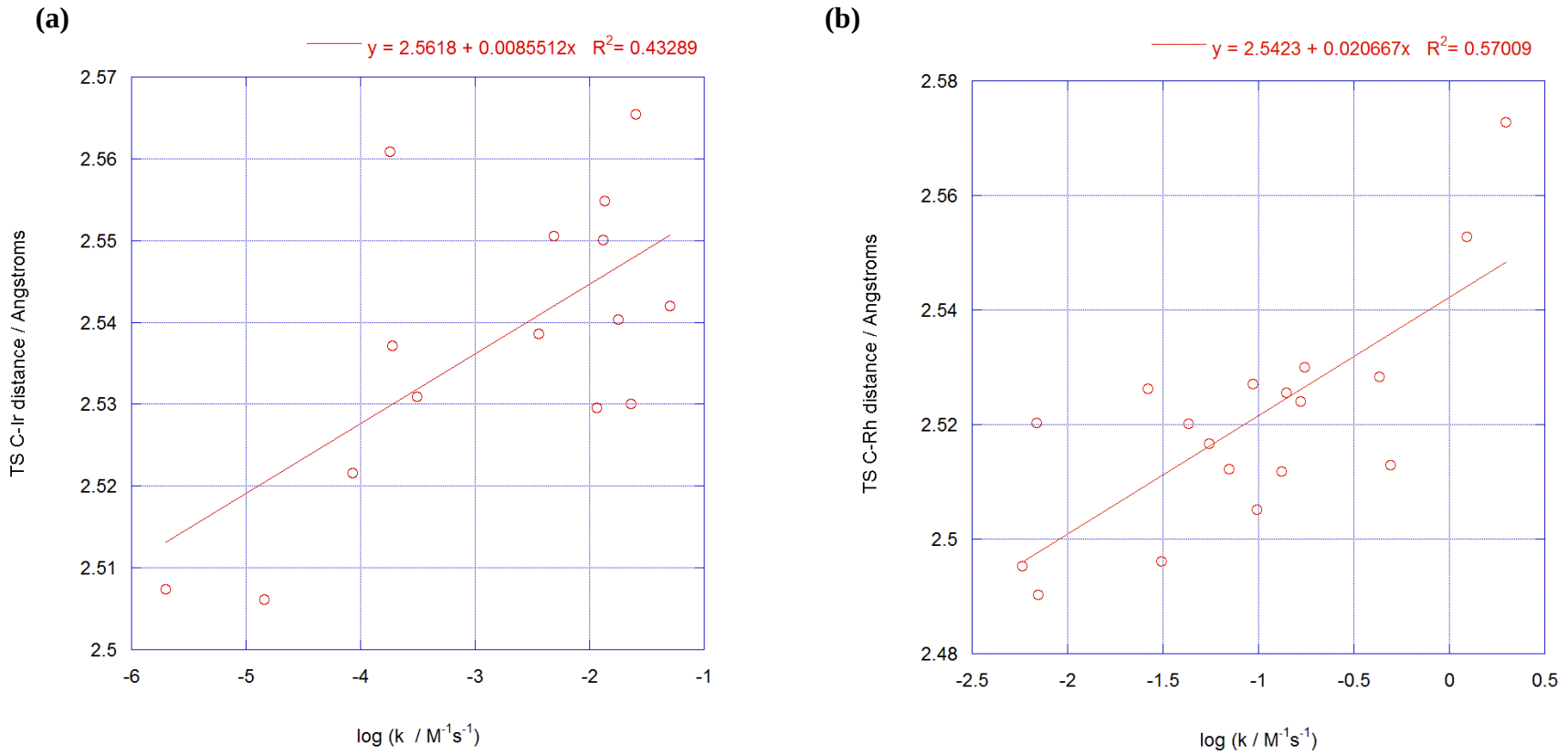


**Figure 4.13:** Plots of transition state C-M distance against experimental log *k* for the reaction of **(a)** [IrCl(CO)(L)$_2$] and **(b)** [Rh(acac)(CO)L] complexes with MeI (DFT-B3LYP / Mixed basis)

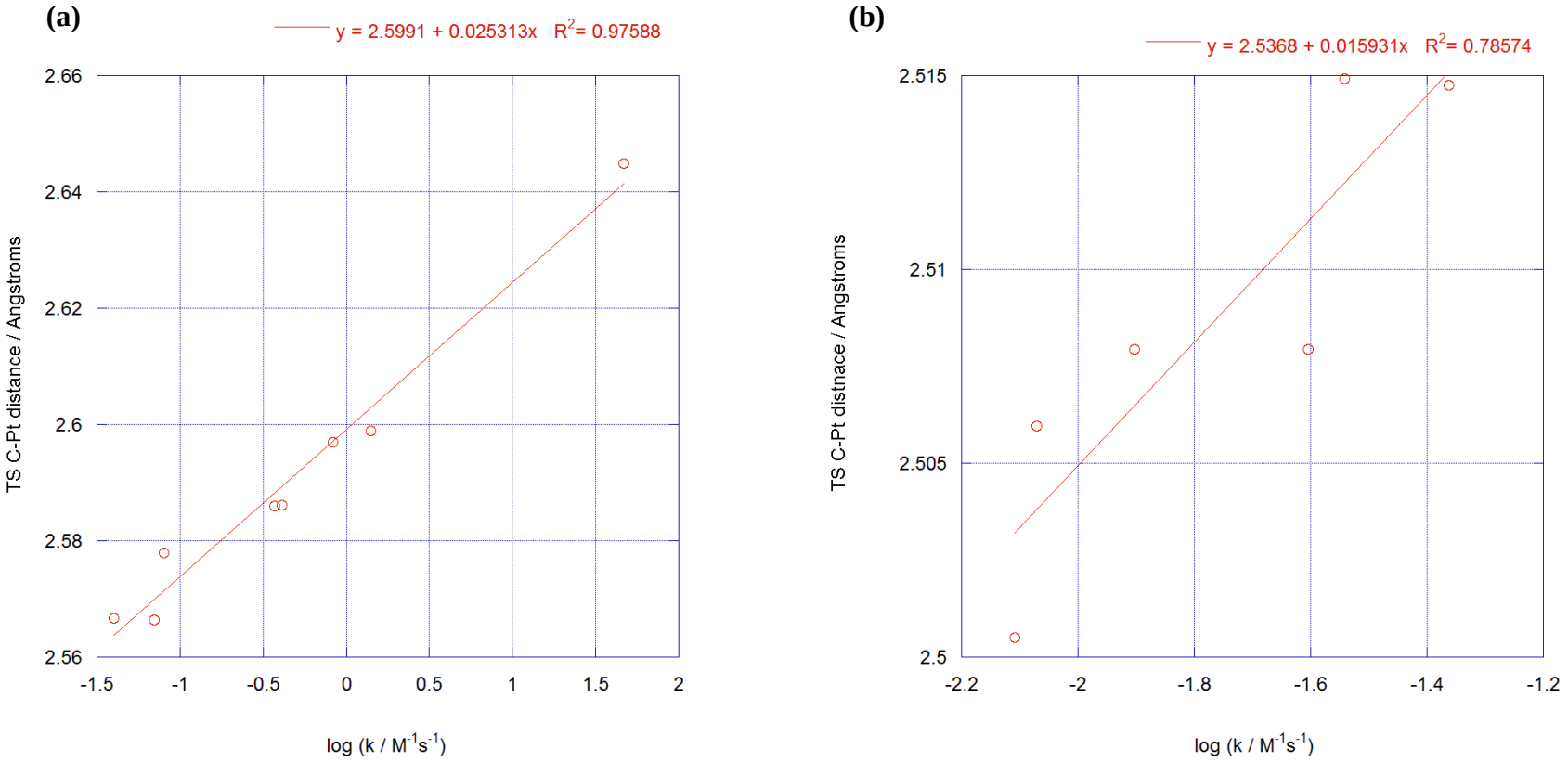


**Figure 4.14:** Plots of transition state C-M distance against experimental log *k* for the reaction of **(a)** [Pt(bpy)($R)_2$] and **(b)** [PtX(Me)(L)] complexes with MeI (DFT-B3LYP / Mixed basis)

### 4.2.4 Reactant HOMO energies

Reactant HOMO energies for these 16-electron square-planar metal complexes strongly resemble a metal $d_z^2$ orbital. Representations of these orbitals for [(NN)Pt(Me)$_2$] and [Rh(acac)(CO)(PMe$_3$)] are shown in **Figure 4.15.**

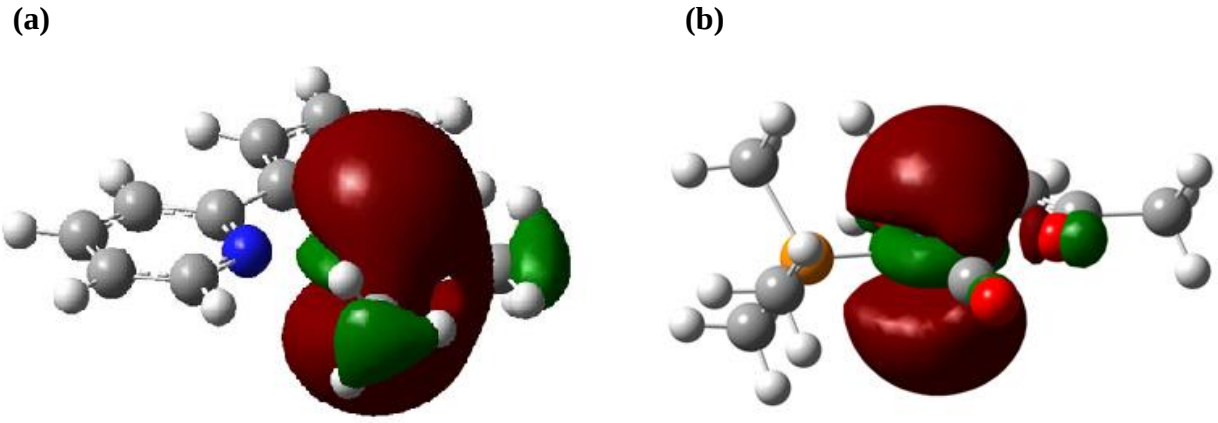


**Figure 4.15**: Reactant HOMO for **(a)** [(bpy)Pt(Me)$_2$] and **(b)** [Rh(acac)(CO)(PMe$_3$)] (DFT-B3LYP / Mixed basis)

**Figures 4.16** and **4.17** show plots of the DFT-calculated HOMO energy against log *k*. For the [IrCl(CO)(L)$_2$] and [Rh(acac)(CO)L] systems a reasonable trend can be discerned for each series for the majority of complexes within the series (shown in red) but the remaining complexes (shown in blue) are clearly outliers. These are for complexes bearing PCy$_3$, PCy$_2$Ph and PtBuPh$_2$ for the Ir(I) series and PCy$_3$ and PCy$_2$Ph for the Rh(I) series. The donor strength of the phosphine is reflected in the high HOMO energies but evidently the steric bulk of the ligands reduces the observed reactivity of these complexes.

A better correlation was observed for the [(bpy)Pt(R)$_2$] series where the steric bulk of the complexes is more consistent than for the Vaska series. For the [PtX(Me)(L)] series the data can be separated into two distinct series based upon the phosphine. The three complexes in **Figure 4.17** shown in blue contain a PPh$_3$ ligand and the complexes shown in red contain a PPh$_2$Me ligand.

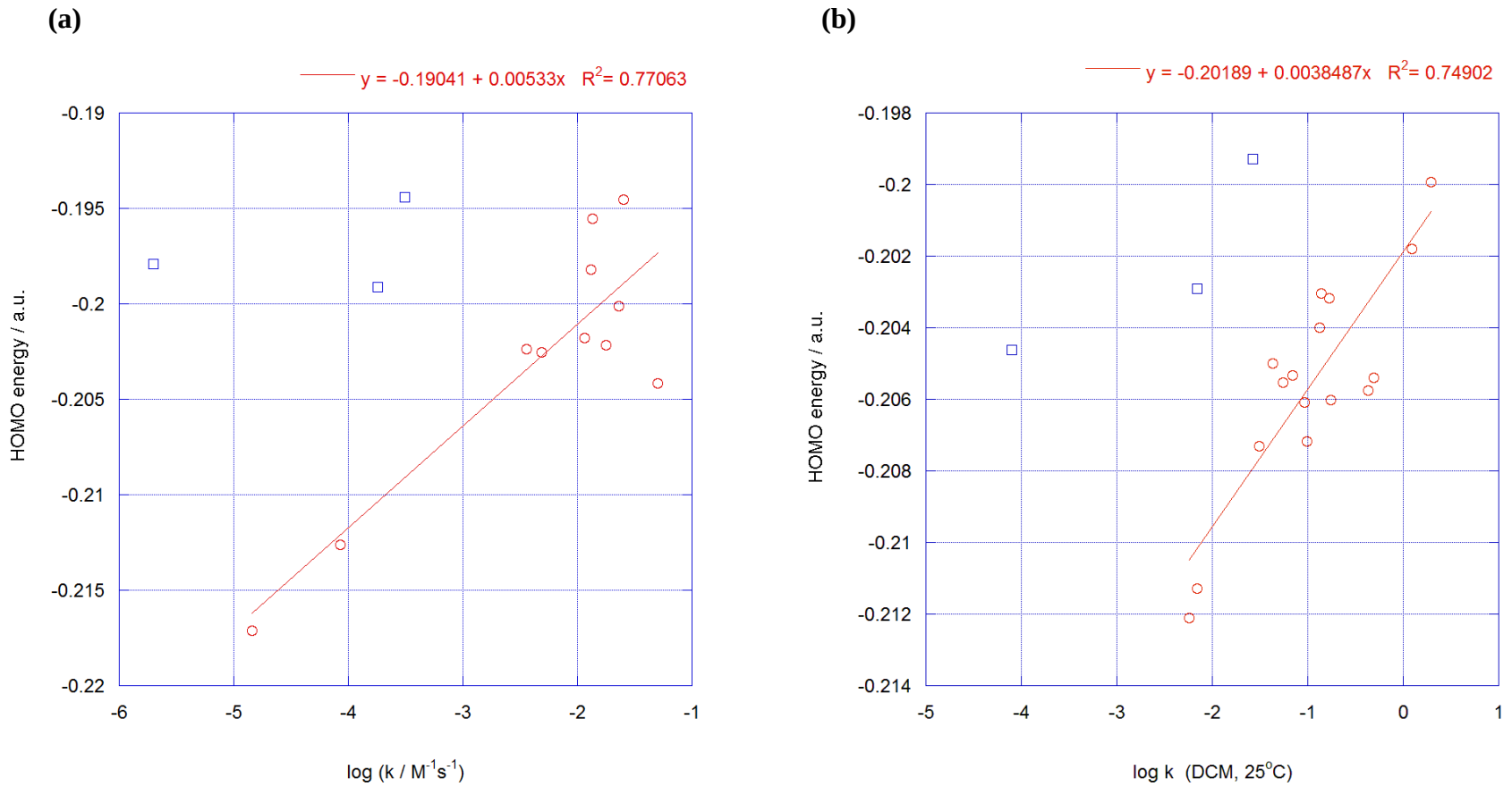


**Figure 4.16:** Plots of reactant HOMO energy against experimental log *k* (25 °C) for **(a)** [IrCl(CO)(L)$_2$] and **(b)** [Rh(acac)(CO)L] complexes. (DFT-B3LYP / Mixed basis)

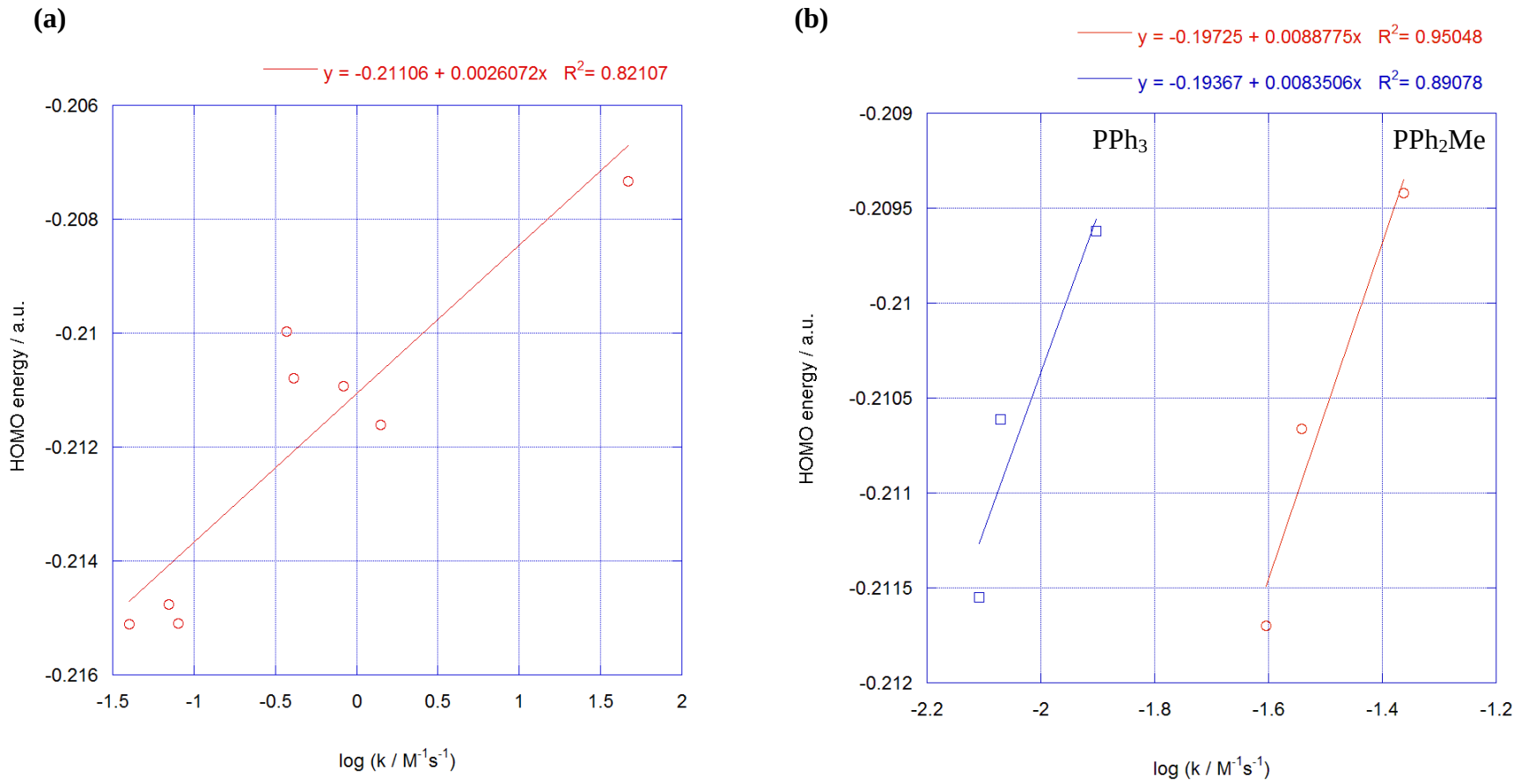


**Figure 4.17:** Plots of reactant HOMO energy against experimental log *k* (25 °C) for **(a)** [Pt(bpy)(R)$_2$] and **(b)** [PtX(Me)(L)] complexes. (DFT-B3LYP / Mixed basis)

### 4.2.5 Vibrational frequencies of [Rh(acac)(CO)L] and [IrCl(CO)(L)$_2$]

The [Rh(acac)(CO)L] and [IrCl(CO)(L)$_2$] series of complexes both contain a carbonyl ligand. The carbonyl stretching frequency can be measured experimentally and is often used as an indicator of the level of electron density on the metal. The lower the carbonyl frequency, the more electron rich the metal. The amount of electron density on the metal can be related to the nucleophilicity of the complex. Plots of the calculated against experimental ν(CO) for both systems are shown in **Figure 4.18.**

A better $R^2$ value is found for the [Rh(acac)(CO)L] series than for the Vaska-series. In the Vaska-series, there are two obvious outliers which bear the ligands P$^t$BuPh$_2$ and PCyPh$_2$. Both of these ligands are bulky and it is possible that the complex reactant geometry is not in the lowest energy conformation.

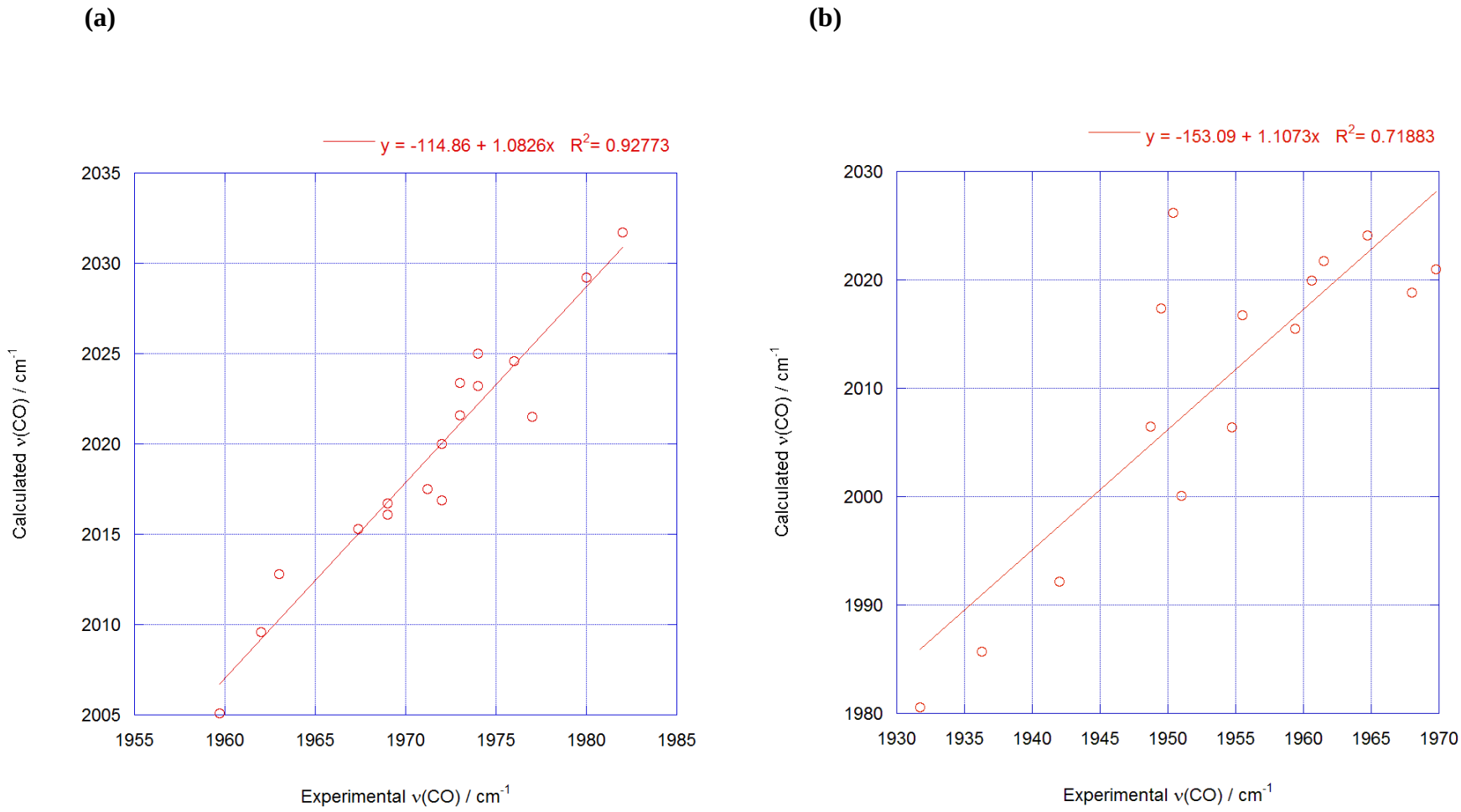


**Figure 4.18:** Plot of DFT computed against experimental stretching frequencies for **(a)** [Rh(acac)(CO)L] and **(b)** [IrCl(CO)$(L)_2$] Trend line equations and $R^2$ values given in key.

## 4.3 General conclusions

The calculated barriers ($\Delta H^{\ddagger}$) show a good correlation with the experimental rate constants across all metal complexes. Good correlations were also observed for each individual series with the best correlation being observed for the [Pt(bpy)$(R)_2$] series where the steric environment around the metal was comparable for each complex. Gas-phase transition states were difficult to optimise due to a lack of an obvious minima in the reaction coordinate caused by very similar energies for the transition state and ion-pair.

The carbon-iodide and carbon-metal distances in the transition state generally do not correlate well with the experimental rates for all series. Whilst good correlations were again found for the [Pt(bpy)$(R)_2$] series, the remaining series which all contain phosphine ligands showed poorer correlations.

DFT-calculated stretching frequencies for the metal-carbonyl bond correlate well with experimental values. The correlation is better for the [Rh(acac)(CO)L] series than for the [IrCl(CO)$(L)_2$] series.

HOMO energies resemble a metal $d_z^2$ orbital in character and correlate well with experimental rate constants providing the steric bulk of the complexes is comparable. HOMO energies for complexes bearing very bulky phosphine substituents such as $PCy_3$ and $PCy_2Ph$ suggest a very rich nucleophilic centre but they react slowly with iodomethane because of the steric hindrance of the ligand.

## 4.4 References


(1) Paulik, F. E.; Roth, J. F. *Chem. Comm.* **1968**, 11, 1578.

(2) Forster, D. *Inorg. Chem.* **1969**, *8*, 2556.

(3) Forster, D. *Inorg. Chem.* **1972**, *11*, 1686.

(4) Haynes, A.; Mann, B. E.; Gulliver, D. J.; Morris, G. E.; Maitlis, P. M. *J. Am. Chem. Soc.* **1991**, *113*, 8567.

(5) Maitlis, P. M.; Haynes, A.; Sunley, G. J.; Howard, M. J. *Dalton Trans.* **1996**, 11, 2187.

(6) Griffin, T. R.; Cook, D. B.; Haynes, A.; Pearson, J. M.; Monti, D.; Morris, G. E. *J. Am. Chem. Soc.* **1996**, *118*, 3029

(7) Ivanova, E. A.; Gisdakis, P.; Nasluzov, V. A.; Rubailo, A. I.; Rosch, N. *Organometallics* **2001**, *20*, 1161.

(8) Kinnunen, T.; Laasonen, K. *J. Mol.Struct.,* **2000**, *540,* 910.

(9) Kinnunen, T.; Laasonen, K. *J. Mol.Struct.,* **2001**, *542*, 272.

(10) Kinnunen, T.; Laasonen, K. *J. Mol.Struct.,* **2003**, *665,* 150.

(11) Cheong, M.; Ziegler, T. *Organometallics,* **2005**, *24*, 3053.

(12) Wilson, M. R.; Liu, H.; Prock, A.; Giering, W. P. *Organometallics,* **1993**, *19*, 2044.

(13) Nabavizadeh, S. M.; Amini, H.; Jame, F.; Khosraviolya, S.; Shahsavari, H. R.; Hosseini, F. N.; Rashidi, M. *J.Organomet. Chem.,* **2012**, *698*, 53.

(14) Jawad, J. K.; Al-Obaidy, F. N. K.; Hammud, J. A.; Al-Azab, F. *J.Organomet. Chem.,* **2000**, *599*, 166.

(15) Conradie, J. *Dalton Trans.,* **2012,** *41,* 10633.

(16) Costello, J. F.; Davies, S. G. *J. Chem. Soc., Perkin Trans.* **1998**, *2*, 1682.

(17) Costello, J. F.; Davies, S. G.; McNally, D. *J. Chem. Soc., Perkin Trans.* **1999**, *2*, 465.

(18) Brink, A.; Roodt, A.; Steyl, G.; Visser, H. G. *Dalton Trans.,* **2010**, *39*, 5572.

# CHAPTER 5

# Combined data set analysis

## 5.1 Introduction

The work undertaken **in Chapters 2, 3 and 4** has established a good relationship between the calculated barrier height and the experimental rate constants especially for series where the steric environment around the metal is similar. The relationship between the transition-state C-I and C-M distances and the rate constant is more tenuous with good correlations only being found for series where the steric environment is similar and the metal is the same. For series where either the metal or the steric environment changes, the correlations are significantly poorer.

Further work was undertaken herein to investigate whether there is a relationship between calculated parameters and reactivity which would afford a suitable method of predicting the nucleophilicity for new complexes without having to resort to calculating a full potential energy surface for each complex.

In this chapter, the data from the preceding three chapters is analyzed as one combined data set to establish whether an overall correlation exists between the computed and experimental parameters. The data set was then supplemented with further data from both the literature and our laboratory.[1-11]

## 5.2 Barrier height analysis

A number of series were initially analysed in the gas-phase for computational ease. **Figure 5.1** shows a plot of the DFT-calculated barrier heights ($\Delta H^{\ddagger}$) against the experimental rate constants.

A number of things can be interpreted from the collated plot. Initially, there does seem to be a general relationship between the calculated barrier heights and the experimental rate constants independent of the system in question across fourteen orders of magnitude. Whilst there is a degree of scatter on the plot, the most nucleophilic complexes generally have the lowest calculated barrier heights.

The anionic systems (marked with red circles and pink diamonds on **Figure 5.1**) seem to follow a slightly steeper, offset trend line than the remaining data which are all neutral systems. The iridium complexes bearing Cp* rings follow the same trend line as the complexes with Cp rings which is expected as the two series are very similar in structure. The platinum, [Pt(bpy)($R_2$] and [IrCl(CO)($L)_2$] series which are all square-planar complexes seem to follow the same general trend as well. The data set can be better described by using two trend lines – one for the anionic complexes and one for the neutral species.

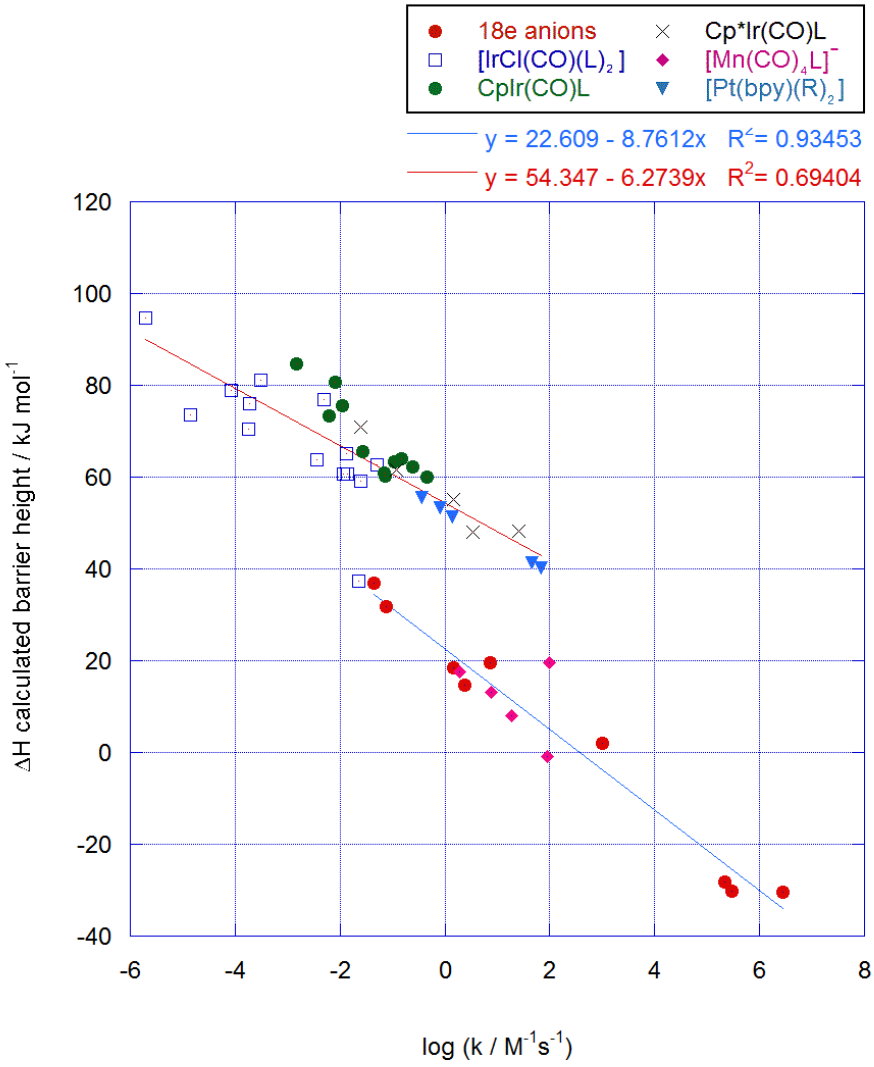


**Figure 5.1:** Plot of calculated barrier heights ($\Delta H^{\ddagger}$) against experimental log *k* for the reaction of metal complexes with iodomethane. (DFT-B3LYP – Gas-Phase) Complexes investigated, linear fit equation and $R^2$ value given in key.

Some issues were encountered in locating transition states for the more reactive rhodium and iridium complexes in the gas-phase. It was clear that more robust conclusions could be drawn by including solvent in the calculations and by using a better basis set. The best basis set based upon the work in **Chapters 3** and **4** was a mixed basis set with SDD on the metal and 6-311G(d,p) on all other atoms. All of the series analysed in the gas-phase were re-examined using the basis set. Inclusion of the solvent also allowed for further systems to be analysed which were proving problematic to analyse in the gas-phase. A plot of the DFT calculated barrier heights ($\Delta H^{\ddagger}$) against the experimental rate constants (log *k*) is shown in **Figure 5.2.**

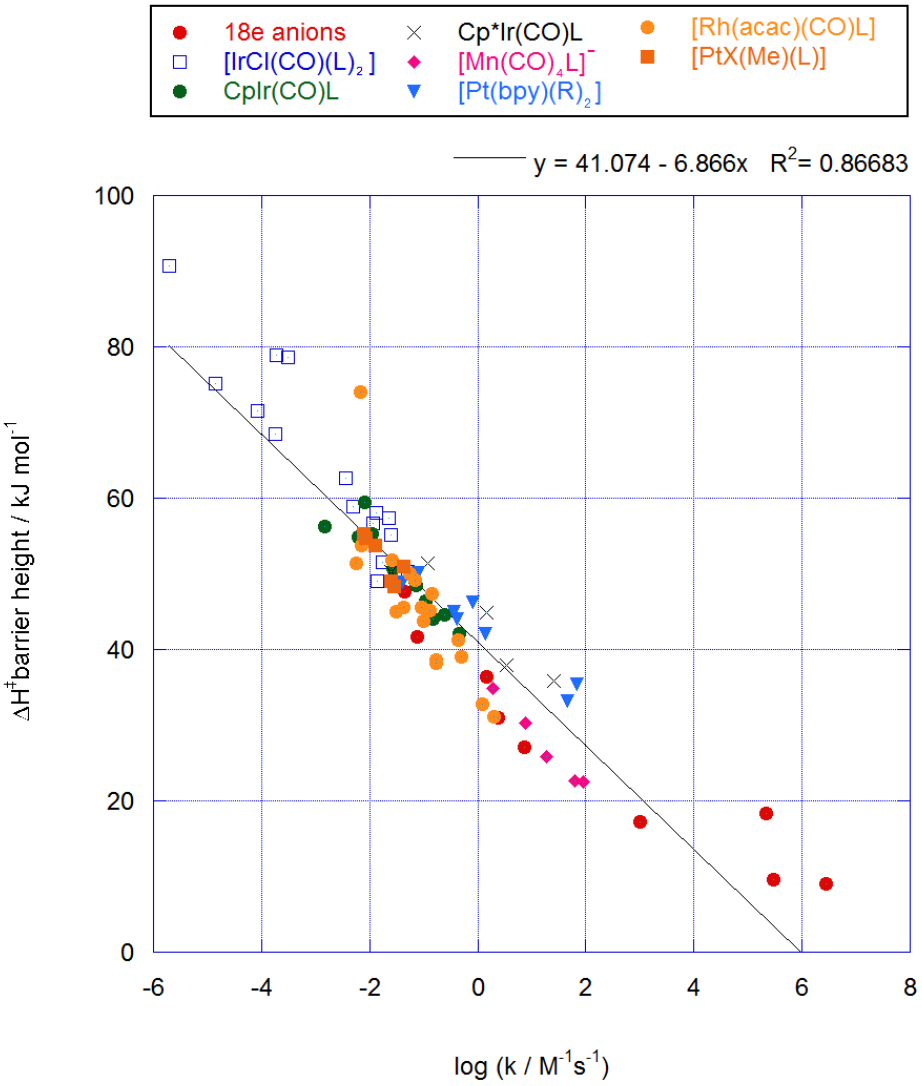


**Figure 5.2:** Plot of calculated barrier heights ($\Delta H^{\ddagger}$) against experimental log *k* for the reaction of metal complexes with iodomethane. (DFT-B3LYP – mixed basis) Complexes investigated, linear fit equation and $R^2$ value given in key.

A better correlation was observed overall when compared to the gas-phase data with a $R^2$ value of 0.86. The addition of solvent in the calculations has a large effect. The calculated barrier heights for the anionic complexes are higher than in the gas-phase whereas the barrier heights for the neutral species are relatively unchanged. Consequently, all the data now seems to follow the same trend line in contrast to the gas-phase data where two distinct types of complexes (anionic and neutral) could be discerned from the data.

## 5.3 Transition-state geometries

As with each of the individual series, the transition-state geometries were also compared to the experimental reactivity across all series investigated to identify whether a correlation exists between the parameters or whether the observed correlations are only good when the complexes can be related to one another.

**Figure 5.3** shows a plot of the C-I distances against experimental rate constants. A poorer correlation was observed than for the DFT calculated barrier heights with a $R^2$ value of 0.732. Generally, the most nucleophilic complexes were predicted to have the shortest C-I distances and thus have an earlier transition state.

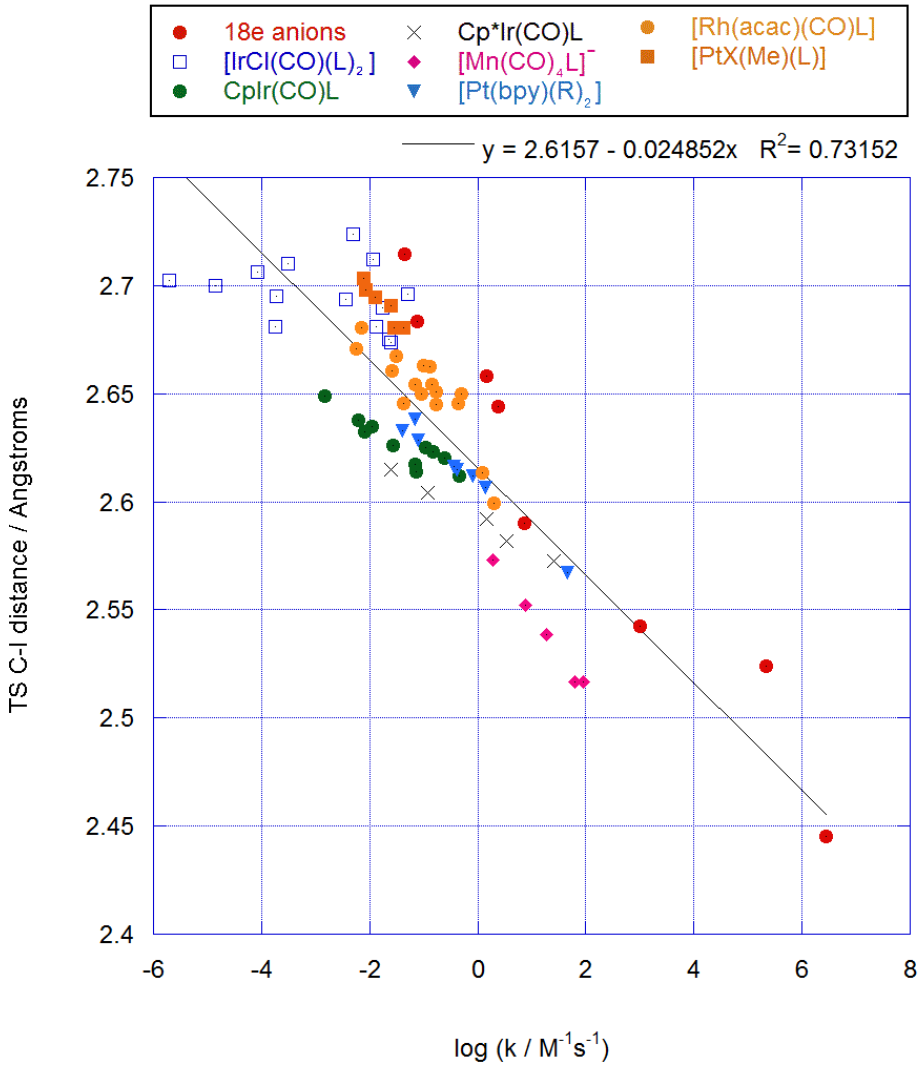


**Figure 5.3:** Plot of TS C-I distance against experimental log *k* for the reaction of metal complexes with iodomethane. (DFT-B3LYP – mixed basis – solution phase) Linear fit equation and $R^2$ value given in key.

The transition state C-M distance was also plotted against the experimental rate constant as shown in **Figure 5.4**. There may be a very loose trend in the data in that the most nucleophilic complexes do feature longer C-M distances in the transition state in general but the correlation is still much lower than was observed for the DFT calculated barrier heights. A very good correlation across so many different complexes might not be expected for the C-M distance as each complex features a different nucleophilic centre which is turn has a different radius which will affect how close the iodomethane molecule will approach. Each individual series is clearly discernible from the rest of the data.

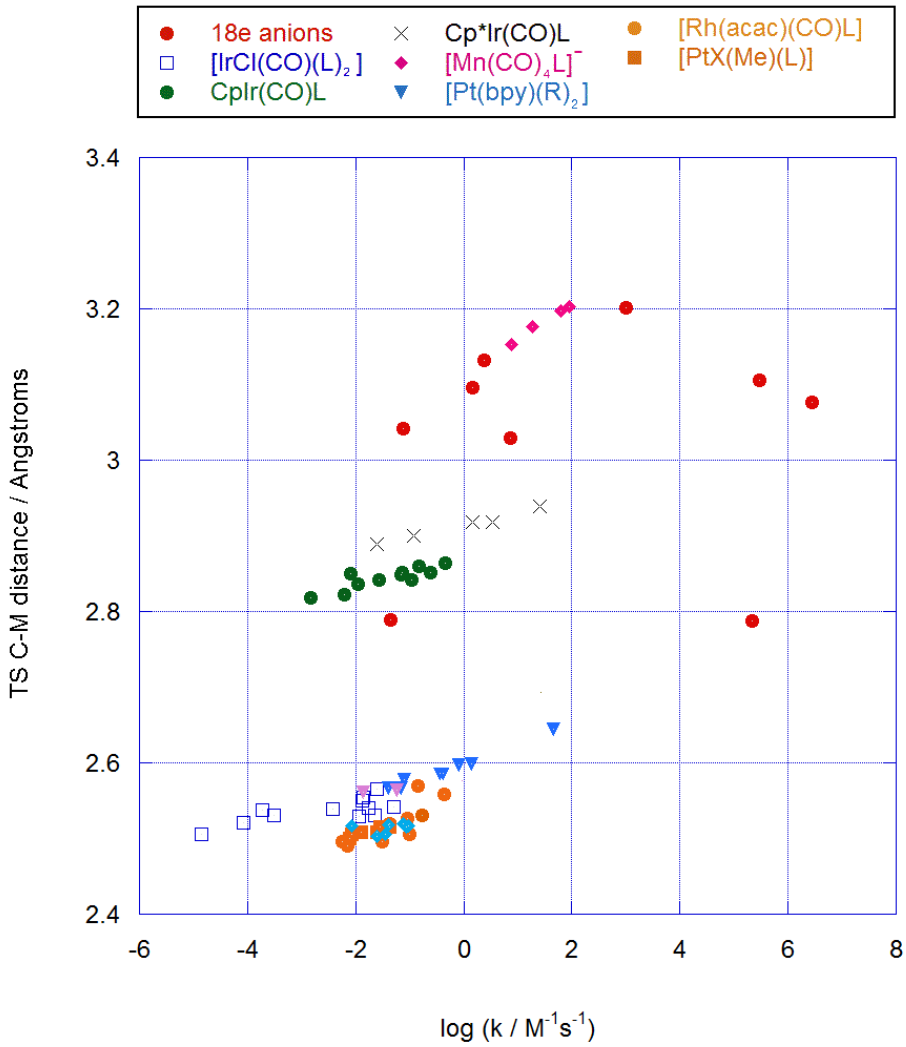


**Figure 5.4:** Plot of TS C-M distance against experimental log *k* for the reaction of metal complexes with iodomethane. (DFT-B3LYP – mixed basis – solution phase)

However, some trends can be discerned from the plot. The anionic complexes feature the longest C-M distances and are separated towards the top of the plot. The central area is dominated by Cp and Cp* complexes which follow a similar trend with the Cp* containing complexes featuring marginally longer C-M distances presumably due to the increased steric bulk of the ring and the enhanced nucleophilicity of the complex. The remainder of the complexes which feature shorter C-M distances are all neutral square-planar complexes. These all follow a reasonable trend suggesting that the C-M distance is more sensitive to the steric environment around the metal when compared to the C-I distance.

## 5.4 Inclusion of new complexes

The data from **Chapters 2-4** was further supplemented with data from the literature and our own laboratory. **Figure 5.5** summarises their structures and respective experimental rate constants and computed barrier heights are given in **Table 5.1.** Reaction profiles were generated for each complex using the methodology discussed in the preceding chapters to yield barrier heights.

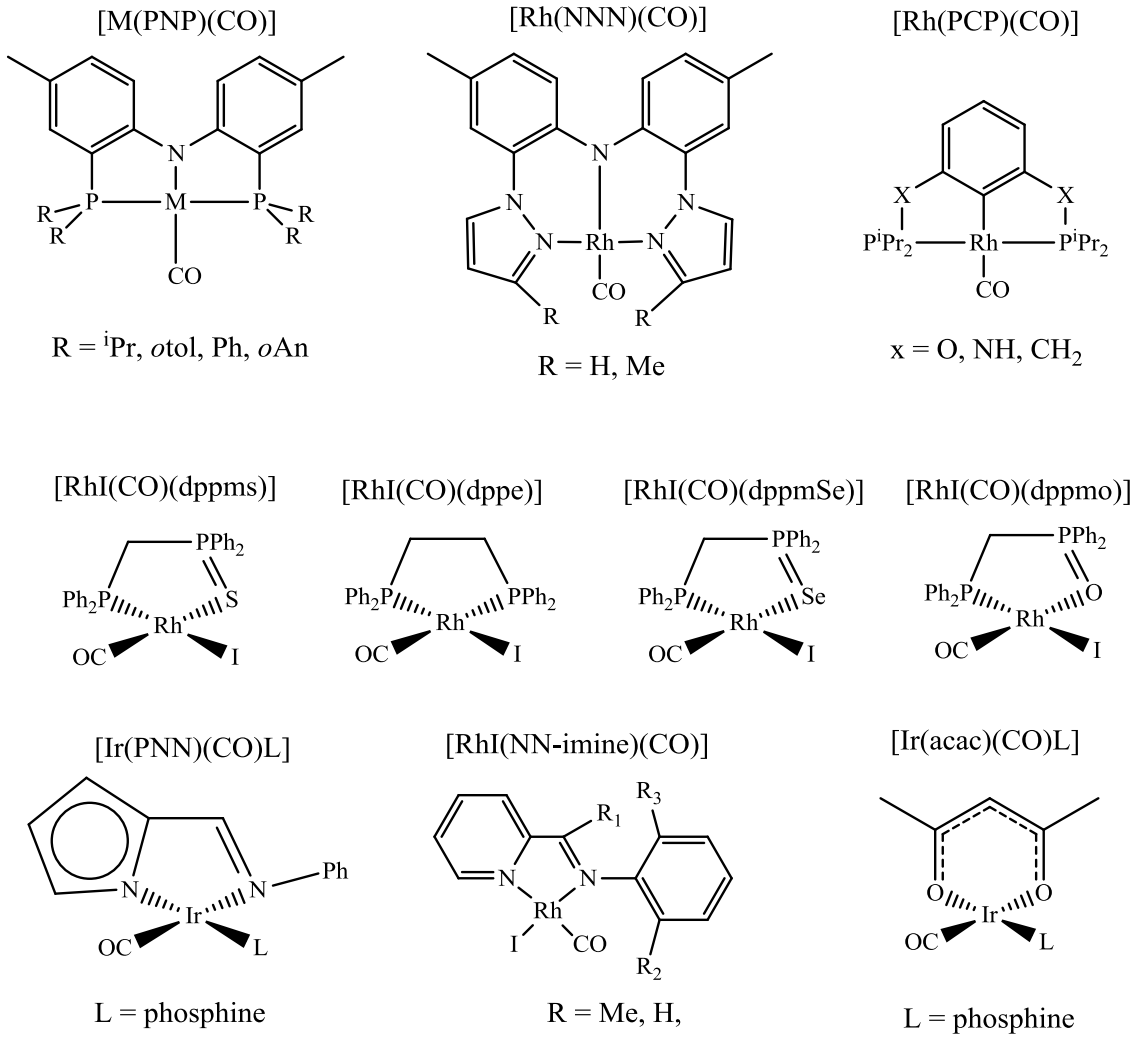


**Figure 5.5:** Structures of Rh(I) and Ir(I) complexes investigated

| Complex | L / R / X | log ($k$ / $M^{-1}s^{-1}$) | $\Delta H^{\ddagger}$ Barrier heights / kJ $mol^{-1}$ |
|---|---|---|---|
| [Rh(RNNN)(CO)] | H | 0.702 | 38.1 |
| | Me | -0.154 | 43.6 |
| [Rh(RPNP)(CO)] | $^{i}$Pr | 0.0141 | 63.4 |
| | *o*tol | 0.0211 | 26.7 |
| | Ph | 0.0926 | 50.7 |
| | *o*An | 23.0 | 33.3 |
| [Rh(PXCXP)(CO)] | O | -2.41 | 42.0 |
| | NH | -2.11 | 33.4 |
| | $CH_2$ | -0.747 | 27.3 |
| [Ir(PNN)(CO)L] | $PPh_3$ | -0.284 | 37.0 |
| | P*o*$tol_3$ | -1.51 | 54.6 |
| | P*p*$tol_3$ | -0.194 | 36.2 |
| | P*o*$An_3$ | 1.51 | 9.70 |
| | P(4-F-$C_6H_4)_3$ | -0.886 | 44.5 |
| [RhI(NN-imine)(CO)] | $R_1$ $R_2$ $R_3$ | | |
| | Me H H | -1.01 | 45.3 |
| | Me H $^{i}$Pr | -1.05 | 45.9 |
| | Me $^{i}$Pr $^{i}$Pr | -2.08 | 53.0 |
| | Me H $^{t}$Bu | -1.38 | 46.8 |
| | H H H | -1.45 | 47.7 |
| | H H $^{i}$Pr | -1.61 | 48.4 |
| | H $^{i}$Pr $^{i}$Pr | -0.70 | 43.9 |
| | H H $^{t}$Bu | -1.12 | 45.5 |
| [Ir(acac)(CO)L] | $PPh_3$ | -0.456 | 40.3 |
| | P(4-Cl-$C_6H_4)_3$ | -0.931 | 44.8 |
| | P(4-F-$C_6H_4)_3$ | -0.907 | |
| [RhI(CO)L] | dppms | -2.32 | 52.4 |
| | dppmeSe | -2.74 | 51.5 |
| | dppmo | -2.34 | 49.7 |
| | dppe | -2.65 | 59.0 |

**Table 5.1:** Table of DFT $\Delta H^{\ddagger}$ calculated barrier heights and experimental data for reactions of various Rh(I) and Ir(I) complexes with iodomethane. (DFT-B3LYP Mixed basis with solvent) [12-14]

**Figure 5.6** shows a plot of the $\Delta H^{\ddagger}$ calculated barrier height against log *k*. The addition of the new complexes, which are clustered in the centre of the graph, lowers the correlation from 0.86 to 0.82 but there is still a strong correlation across the data.

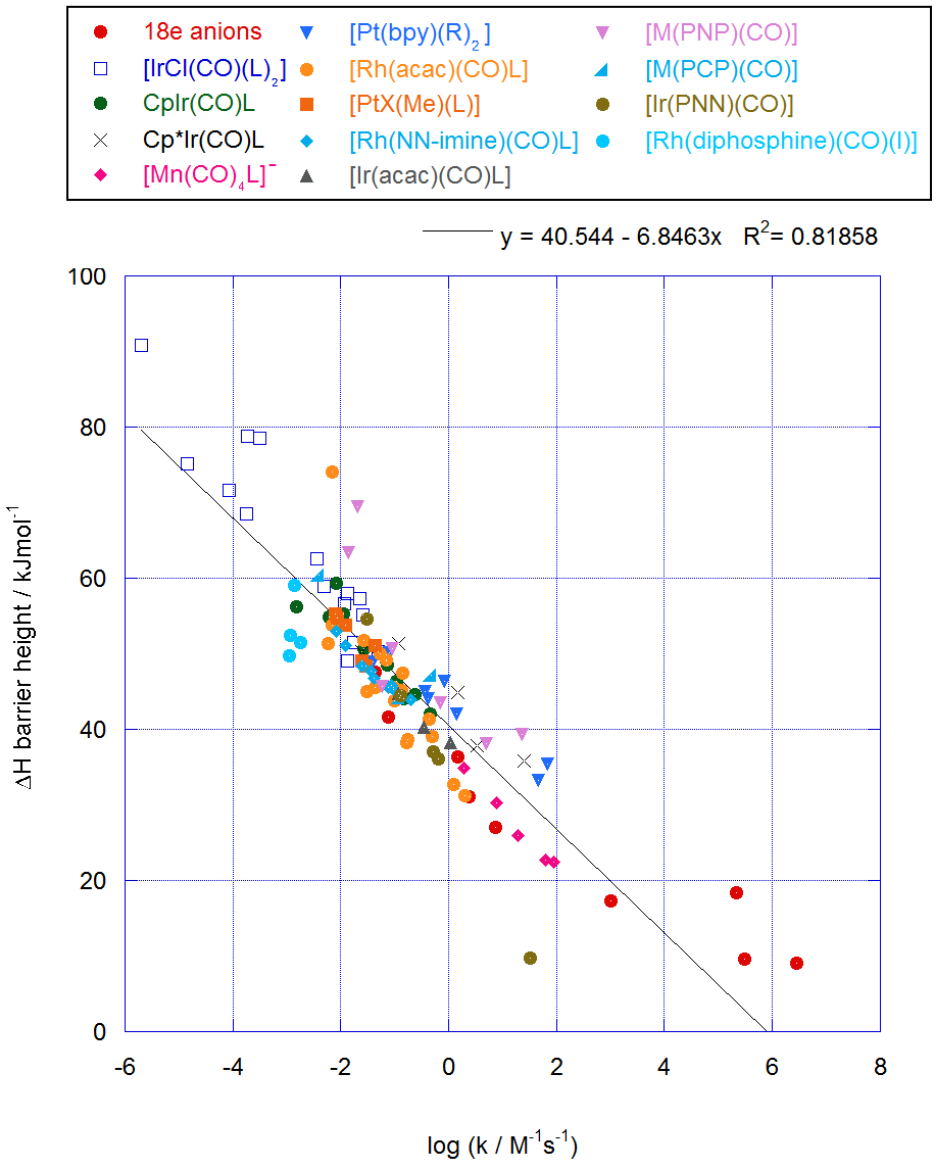


**Figure 5.6:** Plot of calculated barrier heights ($\Delta H^{\ddagger}$) against experimental log *k* for the reaction of metal complexes with iodomethane. (DFT-B3LYP – mixed basis / solution phase) Complexes investigated, linear fit equation and $R^2$ value given in key.

## 5.5 Conclusions

Multiple series of metal complexes have been analysed collectively to investigate whether DFT-computed barrier heights and transition-state atom-distances show a general trend to experimental rates or whether good correlations are only observed when the structure of the complex is comparable. The DFT-computed barrier heights show a good correlation to experimental rate constants over 14 orders of magnitude with an overall correlation coefficient of 0.80 for complexes analysed using the mixed basis with solvent accounted for using the default PCM method. Data analysed in the gas-phase can be separated into two distinct series – neutral and anionic complexes.

The transition state C-M distances show very little correlation to experimental rate constants when analysed as one large series, possibly because the nucleophilic centre in each case is different. The C-M distance is sensitive to the steric environment around the metal as reasonable trends were found when the data is broken down into three series: anionic complexes, complexes with Cp and Cp* rings and neutral square-planar complexes. There is a reasonable correlation between the transition state C-I distance and experimental rate constant with a $R^2$ value of 0.74.

The strong correlation between the DFT-calculated barrier heights and experimental log *k* values is potentially useful for predicting the nucleophilicity of new complexes. Complexes with a similar structure to any of the individual series can be compared solely with that series but complexes which bear no resemblance to any of the other series can be compared against all the data at once which should give some indication as to how the complex will behave experimentally.

## 5.6 References


(1) Best, J.; Wilson, J. M.; Adams, H.; Gonsalvi, L.; Perruzzini, M.; Haynes, A. *Organometallics*, **2007**, *26*, 1960.

(2) Brink, A.; Roodt, A.; Steyl, G.; Visser, H. *Dalton Trans*, **2010**, *39*, 5572.

(3) Dessy, R. E.; Pohl, R. L.; King, R. B. *J. Am. Chem. Soc.*, **1966**, *88*, 5121.

(4) Gonsalvi, L.; Gaunt, J.; Adams, H.; Castro, A.; Sunley, G. J.; Haynes, A. *Organometallics*, **2003**, *22*, 1047.

(5) Jawad, J. K.; Al-Obaidy, F. N. K.; Hammond, J. A. *J. Organomet. Chem.*, **2000**, *599*, 166.

(6) Lai, C. K.; Feighery, W. G.; Zhen, Y.; Atwood, J. D. *Inorg. Chem.*, **1989**, *28*, 3929.

(7) Nabavizaseh, S. M.; Amini, H.; Jame, F.; Khosraviolya, S.; Shahsavari, H. R.; Hosseini, F. N.; Rashidi, M. *Journal of Ornganometallic Chemistry*, **2012**, *698*, 53.

(8) Pearson, R. G.; Figdore, P. E. *J. Am. Chem. Soc.*, **1980**, *102*, 1541.

(9) Wang, D.; Angelici, R. *Inorg. Chem.*, **1996**, *35*, 1321.

(10) Wilson, J. M.; Sunley, G. J.; Adams, H.; Haynes, A. *J. Organomet. Chem.*, **2005**, *690*, 6089.

(11) Wilson, M. R.; Liu, H.; Prock, A.; Giering, W. P. *Organometallics*, **1993**, *19*, 2044.

(12) Cocker, D. *Unpublished work*, **2015**.

(13) Wells, J. *Unpublished work*, **2010**.

(14) Gonsalvi, L.; Gaunt, J.; Adams, H.; Castro, A.; Sunley, G. J.; Haynes, A. *Organometallics*, **2003**, *22*, 1047.

# CHAPTER 6

# Modelling the nucleophilicity of cobalt complexes towards alkyl halides

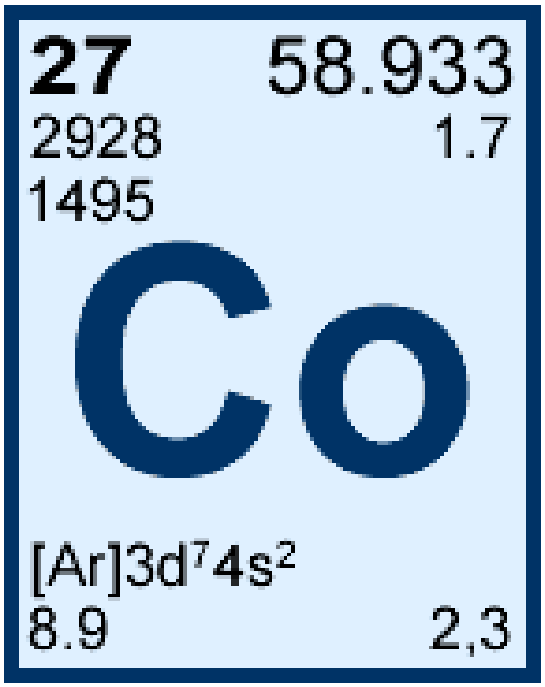

## 6.1 Introduction

Cobalamins are an interesting group of cobalt containing complexes which act as cofactors for enzymes in the body, for example in vitamin $B_{12}$. The structure of three of these complexes is presented in **Figure 6.1**, which clearly shows that the central cobalt atom is surrounded by a corrin ring. The complexes only differ in the nature of the axial ligand, R. Cobalamin complexes can contain cobalt in three oxidation states (I, II and III) with the latter being the least common. The exceptional nucleophilicity of the Co(I) complexes has been attributed to two electrons present in an axial $3d_z^2$ orbital which is orientated correctly to interact with the LUMO of an incoming electrophile.[1]

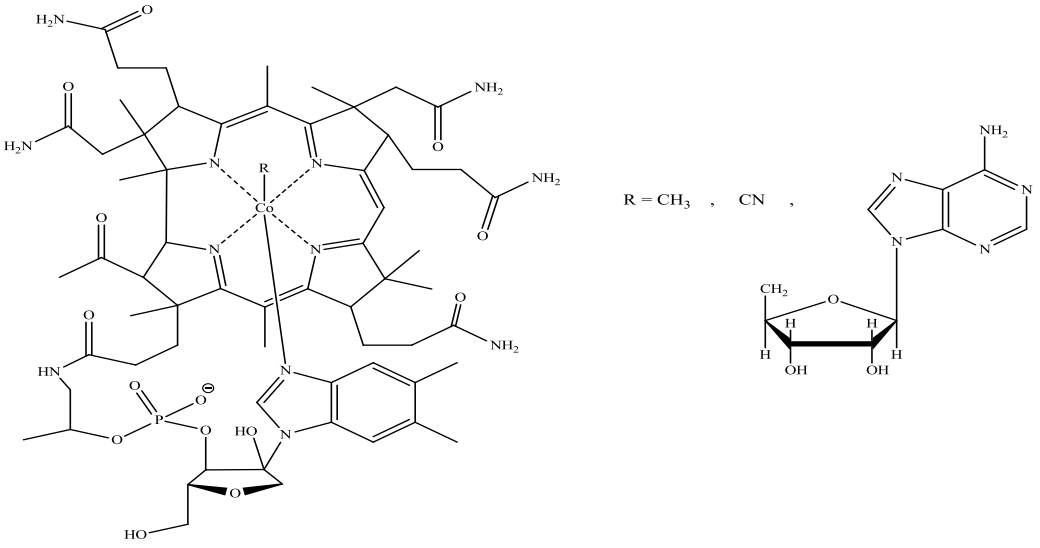


**Figure 6.1:** Cobalamin cofactors with varying R groups – methyl (MeCbl), adenosyl (AdoCbl) and cyanide (vitamin $B_{12}$)

These complexes are of great importance biologically in facilitating methyl transfer. The formation of methionine, which is an essential amino acid, is achieved using cobalamin complexes. Deficiencies in these complexes can cause fatigue, paranoia and even serious long term brain injury if left untreated.[2,3]

Understanding how and why the cobalt-carbon bond is broken in these complexes has led to a great deal of computational interest in these systems. A recent review by Jenson summarises work which has been undertaken already. This work has focused on

predicting the strength of the cobalt-carbon bond accurately.[4] Initially, for computational ease, model complexes were investigated before full cobalamin systems were modelled with simplified quantum mechanical methods. Further studies have been carried out computationally on these systems, looking into methyl transfer in $S_N2$ reactions.[5-7]

Experimentally, a number of cobaloxime complexes were investigated by Shrauzer et al. with a view to gaining insight into how vitamin $B_{12}$ may react with the similar electrophiles.[8,9] Cobaloximes are $Co(dmg)_2$ complexes where dmg is dimethylgloxime. They concluded that the model cobaloxime complexes all react *via* a classic $S_N2$ mechanism and by analogy so should vitamin $B_{12}$. They also observed that the reactivity of the cobalt complexes could be influenced by changing the coordinated axial ligand.

The reactivity of a tributylphosphine cobaloxime complex (**1a**) towards multiple alkyl chlorides was studied experimentally. The structure of this complex and its reactivity with a general alkyl halide is shown in **Figure 6.2**.

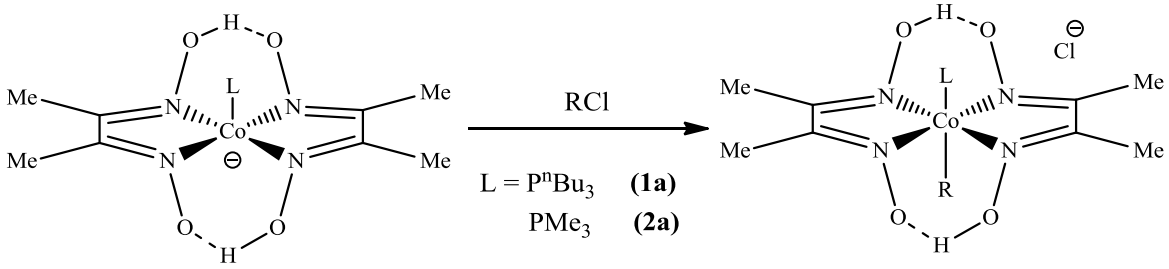


**Figure 6.2:** General reaction of Co(I) complexes with RCl.

In this chapter, the reactivity of various electrophiles with the same nucleophile, **2a**, is modelled. All of the data in the preceding chapters focussed on reactions of various nucleophiles with the same electrophile so it was of interest to investigate whether the effect of changing the electrophile can be modelled. The reactivity of **2a** with a series of alkyl chlorides provided an ideal series to investigate computationally as the complex is relatively small and facile to optimise.

## 6.2 Computational modelling

For computational ease, the axial tributyl phosphine was replaced with $PMe_3$ **(2a)**. To ensure that this simplification didn't unduly affect the results, two of the electrophiles were selected and the transition states optimised for **1a**. In general the barrier heights were lower than when the nucleophile was **2a** – typically around 4-5 kJ $mol^{-1}$ Prior to optimising transition states, the electrophiles were first investigated to ensure that the lowest energy conformation had been correctly identified.

A profile for the reaction of **2a** with MeCl is shown in **Figure 6.3**. Comparisons can be made with the anionic complexes in C**hapter 2**. The profile shows a small barrier height to the transition state and a very stable product, which reflects the high experimental nucleophilicity.

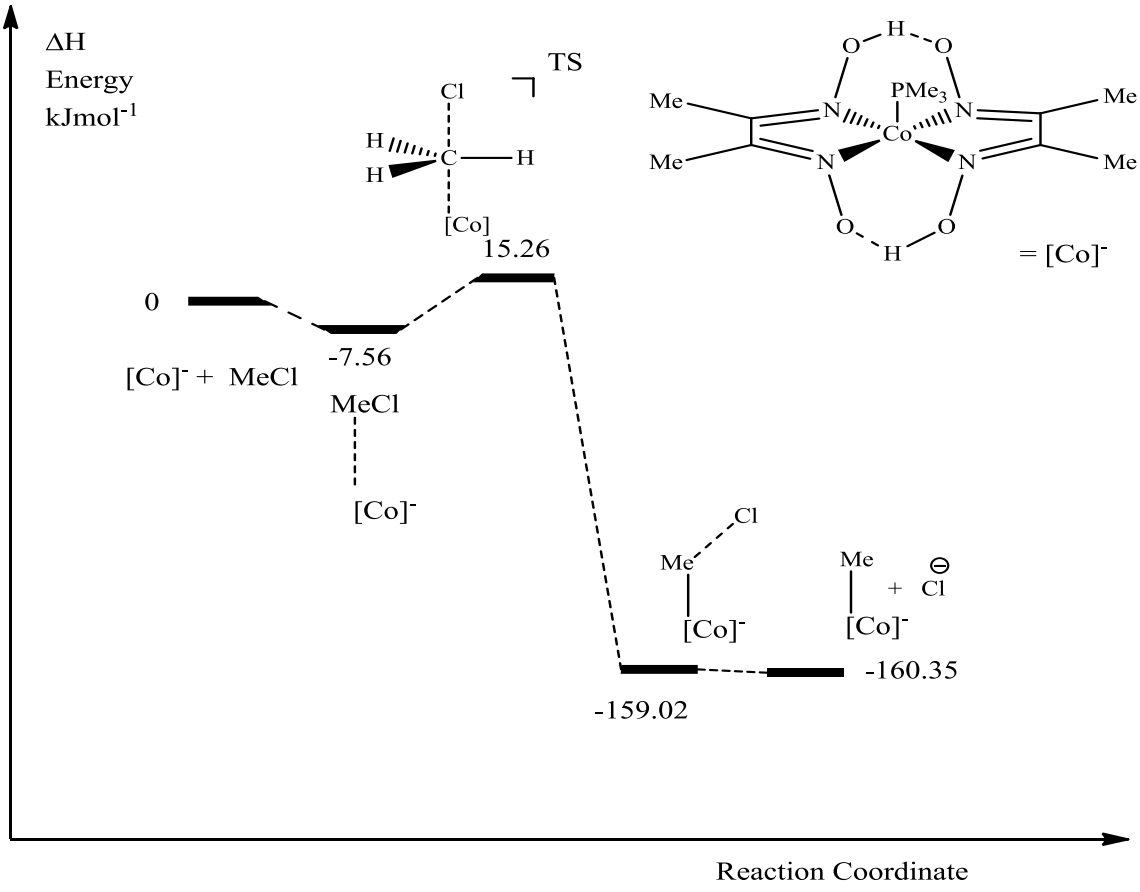


**Figure 6.3:** Energy profile ($\Delta H^{\ddagger}$) for the reaction of **2a** with chloromethane. (DFT-B3LYP/Mixed basis MeOH)

Selected transition state structures are shown in **Figure 6.4.** The Co-C-Cl angle in the transition state for reaction with iodomethane **(a)** is linear as would be expected for a typical $S_N2$ reaction. The remaining angles for the other electrophiles deviate significantly from linearity with the smallest angle of 140° observed for $C_6H_5CH(CH_3)Cl$. This deviation from linearity is attributed to the steric bulk of the alkyl chloride which inhibits the approach of the complex.

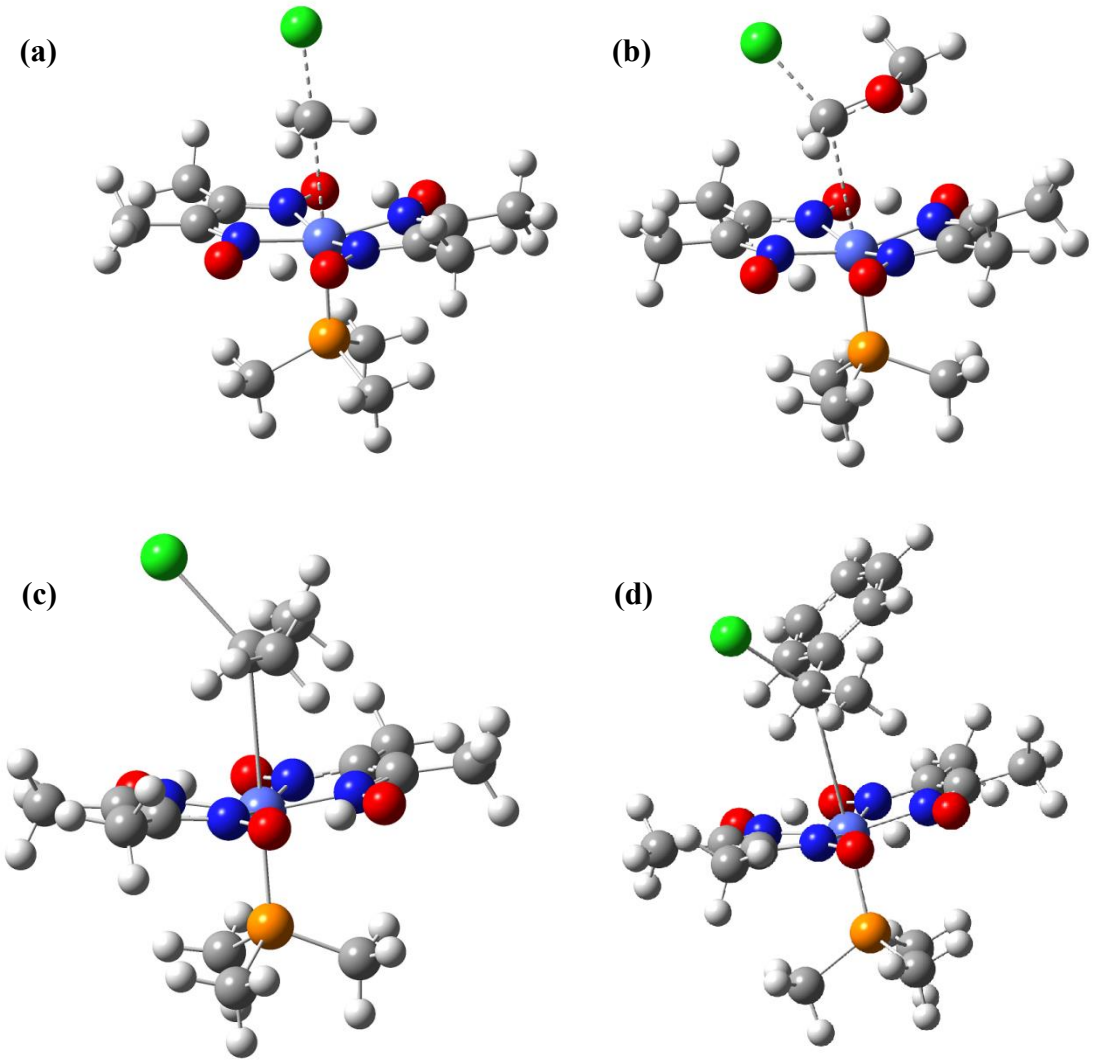


**Figure 6.4:** Optimised transition states for reaction of **2a** with MeCl **(a)**, $MeOCH_2Cl$ **(b)**, $^{i}PrCl$ **(c)** and $PhCH(Cl)CH_3$ **(d)**

The calculated barrier heights and experimental log *k* values are given in **Table 6.1.** A general inspection of the calculated barrier heights showed them to be significantly

lower than those observed for $[Co(CO)_4]^-$ in **Chapter 2**, which can be attributed to the greater donor strength of the dmg and $PMe_3$ ligands compared to carbonyls.

| Alkyl Halide | log ($k$ / $M^{-1}s^{-1}$) | $\Delta H^{\ddagger}$ barrier height / kJ $mol^{-1}$ | Co-C-X angle / ° |
|---|---|---|---|
| **MeI** | **3.36** | **0.96** | **178** |
| MeCl | -0.07 | 15.4 | 178 |
| EtCl | -2.05 | 21.4 | 151 |
| $^{n}$PrCl | -2.21 | 23.1 | 149 |
| $^{n}$BuCl | -2.13 | 22.7 | 149 |
| $Me_2CHCH_2Cl$ | -3.11 | 29.2 | 146 |
| $CH_3OCH_2Cl$ | 4.00 | -5.14 | 149 |
| $C_6H_5CH(CH_3)Cl$ | 0.36 | 10.3 | 141 |
| $^{n}$PentylCl | -2.17 | 23.0 | 149 |
| $^{n}$HexylCl | -2.20 | 23.0 | 149 |
| $^{i}$PrCl | -3.49 | 28.8 | 141 |
| 1-chloromethylnapthalene | 3.15 | 1.76 | 153 |

**Table 6.1:** Experimental rate constants for the reaction of **1a** with alkylhalides and computed barrier heights ($\Delta H^{\ddagger}$) and transition sate Co-C-X angles for the reaction of **2a** with alkylhalides (DFT-B3LYP- Mixed basis, MeOH)

A plot of the calculated barrier heights against experimental rate constant is shown in **Figure 6.5.** A strong correlation was found with an observed $R^2$ value of 0.987. A barrier height was also obtained for the reaction with iodomethane for comparison (shown in solid blue in **Figure 6.5**). In relation to the complexes discussed in **Chapter 5**, this complex is of similar reactivity to the 18-electron carbonyl complexes, which illustrates the donor strength of the dmg and phosphine ligand. All of the alkyl chlorides reacted slower with **2a** compared to iodomethane except for $CH_3OCH_2Cl$.

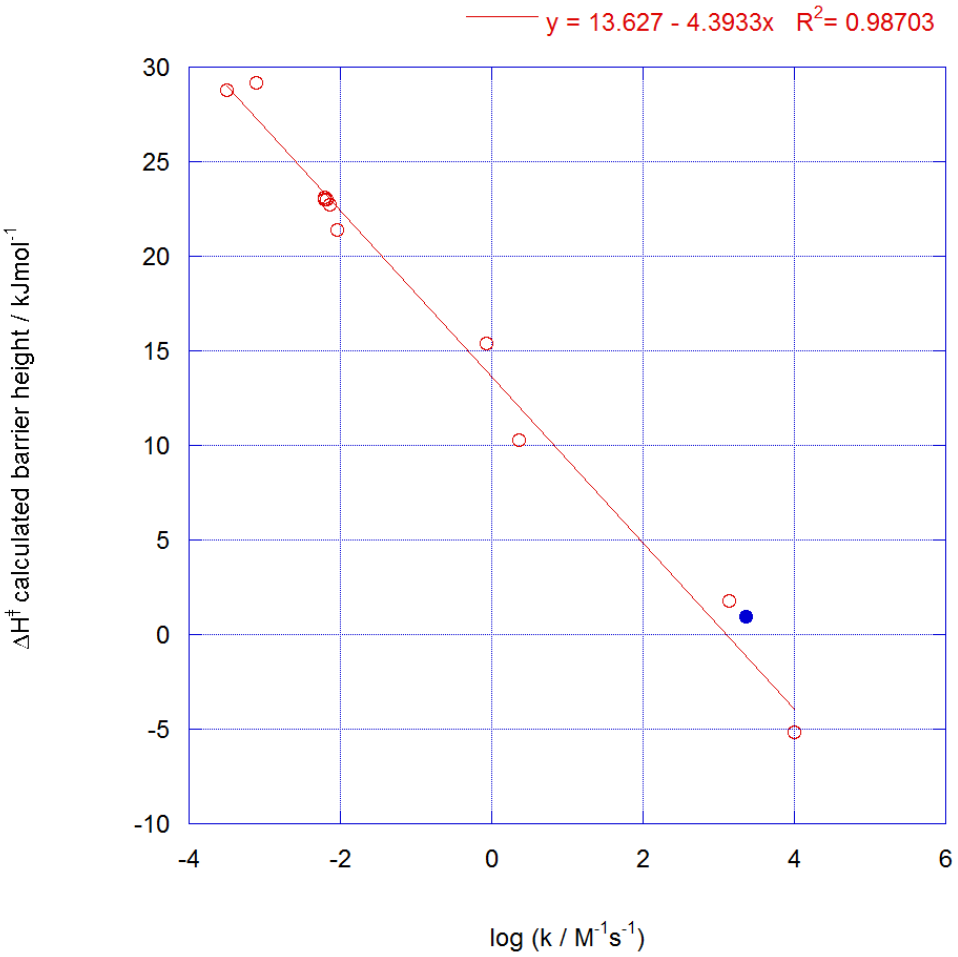


**Figure 6.5:** Plot of calculated barrier height ($\Delta H^{\ddagger}$) against experimental log *k* for the reaction of **2a** with various alkyl chlorides. Data for reaction with iodomethane shown for comparison in solid blue.

### 6.2.1 Electrophile LUMO energies

As discussed earlier in **Chapter 4**, the reactivity of a $d^8$ metal complex with an electrophile can be thought of as a lone pair of electrons located on the metal $d_z^2$ oribital which acts as a donor towards the LUMO of the electrophile. A reasonable relationship was established for the Ir-Vaska systems between the experimental log *k* and the energy of the $d_z^2$ orbital. For the cobalt series the situation is a little bit different as the nucleophile is kept the same so the LUMO energy of the electrophile was instead

investigated. A plot of the electrophile LUMO energy and experimental rate constants is shown in **Figure 6.6.**

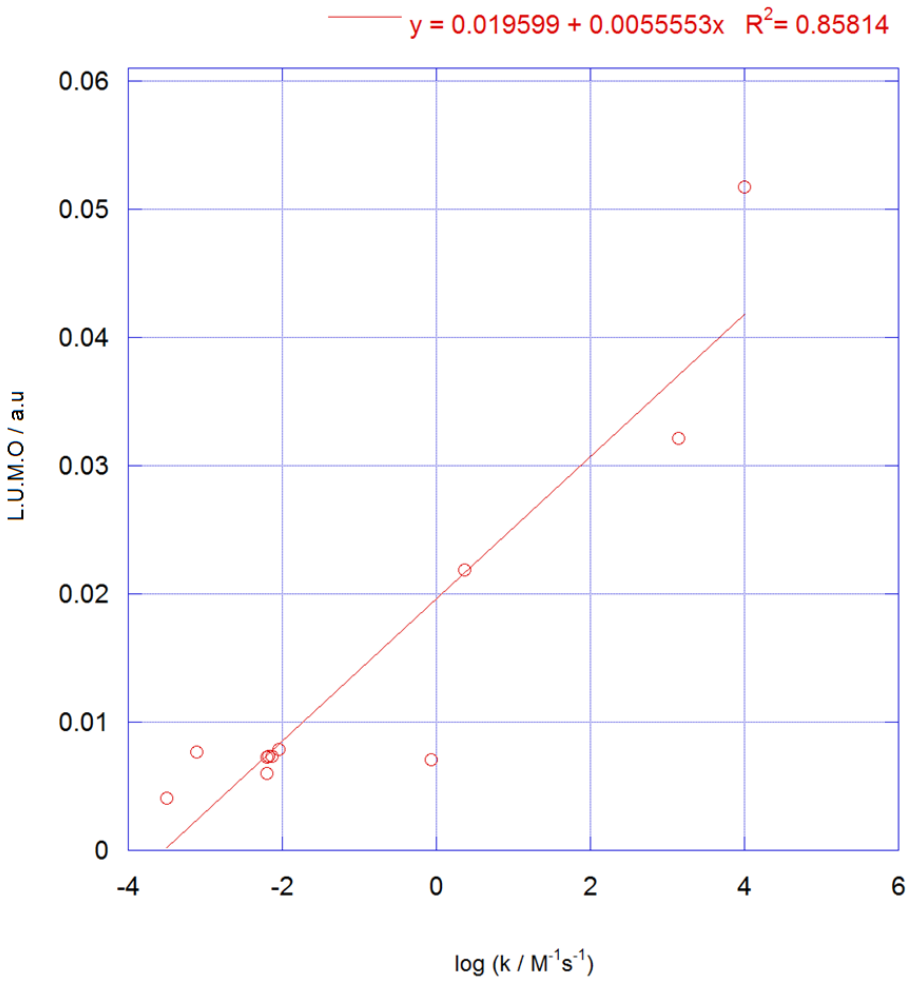


**Figure 6.6:** Plot of electrophile LUMO energy against log *k* (MeOH, 25 °C) for the reaction of **2a** with RCl.

Again, a reasonable correlation was established between the two parameters for this series. The most reactive electrophiles had the highest LUMO energies. The observed scatter in the plot is likely due to the sterics of the alkyl chloride.

### 6.2.2 Transition state geometries

A plot of the Co-C and C-Cl distances against experimental log *k* is shown in **Figures 6.7 and 6.8.**

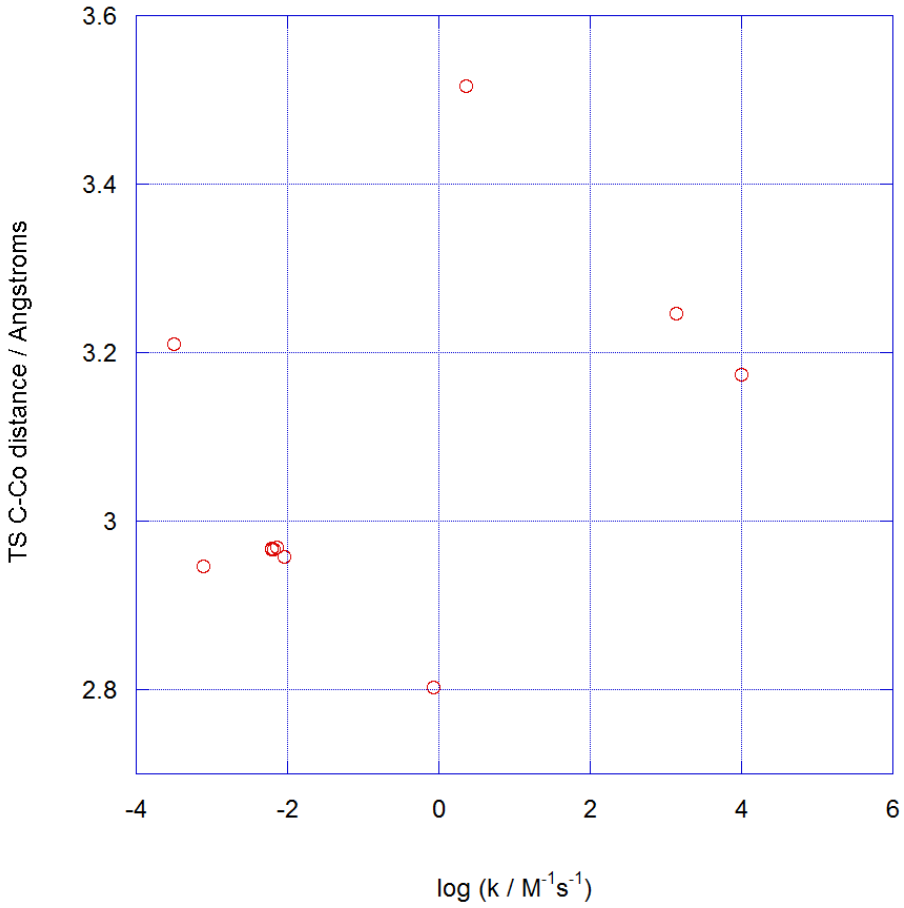


**Figure 6.7:** Plot of transition state C-Co distance against log *k* (MeOH, 25 °C) for the reaction of **2a** with RCl.

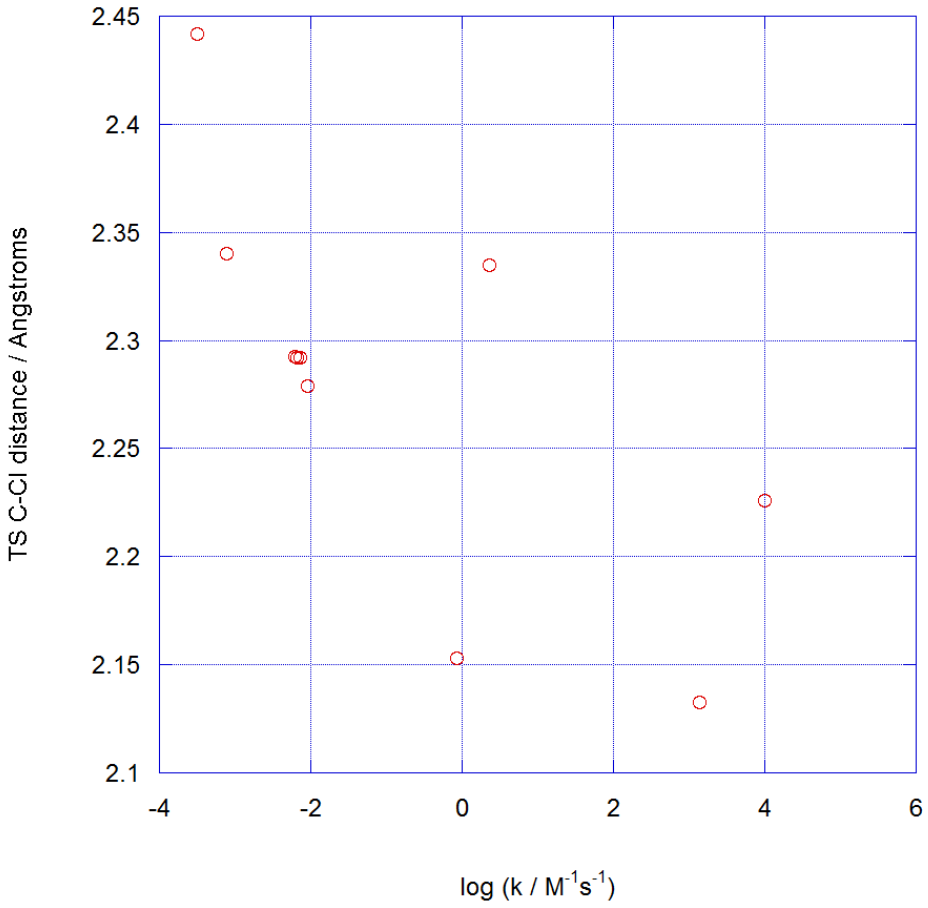


**Figure 6.8:** Plot of transition state C-Cl distance against log *k* (MeOH, 25 °C) for the reaction of **2a** with RCl.

Somewhat disappointingly, there was very little correlation for either the C-Co or the C-Cl distance in the transition state. Inspection of each individual transition state showed that the metal-carbon-chloride angle deviated significantly from linearity. For the platinum series in **Chapter 2**, the corresponding angle in the transition state was very close to linear in each case but for this series angles as low as 140$^{o}$ were observed. This is attributed to the bulkiness of some of the electrophiles where the nucleophile has to attack the carbon at a different angle to minimise unfavourable steric interactions. Such deviations from linearity may explain why poorer correlations were observed for the transition state distances.

## 6.3 Conclusions

The reactivity of a model cobaloxime complex, **2a**, with various alkyl halides was probed in order to see whether similar trends are observed when the electrophile is changed and the nucleophile is kept constant. Low barrier height values ($\Delta H^{\ddagger}$) are observed for this series, reflecting the reactive nature of the complex. The DFT calculated barrier height shows a strong correlation with experimental log *k* values with a $R^2$ value of 0.929 over eight orders of magnitude.

Poorer correlations were found between the transition state C-Cl and Co-C distances and the experimental log *k* values possibly due to the transition states deviating from linearity. The LUMO energies of the alkyl halide correlated well with the experimental rate constants.

## 6.4 References

(1) Liptak, M. D.; Brunold, T. C. *J. Am. Chem. Soc.* **2006**, *128*, 9144.

(2) Masalha, R.; Chudakov, B.; Muhamad, M.; Rudoy, I.; Volkov, I.; Wirguin, I. *Israeli Medical Association Journal,* **2001**, *3*, 701.

(3) Sethi, N. K.; Robilotti, E.; Sadan, Y. *The Internet Journal of Nutrition and Wellness,* **2005**, *2*, 1.

(4) Jensen, K. P. *J. Phys. Chem. B,* **2005**, *109*, 10505.

(5) Alfonso-Prieto, M.; Biarnés, X.; Kumar, M.; Rovira, C.; Kozlowski, P. M. *J. Phys. Chem. B,* **2010**, *114*, 12965.

(6) Chen, S.-L.; Blomberg, M. R. A.; Siegbahn, P. E. M. *J. Phys. Chem. B.,* **2011**, *115*, 4066.

(7) Jensen, K. P.; Ryde, U. *j. Am. Chem. Soc.,* **2003**, *125*, 13970.

(8) Schrauzer, G. N.; Deutch, E. *J. Am. Chem. Soc.* **1969**, *91*, 12.

(9) Schrauzer, G. N.; Deutch, E.; Windgassen, R. J. *J. Am. Chem. Soc.* **1968**, *90*, 2441.

# CHAPTER 7

# Experimental and computational investigations into [Rh(acac)(CO)L] complexes

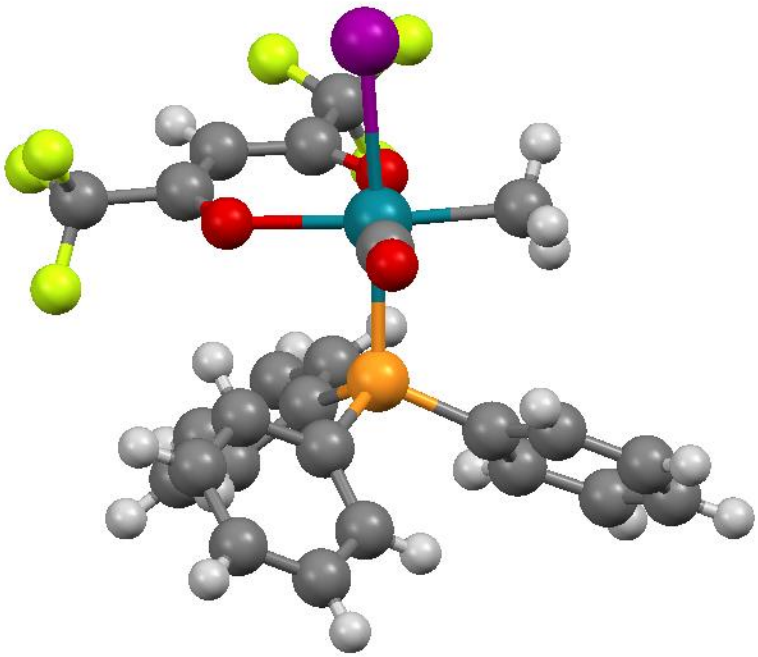

## 7.1 Introduction

The computational investigations in the preceding chapters established a general correlation between the DFT-calculated barrier heights and the experimental rate constants. The majority of experimental data for this has been taken from the literature. Therefore a series of complexes were investigated in our laboratory to undertake the same computational investigations to see whether similar trends were found. To do this, a series of rhodium-phosphine complexes were chosen containing an acetyl-acetonate (acac) ligand as shown in **Figure 7.1.** These complexes were selected as some data was already in the literature and they were simple to synthesize. This meant a large number of complexes could be investigated in a short space of time to generate the required data for further computational investigation.

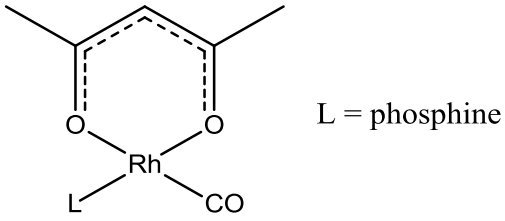


**Figure 7.1:** [Rh(acac)(CO)L] general structure

$[Rh(acac)(CO)_2]$, which is a precursor to the complexes shown in **Figure 7.1** was reported in 1964 by Bonita and Wilkinson.[1] The reaction of $[Rh(acac)(CO)(PPh_3)]$ with iodomethane was first investigated by Basson et al. and was found to have similar reactivity as $[RhI_2(CO)_2]^-$ towards iodomethane.[2] A detailed investigation into the reactivity of $[Rh(acac)(CO)(PPh_3)]$ was undertaken by Conradie et al.. The complex was found to react with iodomethane to form a mixture of Rh(III)-alkyl and Rh(III)-acyl species.[3] In subsequent publications, the reactions of various other phosphine containing complexes with iodomethane (L = $P(4\text{-}Cl\text{-}C_6H_4)_3$, $P(4\text{-}OMe\text{-}C_6H_4)_3$ and $P(4\text{-}Me\text{-}C_6H_4)_3$) were probed and shown to result in formation of both alkyl and acyl products.[4]

Brink et al. studied the sequential replacement of phenyl rings for cyclohexyl rings in $[Rh(acac)(CO)(PPh_nCy_{(3-n)})]$ (n = 0-3) and found a systematic increase in electron

density on the complex as evidenced by the carbonyl stretching frequency.[5] The rates of reaction with iodomethane follow the order $PCyPh_2 > PPh_3 \sim PCy_3 > PCy_2Ph$ due to a combination of electronic and steric effects. These complexes were found to undergo a series of isomerisations as summarized in **Scheme 7.1.**

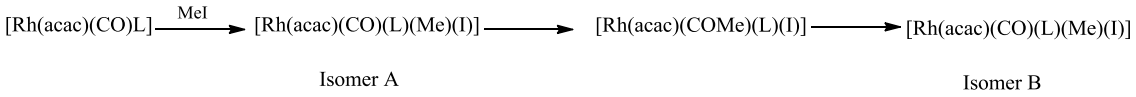


**Scheme 7.1:** Reaction of [Rh(acac)(CO)(L)] with iodomethane.

Various related complexes have also been investigated. Complexes bearing thioacetylacetonate (SacAc) ligands have been shown to react with iodomethane to form Rh(III) acyl species.[6,7] The reaction of [Rh(acac)(CO)L] complexes with iodomethane generally leads to the formation of multiple species. Modified complexes bearing two phosphite ligands were investigated as model complexes for the carbonyl complexes as isomerisation is less likely in the absence of a carbonyl ligand.[8-11] More recently, ferrocenyl-modified complexes have been investigated by Conradie et al., which proved to be extremely nucleophilic.[12,13] A modified complex where the phosphine was replaced with a carbene has also been investigated.[14]

Serron et al. investigated the enthalpy of the reaction of $[Rh(acac)(CO)_2]$ with various phosphine ligands and found they spanned a range of 12 kcal $mol^{-1}$. A good relationship was found between the ligand electronic parameter and the measured reaction enthalpy.[15,16]

Most recently, a comprehensive review of computational investigations on [Rh(acac)(CO)L] complexes has been presented.[17] Multiple geometric isomers were investigated for the reactants, transition states and products to gain more understanding on how the orientation of the ligands affects the energies of the complexes. Correlations between the experimental rate constants and DFT-calculated energies and charges were investigated with the hope of enabling the design of new complexes with specific reactivity.

In this chapter, the reactions of a number of [Rh(acac)(CO)L] complexes with iodomethane are probed. The effect of changing the β-diketonate ligand on the nucleophilicity of the complex is also investigated along with varying the alkyl iodide chain length.

## 7.2 Synthesis and characterization of [Rh(acac)(CO)L] complexes

Synthesis of the Rh(I) complexes was achieved by substitution of a carbonyl ligand from $[Rh(acac)(CO)_2]$ according to **Scheme 7.2**.

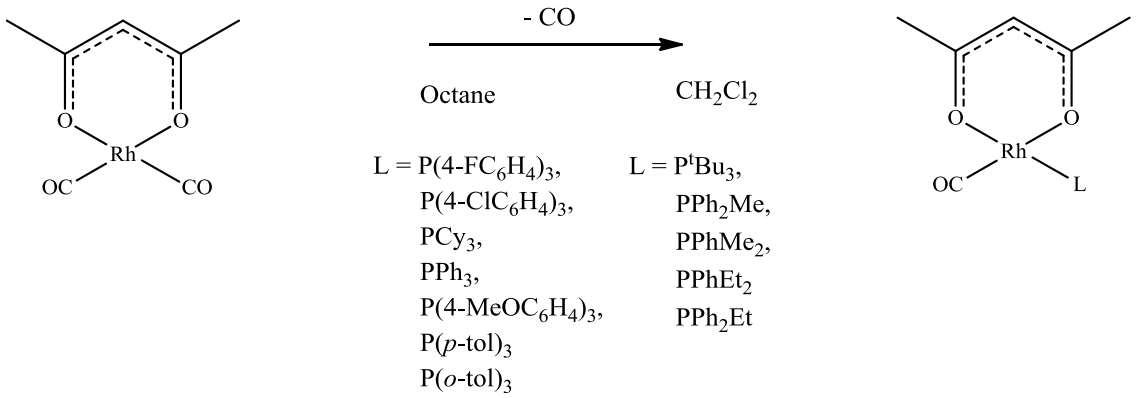


**Scheme 7.2:** General synthesis of [Rh(acac)(CO)L] complexes

The phosphines $PMe_3$ and $PEt_3$ are pyrophoric and difficult to handle. Hence an alternative preparation was employed for the complexes bearing these ligands using the appropriate $HBF_4$ salt of the free phosphine according to **Scheme 7.3.**

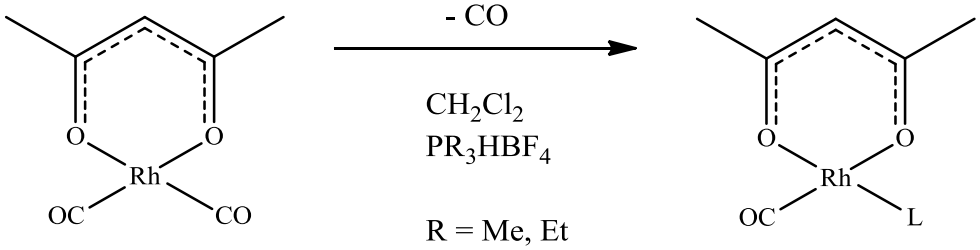


**Scheme 7.3:** Synthesis of $[Rh(acac)(CO)(PR_3)]$ (R = Me, Et)

Selected spectroscopic data for the complexes are presented in **Table 7.1**. For each complex, a single ν(CO) band is observed in the IR spectrum. For the series based upon systematic changes at the 4-position of the rings on triphenylphosphine there is a decrease in ν(CO) Cl>F>H>Me~OMe consistent with increasing electron density at the metal center. As the phenyl groups in triphenyl phosphine are systematically replaced with methyl or ethyl groups, so the ν(CO) of the complex decreases, again consistent with a more electron rich metal center.

| L | Complex | ν(CO) / $cm^{-1}$ ($CH_2Cl_2$) | δ $^{31}P$ ($J_{Rh-P}$ / Hz) | δ $^{1}H$ |
|---|---|---|---|---|
| $PPh_3$ | **1a** | 1977 | 48.7 (176) | 1.60, 2.08, 5.42 |
| $PPh_2Me$ | **1b** | 1975 | 33.9 (170) | 1.80, 1.95, 5.31 |
| $PPhMe_2$ | **1c** | 1970 | 19.8 (167) | 1.90, 2.10, 5.49 |
| $PMe_3$ | **1d** | 1967 | 10.2 (160) | 1.93, 2.07, 5.47 |
| $PPh_2Et$ | **1e** | 1973 | 46.2 (173) | 1.87, 2.09 5.48 |
| $PPhEt_2$ | **1f** | 1968 | 44.3 (168) | 1.88, 2.10, 5.49 |
| $PEt_3$ | **1g** | 1963 | 44.6 (163) | 1.77, 1.91, 5.31 |
| P(*o*-tol)$_3$ | **1h** | 1973 | 44.9 (173) | 1.38, 1.96, 5.28 |
| P(*p*-tol)$_3$ | **1i** | 1973 | 46.1 (175) | 1.66, 2.11, 5.44 |
| P(4-$FC_6H_4$)$_3$ | **1j** | 1980 | 46.6 (175) | 1.66, 2.12, 5.47 |
| P(4-$ClC_6H_4$)$_3$ | **1k** | 1982 | 47.6 (178) | 1.67, 2.13, 5.47 |
| P(*p*-anisyl)$_3$ | **1l** | 1973 | 44.1 (174) | 1.66, 2.22, 5.44 |
| P(4-$CF_3C_6H_4$)$_3$ | **1m** | 1985 | 50.1 (178) | 1.63, 2.14, 5.51 |
| P(*o*-anisyl)$_3$ | **1n** | 1969 | 33.1 (180) | 1.60, 2.10, 5.40 |
| PPh(*o*-anisyl)$_2$ | **1o** | 1972 | 36.7 (179) | 1.60, 2.10, 5.50 |
| $PPh_2$(*o*-anisyl) | **1p** | 1974 | 41.2 (178) | 1.70, 2.10, 5.40 |
| $PCy_3$ | **1q** | 1960 | 58.5 (167) | 1.86, 2.05, 5.43 |
| $P^tBu_3$ | **1r** | 1960 | 100.2 (179) | 1.76, 1.89, 5.39 |
| $PCy_2Ph$ | **1s** | 1967 | 58.8 (168) | 1.81, 2.09, 5.46 |
| $PCyPh_2$ | **1t** | 1971 | 53.3 (171) | 1.77, 2.05, 5.44 |

**Table 7.1:** Summary of selected spectroscopic data for [Rh(acac)(CO)L] complexes.

Each complex showed a doublet in the $^{31}P\{^{1}H\}$ NMR with a $J_{Rh-P}$ coupling constant typical of Rh(I) complexes. The methyl substituents on the acac ligand are chemically equivalent in $[Rh(acac)(CO)_2]$. The substitution of one carbonyl ligand with a phosphine leads to these environments being chemically inequivalent and two singlets are observed in the $^{1}H$ NMR spectrum. The backbone methine proton appears as a singlet typically between 5.28 and 5.51 ppm. In the $^{13}C$ NMR spectrum the acac methyl groups also give two signals, one of which is a doublet due to coupling to $^{31}P$. The carbonyl carbon is observed as a doublet of doublets due to coupling to $^{31}P$ and $^{103}Rh$. **Figures 7.2** and **7.3** show the $^{1}H$, $^{31}P$ and $^{13}C$ NMR spectra for $[Rh(acac)(CO)(PMe_3)]$.

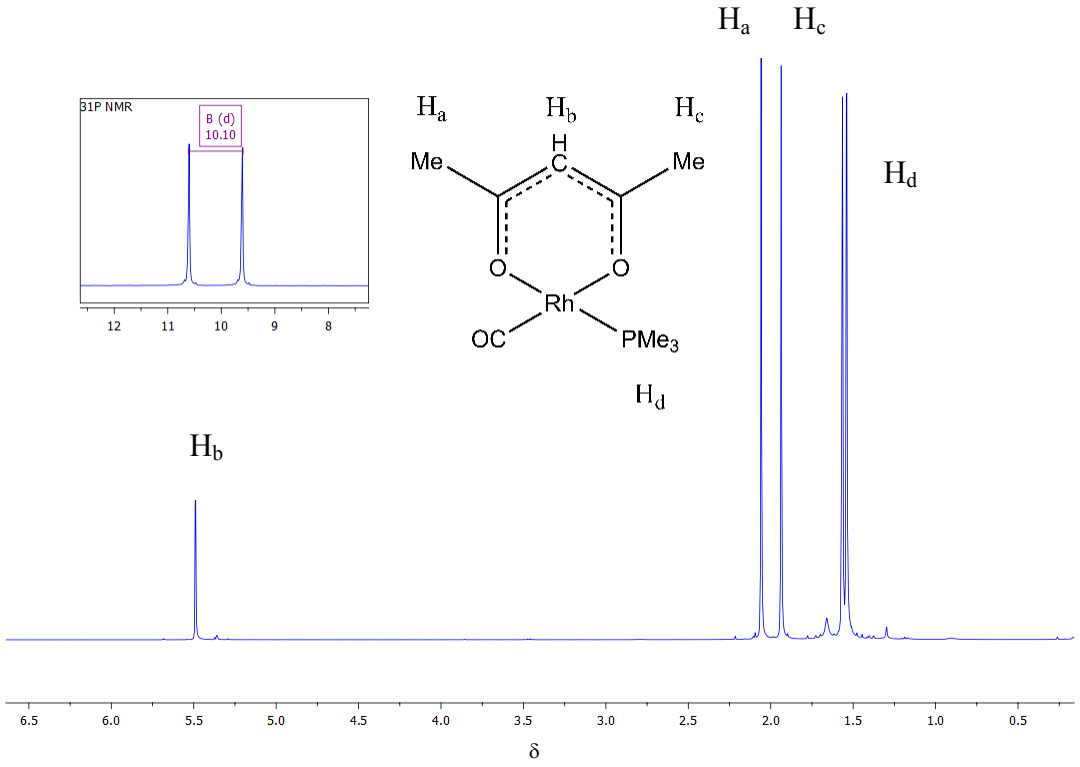


**Figure 7.2:** $^{1}H$ and $^{31}P$ NMR (inset) spectra of $[Rh(acac)(CO)(PMe_3)]$ ($CD_2Cl_2$)

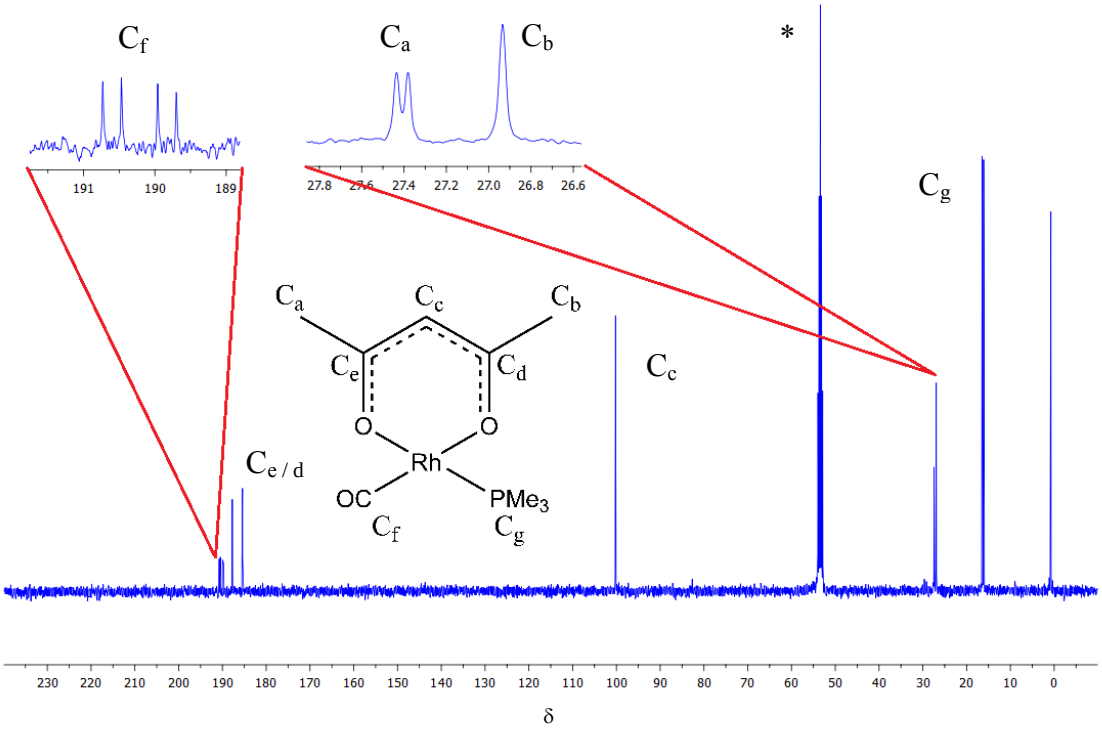


**Figure 7.3:** $^{13}C\{^{1}H\}$ NMR spectrum of [Rh(acac)(CO)($PMe_3$)] (*$CD_2Cl_2$)

A crystal suitable for X-ray diffraction was obtained for [Rh(acac)(CO)P(*o*-tol)$_3$] by slow evaporation of octane into a concentrated $CH_2Cl_2$ solution. **Figure 7.4** shows the crystal structure and selected bond lengths and angles are given in **Table 7.2**. There are two unique molecules in the unit cell. The complex adopts a square-planar geometry. Related structures have been reported with similar Rh-P bond lengths ($PCy_3$ – 2.254 Å, $PCy_2Ph$ – 2.242 Å, $PCyPh_2$ – 2.232 Å, $PPh_3$ – 2.241 Å).[5]

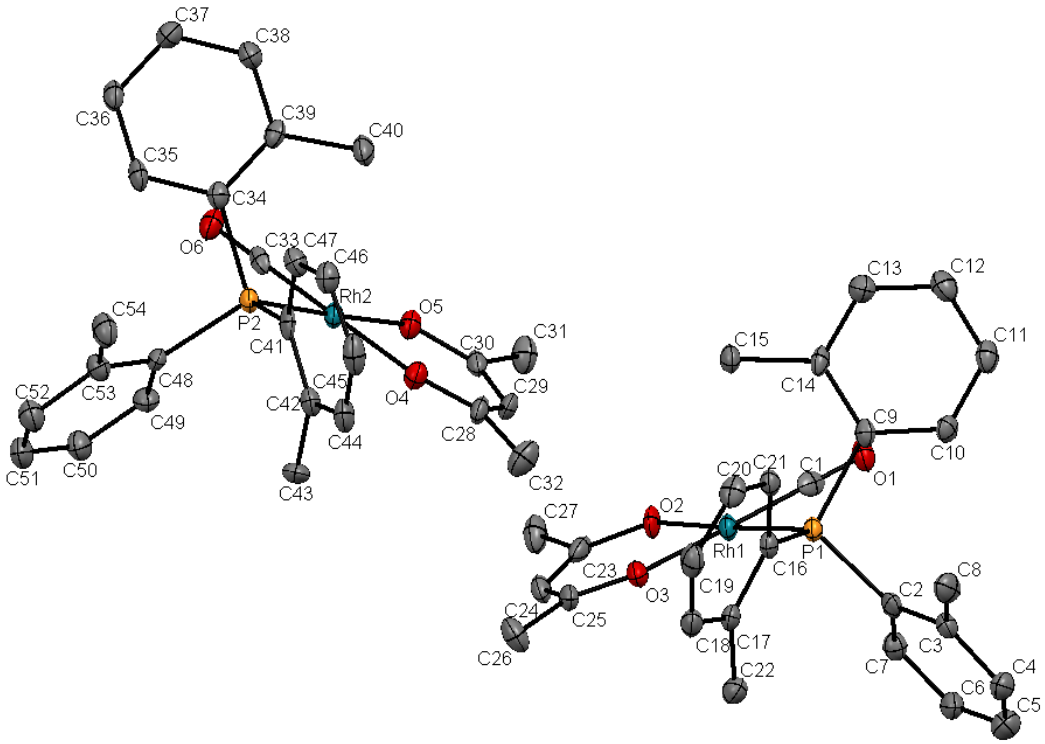


**Figure 7.4:** Crystal structure of **1h**. Hydrogen atoms omitted for clarity.

| Molecule A | Length / Å | Molecule B | Length / Å |
|---|---|---|---|
| **Rh(1) – P(1)** | 2.261(1) | **Rh(2) – P(2)** | 2.259(2) |
| **C(1) – O(1)** | 1.143(7) | **C(28) – O(4)** | 1.160(7) |
| **Rh(1) – C (1)** | 1.824(6) | **Rh(2) – C (33)** | 1.805(6) |
| **Rh(1) – O(2)** | 2.039(4) | **Rh(2) – O(4)** | 2.053(4) |
| **Rh(1) – O(3)** | 2.088(4) | **Rh(2) – O(5)** | 2.079(4) |
| | **Angle / °** | | **Angle / °** |
| **O(2) – Rh(1)-O(3)** | 89.64(15) | **O(4) – Rh(1)- O(5)** | 89.24(15) |
| **O(2) – Rh(1)- P(1)** | 177.85(12) | **O(5) – Rh(1)- P(2)** | 177.80(11) |

**Table 7.2:** Selected bond distances and angles in **1h**

**Figure 7.5** illustrates two complexes bearing different β-diketonate ligands, which were investigated in this study: 2,2,6,6-tetramethylheptane-3,5-dione (**$^t$Bu-acac**) and hexafluoroacetylacetone (**$CF_3$-acac**). The complexes were synthesized by addition of two equivalents of the β-diketone and NaOEt to trans-$[Rh(\mu{-}Cl)(CO)(PPh_3)]_2$ in $CH_2Cl_2$. Selected spectroscopic data are presented in **Table 7.3.**

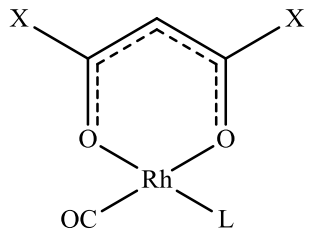


X = $CF_3$ **(1u)**, $^t$Bu **(1v)**

**Figure 7.5:** Structures of modified [Rh(β-diketonate)(CO)L] complexes

| X | Complex | L | ν(CO) / $cm^{-1}$ ($CH_2Cl_2$) | δ $^{31}$P ($J_{Rh-P}$ / Hz) | δ $^1$H |
|---|---|---|---|---|---|
| $CH_3$ | **1a** | $PPh_3$ | 1977 | 48.7 (176) | 5.42 |
| $^t$Bu | **1u** | $PPh_3$ | 1977 | 47.4 (175) | 5.81 |
| $CF_3$ | **1v** | $PPh_3$ | 1997 | 47.8 (178) | 6.25 |

**Table 7.3:** Summary of selected spectroscopic data for [Rh(β -diketone)(CO)L] complexes.

The replacement of methyl groups **(1a)** with *tert*-butyl groups **(1u)** does not affect the ν(CO) value, whereas the introduction of trifluoro-methyl groups raises the ν(CO) by 20 $cm^{-1}$ due to the electron withdrawing effect of the fluorine atoms.

## 7.3 Reactions of [Rh(acac)(CO)L] with MeI

### 7.3.1 [Rh(acac)(CO)($PMe_3$)] (1d) and [Rh(acac)(CO)($PEt_3$)] (1g)

Complexes **1d** and **1g** react with iodomethane to form Rh(III)-alkyl species according to **Scheme 7.4.** Selected spectroscopic data for **2d** and **2g** are given in **Table 7.4.** Both products show a doublet in the $^{31}P\{^1H\}$ NMR and a ν(CO) band at higher frequency consistent with the formation of a Rh(III) species. There is no evidence for migratory insertion to form an acetyl species in contrast to examples reported previously with other phosphine ligands.

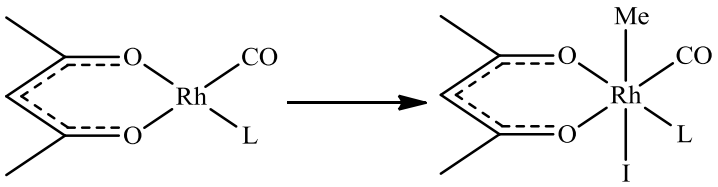


**1d, 1g** **2d, 2g**

**Scheme 7.4:** Reaction of **1d** and **1g** with iodomethane.

| Complex | ν(CO) / cm$^{-1}$ ($CH_2Cl_2$) | δ $^{31}$P ($J_{Rh-P}$ / Hz) | δ $^{1}$H |
|---|---|---|---|
| **2d** | 2063 | 16.4 (117) | 1.99, 2.07, 5.46 |
| **2g** | 2060 | 41.4 (116) | 1.78, 1.89, 5.28 |

**Table 7.4:** Summary of principal spectroscopic data for **2d** and **2g**.

**Figure 7.6** shows the $^{1}$H and $^{31}$P (inset) NMR spectra for **2d.** The acac - methine and methyl protons are at a higher chemical shift than in **1d.** A triplet was observed for the Rh-Me protons at 1.38 ppm (1.9 Hz). A doublet of doublets would normally be expected due to coupling to $^{31}$P and to $^{103}$Rh. A further $^{1}$H NMR spectrum was acquired with phosphorus decoupling which resulted in this resonance collapsing to a doublet. The observed triplet arises due to the similar values of $J_{Rh-H}$ and $J_{H-P}$.

**Figure 7.7** shows the $^{13}$C NMR spectrum for **2d**. The signal for the Rh-Me carbon appears as a doublet of doublets at δ 14.91 ($J_{C-Rh}$ = 20.3, $J_{C-P}$ = 4.3 Hz) and the terminal CO ligand also gives a doublet of doublets at 185.61 ($J_{C-P}$ = 64.1, $J_{C-Rh}$ = 20.0 Hz).

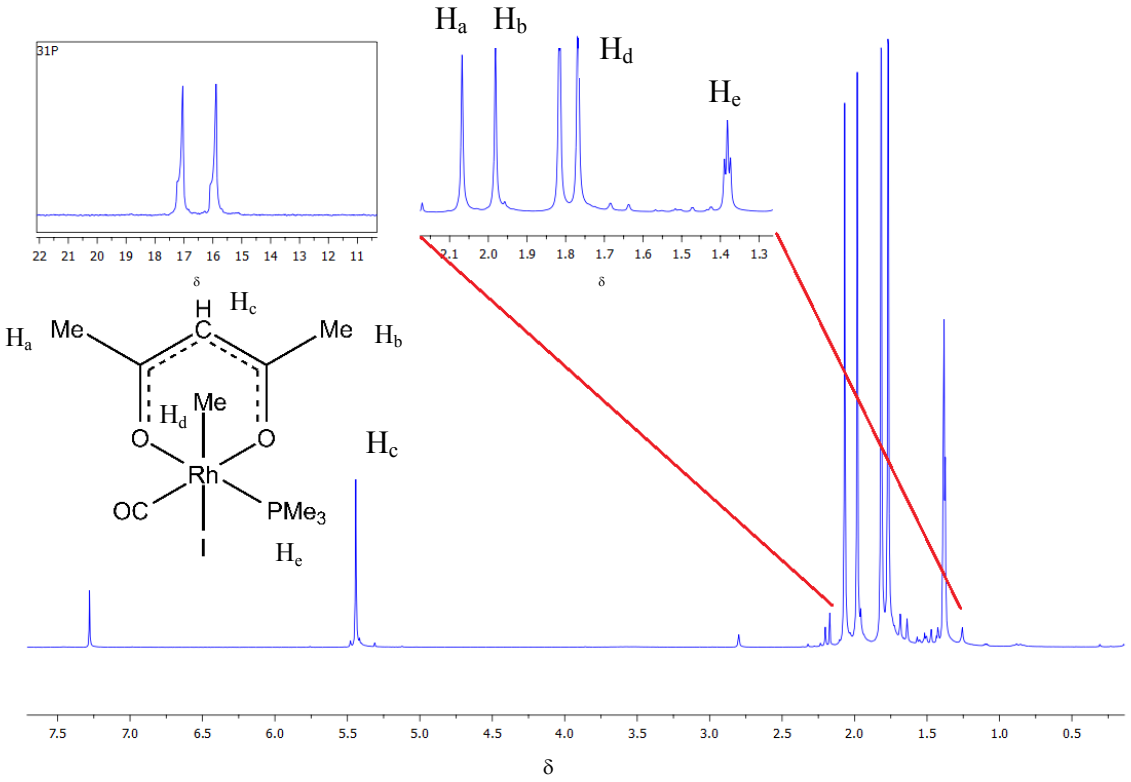


**Figure 7.6:** $^{1}H$ and $^{31}P$ (inset) NMR spectra of **2d** ($CD_2Cl_2$)

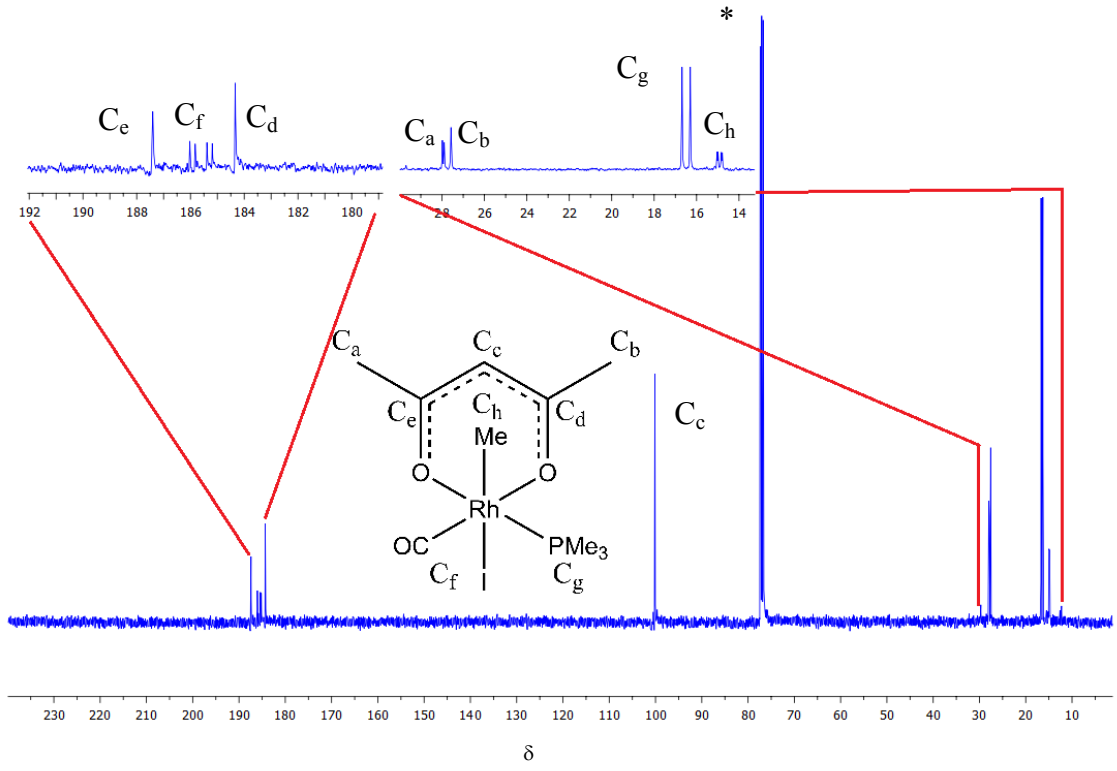


**Figure 7.7:** $^{13}C\{^{1}H\}$ NMR spectrum of **2d** (*$CD_2Cl_2$)

Crystals of **2d** suitable for X-ray diffraction were grown by slow evaporation of diethyl ether into a concentrated $CH_2Cl_2$ solution of the complex. The structure shown in **Figure 7.8** confirms that the complex is indeed a Rh(III) alkyl species with the methyl and iodide ligands mutually trans. Selected bond lengths and angles are given in **Table 7.5.**

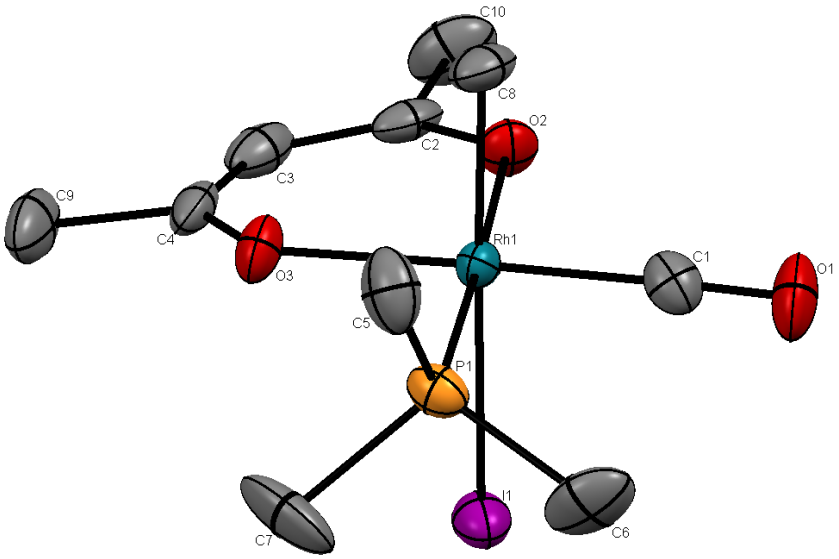


**Figure 7.8:** Crystal structure of **2d**. Hydrogen atoms omitted for clarity.

| | **Length / Å** | | **Length / Å** |
|---|---|---|---|
| **Rh(1) – P(1)** | 2.263(2) | **Rh(1) – C (8)** | 2.094(7) |
| **Rh(1) – I(1)** | 2.8102(6) | **Rh(1) – C (1)** | 1.826(6) |
| **Rh(1) – O(2)** | 2.091(4) | **C(1) – O(1)** | 1.144(8) |
| **Rh(1) – O(3)** | 2.034(5) | | |
| | **Angle / °** | | **Angle / °** |
| **O(3) – Rh(1)- C(1)** | 176.78(2) | **O(1) – Rh(1)- O(2)** | 90.86(17) |
| **O(2) – Rh(1)- P(1)** | 177.92(13) | **C(8) – Rh(1)- I(1)** | 176.49(19) |

**Table 7.5:** Selected bond distances and angles in **2d**

### 7.3.2 Complexes bearing aryl phosphines

The detailed reaction mechanism of the $PPh_3$ complex **1a** with MeI was investigated by Conradie et al.. Initially, oxidative addition of iodomethane leads to the formation of a Rh(III)-alkyl complex with iodide and methyl mutually trans. Subsequent methyl migration forms a Rh(III)-acyl species. This acyl complex was found to undergo migratory deinsertion to form a more stable Rh(III)-alkyl complex

The reactions of the complexes **1a-1w** with MeI were carried out under Schlenk conditions and monitored periodically by IR spectroscopy. Similar studies were also conducted and monitored by $^{31}P\{^1H\}$ and $^1H$ NMR where a sample of complex (typically around 15 – 20 mg) was dissolved in a 0.16 M MeI in $CDCl_3$ solution and monitored periodically until no further changes were observed. The numbering scheme used for the isomeric products is shown in **Scheme 7.5.**

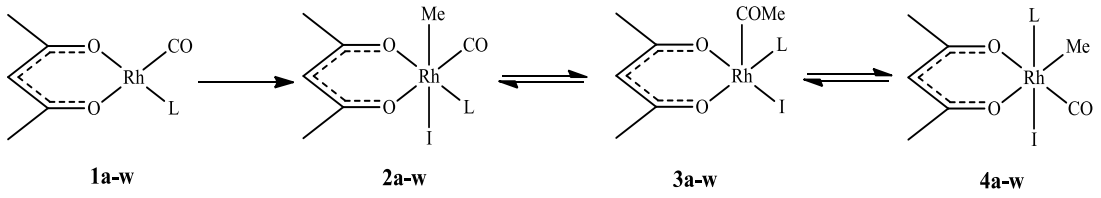


**1a-w** **2a-w** **3a-w** **4a-w**

**Scheme 7.5:** Proposed mechanism of iodomethane reaction with a rhodium acetylacetonate complex.

### 7.3.3 P(4-X-$C_6H_4$) series (x= F, Cl, H, OMe, Me)

For the series based upon changes at the 4-position in triphenyl phosphine a mixture of products is observed in each case upon reaction of the complex with iodomethane **Figure 7.9** shows a series of spectra for the reaction of **1i** with 0.16 M MeI. Initially, disappearance of the Rh(I) starting material (δ 47.55, $J_{Rh-P}$ = 178 Hz) is observed accompanied by the rapid growth of an alkyl species (δ 31.6, $J_{Rh-P}$ = 126 Hz). A corresponding $^1H$ resonance is observed as a triplet at δ 1.36 assigned to the Rh-Me protons. As the peak for the alkyl species increases in intensity a doublet is observed (δ 35.54, $J_{Rh-P}$ = 155 Hz) which is assigned to an acyl species. A singlet is observed in the $^1H$ NMR spectrum at 2.95 ppm for the acetyl protons. As these two species reach

maximum intensity, a second alkyl species is also observed to form (δ 24.82, $J_{Rh-P}$ = 119 Hz) with a corresponding doublet of doublets in the $^{1}$H NMR spectrum at δ 1.64 ppm. The monitoring was continued for 24 hours but no further changes were observed.

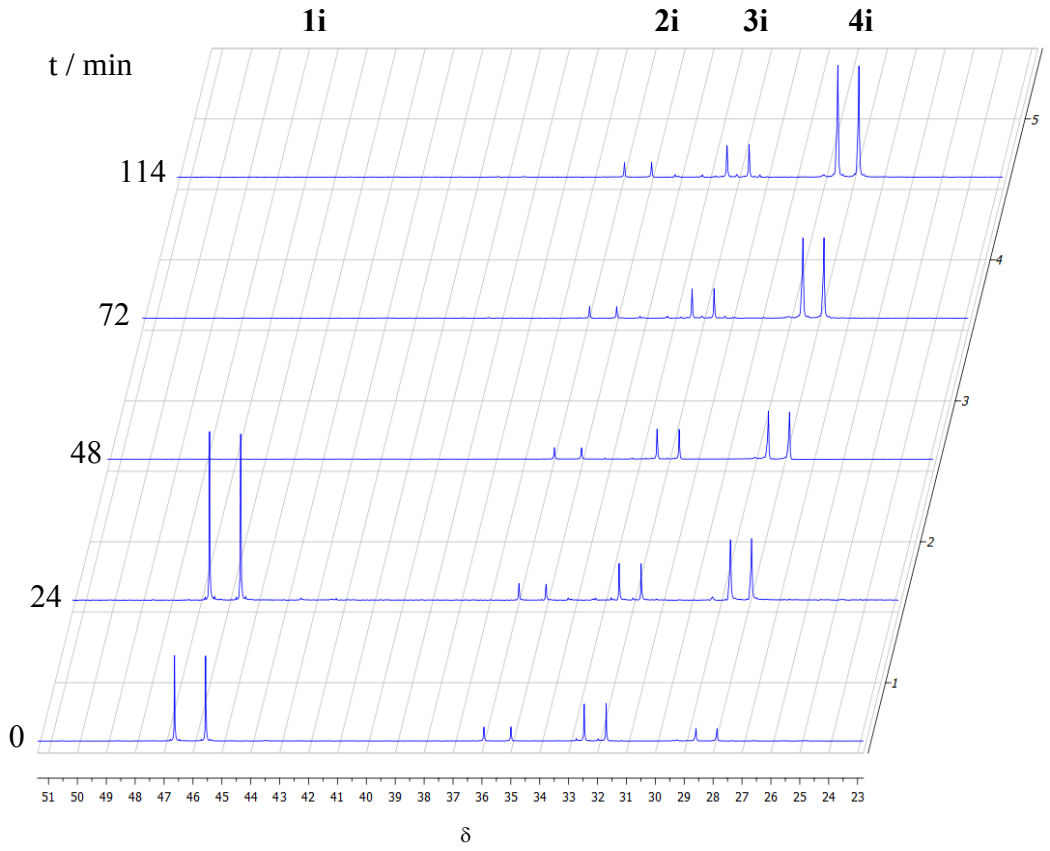


**Figure 7.9:** $^{31}$P{$^{1}$H}-NMR spectra recorded during the reaction of [Rh(acac)(CO)P(*p*tol)$_3$] **(1i)** with MeI [MeI] = 0.16 M.

Similar behavior is observed for each complex in this series giving two rhodium(III) alkyl species and one rhodium(III) acyl species based upon the spectroscopic data. The relative intensities at equilibrium are given in **Table 7.6.** As the donor strength of the phosphine increases the relative percentage of the alkyl isomer, **4,** increases and the percentage of **2** and **3** observed decreases.

| | | Product Distribution / % | | |
|---|---|---|---|---|
| **Reactant Complex** | **L** | **2** | **3** | **4** |
| **1m** | $P(4\text{-}CF_3C_6H_4)_3$ | 18 | 74 | 9 |
| **1k** | $P(4\text{-}ClC_6H_4)_3$ | 30 | 55 | 14 |
| **1j** | $P(4\text{-}FC_6H_4)_3$ | 30 | 54 | 15 |
| **1a** | $PPh_3$ | 14 | 13 | 73 |
| **1l** | $P(4\text{-}OMeC_6H_4)_3$ | 18 | 7 | 75 |
| **1i** | $P(4\text{-}MeC_6H_4)_3$ | 17 | 6 | 76 |

**Table 7.6:** Relative product abundance at the end of the reactions of [Rh(acac)(CO)L] complexes with MeI for para-substituted $PAr_3$.

### 7.3.4 [Rh(acac)(CO)$PPh_{(3-x)}R_{(x)}$] x = 0,1,2,3 R = Me, Et

The effect on the product distribution of sequentially replacing phenyl rings in $PPh_3$ by alkyl groups is shown in **Table 7.7.** The formation of acetyl **(3)** and alkyl isomer **(4)** is only observed for L = $PPh_3$ **(1a)** and $PPh_2Me$ **(1b).** No further isomerisation is observed for the remaining complexes after initial oxidative addition.

| | | Product Distribution / % | | |
|---|---|---|---|---|
| **Reactant Complex** | **L** | **2** | **3** | **4** |
| **1g** | $PEt_3$ | 100 | 0 | 0 |
| **1f** | $PPhEt_2$ | 100 | 0 | 0 |
| **1a** | $PPh_3$ | 14 | 13 | 73 |
| **1c** | $PPhMe_2$ | 100 | 0 | 0 |
| **1b** | $PPh_2Me$ | 62 | 22 | 16 |
| **1d** | $PMe_3$ | 100 | 0 | 0 |

**Table 7.7:** Relative product abundance at the end of the reactions of [Rh(acac)(CO)L] complexes with MeI.

### 7.3.5 [Rh(acac)(CO)(P*o*-tol$_3$)] (1h) and [Rh(acac)(CO)(P$^t$Bu$_3$)] (1r)

**Figure 7.10** shows that the $^{31}P\{^1H\}$ NMR study of the reaction of **1h** and MeI did not follow the same pattern that was observed for the other cases. A doublet was initially observed growing in at δ 30.49 with a coupling constant of 156 Hz, indicating a rhodium phosphine species. At the same time a singlet was observed at δ -29.60 which is consistent with the free ligand. Over 2 days the relative abundance of the doublet at δ 30.49 did not increase significantly but further singlets were observed at δ 37.03 and δ 21.67 and are assigned to the oxidized and methylated phosphine respectively.

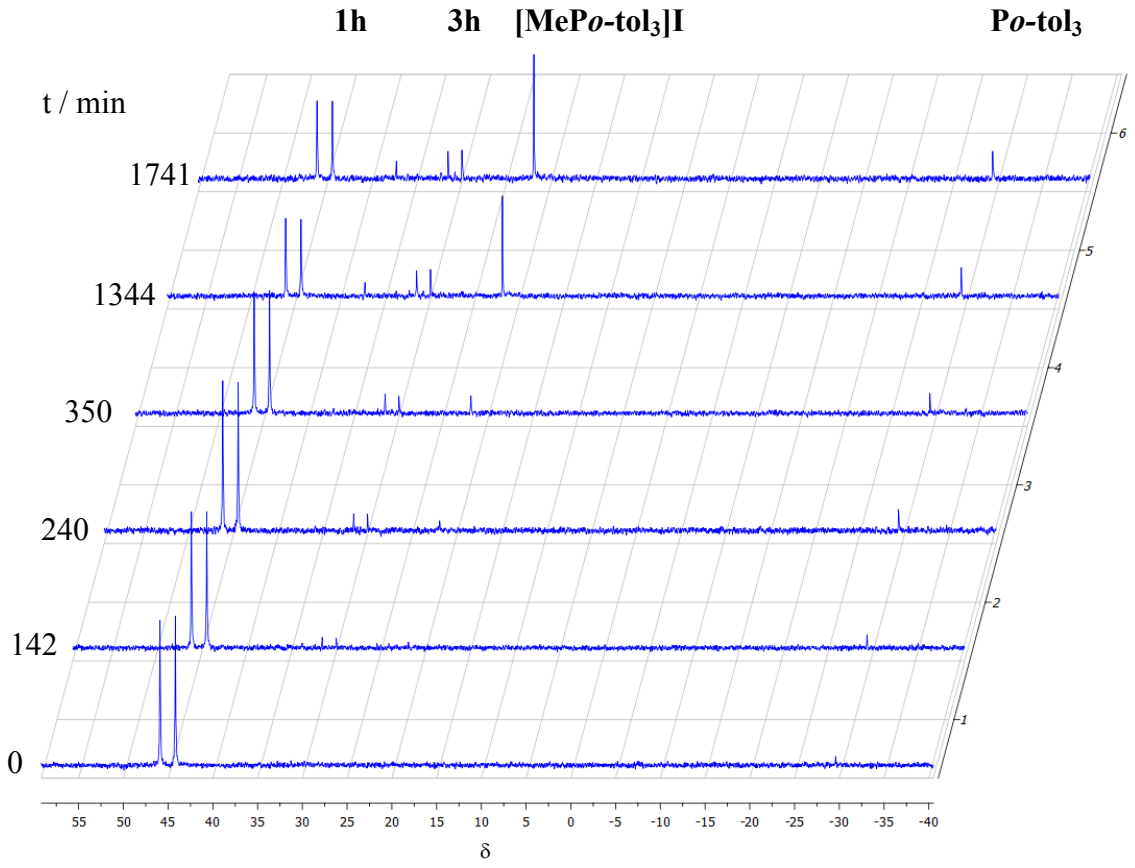


**Figure 7.10:** $^{31}P\{^1H\}$ NMR spectra for the reaction between **1h** and MeI. [MeI] = 0.16 M in $CDCl_3$.

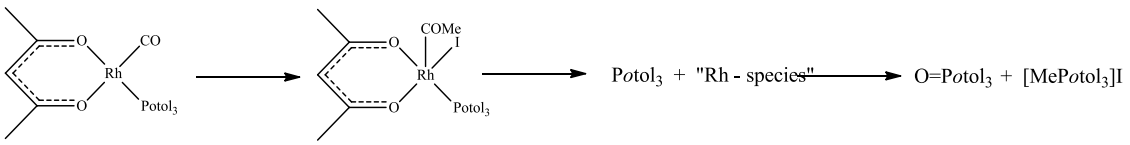


**Scheme 7.6:** Proposed decomposition pathway for the reaction of **1h** with MeI.

Based on these observations, the reaction shown in **Scheme 7.6** is proposed. The initial formation of a doublet in the $^{31}P\{^{1}H\}$ NMR suggests that the mechanism does proceed by nucleophilic attack of the metal on iodomethane and not by quarternisation of the phosphine. The singlet due to the free phosphine only grows once the doublet for the rhodium(III) species has built up. The free phosphine then undergoes subsequent reactions with either oxygen or iodomethane.

DFT calculations on **2h** indicated a Rh-P distance of 2.46 Å which is appreciably longer than the computed bond lengths for any other complex in this series (2.29 – 2.33 Å). It is also longer than the experimental value observed for **2d** which was 2.263 Å. This suggests that the steric bulk of the P(*o*tol)$_3$ ligand may increase its lability.

The reaction of **1r** with iodomethane proceeded very slowly with complete conversion only being observed when the reaction was left overnight. The IR spectrum showed a ν(CO) band at 2038 cm$^{-1}$. The $^{31}P\{^{1}H\}$ NMR spectrum contained a singlet at 50.4 ppm consistent with the phosphine no longer being attached to the rhodium centre which would present as a doublet. It is clear that the complex undergoes a decomposition reaction similar to that observed for **1h** and hence it was not further investigated.

### 7.3.6 Reactions of modified β-diketonato complexes with MeI

Spectroscopic data for the reactions of **1u** and **1v** with iodomethane are given in **Table 7.8**. Complex **1u** reacts with iodomethane to form a mixture of products assigned as an acyl and two alkyl species respectively by analogy to **1a**.

| Reactant Complex | β-diketonate | ν(CO) / cm$^{-1}$ $CH_2Cl_2$ | δ $^{31}$P ($J_{Rh-P}$ / Hz) |
|---|---|---|---|
| **1u** | $^{t}$Bu-acac | 2072, 2048, 1720 | 36.7 (154), 31.3 (125), 26.76 (121) |
| **1v** | $CF_3$-acac | 2071 | 26.6 (111) |

**Table 7.8:** Summary of principal spectroscopic data for reactions of **1u** and **1v** with MeI.

The reaction of **1v** with iodomethane yielded a product with a ν(CO) band at 2071 $cm^{-1}$ and a doublet in the $^{31}P\{^{1}H\}$spectrum at (δ 26.58, $J_{Rh-P}$ = 111 Hz). No acyl species was observed. The $^{1}H$ NMR spectrum contained a doublet of doublets for the methyl ligand at δ 1.98 ($J$ = 4.0, 1.9 Hz).

Crystals suitable for X-ray analysis were grown by slow evaporation of octane into a concentrated $CH_2Cl_2$ solution. The structure is shown in **Figure 7.11** and selected bond lengths and angles are given in **Table 7.9.** There are two unique molecules within the unit cell and some disorder of the fluorine atoms is noted.

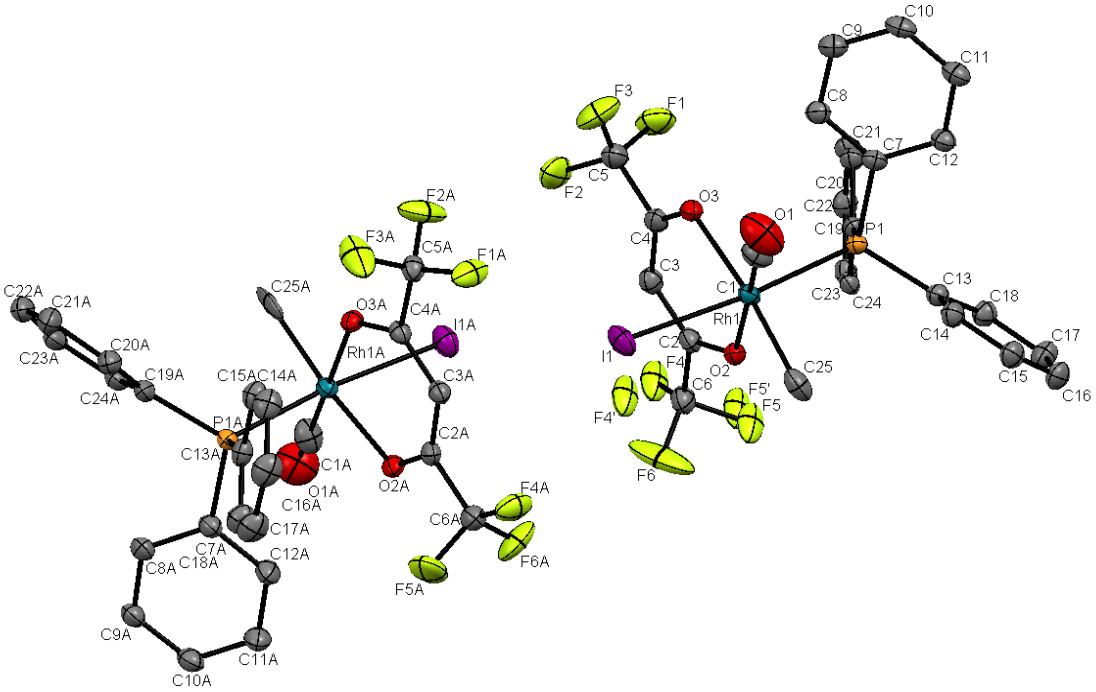


**Figure 7.11:** Crystal structure of **4v.** Hydrogen atoms are omitted for clarity.

| Molecule A | Length / Å | Molecule B | Length / Å |
|---|---|---|---|
| **Rh(1) – P(1)** | 2.345(1) | **Rh1A – P1A** | 2.347(1) |
| **Rh(1) – I(1)** | 2.6933(5) | **Rh1A – I1A** | 2.7012(5) |
| **Rh(1) – O(2)** | 2.078(3) | **Rh1A – O2A** | 2.177(3) |
| **Rh(1) – O(3)** | 2.203(3) | **Rh1A – O3A** | 2.091(3) |
| **Rh(1) – C(25)** | 2.091(5) | **Rh1A – C25A** | 2.091(5) |
| **Rh(1) – C(1)** | 1.833(5) | **Rh1A – C1A** | 1.812(6) |
| **C(1) – O(1)** | 1.115(7) | **C1A – O1A** | 1.114(8) |

| | Angle / ° | | Angle / ° |
|---|---|---|---|
| **O(3) – Rh(1)- O(2)** | 86.77() | **O2A – Rh1A- O3A** | 87.08() |
| **I(1) – Rh(1)- P(1)** | 174.70() | **I1A – Rh1A- P1A** | 174.20() |

**Table 7.9:** Selected bond distances and angles in **4v**

The structure reveals an isomerized methyl complex **4v** in which the methyl and phosphine ligands have exchanged positions relative to the presumed initial oxidative addition product with methyl *trans* to iodide.

### 7.3.7 [Rh(acac)(CO)PPh$_{(3-x)}$oAn$_{(x)}$] x = 1,2,3

The reactivity of complexes **1n-1p** containing phosphines with ortho-anisyl substituents were investigated by Claire John as part of a fourth year project and are reported here for comparison.[18] They react with MeI to form one species in each case with a ν(CO) band between 1695 and 1710 cm$^{-1}$. The $^{31}P\{^{1}H\}$ NMR spectrum showed one doublet for each complex. (**Table 7.11**) Such data is consistent with the formation of acyl complexes. In contrast to other similarly reactive complexes in this study, these three complexes undergo rapid migratory insertion presumably facilitated by the coordination of the pendant methoxy groups on the phenyl rings. (**Scheme 7.7**) A rhodium-oxygen interaction was confirmed by X-ray analysis of a suitable crystal of **3p** grown from slow evaporation of diethyl ether into a concentrated $CH_2Cl_2$ solution.

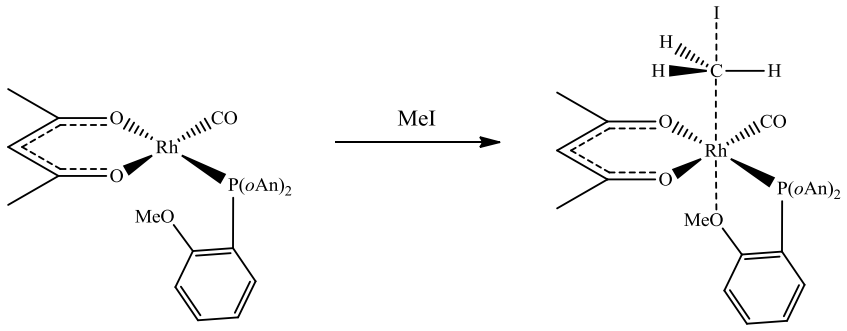


**Scheme 7.7:** Proposed stablilisation of the transition state by the pendent methoxy group.

| Reactant Complex | ν(CO) / cm$^{-1}$ ($CH_2Cl_2$) | δ $^{31}$P ($J_{Rh-P}$ / Hz) |
|---|---|---|
| **1n** | 1710 | 22.4 (156) |
| **1o** | 1705 | 30.5 (165) |
| **1p** | 1695 | 32.6 (154) |

**Table 7.10:** Summary of selected spectroscopic data for reactions of **1m, 1n** and **1o** with iodomethane.

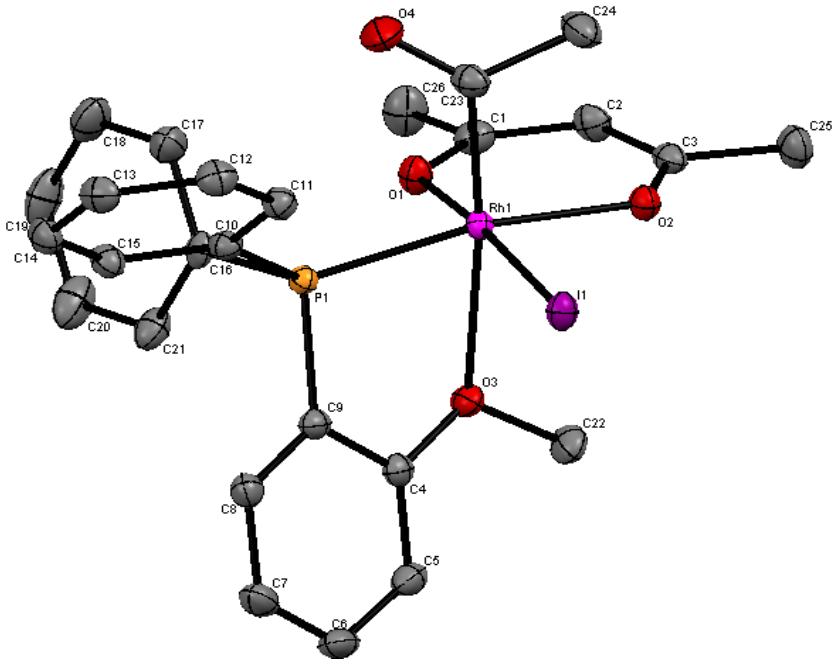


**Figure 7.12**. Crystal structure of **3p**. Hydrogen atoms are omitted for clarity.

| | Length / Å | | Length / Å |
|---|---|---|---|
| **Rh(1) – P(1)** | 2.249(4) | **Rh(1) – C (23)** | 2.091(1) |
| **Rh(1) – I(1)** | 2.639(2) | **Rh(1) – O(2)** | 2.077(1) |
| **Rh(1) – O(3)** | 2.430(1) | **Rh(1) – O(1)** | 2.032(1) |
| | **Angle / °** | | **Angle / °** |
| **O(1) – Rh(1)-O(3)** | 90.63() | **O(1) – Rh(1)- I(1)** | 173.75() |
| **O(2) – Rh(1)- P(1)** | 166.94() | **O(3) – Rh(1)- C(23)** | 173.36() |

**Table 7.11:** Selected bond distances and angles in **3p**

The crystal structure in **Figure 7.12** shows an interaction between the methoxy group on the ligand and the rhodium centre. In contrast to many of the other complexes in this study, these complexes do not show any tendency to undergo migratory de-insertion to form a further alkyl species. This is attributed to the rhodium oxygen interaction in the acyl species which would need to be overcome before any deinsertion could occur.

## 7.4 Oxidative addition kinetics

For most of the complexes, kinetic data for the reaction with iodomethane were obtained using infra-red spectroscopy to monitor the decay of the ν(CO) band of the reactant. Pseudo first-order conditions were maintained throughout by ensuring the concentration of methyl iodide was at least ten times that of the reactant complex. The complexes fell into two broad categories – those which formed a single Rh(III) species and those which formed multiple isomers. **Figure 7.13** shows a series of spectra for reaction of **1d** with 0.008 M MeI. A typical series of spectra showing multiple isomer formation is shown in **Figure 7.14** for the reaction of **1i** with 0.16 M MeI.

Kinetic data for the reactions of **1n-1p** were obtained using UV-Vis-spectroscopy by monitoring the decay at 300, 305 and 302 nm for **1n, 1o** and **1p** respectively. Plots of absorbance *vs.* time were well fitted by exponential decay curves ($R^2 > 0.99$ in each case) showing that the reactions are first order in Rh(I) complex. An example kinetic plot for this type of reaction is shown in **Figure 7.15.** Plots of $k_{obs}$ *vs.* [MeI] were linear indicating that the reactions are first order in [MeI] and thus second order overall. An example is shown in **Figure 7.15.** Values of $k_{obs}$ are listed in the appendix. Values of second order rate constants and activation parameters from Eyring plots for these reactions are given in **Table 7.12.** The activation entropies are all large and negative which is typical for such reactions proceeding via an $S_N2$ mechanism.

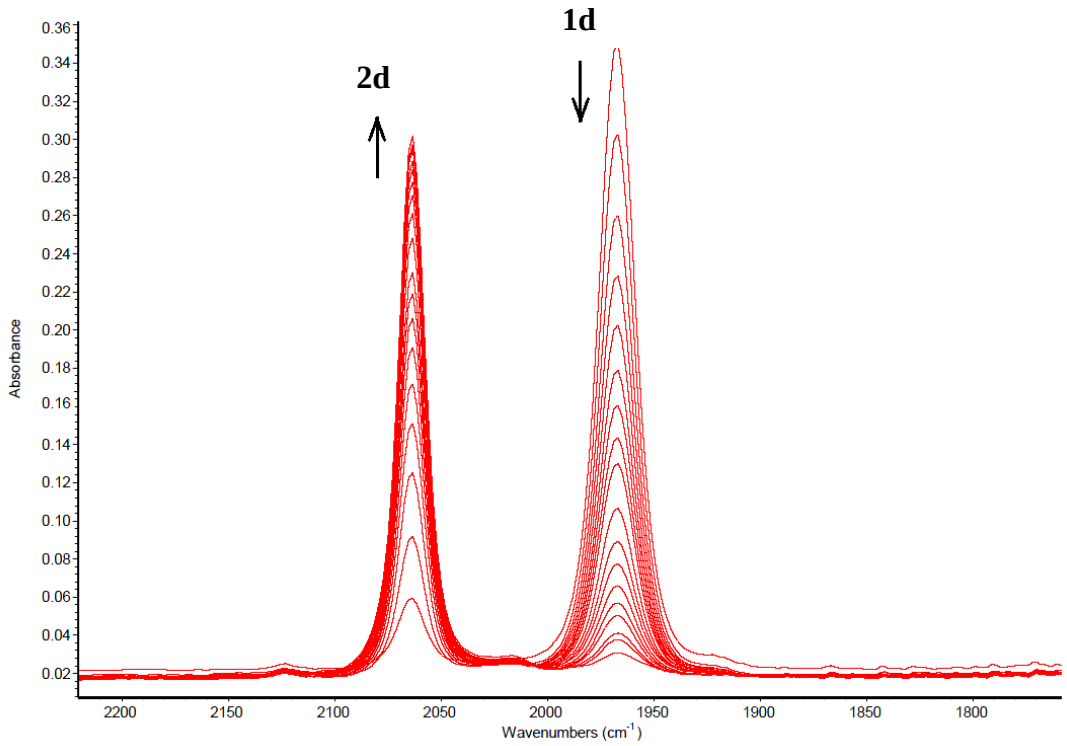


**Figure 7.13:** Series of infrared spectra observed during the reaction of **1d** and MeI in $CH_2Cl_2$. [MeI] = 0.008 M Temp = 25 °C

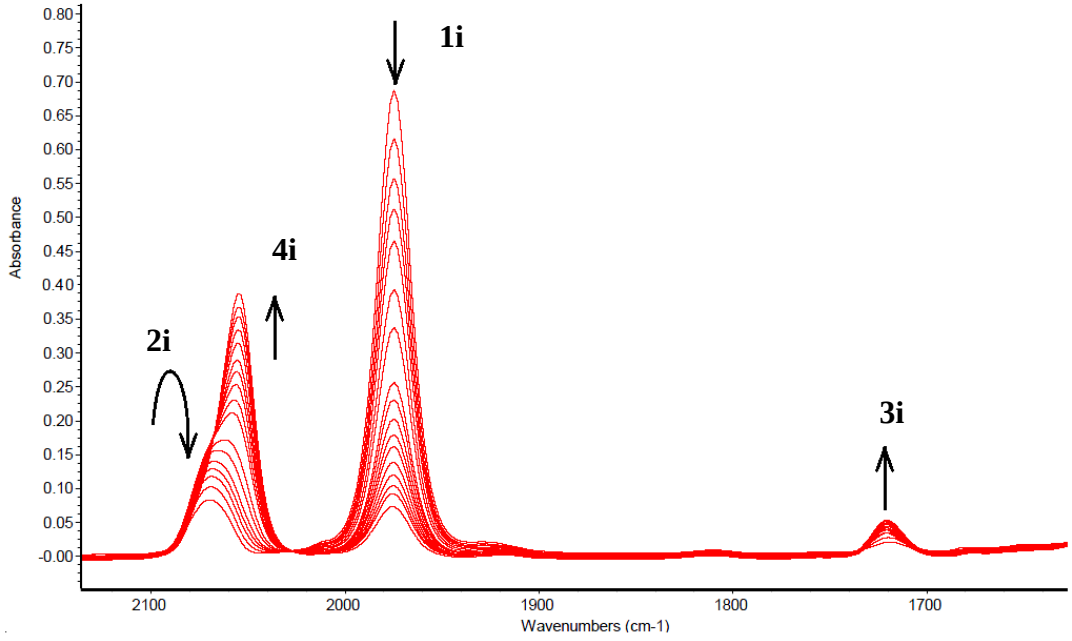


**Figure 7.14:** Series of infrared spectra observed during the reaction of **1i** and MeI in $CH_2Cl_2$. [MeI] = 0.16 M Temp = 25 °C

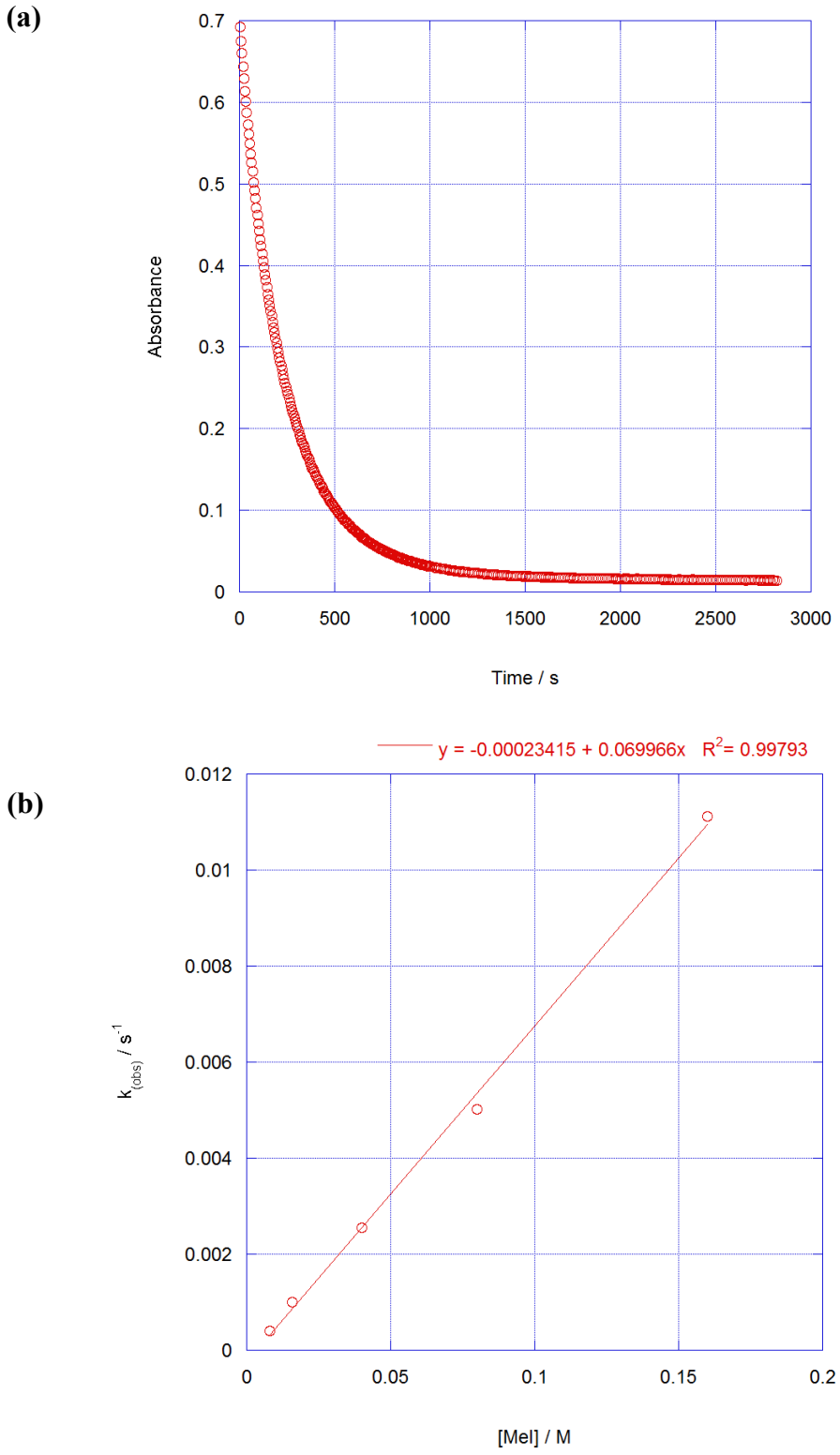


**Figure 7.15: (a)** Absorbance (1975 $cm^{-1}$) versus time plot for the reaction of **1i** with MeI. (0.16 M MeI in $CH_2Cl_2$, 25 °C)

**(b)** Plot of $k_{obs}$ against [MeI] for reaction of **1i** with MeI

| Complex | L | $10^3.k_2$ / $M^{-1}$ $s^{-1}$ ($CH_2Cl_2$) | $\Delta H^{\ddagger}$ / kJ $mol^{-1}$ | $\Delta S^{\ddagger}$ / J $K^{-1}$ $mol^{-1}$ |
|---|---|---|---|---|
| **1a**[5] | $PPh_3$ | 30.9±0.63 | 38±1 | -146±4 |
| **1b** | $PPh_2Me$ | 98.1±0.9 | 34±7 | -183±25 |
| **1c** | $PPhMe_2$ | 175±5.6 | 31±4 | -182±12 |
| **1d** | $PMe_3$ | 431±39 | 74 ±2 | -53±5 |
| **1e** | $PPh_2Et$ | 93.3±1.4 | 30±5 | -197±17 |
| **1f** | $PPhEt_2$ | 133±6.2 | 29±3 | -198±9 |
| **1g** | $PEt_3$ | 139±6.6 | 27±3 | -210±10 |
| **1h** | P(*o*-tol)$_3$ | 0.08±0.008 | 51±4 | -133±14 |
| **1i** | P(*p*-tol)$_3$ | 70.0±1.8 | 30±1 | -188±4 |
| **1j** | P(4-$FC_6H_4$)$_3$ | 5.80±0.36 | 44±3 | -148±9 |
| **1k** | P(4-$ClC_6H_4$)$_3$ | 6.80±0.6 | 43±2 | -156±8 |
| **1l**[19] | P(*p*-anisyl)$_3$ | 43.2±2.3 | 37± | -171± |
| **1m** | P(4-$CF_3C_6H_4$)$_3$ | 0.481±0.04 | 30±4 | -194±14 |
| **1n** | P(*o*-anisyl)$_3$ | 1970±15.3 | 31±1 | -136±2 |
| **1o** | PPh(*o*-anisyl)$_2$ | 1240±8.4 | 16±2 | -186±8 |
| **1p** | $PPh_2$(*o*-anisyl) | 485±23 | 37±4 | -124±14 |
| **1q**[5] | $PCy_3$ | 26.4[a] | 36±3 | -154±9 |
| **1r** | $P^tBu_3$ | - | - | - |
| **1s**[5] | $PCy_2Ph$ | 6.92[a] | 44±1 | -140±5 |
| **1t**[5] | $PCyPh_2$ | 52.9[a] | 35±3 | -152±9 |
| **1u** | $PPh_3$ | 38.9±2.4 | 29±3 | -196±11 |
| **1v** | $PPh_3$ | - | - | - |

a – error values not reported.

**Table 7.12:** Second-order rate constants ($k_2$ / $M^{-1}s^{-1}$) and activation parameters for the oxidative addition of MeI to [Rh(acac)(CO)L] complexes in $CH_2Cl_2$ at 25 °C.

**Figure 7.16** shows a bar chart of the observed rate constants. The sequential replacement of phenyl substituents by methyl groups results in a systematic increase in the observed reactivity **1a < 1b < 1c < 1d** spanning an order of magnitude. The same is true for the analogous series using ethyl substituents **1a < 1e < 1f ~ 1g**. The increased

reactivity is attributed to both the reduced steric bulk around the metal centre and increased electron donating properties of the alkyl group in comparison to a phenyl ring.

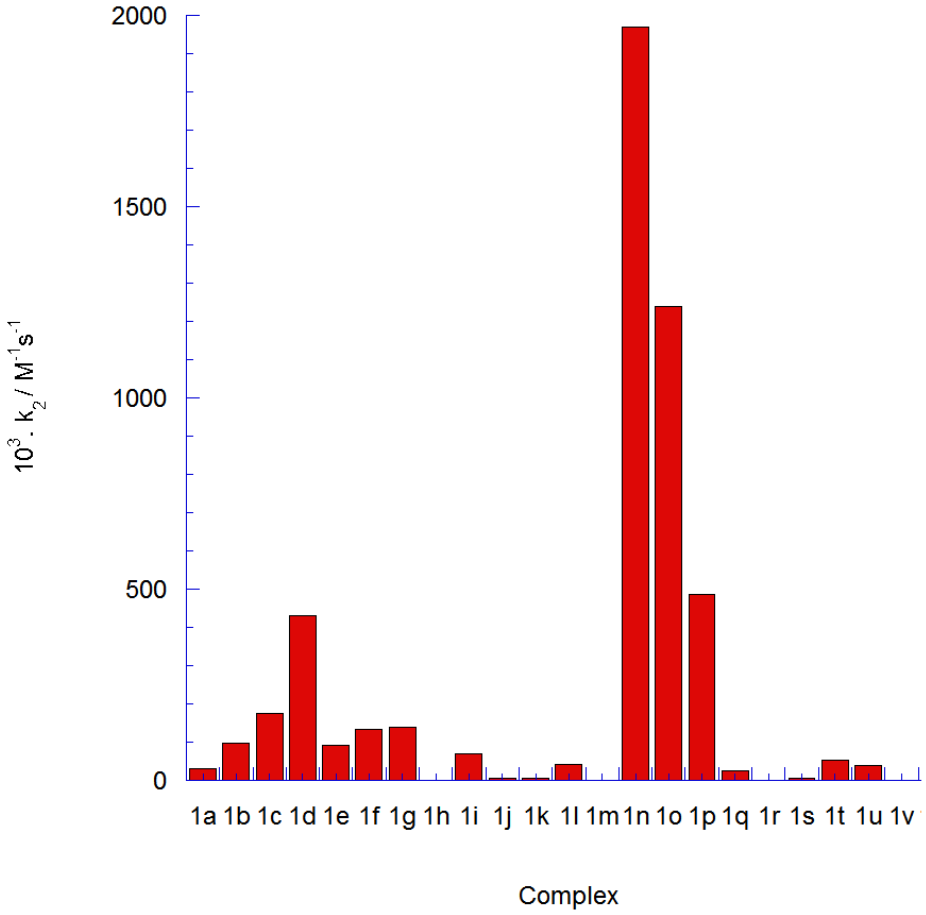


**Figure 7.16:** Bar chart of second order rate constants ($k_2$ / $M^{-1}s^{-1}$) for the reaction of [Rh(acac)(CO)L] complexes with MeI.

For the series featuring changes to the para position in $P(4\text{-}XC_6H_4)_3$, the observed reactivity towards iodomethane varies over an order of magnitude in the order **1j < 1k < 1a < 1l < 1i.** The replacement of methyl groups by *tert*-butyl groups on β-diketonate results in a rate enhancement by a factor of 1.22 for **1u** compared to **1**. Unfortunately, an accurate rate constant for **1v** could not be obtained due to poor solubility and prohibitively long reaction times.

The observed rate constant for the reaction of **1h** with MeI was small in comparison to the remainder of the complexes in this series. It has already been established that the metal centre is sterically crowded by the bulky *o*-tol groups and that the complex

decomposes upon exposure to MeI. The experimental evidence suggests that the decomposition occurs once the complex has undergone oxidative addition rather than prior to this reaction. However, the value of $k_2$ for this complex should be treated with caution as it is not clear what process the value is measuring.

The fastest observed rate constants are for complexes bearing *o*-anisyl substituents on the phosphine ligand, **1n-1p**. The second order rate constant for **1n** is 49 times that for its para isomer **1l** and 63 times that of **1a**. The increased reactivity of **1n** is proposed to be down to stabilisation of the transition state by the pendant methoxy group. A further mechanism for the enhanced reactivity will be discussed in **Section 7.5.1.**

Such an effect has been reported previously. Shaw et al. reported that the reactivity of [IrCl(CO)($PMe_2$*o*-anisyl)] was over 100 times greater than the phenyl or para-anisyl complexes.[20] Dutta et al. reported that the rate of catalytic methanol carbonylation could be enhanced using rhodium complexes bearing $PPh_2(2\text{-}C_6H_4CO_2Me)$. More recently Haynes et al. observed similarly enhanced reactivity for complexes bearing imino-phosphine ligands with *o*-anisyl substituents.[21]

The reaction of **1n** with both EtI and $^n$PrI was also probed. Rate constants and activation parameters for these reactions are shown in **Table 7.13.** The observed rate constant decreases with increasing alkyl chain length. There is almost a 400 fold drop in reactivity in moving from iodomethane to iodoethane and a further 5 fold drop in moving to 1-iodo-propane. Similar reactivity trends have been observed by Haynes et al. for reactions of RI with $[Rh(CO)_2I_2]^-$.[22]

| **RI** | $k_2$ / $M^{-1}s^{-1}$ | $\Delta H^{\ddagger}$ / kJ $mol^{-1}$ | $\Delta S^{\ddagger}$ / $JK^{-1}mol^{-1}$ |
|---|---|---|---|
| MeI | 1.97±0.01 | 30 ±1 | -136 ± 2 |
| EtI | 0.0051±0.0005 | 56 ±4 | -108 ± 13 |
| $^n$PrI | 0.0010±0.00002 | 68 ±7 | -66 ± 23 |

**Table 7.13:** Second-order rate constants ($k_2$ / $M^{-1}s^{-1}$) and activation parameters for the reaction of **1n** with MeI, EtI and $^n$PrI in $CH_2Cl_2$

## 7.5 Computational investigations into complexes bearing anisyl ligands

It is clear from **Figure 7.16** that complexes **1n**, **1o** and **1p** have the fastest rate constants for the reaction with iodomethane. The mechanism suggested previously for the enhanced reactivity is shown in **Figure 7.17,** based on a proposal by Shaw. [20]

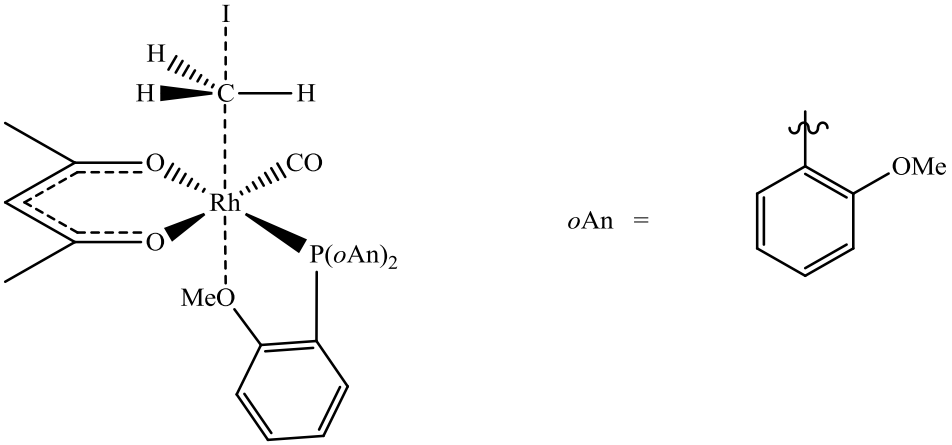


**Figure 7.17:** Proposed stabilisation effect of the pedant methoxy group.

The transition state is stabilised by an interaction of the metal centre with a lone pair of electrons of a pendant methoxy group.

Computational work was undertaken to probe the nature of the enhanced reactivity. In order to do this, the structure of the reactant needed to be probed first to investigate where the methoxy group is orientated with respect to the rest of the molecule. Once a suitable reactant structure was optimised, the positioning of the methoxy group in the transition state was probed.

### 7.5.1 Investigations into [Rh(acac)(CO)(PMe$_2$*o*An)] 1w

The first issue to be addressed was the positioning of the anisyl group relative to the metal centre in the reactant. To do this, a simplified complex, [Rh(acac)(CO)(PMe$_2$*o*An)] **1w**, was investigated, to lower the number of possible conformations. Multiple energy scans were conducted around **Dihedral A** and

**Dihedral B** to create a potential energy surface (**PES**) for rotation of the anisyl group. The dihedrals investigated are shown in **Figure 7.18.**

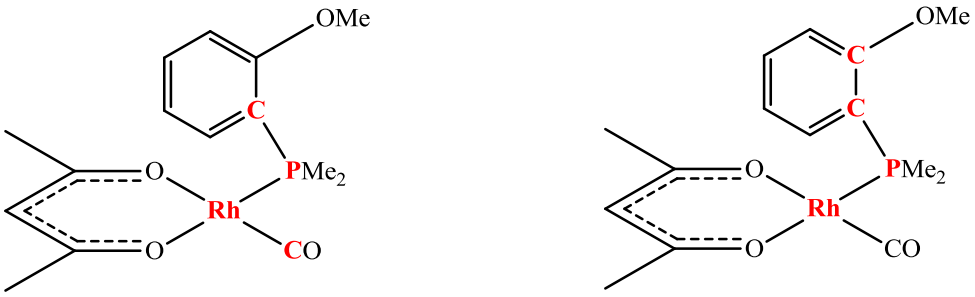


Dihedral-A Dihedral-B

**Figure 7.18:** Schematics of two dihedral angles investigated – C-Rh-P-C (**Dihedral A**) and Rh-P-C-C (**Dihedral B**).

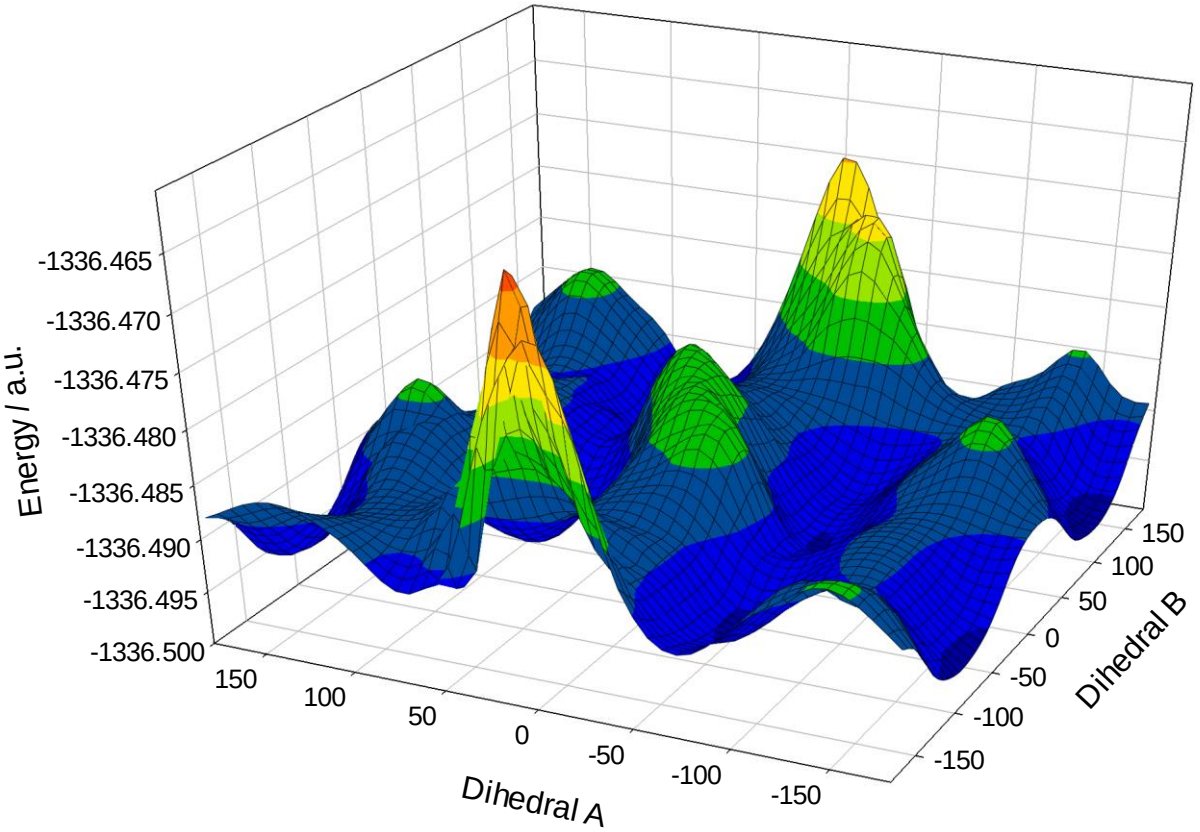


**Figure 7.19:** Potential energy surface for free rotation around **Dihedral A** and **B** in **1w**

The PES contains one region of high energy structures where the methoxy group comes into close proximity with an oxygen atom on the acac ligand. Inspection of the low-energy regions revealed a structure as shown in **Figure 7.20.** In this structure, the ring methoxy group points between the methyl groups attached to the phosphine.

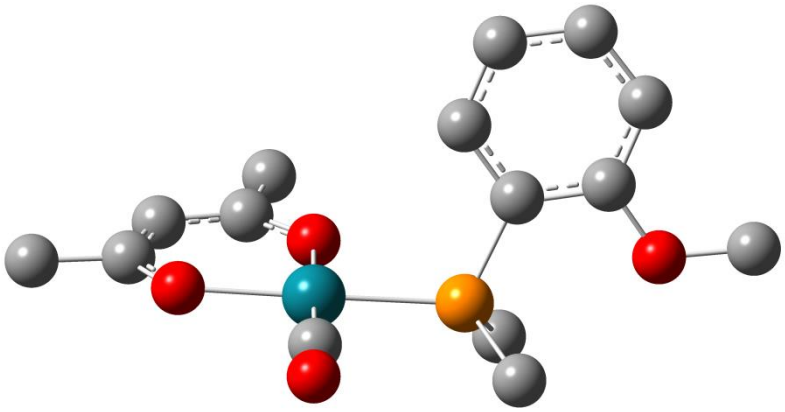

**Figure 7.20:** Ground state structure of **1w** (DFT-B3LYP/Mixed – $CH_2Cl_2$)

**Figure 7.21** shows the structures of two transition states which were located for the reaction of **1w** with iodomethane. The enhanced reactivity of complexes bearing anisyl ligands has been postulated to be down to stabilisation of the transition state by the anisyl oxygen. The structure of $\mathbf{1w^{TS1}}$ was based upon this structure. In $\mathbf{1w^{TS2}}$, the anisyl group forms a loose interaction with the iodomethane molecule in the transition state with an oxygen – hydrogen distance of 2.319 Å. Such a transition state was also observed for a series of Rh-iminophosphine complexes which were investigated as part of a fourth year project by Theo Keane undertaken at the same time as this study.[23]

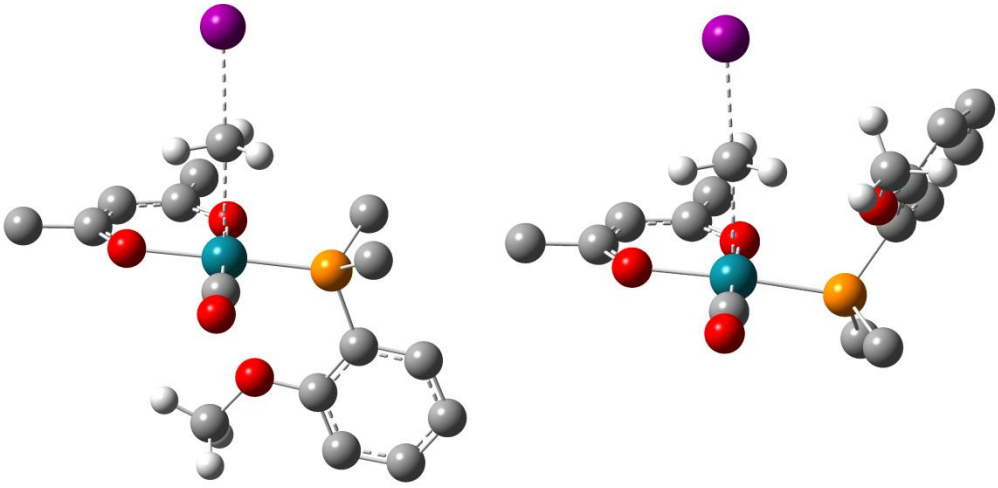

**1w$^{TS1}$** **1w$^{TS2}$**

**Figure 7.21:** Optimised transition states for reaction of [Rh(acac)(CO)($PMe_2$oAn)] with iodomethane illustrating two potential interactions – **1w$^{TS1}$** methoxy interacting with the metal centre and **1w$^{TS2}$**methoxy interacting with iodomethane. (DFT-B3LYP/Mixed – $CH_2Cl_2$)

**1w$^{TS2}$** was by far the most stable transition state. The calculated barrier height ($\Delta H^{\ddagger}$) was 29.76 compared to 44.31 kJ mol$^{-1}$ for **1w$^{TS1}$**. This data suggests that the reaction of this complex with iodomethane proceeds via **1w$^{TS2}$** where the methoxy group interacts with the iodomethane molecule in the transition state as opposed to donating electron density to the metal centre.

### 7.5.2 Investigations into [Rh(acac)(CO)($PPh_2$*o*An)] (1p)

The work on the model system showed that the most likely mechanism to rationalise the observed enhanced reactivity is when the methoxy group interacts with the iodomethane molecule. The reactant geometry however was not truly representative of the geometry for the experimental system which did not contain methyl groups on the phosphine atom. To address this, the simplest of the anisyl systems was selected, [Rh(acac)(CO)($PPh_2$*o*An)] **1p**. A comparable analysis was carried out for this system as was done for the model system. Tighter intervals were used for each energy scan to avoid overlooking any important geometry. The resulting PES is shown in **Figure 7.22.**

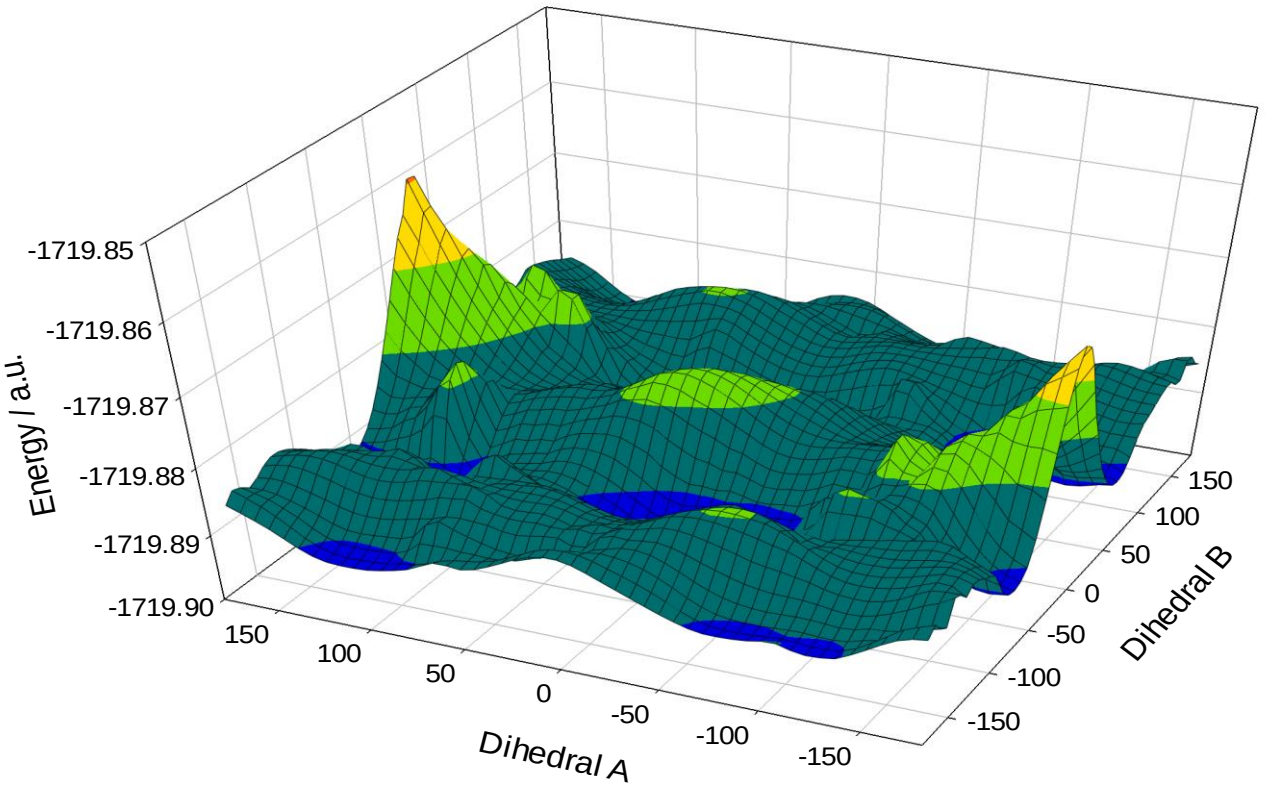


**Figure 7.22:** Potential energy surface for free rotation around **Dihedral A** and **B** in **1p.**

The PES for **1p i**s similar to that of **1w.** Unfavourable interactions between the anisyl group and an oxygen atom on the acac ligand results in a region of high energy structures. Inspection of all the low energy regions allowed for the isolation of a low energy structure as shown in **Figure 7.23.** In this structure, the methoxy group is orientated close to the carbonyl ligand.

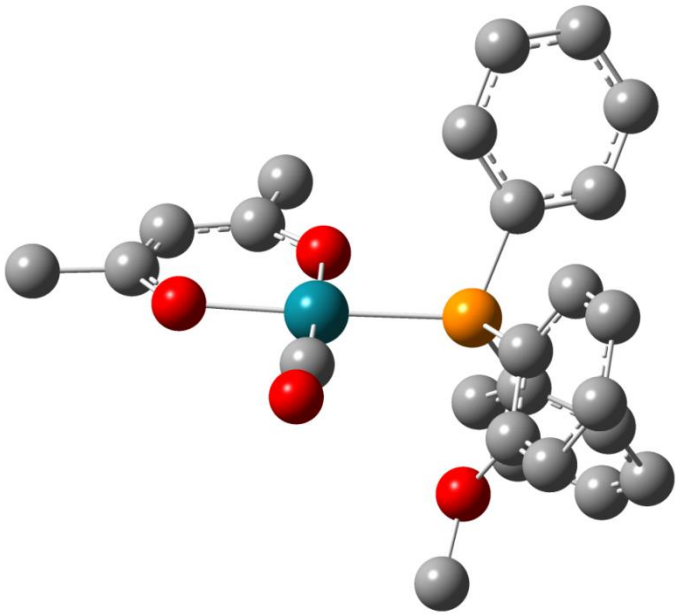

**Figure 7.23:** Lowest energy conformer of **1p**. Hydrogen atoms omitted for clarity.

With more confidence that the lowest energy conformer had been located, two transition states were optimised as before for the model complex for reaction with iodomethane. The optimised transition states are shown in **Figure 7.24.**

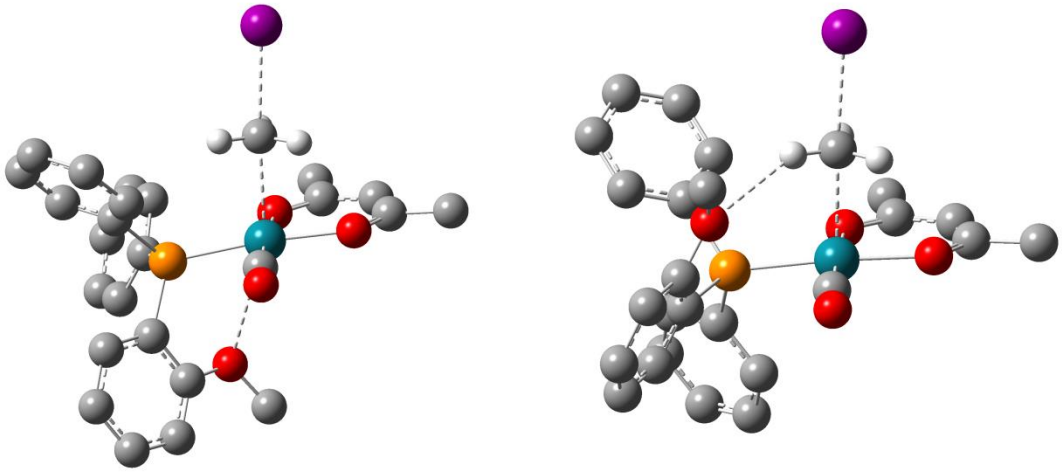

**1p$^{TS1}$** **1p$^{TS2}$**

**Figure 7.24:** Optimised transition state structures for reaction of **1p** with iodomethane. (DFT-B3LYP/Mixed – $CH_2Cl_2$) Selected hydrogen atoms omitted for clarity.

The calculated barrier height for the reaction via **1p$^{TS1}$** is 48.99 kJ mol$^{-1}$. This is significantly higher than for **1p$^{TS2}$** which is 39.11 kJ mol$^{-1}$. The data suggest that the dominant mechanism is where the OMe group is interacting with the iodomethane molecule. The calculated barrier height via **1p$^{TS2}$** is also lower than that of **1a,** as expected, whereas the value *via* **1p$^{TS}$** is higher.

### 7.5.3 Investigations into [Rh(acac)(CO)(PPh*o*An$_2$)] (1o) and [Rh(acac)(CO)(P*o*An$_3$)] (1n)

The reactant geometries of the complexes bearing two and three anisyl substituents could not be investigated as simply through the use of multiple energy scans around the dihedrals. The presence of more anisyl groups on the complex would require a significant number of scans as fixing the position of one or two groups and scanning only one anisyl group would not afford a true description of the structure. Such analysis would be very time consuming and computationally expensive to undertake so a different approach was undertaken. The lowest energy structure from the scans on [Rh(acac)(CO)(PPh$_2$*o*An)] was taken and the requisite number of methoxy substituents

were added to the phenyl rings in such a way as to minimise any obvious unfavourable steric interactions. The structures are shown in **Figure 7.25.**

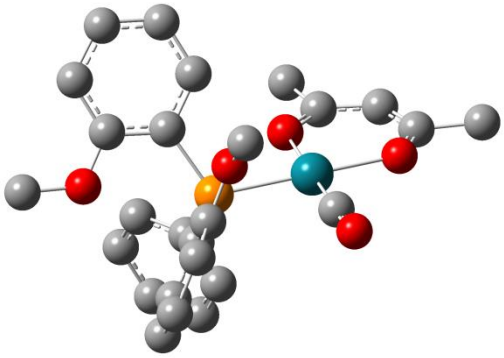

**1o**

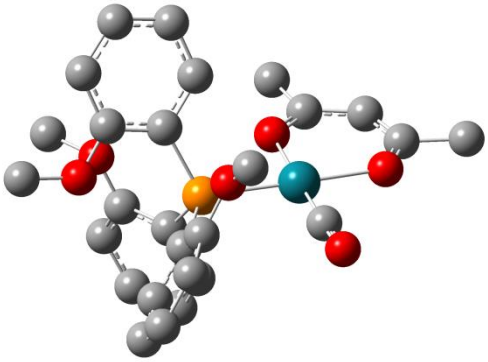

**1n**

**Figure 7.25:** Optimised structures of **1o** [Rh(acac)(CO)(PPh*o*An$_2$)] and **1n** [Rh(acac)(CO)(P*o*An$_3$)] (DFT-B3LYP/Mixed – $CH_2Cl_2$)

The results presented above for **1a** and **1p** suggests that a transition state in which the methoxy group interacts with the iodomethane is most likely energetically. The addition of further anisyl groups leads to an interesting question: namely, where do the other anisyl groups orientate relative to the metal in the transition state? Orientation of a methoxy substituent on the same side as the incoming MeI molecule is defined here as **UP** and orientation on the opposite side of the molecule is defined as **DOWN.** Several transition states were optimised for both pathways where the other anisyl groups were positioned in such a way as to minimise steric interactions. Barrier heights for the structures investigated are shown in **Table 7.14** along with comparative data for **1a.**

| Reactant Complex | Ligand Orientation | Barrier height / kJ mol$^{-1}$ |
|---|---|---|
| **1a** | - | 45.06 |
| **1n** | 1 Up, 1 Down | 32.75 |
| **1n** | 2 Up | 49.95 |
| **1o** | 2 Up. 1 Down | 31.17 |
| **1o** | 3 Up | 42.89 |

**Table 7.14:** Barrier height ($\Delta H^{\ddagger}$) for optimised transition states with varying ligand orientations.

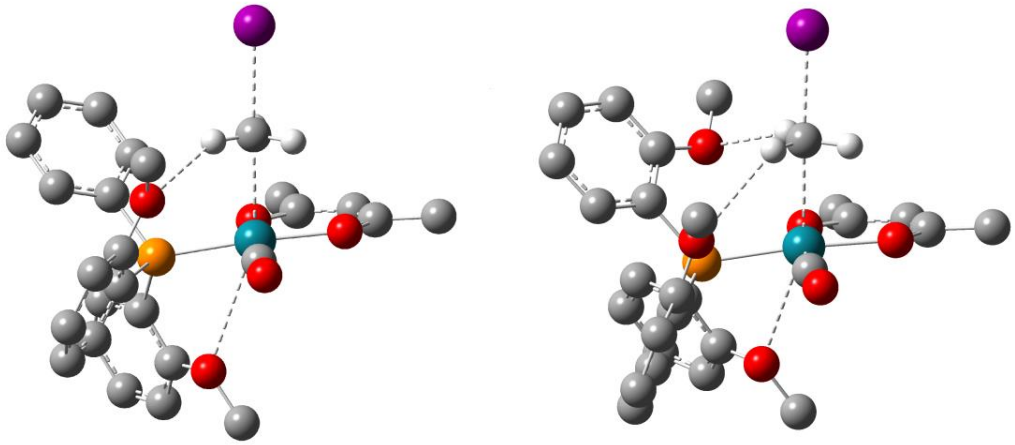

**1o$^{TS}$** **1n$^{TS}$**

**Figure 7.26:** Optimised transition states [Rh(acac)(CO)(PPh*o*An$_2$)] (**1o$^{TS}$ )** and [Rh(acac)(CO)(P*o*An$_3$)] **(1n$^{TS}$)** (DFT-B3LYP/Mixed – $CH_2Cl_2$) Selected hydrogen atoms omitted for clarity.

**Figure 7.26** shows that the most stable transition state for reactant **1o** has a methoxy group closely associated with the incoming iodomethane molecule and a further anisyl group close to the metal centre on the opposite side of the molecule. The enhanced reactivity of the complex compared to the complex with only one anisyl group can potentially arise from stabilisation through both interactions.

The addition of a third anisyl group on the complex increases the nucleophilicity further. The most stable transition state has one methoxy group close to the metal centre and the other two anisyl groups closely associated with the iodomethane molecule.

### 7.5.4 Barrier height analysis

Each of the calculated barrier heights for **1n-1p** is calculated from the lowest energy conformer of the reactant and the transition state. A plot of the calculated barrier heights against experimental log *k* for the series [Rh(acac)(CO)(PPh$_x$*o*An$_{(3-x)}$)] (x = 0-3) is shown in **Figure 7.27**.

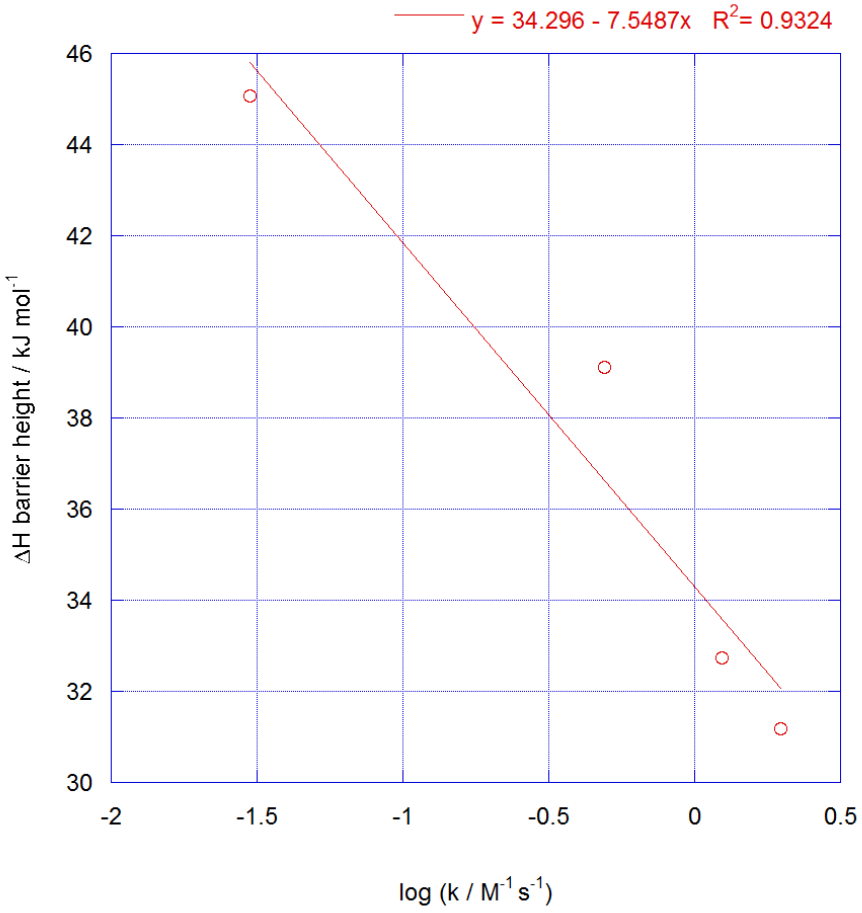


**Figure 7.27:** Plot of calculated barrier height ($\Delta H^{\ddagger}$) against experimental log *k* ($CH_2Cl_2$, 25 °C) for the series [Rh(acac)(CO)$PPh_xoAn_{(3-x)}$] (x = 0-3)

A good correlation was found for the series with a $R^2$ value of 0.932 suggesting that the optimised transition states are all in the correct geometry.

## 7.6 Conclusions

A systematic investigation on how changing the phosphine in [Rh(acac)(CO)L] complexes affects the reactivity towards MeI has been presented. Complexes bearing aryl phosphines generally form a mixture of Rh(III) products characterized as two alkyl and one acyl species. Complexes bearing less basic phosphines favour the formation of acyl products. Alkyl species are observed as the principal products when the complex bears a very basic phosphine.

The series of complexes bearing changes to the *para*-position on $PPh_3$ have reactivities that span an order of magnitude. Sequential replacement of phenyl rings with either ethyl or methyl groups results in enhanced reactivity attributed to the reduced steric interference and increased donor power of the ligand.

Significantly enhanced reactivity is observed for complexes bearing *o*-anisyl substituents, which is suggested to arise from the stabilization of the transition state by the pendant methoxy groups. **1n** reacts 300 times slower with iodoethane compared to iodomethane and a further five times slower with 1-iodopropane.

Modifications to the β-diketone ligand were investigated. Complexes bearing a $^{t}$Bu-modified ligand reacted with iodomethane marginally faster than complexes with an acac ligand. Replacing the methyl groups on the backbone with fluorinated methyl groups reduced the reactivity of the complex significantly. Reaction of **1v** with iodomethane resulted in the formation of an alkyl complex where the phosphine was in the axial position relative to the acac ligand.

Computational investigations on complexes bearing anisyl modified phosphines showed that the most stable transition state for the reaction with iodomethane was where the anisyl group interacts with the methyl group of iodomethane in the transition state.

## 7.7 References


(1) Bonati, F.; Wilkinson, G. *J. Chem. Soc.,* **1964**, 3156

(2) Basson, S., S; Leipoldt, J. G.; Nel, J. T. *Inorg. Chim. Acta.,* **1984**, *84*, 167.

(3) Conradie, J.; Conradie, M. M. *Dalton Trans.,* **2011**, 40, 8226.

(4) Basson, S., S; Leipoldt, J. G.; Roodt, A.; Venter, A.; Van der Walt, T. J. *Inorg. Chim. Acta.,* **1986**, *119*, 35.

(5) Brink, A.; Roodt, A.; Steyl, G.; Visser, H. G. *Dalton Trans.,* **2010**, *39*, 5572.

(6) Basson, S., S; Botha, L. J.; Leipoldt, J. G. *Inorg. Chim. Acta.,* **1987**, 126, 25-28

(7) Leipoldt, J. G.; Basson, S., S;; Botha, L. J. **1990**, *168*, 215.

(8) Erasmus, J. J. C.; Conradie, J. *Cent. Eur. J. Chem.,* **2012**, 10, 256-266.

(9) Van zyl, G. J.; Lamprecht, G. J.; Leipoldt, J. G. *Inorg. Chim. Acta.,* **1988**, *143*, 223.

(10) Conradie, M. M.; Erasmus, J. J. C.; Conradie, J. *Polyhedron,* **2011**, 30, 2345.

(11) Erasmus, J. J. C.; Conradie, M. M.; Conradie, J. *Reac Kinet Mech Cat,* **2012**, 105, 233.

(12) Conradie, J.; Swarts, J. C. *Organometallics,* **2009**, 28, 1018.

(13) Conradie, J.; Lamprecht, G. J.; Otto, S.; swarts, J. C. *Inorganica Chim. Acta.,* **2002**, *218*.

(14) Datt, M. S.; Nair, J. J.; Otto, S. *J.Organomet. Chem.,* **2005**, 690, 3422.

(15) Serron, S.; Huang, J.; Nolan, S. P. *Organometallics,* **1998**, *17*, 534.

(16) Simanko, W.; Mereiter, K.; Schmid, R.; Kirchner, K.; Trzeciak, A., M;; Ziolkowski, J., J; *J.Organomet. Chem.,* **2000**, *602*, 59.

(17) Conradie, J. *Dalton Trans* **2015**, *44*, 1503.

(18) John, C. *The Effect of o- anisyl Substituted Phosphines on the Reactivity of Rh Complexes, MChem Thesis,* University of Sheffield*,* **2011**.

(19) Cletheroe, L. *A Study of the Oxidative Addition of MeI to [M(acac)(CO)(L)] M = Rh, Ir , MChem Thesis,* University of Sheffield*,* **2012**.

(20) Miller, E. M.; Shaw, E. L. *J.Chem. Soc., Dalton Trans* **1974**, *480*.

(21) Best, J.; Wilson, J. M.; Adams, H.; Gonsalvi, L.; Peruzzini, M.; Haynes, A. *Organometallics,* **2007**, *25*, 1960.

(22) Ellis, P. R.; Pearson, J. M.; Haynes, A.; Adams, H.; Bailey, H. A.; Maitlis, P. M. *Organometallics,* **1994**, *18*, 3215.

(23) Keane, T. *Computational Investigations into organometallics compounds using DFT, MChem Thesis, University of Sheffield,* **2013**.

# CHAPTER 8

# Experimental and computational investigations into iridium-xantphos complexes

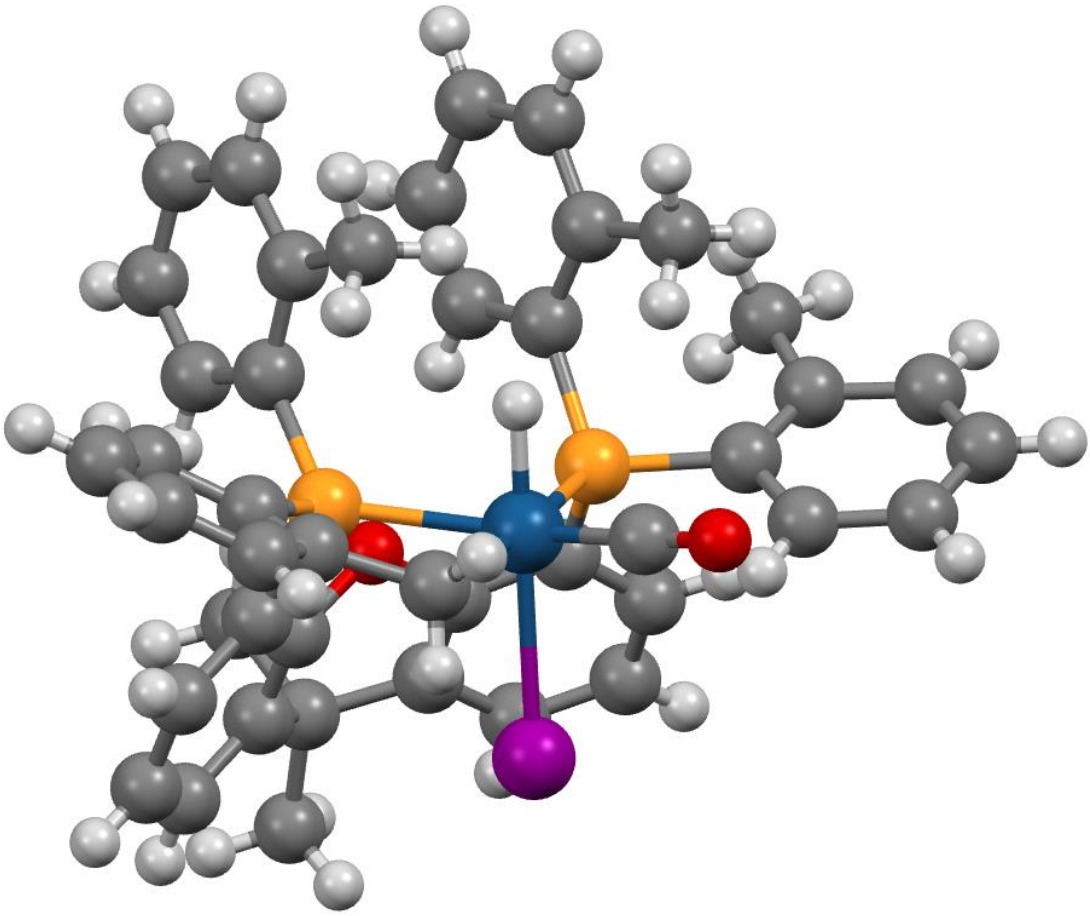

## 8.1 Introduction

The xantphos family of ligands was initially developed by van Leeuwen et al. as potential ligands for Rh-catalysed hydroformylation.[1] Xantphos can coordinate to a metal either as a *cis*-bidentate or *mer*-tridentate ligand due to the flexibility of the xanthene backbone as shown in **Figure 8.1.** In trigonal bipryramidal complexes it can coordinate at two equatorial sites (ee) or one axial and one equatorial (ea). Xantphos complex showed remarkable hydroformylation selectivity towards linear aldehydes over branched aldehydes. Xantphos has also been applied to other reactions such as alkene hydrocyanation, styrene hydroxycarbonylation, cross-coupling reactions and allylic alkylations.[2-8]

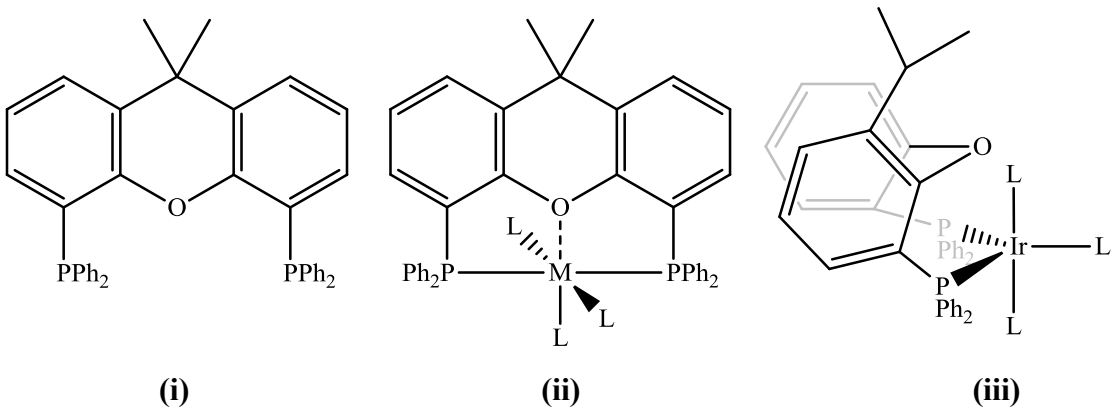


**(i)** **(ii)** **(iii)**

**Figure 8.1:** Structure of xantphos **(i)** and illustrations of coordination modes – *mer* tridentate **(ii)** and *cis* bidentate **(iii)**.

There is little literature data on iridium complexes bearing the xantphos ligand. Fox et al. investigated the reactivity of $[IrX(CO)_2(xantphos)]$ (X = Cl, Br, I).[9] The solid-state structures of these complexes are markedly different. All three complexes adopt a distorted trigonal-bypyramidal structure. However for X = Cl and Br the phosphine donors are in the equatorial plane. For X = I, one phosphorus atom is in the equatorial position and the other is axial. The reactions of these complexes towards hydrogen were probed resulting in the formation of dihydride species.

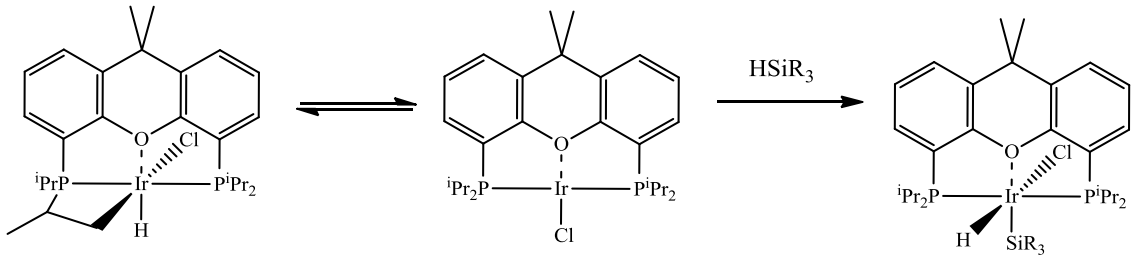


**Scheme 8.1:** Reaction of [IrCl($^{i}$Pr-xantphos)] with silanes.

**Scheme 8.1** shows a recently reported iridium complex bearing an $^{i}$Pr-xantphos ligand. The reactivity of the free ligand with $[IrCl(COD)]_2$ leads to an octahedral Ir(III) hydride complex as a result of intramolecular C-H activation of one of the phosphine's $^{i}$Pr groups. [IrCl($^{i}$Prxantphos)] was found to undergo oxidative addition of secondary and tertiary silanes.[10,11]

Weller et al. investigated the reactivity of a cationic complex, $[Ir(COD)(xantphos)]BF_4$ Reaction of this complex with $H_2$ resulted in the formation of distinct products depending on the solvent.[12] Polar solvents, such as acetone and MeCN, resulted in the formation of hydrido complexes with coordinated solvent. Non-coordinating solvents favoured the formation of dimeric species. Reaction of excess alkenes with $[Ir(xantphos)H_2(MeCN)]BF_4$ led to the formation of Ir-III alkyl hydrido species – a process that could be reversed by heating.

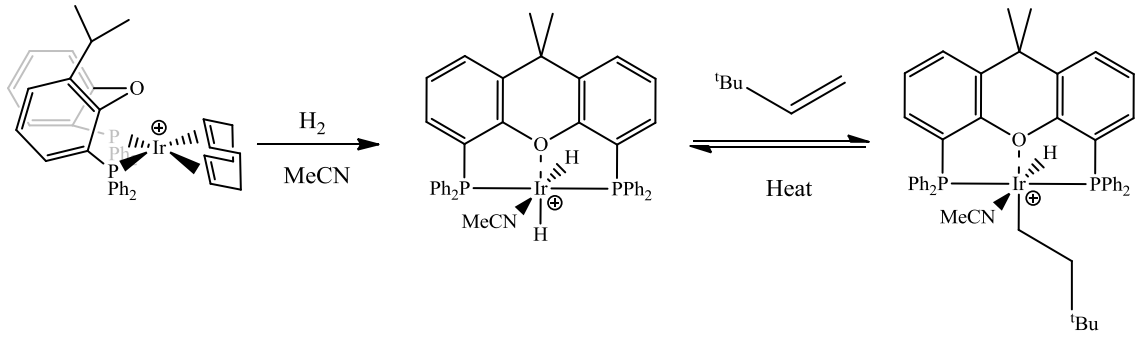


**Scheme 8.2:** Reaction of $[Ir(COD)(xantphos)]^{+}$ with hydrogen

The reactivity of rhodium-xantphos complexes towards iodomethane was investigated by Williams et al..[13] **Scheme 8.3** shows the proposed catalytic cycle for carbonylation of methanol. The cycle closely resembles the $[RhI_2(CO)_2]^{-}$ catalysed process. Initially,

[RhI(CO)(xantphos)] reacts with iodomethane to form a cationic species. Migratory insertion of this complex leads to the formation of an acyl species. Further coordination of CO and reductive elimination results in the formation of acetic acid and regeneration of the nucleophilic complex.

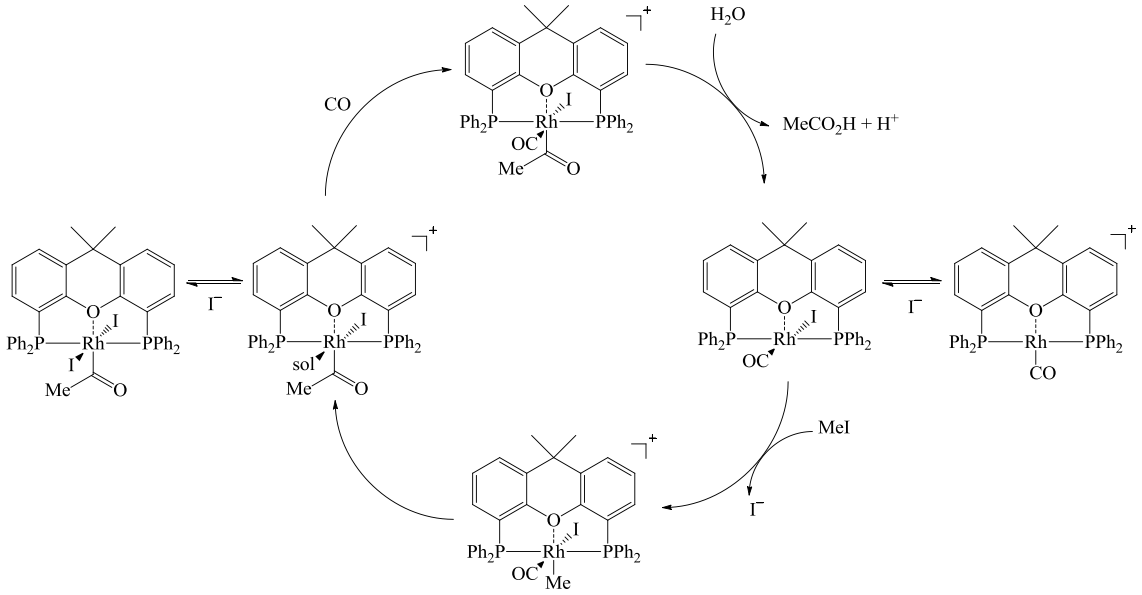


**Scheme 8.3:** Proposed catalytic cycle for rhodium catalysed methanol carbonylation.

In this chapter, it was of interest to synthesise and investigate the reactivity of the analogous iridium complex, [IrI(CO)(xantphos)] to see how its reactivity compared to the rhodium system. Modifications to the phosphine substituents would also be undertaken, replacing the phenyl groups in xantphos with $^{t}$Bu, *o*-tol and $^{i}$Pr groups to alter the steric and electronic properties of the ligand.

## 8.2 Synthesis and characterisation of Ir-complexes

### 8.2.1 Synthesis and characterisation of [IrI(CO)$_2$(xantphos)]

The synthesis of [IrI(CO)$_2$(xantphos)] was first reported by Fox et al..[9] according to **Scheme 8.4** and the product was reported to have ν(CO) bands at 1950 and 2023 cm$^{-1}$ in the solid state.

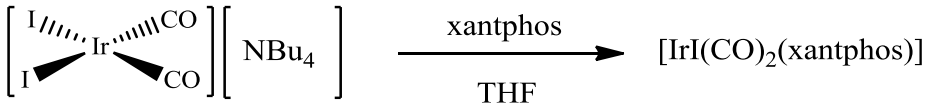


**Scheme 8.4:** Synthesis of $[IrI(CO)_2(xantphos)]$

In the present study, the same synthetic method was used. The $^{31}P\{^1H\}$ NMR spectrum of the product has a broad singlet at δ -18.8 and the mass spectrum has a single molecular ion at m/z 799 which is assigned to $[Ir(CO)(xantphos)]^+$. The IR spectrum of a solution of the product in $CH_2Cl_2$ is shown in **Figure 8.2**. It shows four overlapping ν(CO) bands consistent with the presence of two dicarbonyl products in solution.

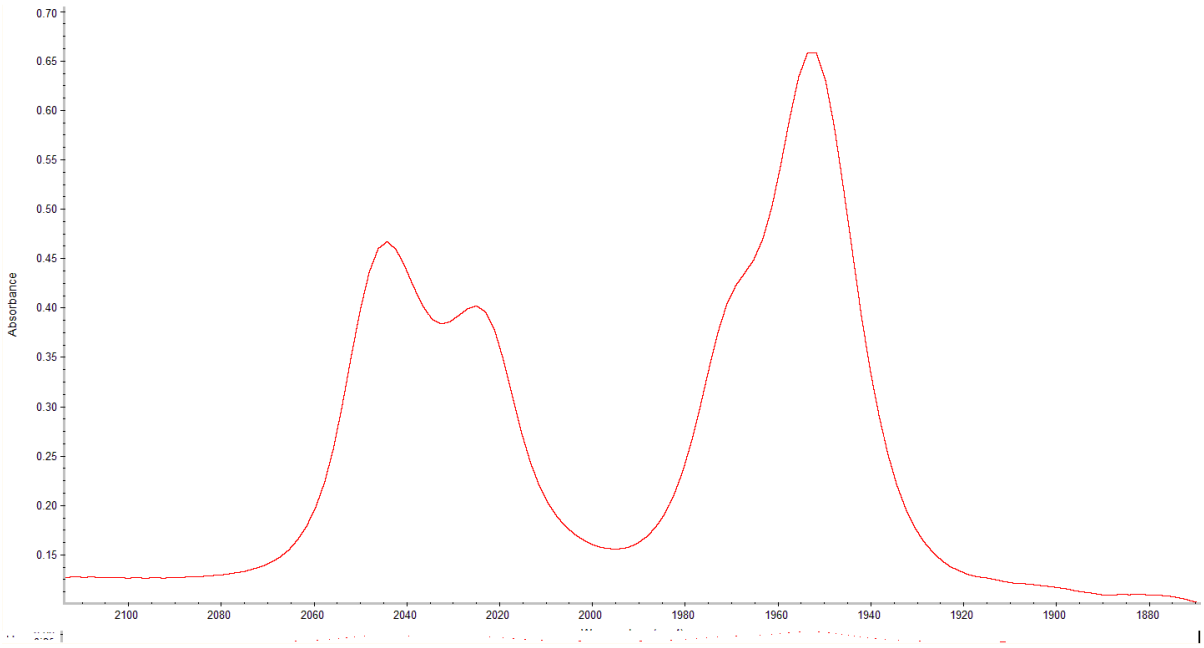


**Figure 8.2:** Infra-red spectrum of $[IrI(CO)_2(xantphos)]$ ($CH_2Cl_2$, 25 °C)

The structures reported by Fox et al. showed that the xantphos ligand can adopt different configurations around the iridium centre. Each of the three complexes $[IrX(CO)_2(xantphos)]$ (X = Cl, Br, I) adopts a trigonal bypyramidal geometry but for X = I, the xantphos ligand coordinates through one axial and one equatorial site. Computational investigations were undertaken in order to probe possible structures for

the isomers of [IrI(CO)$_2$(xantphos)] indicated by the solution IR spectrum. **Figure 8.3** shows the structures of these isomers and **Table 8.1** contains relative energies and computed infrared data.

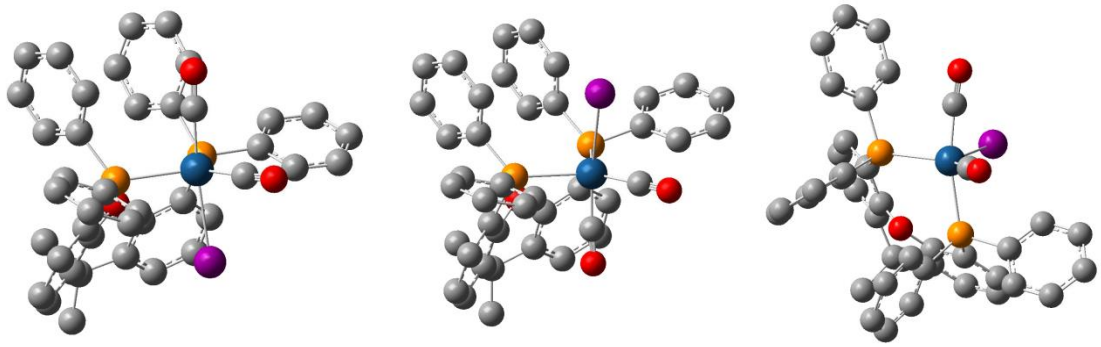

**1a** **1b** **1c**

**Figure 8.3:** Optimised structures of **1a-c.** Hydrogen atoms omitted for clarity. (DFT-B3LYP/Mixed – $CH_2Cl_2$)

| Complex | Relative energy, ΔH / kJ mol$^{-1}$ | ν(CO) / cm$^{-1}$ |
|---|---|---|
| **1a** | 0.00 | 1952, 2051 |
| **1b** | 1.53 | 1951, 2027 |
| **1c** | 6.19 | 1955, 2023 |

**Table 8.1:** Relative energies and scaled (0.98) carbonyl stretching frequencies for **1a-c** (DFT – B3LYP – mixed basis)

Isomers **1a** and **1b** differ only in the position of the carbonyl and iodide ligands whilst the xantphos backbone occupies two equatorial sites. In **1c** the xantphos ligand is bound to the metal centre through one axial and one equatorial site with a carbonyl also axial. The relative energies of the isomers suggest that all three could be present in solution. The scaled DFT calculated frequencies correlate well with the experimental IR spectrum.

### 8.2.2 Attempted decarbonylation of [IrI(CO)$_2$(xantphos)]

In an attempt to prepare an iridium analogue of [RhI(CO)(xantphos)], decarbonylation of [IrI(CO)$_2$(xantphos)] was attempted. A sample was heated to reflux overnight in toluene with nitrogen bubbling through the solution with the aim of driving off the CO ligand. Upon cooling and removing the solvent, an initial IR spectrum contained a ν(CO) band at 2034 cm$^{-1}$. The $^{31}P\{^1H\}$ NMR spectrum contained two doublets at δ –13.6 and –96.9 both with coupling constants of 17 Hz.

The ν(CO) absorption at 2034 cm$^{-1}$ is much too high for an iridium(I) monocarbonyl and is more consistent with an iridium(III) species. A pair of doublets in the $^{31}P$ NMR indicated that the phosphorus atoms are inequivalent. Unfortunately, the formation of this species could not be consistently reproduced so no further characterisation of this product was obtained.

### 8.2.3 Reaction of [IrI(CO)$_2$(xantphos)]with Iodomethane

[IrI(CO)$_2$(xantphos)] reacts with neat iodomethane overnight at room temperature to yield an orange powder which has two ν(CO) bands at 2061 and 2028 cm$^{-1}$ in an approximate 3:1 ratio. The $^{31}P\{^1H\}$ NMR spectrum shows two broad singlets at δ -19.07 and -49.27 and the mass spectrum has a molecular ion at m/z 941 which is consistent with the species [IrI(CO)(xantphos)(Me)]$^+$. Based upon these observations, the reaction in **Scheme 8.5** is proposed.

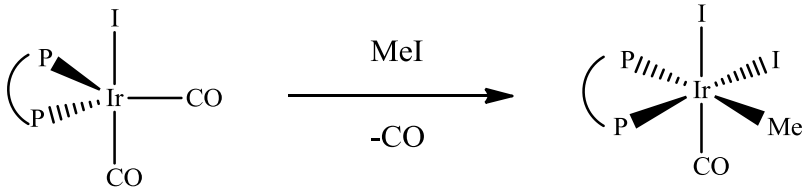


**Scheme 8.5:** Reaction of [IrI(CO)$_2$(xantphos)] with iodomethane.

Due to the broadness of the NMR peaks, it was surmised that an exchange process could be occurring so a low-temperature NMR study was undertaken illustrated in **Figure 8.4.** As the temperature was lowered from 40, the broad peaks sharpened and

two more sharp peaks were observed growing at δ -31.61 and -53.22. The four peaks were in the ratio of 3:1:3:1. At -30 °C the four peaks sharpened further and were resolved into doublets with coupling constants of 8.3 and 9.0 Hz respectively.

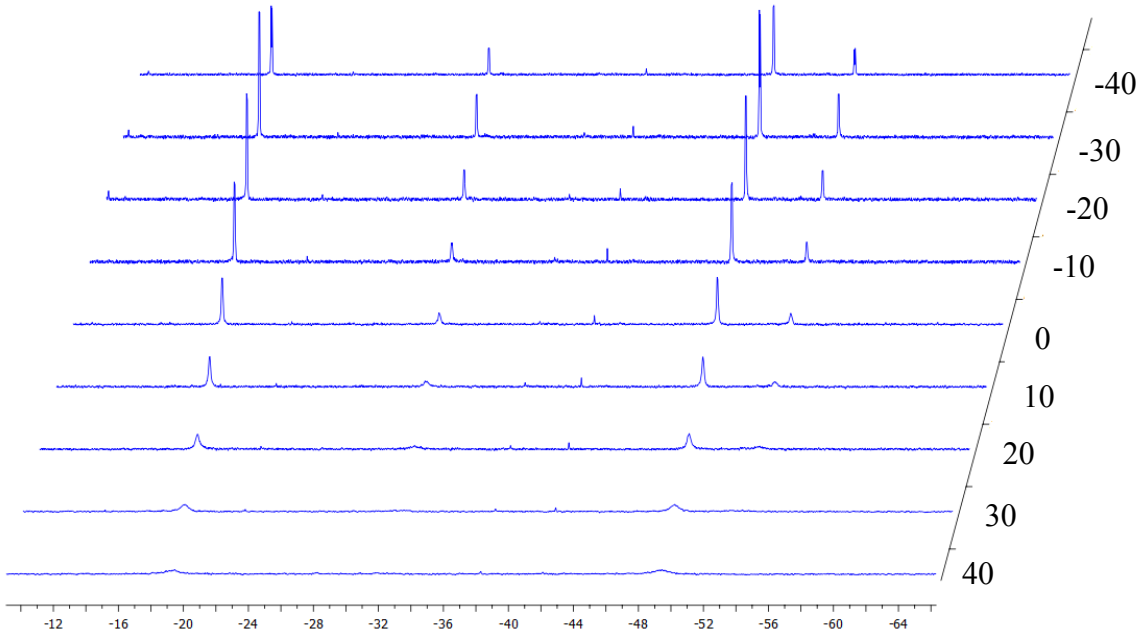


**Figure 8.4:** Variable temperature $^{31}P$ NMR spectra of $[IrI_2(CO)(Me)(xantphos)]$ in $CDCl_3$ from -40 °C to 40 °C.

The low temperature NMR spectra indicate the presence of two main species in an approximate 3:1 ratio which is consistent with the two carbonyl bands observed in the IR spectrum. The size of the coupling constants suggest that in each complex the phosphorus atoms are inequivalent and are *cis* to one another.

Slow evaporation of $CH_2Cl_2$ from a concentrated solution yielded crystals that were suitable for X-ray crystallography. The resulting structure is shown in **Figure 8.5** and selected bond lengths and angles are given in **Table 8.2.**

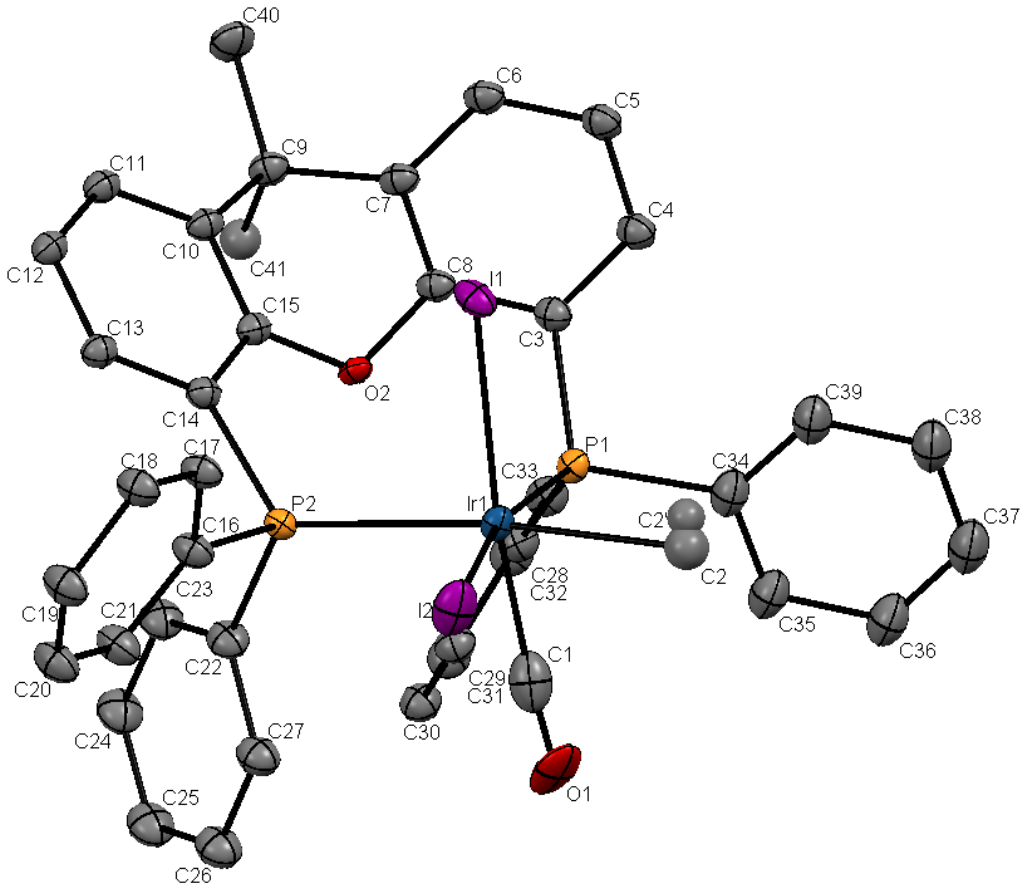


**Figure 8.5:** X-ray crystal structure of $[IrI_2(CO)(Me)(xantphos)]$ **(2a)**. Hydrogen atoms omitted for clarity

| Bond | Length / Å | Bond | Length / Å |
|---|---|---|---|
| **Ir(1) – P(1)** | 2.368(2) | **Ir(1) – I(2)** | 2.737(4) |
| **Ir(1) – P(2)** | 2.511(2) | **Ir(1) – C (1)** | 1.882(8) |
| **Ir(1) – I(1)** | 2.710(4) | **Ir(1) – C (2)** | 2.34(1) |
| | **Angle / °** | | **Angle / °** |
| **P(1) – Ir(I) - P(2)** | 102.93(5) | **P(2) – Ir(1) – C(2)** | 165.78(4) |
| **I(1) – Ir(I) – C(1)** | 170.79(2) | **P(1) – Ir(1) – I(2)** | 168.26(4) |

**Table 8.2:** Selected bond distances and angles in $[IrI_2(CO)(Me)(xantphos)]$.

The complex adopts a distorted octahedral geometry with xantphos coordinating to iridium in a *cis* bidentate manner with a P-Ir-P bond angle of 103 °. Other complexes with xantphos coordinated in this mode have been characterised.[9,14-16] The Ir-P bond lengths are 2.368 Å and 2.511 Å with one bond being significantly longer, presumably

due to the *trans* influence of the methyl group. Some disorder of the methyl ligand is observed.

A computational investigation was undertaken to investigate the nature of the second isomer observed in solution. The crystal structure was used as a start point for these investigations and changes were made to the positions of the iodides, carbonyl and methyl ligands whilst the xantphos ligand was left unchanged. The structures of the two most feasible isomers are given in **Figure 8.6** and their relative energies and scaled carbonyl stretching frequencies are given in **Table 8.3.**

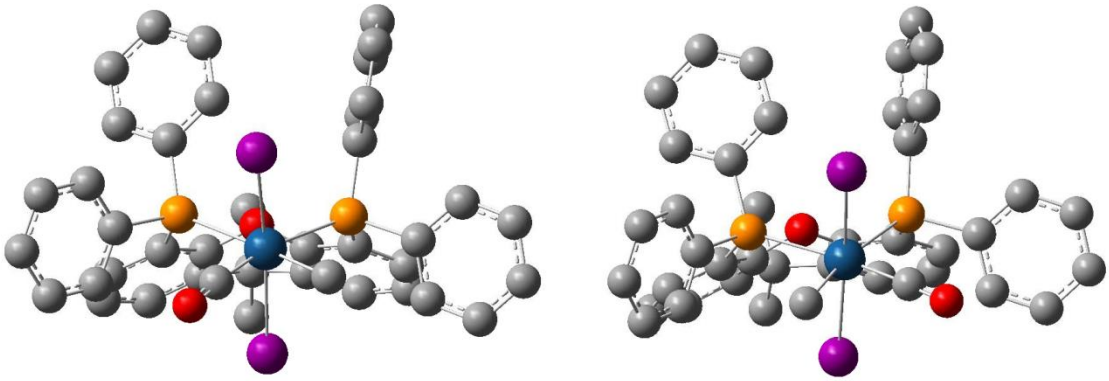

**2b** **2c**

**Figure 8.6:** Schematic representations of isomers of $[IrI_2(CO)(Me)(xantphos)]$ Hydrogen atoms omitted for clarity. (DFT-B3LYP/Mixed – $CH_2Cl_2$)

| Isomer | $\Delta H_{rel}$ / kJ mol$^{-1}$ | $\nu$(CO) / cm$^{-1}$ |
|---|---|---|
| **2a** | 0.00 | 2030 |
| **2b** | 2.79 | 2057 |
| **2c** | 4.56 | 2059 |

**Table 8.3:** Relative energies ($\Delta H$) and scaled carbonyl stretching frequencies (scaling factor 0.98) for isomers of $[IrI_2(CO)(Me)(xantphos)]$ (DFT – B3LYP – mixed basis)

Isomers **2b** and **2c** have iodide ligands mutually *trans* and only differ in the positions of the methyl and carbonyl ligands. The energies of both complexes are higher than that

optimised from the crystal structure. The scaled carbonyl stretching frequencies correlate well with the experimentally observed values of 2061 and 2028 $cm^{-1}$. Data for the remaining isomers investigated can be found in the appendices.

### 8.2.4 Reaction of 2a with $AgSbF_6$

To further investigate the reactivity of **2a**, one equivalent of $AgSbF_6$ was added to a solution of the complex in $CH_2Cl_2$ resulting in a rapid precipitation of AgI. An IR spectrum of the product contained a single ν(CO) at 2064 $cm^{-1}$ and the $^{31}P$ NMR spectrum showed a singlet at δ – 4.88. The $^{1}H$ NMR spectrum contained 2 singlets at δ 1.87 and 1.99 in the ratio 1:1 and a triplet at δ 2.03. The singlet in the phosphorus NMR indicates that the phosphorus atoms are equivalent and cannot be *cis* to one another. The triplet in the $^{1}H$ NMR is assigned to the methyl ligand with $J_{PH}$ = 4.6 Hz. The xanthene backbone methyls are observed as two singlets. **Scheme 8.6** shows the formation of a cationic complex by iodide abstraction from **2a**.

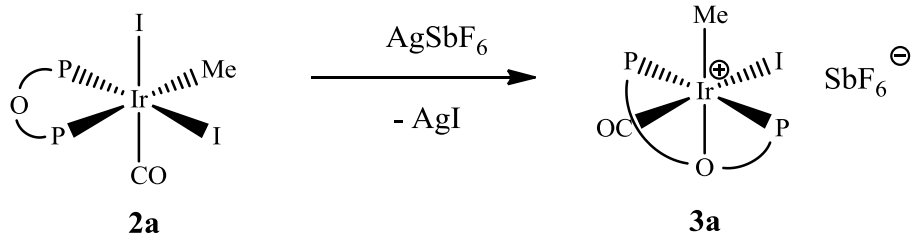


**2a** **3a**

**Scheme 8.6:** Reaction of $[IrI_2(CO)(Me)(xantphos)]$ with $AgSbF_6$.

Slow evaporation of $Et_2O$ into a concentrated $CH_2Cl_2$ solution yielded crystals that were suitable for X-ray crystallography. The resulting structures is shown in **Figure 8.7** and selected bond lengths and angles are given in **Table 8.4.** The complex adopts a distorted octahedral geometry with the xantphos ligand coordinating to iridium as a *mer* tridentate P, O, P chelating ligand. There is a dative bond between the oxygen on the xantphos backbone and the iridium centre with a distance of 2.246 Å. It is noted that the O(1) – Ir(1) – C(40) angle deviates from 90 °, with an angle of 103.25°. This could be a result of the crystal packing in the solid state with the $SbF_6^-$ anion causing this

deviation from 90 °. **Figure 8.8** shows a space filling diagram of **3a** illustrating how close the counter-ion is to the carbonyl ligand.

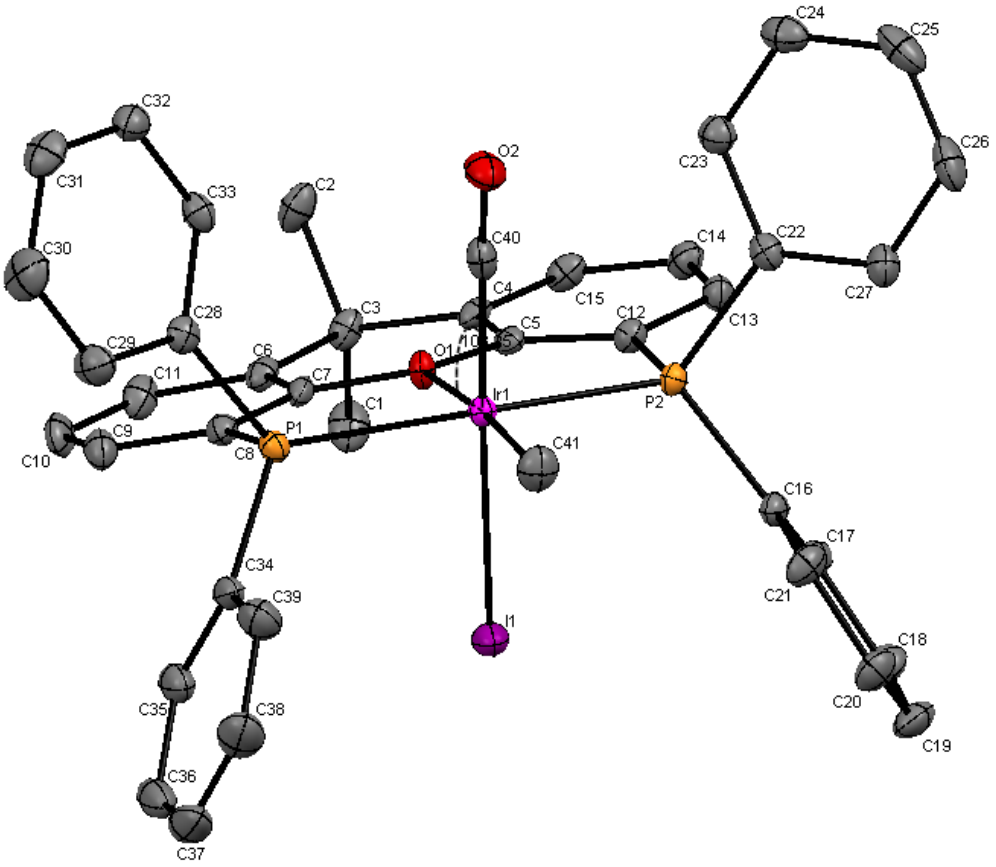


**Figure 8.7:** X-ray crystal structure of [IrI(CO)(Me)(xantphos)]$SbF_6$ **(3a)**. Hydrogen atoms, $SbF_6$ anion and solvent molecule omitted for clarity

| Bond | Length / Å | Bond | Length / Å |
|---|---|---|---|
| **Ir(1) – P(1)** | 2.3389(6) | **Ir(1) – O(1)** | 2.246(2) |
| **Ir(1) – P(2)** | 2.3377(6) | **Ir(1) – C (40)** | 1.872(3) |
| **Ir(1) – I(1)** | 2.6906(2) | **Ir(1) – C (41)** | 2.112(3) |
| | **Angle / °** | | **Angle / °** |
| **P(1) – Ir(I) - P(2)** | 162.43(2) | **C(41) – Ir(1) – O(1)** | 174.17(9) |
| **I(1) – Ir(I) – C(40)** | 174.65(8) | **O(1) – Ir(1) – C(40)** | 103.25(9) |

**Table 8.4:** Selected bond distances and angles in **3a**.

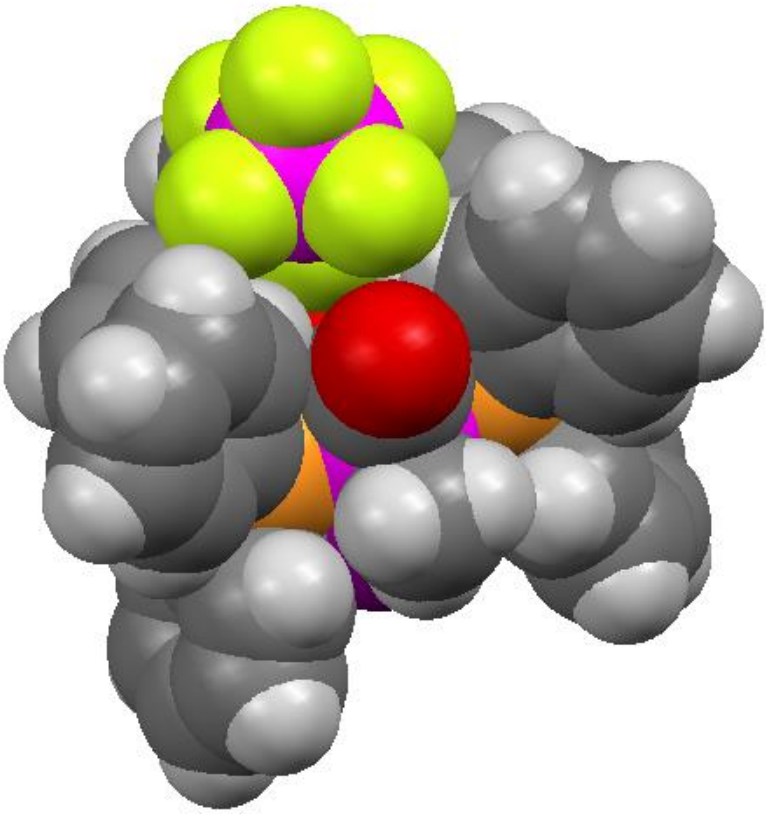

**Figure 8.8:** Space filling model of **3a** illustrating the packing of the counter-ion Solvent molecule omitted for clarity

### 8.2.5 Reaction of $[IrI_2(CO)_2]NBu_4$ and *o*-tol-xantphos – an unusual result

Since the reaction of xantphos with iridium precursors generated dicarbonyl complexes, it was of interest to investigate whether a more bulky xantphos derivative would yield a monocarbonyl complex. The structure of the *o*-tol-xantphos ligand is shown in **Figure 8.9.**

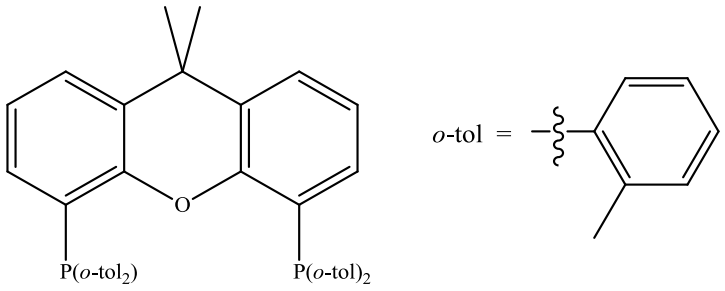


**Figure 8.9:** Structure of *o*-tol-xantphos ligand

The product of the reaction between $[IrI_2(CO)_2]NBu_4$ and *o*-tol-xantphos had a ν(CO) band at 2028 $cm^{-1}$ with a noticeable shoulder at a higher wavenumber and a further unexpected band at 2253 $cm^{-1}$. The mass spectrum contained a signal at m/z 855 consistent with $[Ir(CO)(o\text{-tol-xantphos})]^+$. It is not uncommon to observe the loss of halides for such species in electrospray mass spectrometry. The $^{31}P\{^1H\}$ NMR contained four doublets in a 2:3:3:2 ratio as shown in **Figure 8.10.** Two pairs of doublets would suggest the formation of two species each containing two inequivalent phosphorus atoms.

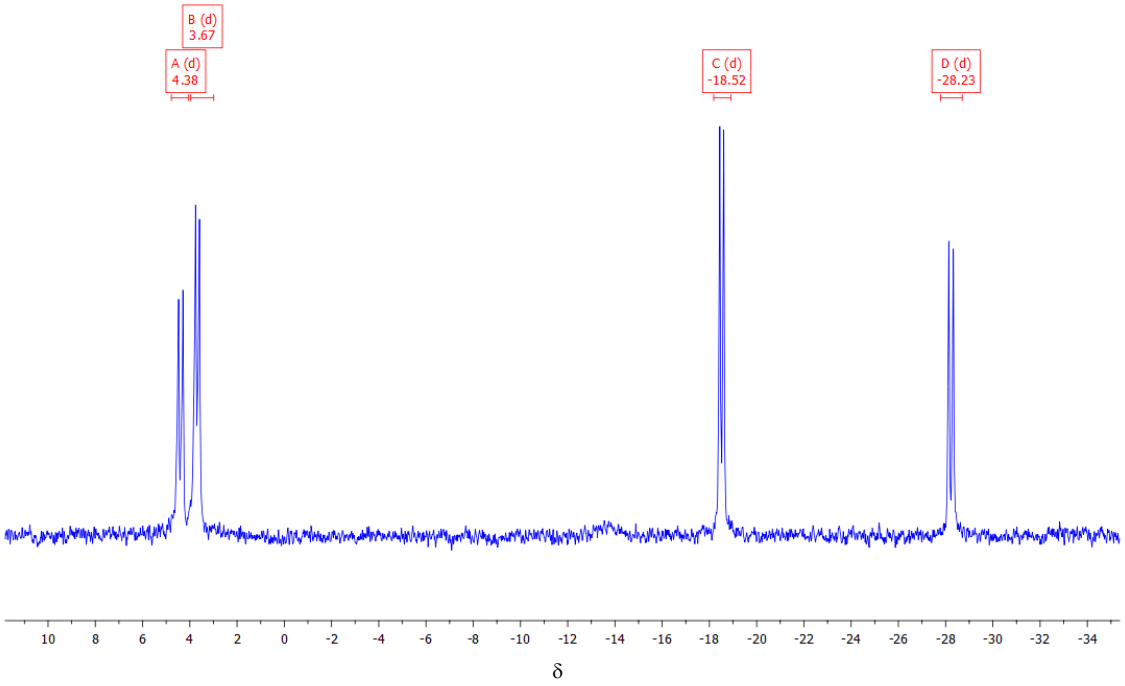


**Figure 8.10:** $^{31}P\{^1H\}$ NMR spectrum for the products of the reaction of $[IrI_2(CO)_2][Bu_4N]$ with *o*-tol-xantphos. ($CDCl_3$)

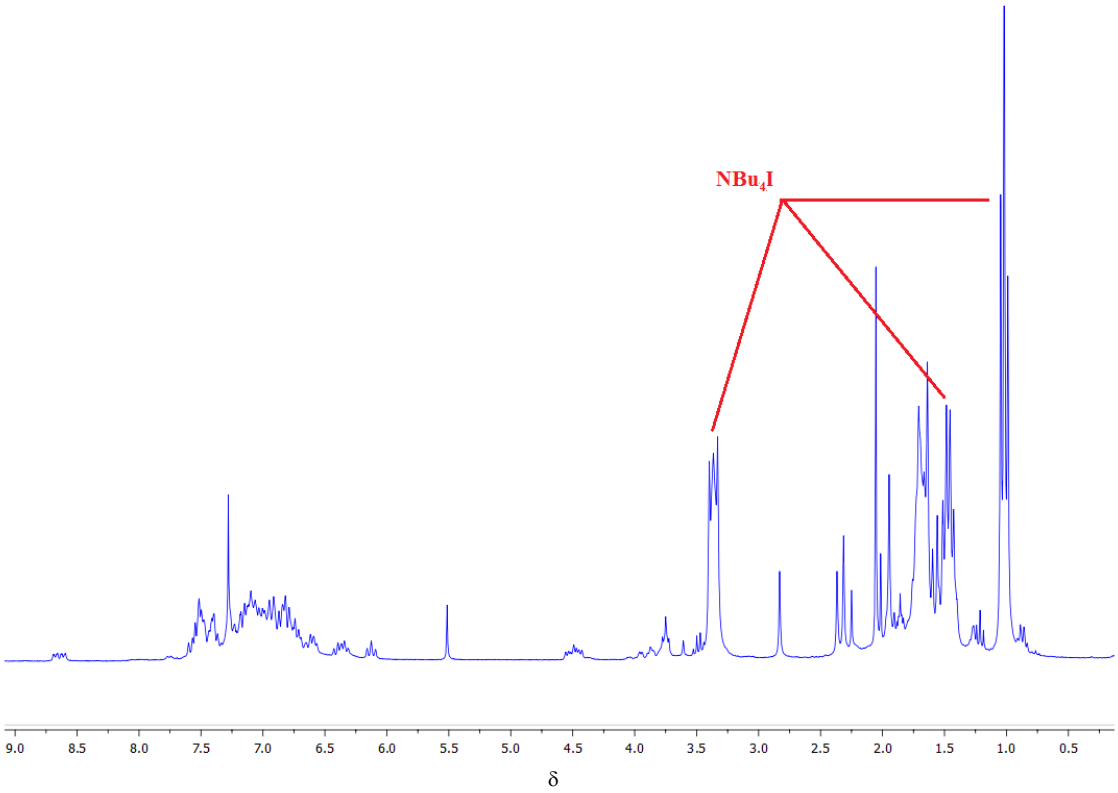


**Figure 8.11:** $^{1}$H NMR spectrum of the products from the reaction of $[IrI_2(CO)_2]Bu_4N$ and *o*-tol-xantphos

Analysis of the $^{1}$H NMR spectrum (shown in **Figure 8.11**) was complicated both by the presence of $Bu_4NI$, which could not be separated from the complex and by the presence of multiple isomers. Interestingly, the hydride region of the $^{1}$H NMR spectrum contained two doublet of doublets in a 3:2 intensity ratio as shown in **Figure 8.12.**

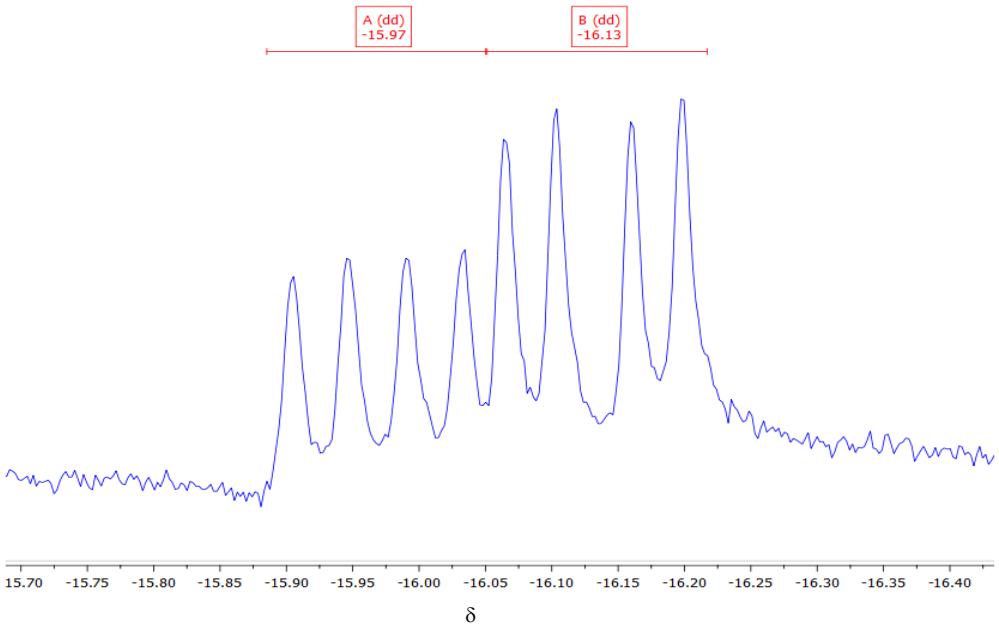


$J_{P\text{-}H}$ = 21.7 Hz $J_{P\text{-}H}$ = 23.9 Hz

$J_{H\text{-}H}$ = 10.6 Hz $J_{H\text{-}H}$ = 9.6 Hz

**Figure 8.12:** Hydride region of the $^{1}H$ spectrum of the products from the reaction of $[IrI_2(CO)_2][Bu_4N]$ and *o*-tol-xantphos

Hydride species are consistent with a C-H activation having taken place. The solvent used to synthesise the complex was THF, which was unlikely to undergo C-H activation. It was therefore believed that the oxidative addition must have occurred intramolecularly. A recent publication containing a variant xantphos ligand underwent C-H activation on iridium. [17] The methyl groups on the *o*-tol-xantphos ligand are close enough to the metal that they could potentially be activated.

A crystal suitable for x-ray analysis was grown from slow evaporation of diethyl ether into a concentrated $CH_2Cl_2$ solution. The structure is shown in **Figure 8.13** and selected geometric data are given in **Table 8.5.** Some disorder of the carbonyl ligand and activated *o*-tol ring is noted. As suggested, one of the methyl ring substituents has undergone C-H activation to form a cyclometallated species containing a five membered ring.

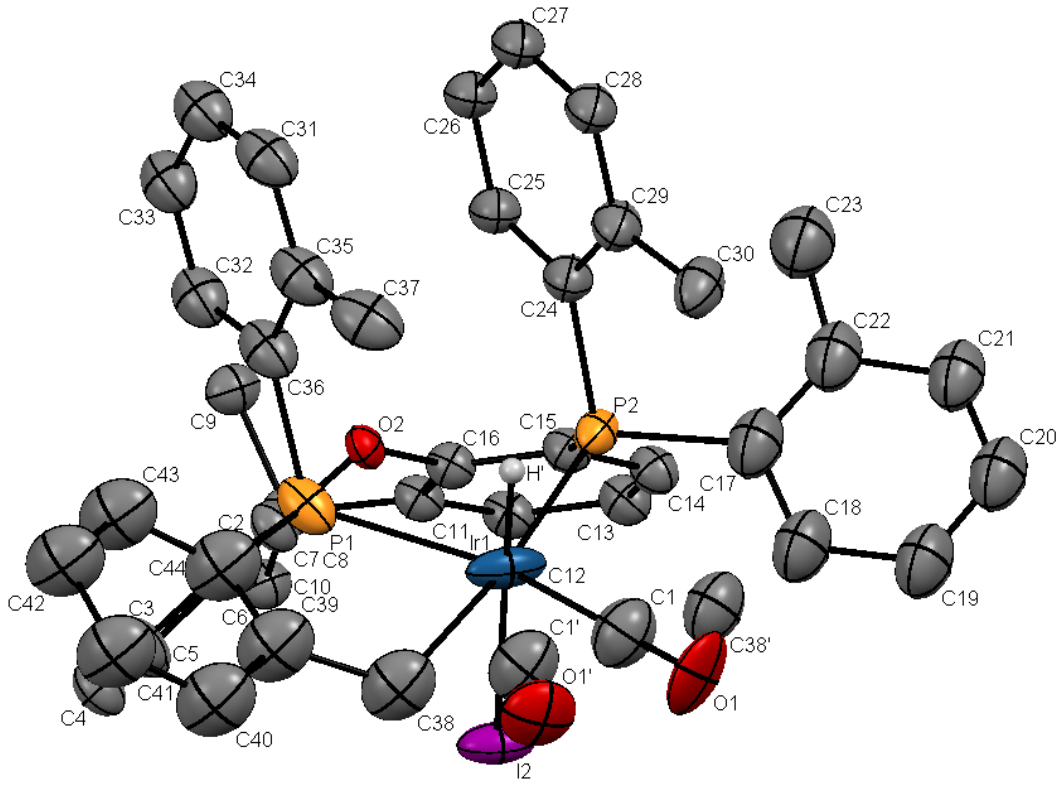


**Figure 8.13:** X-ray crystal structure of **4a.** Hydrogen atoms and solvent molecules omitted for clarity.

| | **Length / Å** | | **Length /Å** |
|---|---|---|---|
| **Ir(1) – P(1)** | 2.384(4) | **Ir(1) – C (1)** | 1.788(2) |
| **C(1) - O(1)** | 1.15(3) | **Ir(1) – I(2)** | 2.793(2) |
| **Ir(1) – P(2)** | 2.404(3) | **Ir(1) – H'** | 1.552(1) |
| | **Angle / °** | | **Angle / °** |
| **P(1) - Ir(1) – P(2)** | 100.20(12) | **P(2) – Ir(1) – C(38)** | 173.34(5) |
| **P(1) – Ir(1) – C(1)** | 150.96(7) | **H' – Ir(1) – I(2)** | 179.53 |

**Table 8.5:** Selected bond distances and angles in **4a**.

The activated *o*-tol-xantphos ligand coordinates to iridium in a *mer* tridentate P, P, C fashion with a P-Ir-P bond angle of 100.2 °. Xantphos complexes have been reported in the literature with P-M-P angles of as low as 98 °. In order for xantphos to coordinate in such a fashion, the backbone must flex considerably. For this complex, the angle between the planes of the aromatic rings is approximately 43 °.

Interestingly, two of the *o*-tol rings are orientated almost parallel, presumably due to favourable π–π stacking interactions. It is also noteworthy that the methyl groups of these two rings are pointed towards the iridium centre. Viewing the crystal structure as a space filling model shows that if the methyl groups were rotated away from the metal centre, there would be an unfavourable steric clash with one of the methyl groups on the xanthene backbone.

From the data collected thus far, the following scheme is proposed where the complex initially formed is the desired [IrI(CO)(*o*-tol-xantphos)], which subsequently undergoes oxidative addition of the C-H bond of a methyl group on the ligand to form a cyclometallated species. Cyclometallated species are well known for ruthenium, palladium, platinum and iridium complexes so there is a precedence for such observations.

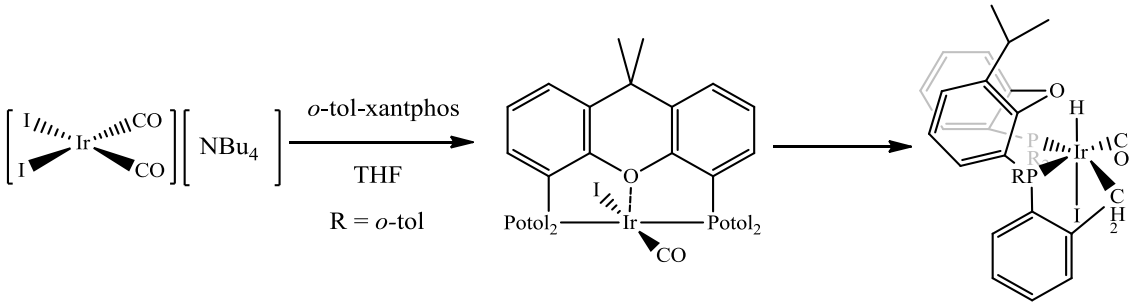


**Scheme 8.7:** Proposed reaction scheme of $[IrI_2(CO)_2][Bu_4N]$ and *o*-tol-xantphos

## 8.2.6 Ligand modification

Difficulties were encountered in synthesising further samples of both *o*-tol-xantphos and variant ligands by the published methods. In some cases a byproduct, identified as $Ar_2PP(=O)Ar_2$ was found to form. A modified high yielding synthetic pathway was therefore adopted as shown in **Scheme 8.8.** This led to a variant of *o*-tol-xantphos having methyl groups in the 2 and 7 position on the xanthene backbone.

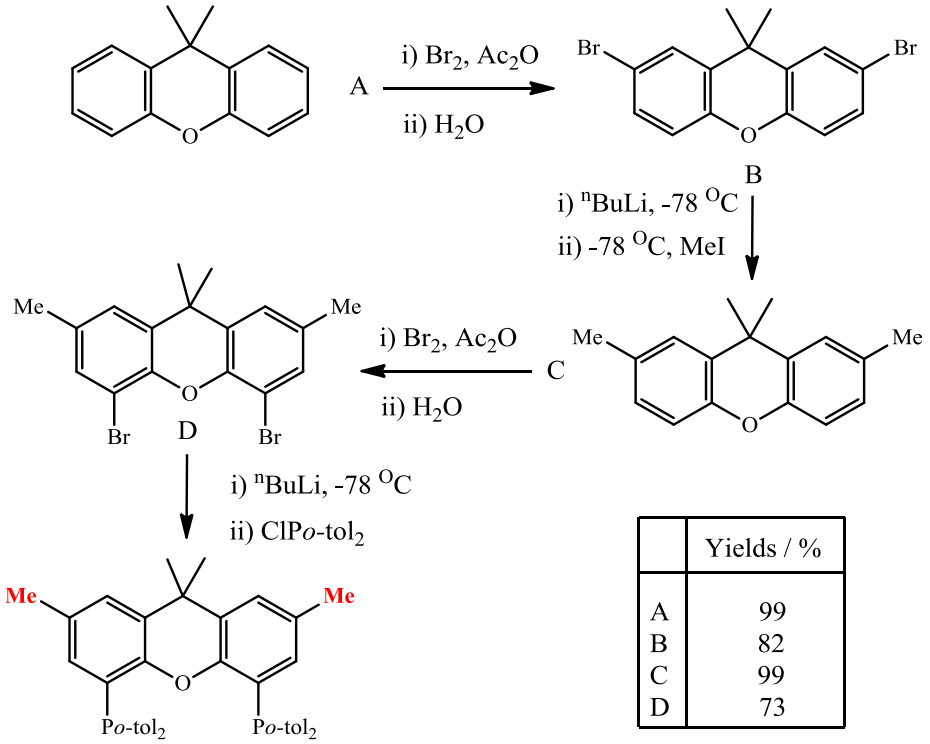


| | Yields / % |
|---|---|
| A | 99 |
| B | 82 |
| C | 99 |
| D | 73 |

**Scheme 8.8:** Synthesis of R-xantphos' ligands with 2-7 dimethyl substitution shown in red.

To ensure that the modification to the ligand did not affect its reactivity towards iridium precursors, the reaction in **Scheme 8.9** was attempted. The cation in the iridium precursor was changed from $NBu_4^+$ to $Ph_4As^+$ which was easier to remove from the product.

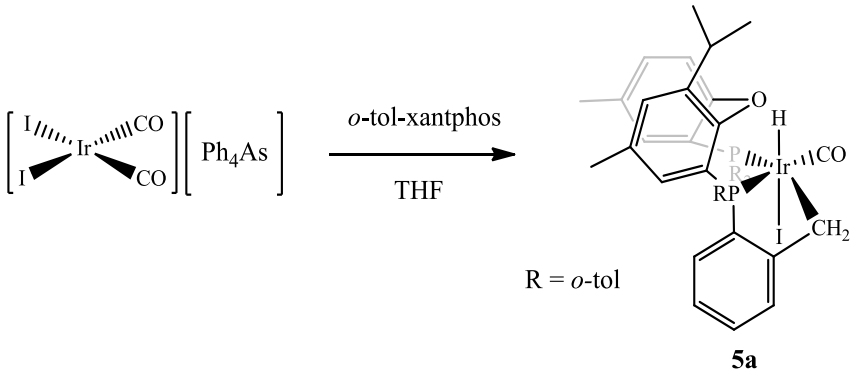


**Scheme 8.9**: Reaction scheme of $[IrI_2(CO)_2][Ph_4As]$ and *o*-tol-xantphos to form **5a**.

**Figure 8.14** shows overlaid $^{31}P$ NMR spectra for **4a** and **5a** and the corresponding hydride regions of the $^{1}H$ NMR spectra are shown in **Figure 8.15.** Modification to the

ligand in **5a** has a minor effect on the chemical shifts of the phosphorus doublets but the product ratios are almost identical. The hydride signals for each isomer are marginally more separated in **5a** than **4a.**

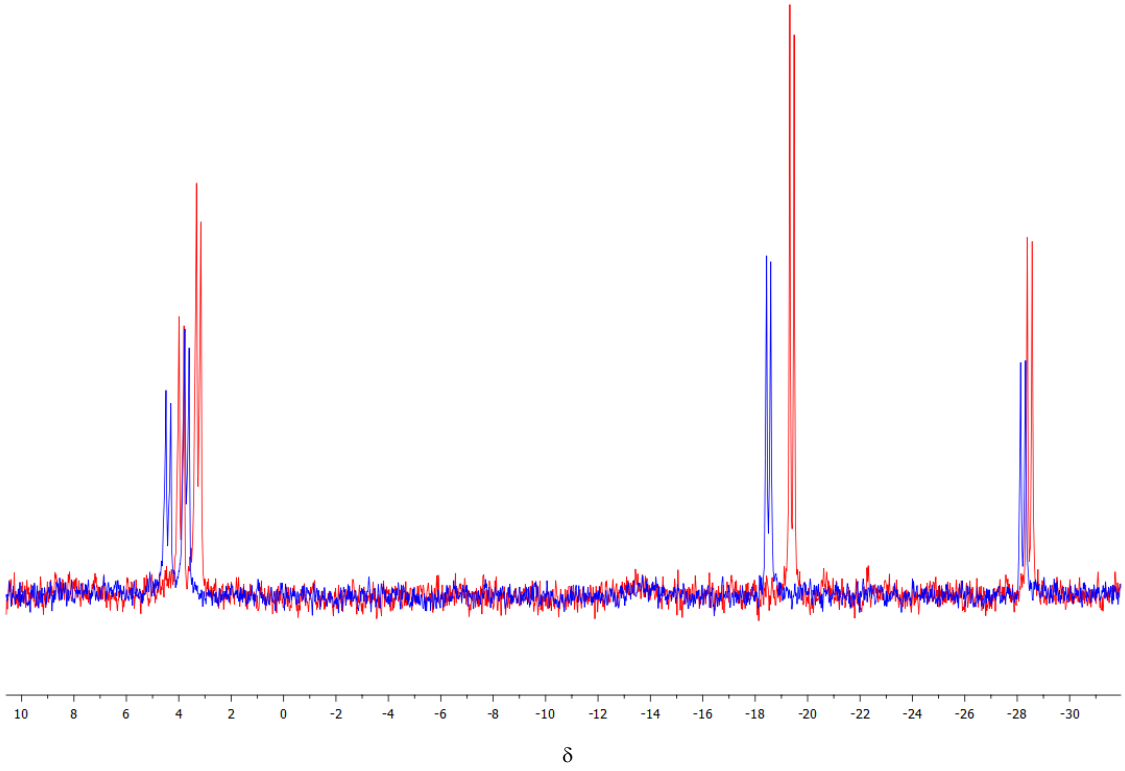


**Figure 8.14**: Overlaid $^{31}P$ NMR spectra of **4a** and **5a**. ($CDCl_3$)

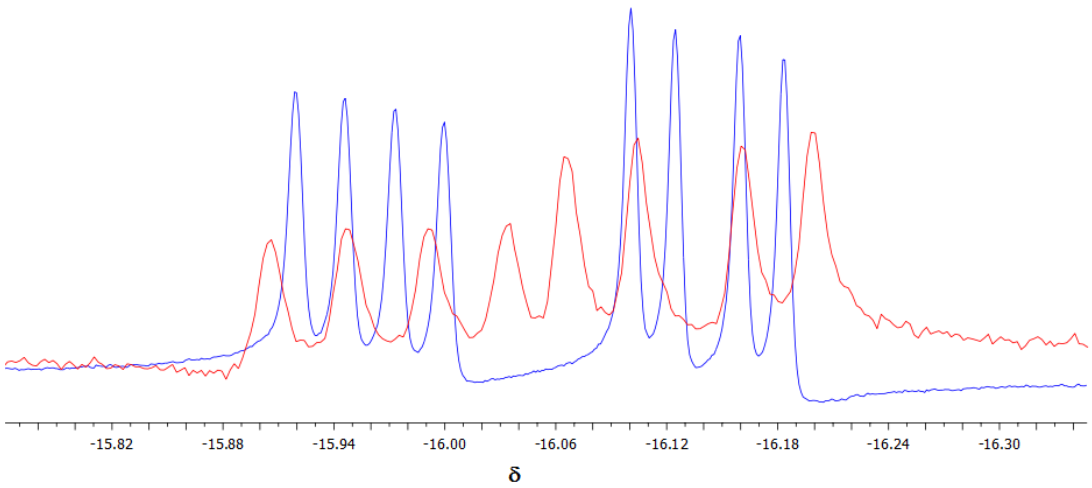


**Figure 8.15**: Overlaid hydride regions of $^{1}H$ NMR spectra of **4a** (red-250MHz) and **5a** (blue – 400 MHz). ($CDCl_3$)

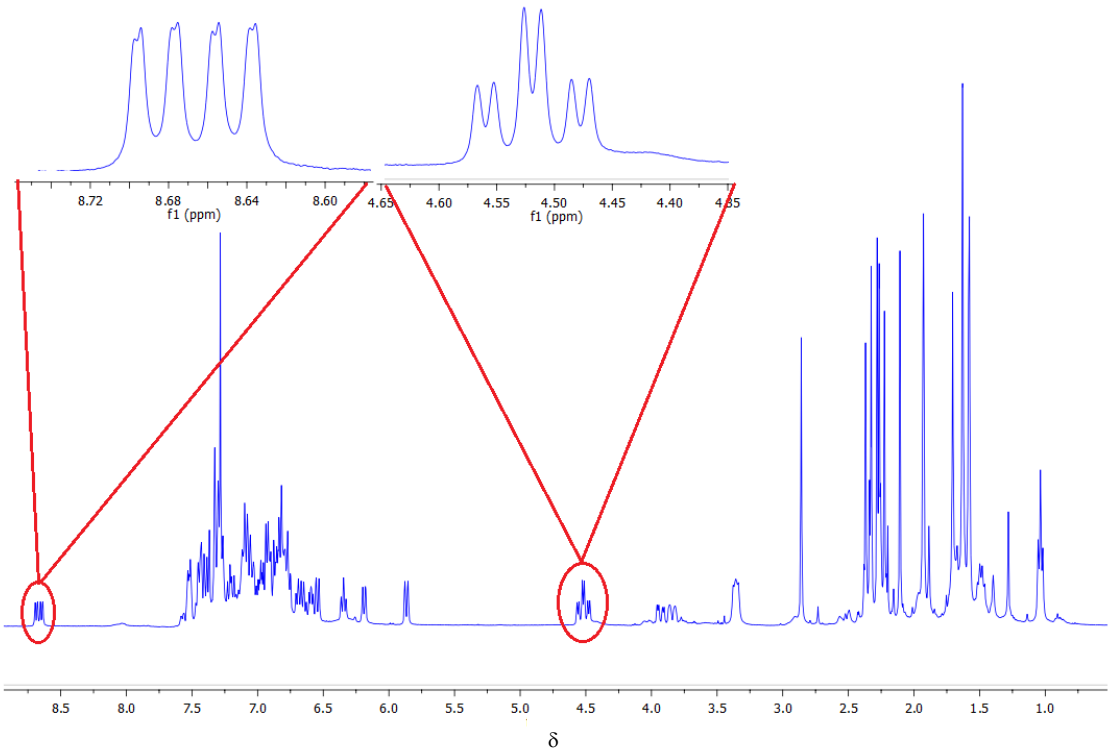


**Figure 8.16**: $^{1}$H NMR spectrum of **5a.** ($CDCl_3$)

The bi-product $Ph_4AsI$ was easily removed from the product complex which allowed the $^{1}$H NMR spectrum, shown in **Figure 8.16,** to be further examined. In the aromatic region, there is a notable multiplet at a high chemical shift (inset in **Figure 8.16**). The aliphatic region shows multiple signals for the methyl groups on the xanthene backbone and the tolyl groups. The region δ 3.0-4.5 shows several multiplets which are assigned to the $CH_2$-Ir protons.

A $^{13}$C and a C-H correlation NMR were also recorded (**Appendix Fig. A6**). Two signals at 174.76 (dd, $J$ = 132.3, 6.6 Hz) and 176.06 (dd, $J$ = 134.6, 6.2 Hz) are assigned to the metal carbonyls of each isomer, split by the *cis* and *trans* phosphorus atoms. Two further signals at 8.57 (dd, $J$ = 72.5, 2.1 Hz) and 7.63 (dd, $J$ = 72.1, 2.1 Hz) correlate with the proton signals at 4.53, 3.94 and 3.89 and hence are assigned to the Ir-$CH_2$ carbons of each isomer.

In order to assist the interpretation of the spectrum, a DFT simulated spectrum was generated. It was reasonable to assume that one isomer had the same structure as the

crystal structure of **4a** so this was used as a starting point with modifications to include the additional methyl substituents. The simulated spectrum is showed in **Figure 8.17.**

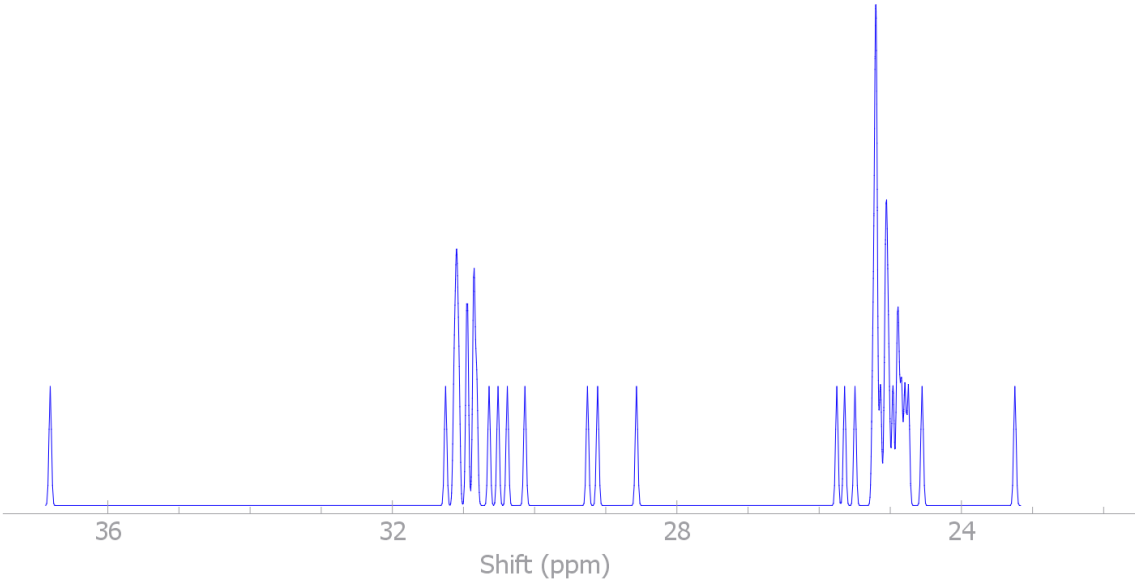


**Figure 8.17:** Simulated $^{1}$H NMR spectrum generated from the crystal structure of **5a**

It is noted that the simulated spectrum has a different scale to the experimental spectrum. However, a number of similarities can be drawn between the simulated and experimental spectra. Initially, a signal is observed in the experimental spectrum at δ 8.67 (expanded in **Figure 8.16**), which appears to be a doublet of doublets. A corresponding signal is observed in the simulated spectrum – shifted downfield relative to the other aromatic protons. This is assigned to one of the phenyl ring protons with the splitting attributed to the neighbouring phosphine and ring protons. **Figure 8.18** shows the proton (highlighted in red). The downfield shift of this proton is potentially due to its proximity to the carbonyl oxygen.

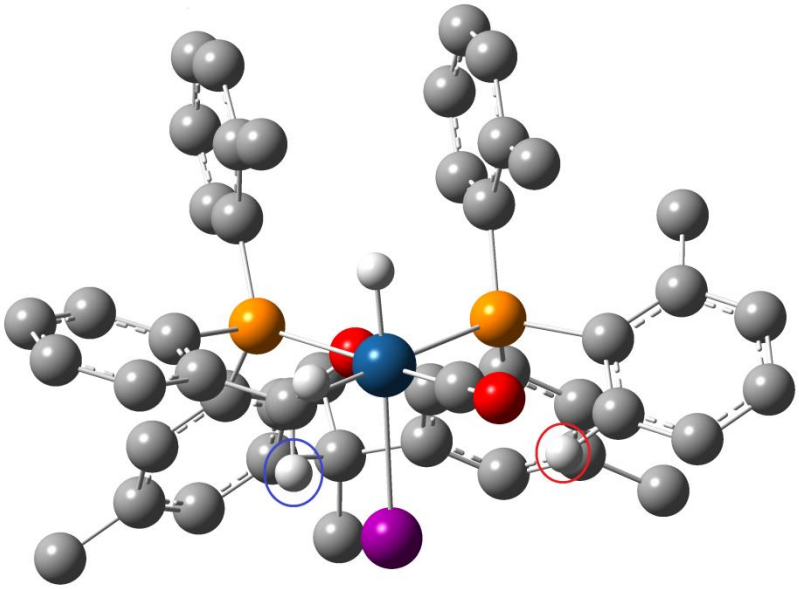

**Figure 8.18:** Optimised structure of **5a** showing the hydrogen atom of interest

There is a triplet of doublets in the experimental spectrum at δ 4.52 (td, $J$ = 16.6, 5.9 Hz), which integrates to one hydrogen. This peak is assigned to one of the hydrogens on the $CH_2$ directly attached to the iridium atom. The splitting pattern is likely a result of coupling to two inequivalent phosphines and the other hydrogen of the $CH_2$.

The experimental $^{31}P$ NMR and hydride region on the $^{1}H$ NMR spectrum confirmed the presence of two isomers. Computational investigations were undertaken to try and identify the structure of the other isomer. Many of the isomers were significantly higher in energy than the optimised crystal structure (12 – 40 kJ $mol^{-1}$). However, one structure was optimised which only differed from the crystal structure of by 0.82 kJ $mol^{-1}$. It's structure is shown in **Figure 8.19.**

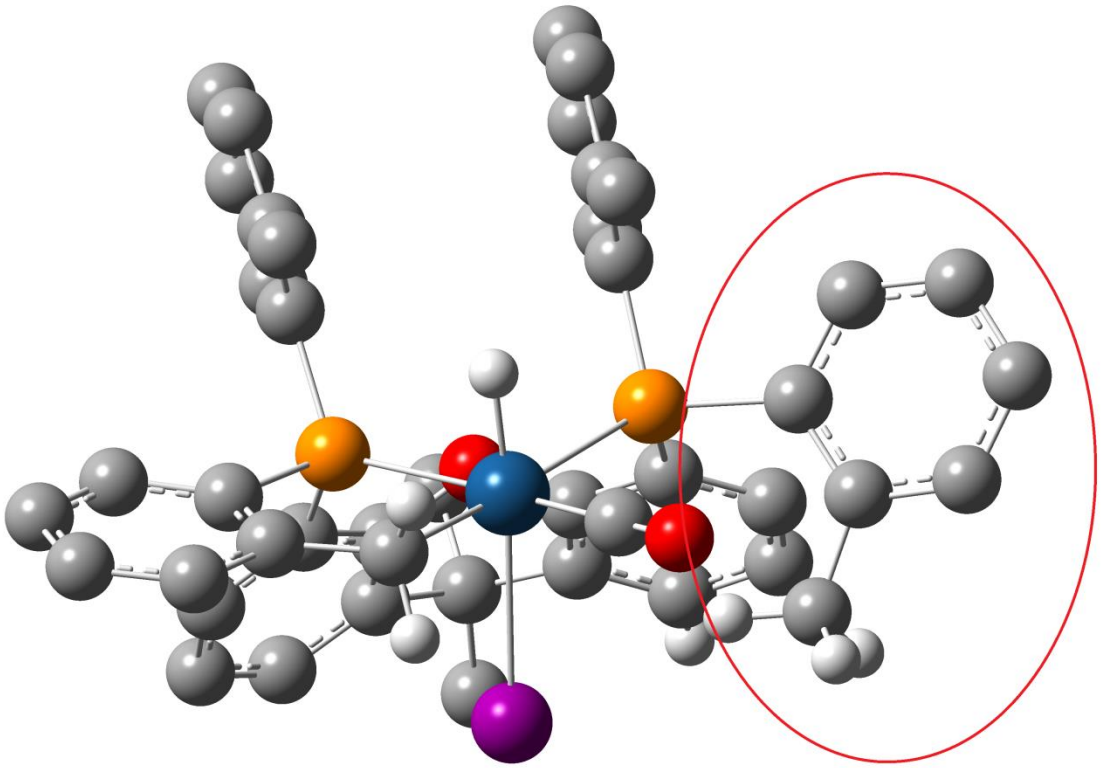

**Figure 8.19:** Optimised isomer of **5a**

The only difference between the two structures is circled in red in **Figure 8.19**. The ring is rotated relatively to the crystal structure. Free rotation around the carbon-phosphorus bond is potentially hindered due to the other rings in the ligand so this could be a unique isomer in its own right. The proximity of the methyl group on the circled ring to the carbonyl has caused a slight distortion and the predicted wavenumber is higher relative to the crystal structure which is consistent with experimental observations. The proton highlighted earlier in red in **Figure 8.18** is now in a significantly different position due to the rotation of the ring which again is consistent with the experimental and simulated NMR spectra. The simulated NMR spectrum of this complex does not have a proton environment downfield of the other aromatic protons.

The differences in the Gibbs energy of the crystal structure and the other potential isomer leads to a predicted isomer ratio of 2:2.5 which is reasonably consistent with the experimentally observed values of 2:3.

### 8.2.7 Reaction of 5a with $AgBF_4$

The reaction of **5a** with $AgBF_4$ in $CH_2Cl_2$ led to immediate precipitation of AgI and a lightening of the solution. The yellow product obtained had a ν(CO) band at 1999 $cm^{-1}$ and the $^{31}P\{^1H\}$ NMR spectra contained only a singlet at δ 25.19, consistent with equivalent phosphorus atoms which must be *trans*. No peaks associated with hydrides were observed in the $^1H$ NMR.

A carbonyl stretching frequency of 1999 $cm^{-1}$ is much lower than would be expected for an iridium(III) cation and is typically associated with iridium (I) cations. A lack of any hydride peaks in the $^1H$ NMR spectrum suggests that the complex has lost its hydride. Prolonged stirring of a solution of this complex with excess $Bu_4NI$ regenerates the C-H activated species.

Based upon this evidence, the reaction scheme in **Scheme 8.10** is proposed. Removal of the iodide initiates CH reductive elimination to form an iridium(I) cationic species.

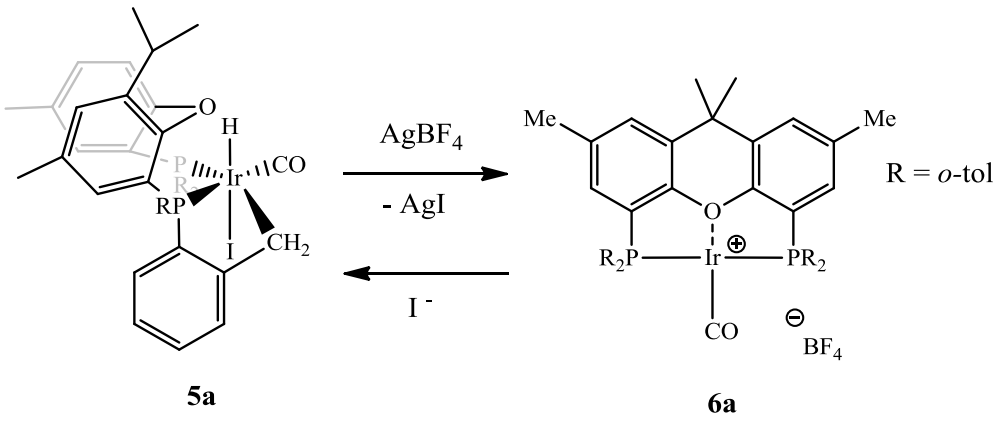


**5a** **6a**

**Scheme 8.10:** Proposed reaction scheme for the halide abstraction from **5a**.

Computational investigations were undertaken on the proposed mechanism as shown in **Figure 8.20.** The cationic reactant structure was based upon the crystal structure of **4a**. Methyl groups were added in the 2 and 7 positions of the xantphos backbone and the iodide ligand was removed before the complex was optimised with no symmetry or geometry constraints. The C-H elimination transition state is 69.6 kJ $mol^{-1}$ higher in

energy than the starting material and the optimised product is 91.0 kJ $mol^{-1}$ more stable than the reactant. Such a barrier height corresponds to an experimental rate constant of about 3 $s^{-1}$, which is consistent with the rapid reaction observed upon addition of the silver salt to abstract an iodide.

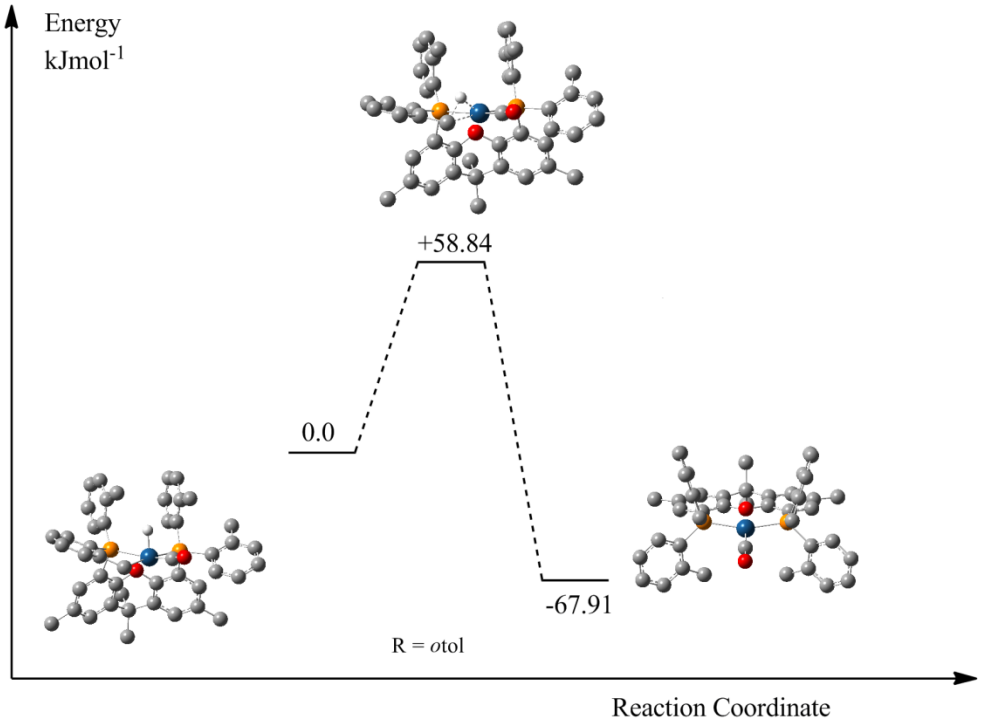


**Figure 8.20:** Energy profile ($\Delta H^{\ddagger}$) for the C-H de-activation reaction.

The C-H activation step was also investigated computationally. **Figure 8.21** shows the reaction profile for activation from the neutral Ir(I) complex with iodide coordinated.

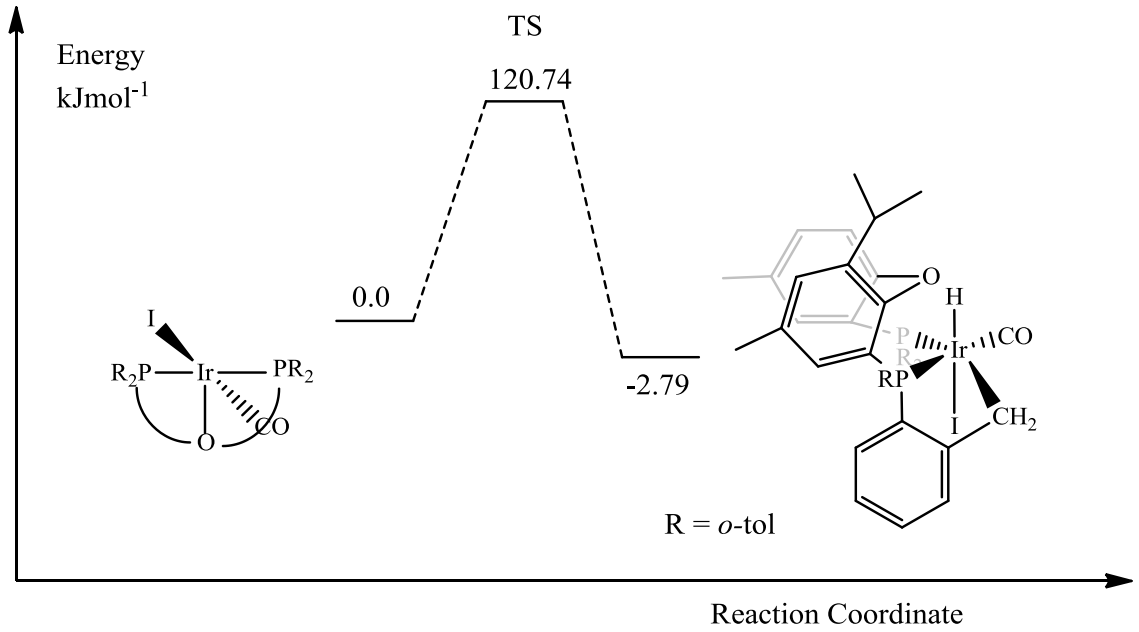


**Figure 8.21:** Energy profile ($\Delta H^{\ddagger}$) for the C-H activation reaction.

There is a larger barrier height than was observed for deactivation from the cationic species. This is consistent with experimental observations where C-H activation was only observed after prolonged stirring.

## 8.2.8 Synthesis and characterisation of [Ir(CO)($^{t}$Bu-xantphos)]I (7a)

The reaction of $^{t}$Bu-xantphos with $[IrI_2(CO)_2]Bu_4N$ gave a product with a ν(CO) band at 1982 cm$^{-1}$. The $^{31}P\{^{1}H\}$ NMR also had a single peak at δ 73.95 and the mass spectrum had a single ion peak at m/z 719.2 assigned to $[Ir(CO)(^{t}Bu\text{-xantphos})]^{+}$. Crystals suitable for X-ray crystallography were grown by slow evaporation of diethyl ether into a concentrated $CH_2Cl_2$ solution of the complex. The structure is shown in **Figure 8.22.**

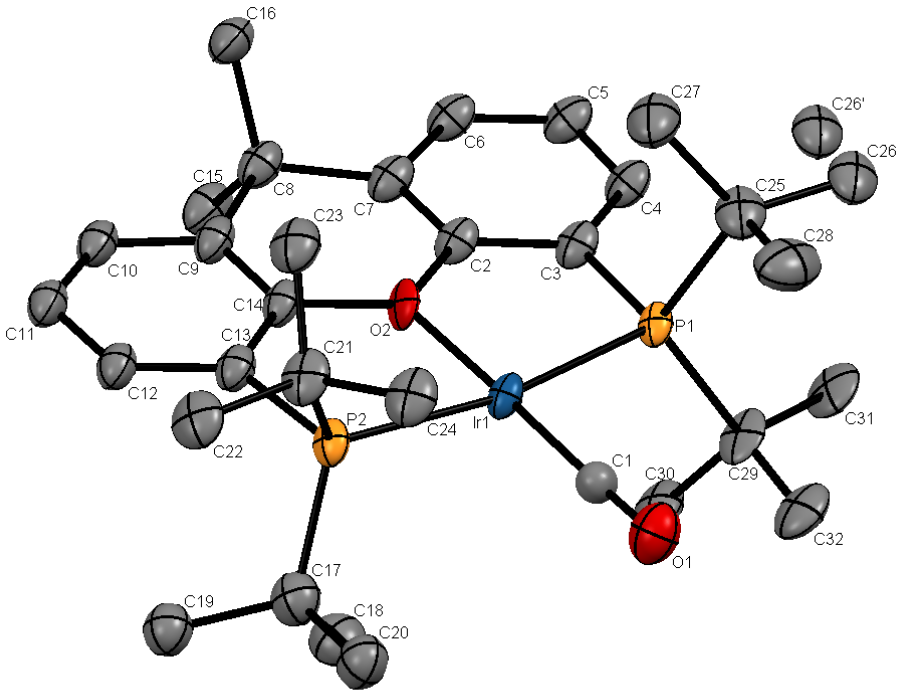


**Figure 8.22:** Crystal structure of **7a.** (Hydrogen atoms, iodide ion and solvent molecules omitted for clarity)

| | **Length / Å** | | **Length / Å** |
|---|---|---|---|
| **Ir(1) – P(1)** | 2.298(4) | **Ir(1) – O(2)** | 2.118(8) |
| **Ir(1) – P(2)** | 2.302(3) | **C(1) – O(1)** | 1.176(5) |
| **Ir(1) – C(1)** | 1.928(3) | | |
| | **Angle / °** | | **Angle / °** |
| **P(1) - Ir(1) – P(2)** | 167.21(11) | **P(2) – Ir(1) – C(1)** | 95.71(4) |
| **O(2) – Ir(1) – C(1)** | 178.73(4) | **P(1) – Ir(1) – C(1)** | 97.06(4) |

**Table 8.6:** Selected bond distances and angles in **7a.**

The complex adopts a distorted square-planar configuration with the $^{t}$Bu-xantphos acting as a *mer*-tridentate P,O,P chelating ligand. Many examples of this coordination mode are present in the literature.[19-23] The Ir-O interatomic distance is 2.118 Å, indicating that there is a dative bond.

The structure and reactivity of a related complex, [Rh(CO)($^{t}$Bu-xantphos)]I was investigated by Williams et al.. Both the iridium and rhodium complexes adopt a similar

structure whereby the halide is not coordinated to the complex and forms an ion-pair. The rhodium complex did not react with iodomethane so it was of interest to investigate the reactivity of the iridium complex. A sample of complex was stirred in neat iodomethane over 24 hours whereupon no change in either the infra-red or $^{31}P\{^{1}H\}$ NMR spectrum was observed. The *tert*-butyl substituents are highly electron donating suggesting that the metal centre will be electron rich. Viewing the crystal structure as a space filling diagram (**Figure 8.23)** shows that the iridium centre is almost completely blocked by the bulky *tert*-butyl groups. It is clear that oxidative addition of iodomethane is inhibited by the steric bulk of the $^{t}$Bu-xantphos ligand.

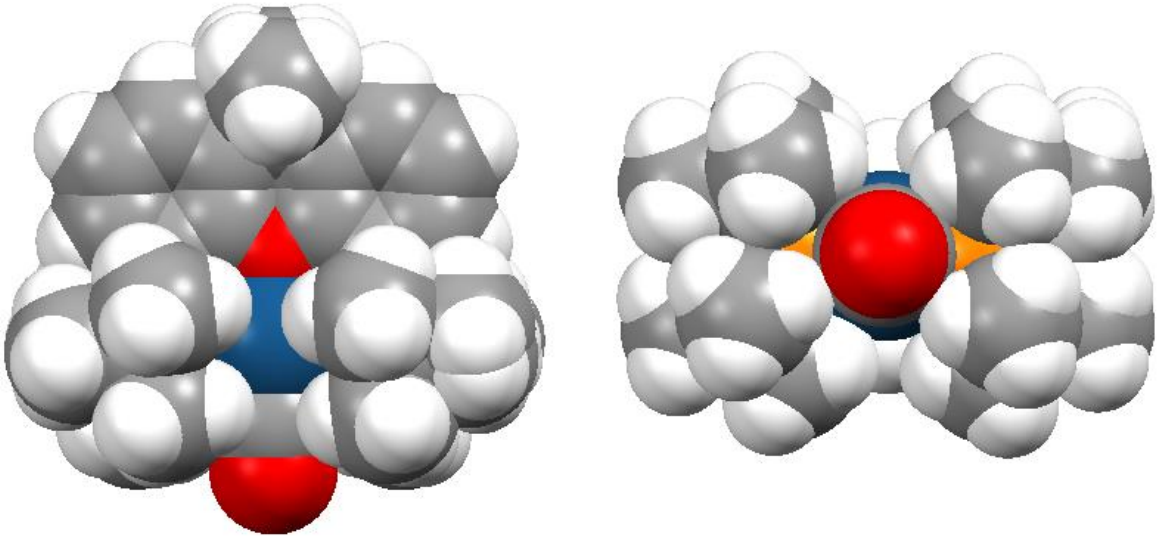

**Figure 8.23:** Crystal structure of **7a** viewed as a space filling diagram from above and along the CO – Ir – O "bond". Iodide ion omitted for clarity.

As the complex was unreactive towards MeI, $H_2$ was investigated to see whether a much smaller molecule could approach the iridium centre. A small sample of **7a** was dissolved in $CH_2Cl_2$ and dihydrogen was bubbled through the solution for around three hours. A new carbonyl band was observed to slowly grow at 2008 $cm^{-1}$, consistent with the formation of an iridium(III) species. The $^{31}P\{^{1}H\}$ NMR spectrum obtained had a principal peak corresponding to the starting material and another singlet at δ 63.79 (11 %) indicating a new complex had formed.

The hydride region of the $^1$H NMR spectrum contained two triplets of doublets with equal intensity as shown in **Figure 8.24.** This is consistent with two inequivalent hydride ligands with $J_{PH}$ and $J_{HH}$ coupling as indicated in the figure.

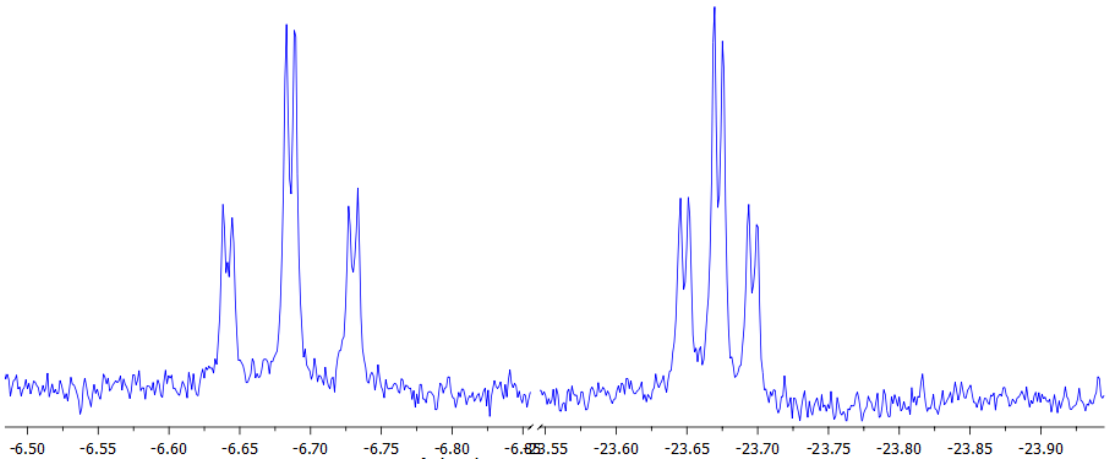


$J_{P-H}$ = 17.8 Hz $J_{P-H}$ = 9.7 Hz

$J_{H-H}$ = 2.4 Hz $J_{H-H}$ = 2.4 Hz

**Figure 8.24:** Hydride region of $^1$H NMR spectrum of [Ir(H)$_2$(CO)($^t$Bu-xantphos)]I

The coupling constants indicate *cis* hydride ligands as expected for a $H_2$ oxidaitcve addition. The proposed reaction scheme is shown in **Scheme 8.11.**

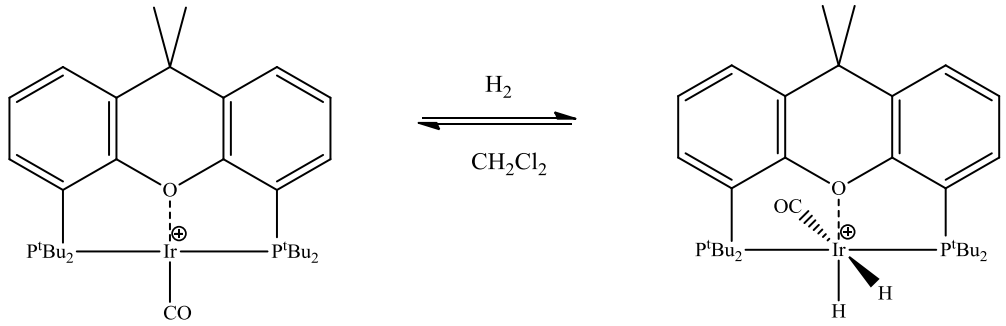


**7a** **8a**

**Scheme 8.11:** Proposed reaction scheme for the reaction of dihydrogen with **7a.**

The addition of hydrogen to the metal complex is reversible in the absence of hydrogen. The infra-red spectrum showed complete conversion back to starting material overnight. This process could be accelerated by bubbling nitrogen through the solution.

## 8.3 Conclusions

The complexation of xantphos to $[IrI_2(CO)_2]Bu_4N$ results in a dicarbonyl species, $[IrI(CO)_2$(xantphos)], **1a.** The reaction of **1a** with iodomethane results in a mixture of two isomers of formula $[IrI_2(CO)(Me)$(xantphos)]. A crystal structure showed that the phosphorus atoms were *cis* to one another and *trans* to a methyl and an iodide ligand. Computational evidence suggests that the other isomer has the iodide ligands *trans* to one other. Iodide abstraction from **2a** forms a cationic species with a singlet in the $^{31}P$ NMR with computational evidence suggesting there are two possible structures consistent with experimental observations.

Reaction of *o*-tol-xantphos with iridium precursors results in the formation of two C-H activated complexes in an approximate 3:2 ratio. The structure of one isomer was confirmed crystallographically and computational evidence suggests the other isomer may have a similar structure where only one of the rings is rotated relative to the crystal structure.

Abstraction of the iodide ion from these isomers facilitates C-H deactivation to form an iridium(I) cation where the phosphorus atoms are now equivalent. Addition of excess iodide to the cationic species results in C-H reactivation to form a mixture of products with a similar isomeric ratio to what was initially observed.

The reaction of $^{t}$Bu-xantphos with $[IrI_2(CO)_2][AsPh_4]$ forms a cationic species **(7a)** which is inert towards iodomethane due to the extreme steric bulk of the ligand. The complex reversibly reacts with hydrogen to form an iridium (III) dihdyride species though the reaction does not go to completion.

## 8.4 References


(1) Kranenburg, M.; van der Burgt, Y. E. M.; Kamer, P. C. J.; van Leeuwen, P. W. M. N.; Goubitz, K.; Fraanje, J. *Organometallics*, **1995**, *14* 3081.

(2) del Rio, I.; Ruiz, N.; Claver, C.; van der Veen, L. A.; van Leeuwen, P. W. N. M. *J. Mol. Catal. A: Chemical* **2000**, *161*, 39.

(3) Guari, Y.; van Es, D. S.; Reek, J. N. H.; Kamer, P. C. J.; van Leeuwen, P. W. N. M. *Tetrahedron Lett.* **1999**, *40*, 3789.

(4) Harris, M. C.; Geis, O.; Buchwald, S. L. *J. Org. Chem.* **1999**, *64*, 6019.

(5) Kranenburg, M.; Kamer, P. C. J.; van Leeuwen, P. W. M. N. *Eur. J.Inorg. Chem.* **1998**, 25.

(6) Kranenburg, M.; Kamer, P. C. J.; van Leeuwen, P. W. N. M. *Eur. J.Inorg. Chem.* **1998**, 155.

(7) Kranenburg, M.; Kamer, P. C. J.; van Leeuwen, P. W. N. M.; Vogt, D.; Keim, W. *J. Chem. Soc. Chem. Commun.* **1995**.

(8) van Leeuwen, P. W. M. N.; Kamer, P. C. J.; Reek, J. N. J.; Dierkes, P. *Chem. Rev.* **2000**, *100*, 2741.

(9) Fox, D. J.; Duckett, S. B.; Flaschenriem, C.; Brennessel, W. W.; Schneider, J.; Gunay, A.; Eisenberg, R. *Inorg Chem.* **2006**, *45* 7197.

(10) Asensio, G.; Cuenca, A. B.; Esteruelas, M. A.; Medio-Simón, M.; Oliván, M.; Valencia, M. *Inorg. Chem.*, **2010**, *49*, 8665.

(11) Esteruelas, M. A.; Oliván, M.; Vélez, A. *Inorg. Chem.*, **2013**, *52*, 5339−5349.

(12) Pontiggia, A. J.; Chaplin, A. B.; Weller, A. S. *J. Organomet. Chem.*, **2011**, *696*, 2870.

(13) Williams, G. L.; Parks, C. M.; Smith, C. R.; Adams, H.; Haynes, A.; Meijer, A. J. H. M.; Sunley, G. J.; Gaemers, S. *Organometallics.*, **2011**, *30*, 6166.

(14) Deb, B.; Borah, B. J.; Sarmah, B. J.; Das, B.; Dutta, D. K. *Inorg Chem. Comm.*, **2009**, *12*, 868.

(15) Ledger, A. E. W.; Mahon, M. F.; Whittlesey, M. K.; Williams, J. M. J. *Dalton Trans.*, **2009**, 6941.

(16) Ledger, A. E. W.; Slatford, P. A.; Lowe, J. P.; Mahon, M. F.; Whittlesey, M. K.; Williams, J. M. J. *Dalton Trans.*, **2008**, 716.

(17) Esteruelas, M. A.; Oliván, M.; Vélez, A. *Inorg. Chem.*, **2013**, *52*, 5339.

(18) Parr, M. L.; Perez-Acosta, C.; Faller, J. W. *New J. Chem.*, **2005**, *29*, 613.

(19) Julian, L. D.; Hartwig, J. F. *J. Am. Chem. Soc.*, **2010**, *132*, 13813.

(20) Ledger, A. E. W.; Moreno, A.; Ellul, C. E.; Mahon, M. F.; Pregosin, P. S.; Whittlesey, M. K.; J.M.J., W. *Inorg Chem.*, **2010**, *49*, 7244.

(21) Nieczypor, P.; van Leeuwen, P. W. N. M.; Mol, J. C.; Lutz, M.; Spek, A. L. *J. Organomet. Chem.*, **2001**, 58.

(22) Sandee, A. J.; van der Veen, L. A.; Reek, J. N. H.; Kamer, P. C. J.; Lutz, M.; Spek, A. L.; van Leeuwen, P. W. N. M. *Angew. Chem. Int. Ed.*, **1999**, 3231.

(23) Zuideveld, M. A.; Swennenhuis, B. H. G.; Boele, M. D. K.; Guari, Y.; van Strijdonck, G. P. F.; Reek, J. N. H.; Kamer, P. C. J.; Goubitz, K.; Fraanje, J.; Lutz, M.; Spek, A. L.; van Leeuwen, P. W. N. M. *J. Chem. Soc. Dalton Trans.* **2002**, 2308.

# CHAPTER 9

# Conclusions and Future Work

## 9.1 General Conclusions

This study has provided a systematic investigation into the nucleophilicity of metal complexes across a wide range of systems. Location of transition states allowed for the calculation of barrier heights which were compared with experimental rate constants. Good correlations were found across 14 orders of magnitude.

Benchmarking work undertaken on a series of 18-electron anionic metal carbonyl complexes has shown that inclusion of solvent in the calculations is critical for accurate representation of the reaction profile. In the absence of solvent, profiles in general were endothermic whereas profiles generated form solution phase calculations correctly predicted the reactions to be exothermic. The most viable computational setup was found to be a mixed basis consisting of SDD on the metal and 6-311G(d,p) on all other atoms. However, calculations employing SDD on all atoms still proved to be useful for rapid geometry optimisations on new complexes before the structures were subsequently re-optimised using the better basis sets.

Work undertaken on several series of complexes containing phosphine ligands has highlighted the importance of performing a configuration analysis on the reactant prior to optimising any transition states. The position of the phosphine has been shown to have a large effect on the energy of the complex. The energy of several [CpIr(CO)$PEt_3$] complexes where the phosphine orientation was changed varied by as much as 27 kJ $mol^{-1}$. Optimising complexes based upon crystal structures helped to identify the lowest energy structures.

Furthermore, a number of other computed parameters have been shown to correlate well with experimental rate constants (log *k*). The energy of the HOMO shows a reasonable correlation with experimental rate constants when the steric bulk of the complexes are related. The correlation between the transition state geometries and the experimental rate constants is dependent on the structure of the complex. Good correlations were only observed for the carbon-metal distances when the central metal was the same.

In order to complement existing literature data, kinetic studies of oxidative addition of iodomethane to [Rh(acac)(CO)L] complexes were undertaken. Complexes bearing aryl phosphines form a mixture of Rh(III) - alkyl and acyl products with the more electron withdrawing ligands favouring formation of the acyl species. Simple alkyl phosphines lead in general to formation of alkyl products. Complexes bearing anisyl-modified phosphines exhibit higher than expected reactivity towards iodomethane compared to $PPh_3$. A new mechanism where the methoxy group hydrogen bonds to the incoming iodomethane molecule has been shown to be energetically the most favourable.

The chemistry of various iridium complexes bearing xantphos-type diphosphine ligands with varying steric and electronic parameters was also explored. The changes in the ligands led to some interesting transformations as summarised in **Figure 9.1.**

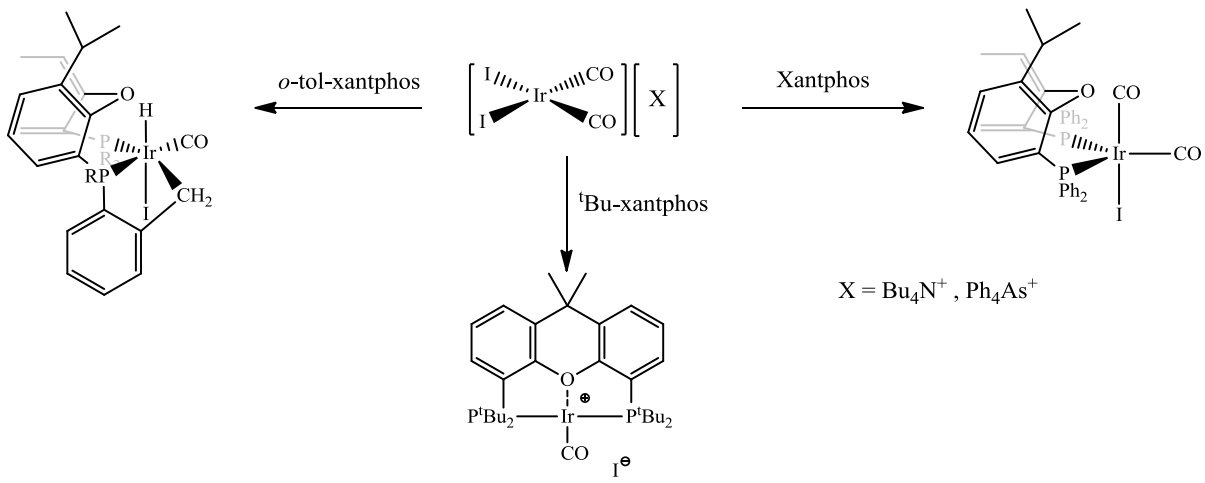


**Figure 9.1:** Summary of reaction of $[IrI_2(CO)_2]^-$ with various xantphos-type ligands

## 9.2 Future work

Explicit inclusion of solvent in DFT calculations on the small 18-electron anionic carbonyl complexes would be of interest both to see whether it has a significant effect on the reaction profile and how computationally expensive such calculations are. Explicit inclusion of solvent can be necessary for coordinating solvents such as water and MeCN. Whilst most solvents investigated in this thesis are relatively non-coordinating, the knowledge of how many solvent molecules are required could be important in future calculations.

Refluxing a solution of $[IrI(CO)_2(xantphos)]$ in benzene, toluene or cyclohexane led to the formation of a mixture of Ir(III) hydrido species which were unidentified. Further work to understand the origin of the hydride – whether from the xantphos ligand or from the solvent would be interesting. An X-ray crystal structure of the product would conclusively characterise the structure.

Initially, the object of changing the phosphine ligand in the iridium complexes was to form a series of monocarbonyl complexes with varying nucleophilicity in order to study their reactivity with iodomethane. Reaction of xantphos with $[IrI_2(CO)_2]AsPh_4$ forms a dicarbonyl complex, whereas the more bulky xantphos derivative *o*-tol-xantphos led to internal C-H activation of one of the tolyl rings. An alternative ligand, shown in **Figure 9.2** containing mixed substituents may be sufficiently bulky to form a monocarbonyl complex which would be suitable to react with iodomethane.

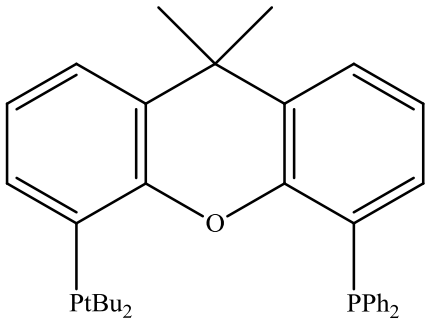


**Figure 9.2:** Structure of a modified xantphos ligand bearing mixed substituents.

# CHAPTER 10

# Experimental and Computational Details

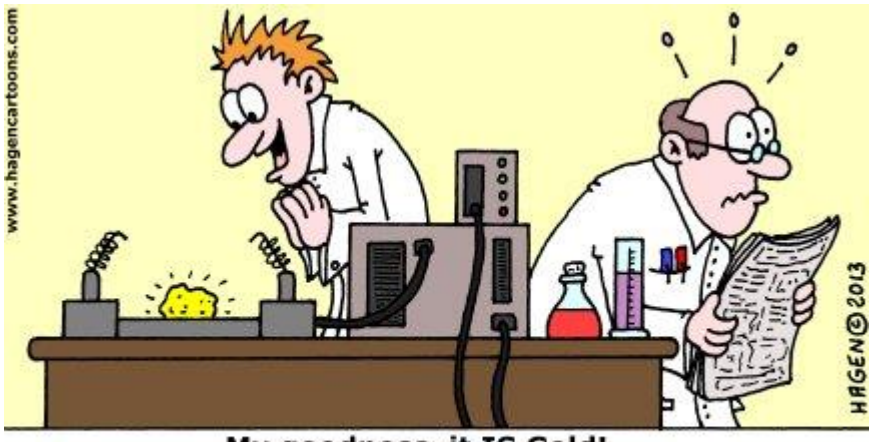

## 10.1 Computational Details

All calculations were performed using the Gaussian 09 computational package on local high performance computers, *Jupiter* and *Iceberg*.

### 10.1.1 *Jupiter and Iceberg* high performance computers

*Jupiter* is a local linux based high performance computer (HPC) cluster located in the theoretical chemistry group in the chemistry department at the University of Sheffield. The operating system is a 64-bit CentOS, with the Sun Grid Engine (SGE) utilised for job scheduling. In total the cluster contains 460 CPUs.

*Iceberg* is a HPC cluster located in the computing services at the University of Sheffield. *Iceberg* has two head nodes and is equipped with both AMD and Intel nodes. In total there are 1544 CPUs. More information regarding the specifications can be found on the University of Sheffield website.[1]

### 10.1.2 Gaussian 09 computational package

Gaussian is a quantum-chemical modelling program of which Gaussian 09 is the most recent version.[2] Each revision was compiled using the Portland compiler using Gaussian supplied BLAS libraries on the EMT64 architecture. The results from Gaussian are visualised using a GUI program, GaussView.

### 10.1.3 Computational methods

All calculations herein were performed at the DFT level of theory using the B3LYP functional unless otherwise stated.[3-5] The metal atoms were generally described using a Stuttgart/Dresden effective core potential (SDD)[6]. Several basis sets were used throughout the investigation including SDD, 6-311G(d,p),[7,8] cc-pVDZ,[9] and a mixed basis set consisting of SDD on the metal and 6-311G(d,p) on all other atoms. Extrabasis functions of 0.60 and 0.35 were employed for phosphorus and chlorine respectively

when the SDD basis set was used. All of the reactants, intermediates and transition states were optimised without symmetry constraints.

Frequency calculations were carried out on all optimised structures to confirm them as minima. Transition states were located generally using the QST3[10,11] method and characterised by having one large imaginary frequency. Intrinsic reaction coordinate (IRC) analysis was also undertaken upon certain transition states to ensure that the correct reactant and products were connected to the transition state.[12]

Solvent effects were taken into account for some systems using the default PCM model implemented through *Gaussian 09* using solvents as stated herein.[13]

## 10.2 Experimental - general

### 10.2.1 Solvents and Reagents

The solvents dichloromethane, acetonitrile, DMF and hexane were obtained from the Grubbs dry-solvent system, in which solvents are vigorously degassed before being passed through two sequential purification columns.[14] Firstly, an activated alumina column removes protic contaminants, followed by a supported copper catalyst that removes trace oxygen from hydrocarbons. The system is fitted with a Schlenk manifold that allows solvents to be collected and stored under a nitrogen atmosphere.

Diethyl ether was distilled after reflux over calcium hydride under a nitrogen atmosphere. Tetrahydrofuran was purified by distillation after reflux over potassium benzoketophenone under an argon atmosphere. Solvents were degassed by a minimum of three successive freeze-pump-thaw operations for air-sensitive work. Methyl iodide was distilled from calcium hydride and stored over mercury in a foil wrapped flask in the refrigerator at ca. 5 °C

All standard reagents were supplied by Sigma-Aldrich Chemicals Ltd and used as supplied, unless otherwise stated. Iridium and rhodium trichloride hydrate ($RhCl_3.xH_2O$) were purchased from Precious Metals Online, Monash University LPO, Melbourne, Australia. 4,5-bis(diphenylphosphino)-9,9-dimethylxanthene (xantphos)

and chlorodi-*iso*-propylphosphine was supplied by Sigma-Aldrich Chemicals Ltd. Chlorodi-*o*-anisylphosphine was supplied by Alfa-Aesar.

Argon and carbon monoxide (99.9 % CP grade) gases were supplied by BOC.

### 10.2.2 Instrumentation

Infrared spectra were measured on a Nicolet 560 FTIR spectrometer controlled by Omnic software. Solution spectra were recorded using a solution cell fitted with $CaF_2$ windows (0.5 mm path length) NMR spectra were recorded on a Bruker AC-250 or AC-400 spectrometer fitted with a Bruker B-ACS60 automated sampler changer and analysed using Topspin. Time of flight electrospray mass spectrometry (TOF-ES-MS) was performed on a Bruker Reflex 3 instrument. Both elemental analysis and mass spectra measurements were determined by the Microanalytical service at the University of Sheffield.

X-ray crystallography data were collected on a Bruker Smart CCD area detector with Oxford Cryosystems low temperature system using Mo Kα radiation (λ = 0.71073 Å). The structures were solved by direct methods and refined by full-matrix least squares methods on $F^2$. Hydrogen atoms were placed geometrically and refined using a riding model (including torsional freedom for methyl groups). Complex scattering factors were taken from the SHELXTL program package as implemented on the Pentium computer. Full listings of crystallographic data are given in the Appendix.

### 10.2.3 *In-situ* Infra-red kinetic experiments

Samples suitable for kinetic analysis were prepared by placing freshly distilled MeI into a 5 mL volumetric flask and making up to the mark with dichloromethane. A sample of this solution was used to obtain a background spectrum. Typically, 2-3 mg of the complex of interest was placed in a sample tube along with a 500 μL aliquot of the MeI solution Rapid mixing with a pipette preceded transferral into a solution cell (0.5 mm path length) before the experiment was started. The cylindrical IR cell (0.5 mm path length with $CaF_2$ windows) fits inside a thermostatted jacket which was used to

maintain a constant temperature throughout the experiment. Kinetic runs were controlled using the Omnic package and analysed using a combination of Omnic and Kaleidagraph software.

### 10.2.4 Schlenk Techniques

As a result of the air sensitive nature of both ligands and complexes herein, syntheses were carried out under inert atmosphere of argon or nitrogen using standard Schlenk techniques. Solid reagents were generally placed in a stoppered side-arm flask and degassed several times before being used. Cannulae were purged with a stream of inert gas prior to use. Needles were degassed by filing with inert gas from a previously degassed flask and expelling the gas outside of the flask. Such manipulations were carried out a minimum of three times.

### 10.2.5 Synthesis of metal precursors

The complexes $[RhCl(CO)_2]_2$,[15] $[RhI(CO)_2]_2$ $[RhI_2(COMe)(NCMe)(CO)]_2$,[16] $[RhCl(CO)(PPh_3)]_2$,[17] $[Ir(COD)Cl]_2$,[18,19] $[IrI_2(CO)_2][Ph_4As]$[18,19] and $[IrI_2(CO)_2][Bu_4N]$ [18,19] were all synthesised by literature procedures.

## 10.3 Experimental details relating to Chapter 7

The following section contains experimental details relating to complexes discussed in **Chapter 7.** The naming system outlined in that chapter is used herein.

### 10.3.1 Synthesis of Rh(I) dicarbonyl precursors

#### 10.3.1.1 Synthesis of $[Rh(acac)(CO)_2]$

$[RhCl(CO)_2]_2$ (0.795 g, 2.04 mmol) was dissolved in DMF (10 mL).[20] To the stirring solution acetylacetone (0.42 mL, 4.08 mmol) was added. Addition of large excess of water caused precipitation of a red / purple sticky solid which was recrystallized from acetone to yield the target complex as a green shiny crystalline solid.

Yield: 770 mg, 2.98 mmol, 73 %

IR: ν(CO) ($CH_2Cl_2$) : 2084, 2011 $cm^{-1}$

$^1H$ NMR: 2.1 (s, 6H), 5.7 (s, 1H)

$^{13}C$ NMR (101 MHz, $CDCl_3$) δ 187.22 (s), 183.66 (d, $J$ = 73.84 Hz), 101.65 (s), 26.99 (s).

Elemental analysis: Analysis calculated for $C_7H_7O_4Rh$ : C, 32.58: H, 2.73; Found: C,32.41; H, 2.38

### 10.3.1.2 Synthesis of [Rh($^t$Bu-acac)$(CO)_2$]

$[RhCl(CO)_2]_2$ (80 mg, 0.2 mmol) was dissolved in 5 mL DMF and stirred under nitrogen. 2,2,6,6-tetramethyl-heptane-dione, (0.09 mL, 0.4 mmol) was added and the solution stirred for ten minutes. An excess of sodium hydrogencarbonate was added to the solution which immediately turned inky black. Upon addition of cold water (300 mL) the product precipitated and the sticky green / brown solid obtained was recrystallized from acetone yielding the target complex as a brown / red solid.

Yield: 41 mg, 0.12 mmol, 28.8 %

IR: ν(CO) ($CH_2Cl_2$): 2009, 2081 $cm^{-1}$

$^1H$ NMR: 5.95 (s, 1H), 1.17 (s, 18H)

$^{13}C$ NMR (101 MHz, $CDCl_3$) δ 196.77 (s), 184.12 (d, $J$ = 72.9 Hz), 92.05 (d, $J$ = 2.5 Hz), 41.63 (s), 28.50 (s).

TOF MS ES+ (m/z): 342.032988

Elemental analysis: Analysis calculated for $C_7H_7O_4Rh$ : C, 45.36: H, 6.15; Found: C,45.12; H, 5.52

### 10.3.1.3 Synthesis of [Rh($CF_3$-acac)$(CO)_2$]

$[RhCl(CO)_2]_2$, (100 mg, 0.26 mmol) was dissolved in DCM (4 mL) under nitrogen. To the stirred solution, hexafluoroacetylacetone (0.1 mL, 0.33 mg) and sodium carbonate (43 mg) were added and the solution monitored by IR spectroscopy until no reactant peaks were observed. After filtration the solution was evaporated to dryness to afford the target complex.

Yield: 154 mg, 0.42 mmol, 82 %

IR: ν(CO) ($CH_2Cl_2$) : 2036, 2101 $cm^{-1}$

$^1H$ NMR: 6.49 (s, 1H)

$^{13}C$ NMR (101 MHz, $CDCl_3$) δ 180.70 (d, $J$ = 72.8 Hz), 175.78 (q, $J$ = 36.2 Hz), 117.24 (q, $J$ = 284.4 Hz), 92.49 (s).

$^{19}F$ NMR (377 MHz, $CDCl_3$) δ -74.61 (s, 6F)

Elemental analysis: Analysis calculated for $C_7HF_6O_4Rh$ : C, 22.97: H, 0.28; Found: C,23.36; H, 0.23

## 10.3.2 Synthesis of Rh(I) complexes

### 10.3.2.1 General ligand substitution method 1

1.01 mole equivalent of phosphine was added to solution of [Rh(acac)$(CO)_2$] in $CH_2Cl_2$ (5 mL) under nitrogen or argon resulting in a rapid evolution of gas. Once no more gas was observed the solution was stirred for a further five minutes before the solvent was removed in vacuo. The resulting yellow complexes were washed with cold hexane.

### 10.3.2.2 General ligand substitution method 2

1.01 mole equivalent of phosphine was added to solution of [Rh(acac)$(CO)_2$] in octane (2 mL) under nitrogen or argon resulting in a rapid evolution of gas. The solution was stirred for a further five minutes during which time the complex precipitated as a yellow powder. Once no more gas was observed the solid was filtered and washed with a little cold octane.

### 10.3.2.3 Synthesis of [Rh(acac)(CO)($PPh_2Me$)] (1b)

The target complex was synthesised according to the general method 1 using [Rh(acac)$(CO)_2$] (80 mg, 0.31 mmol) and $PPh_2Me$ (55 μL, 0.31 mmol).

Yield: 101 mg, 0.23 mmol, 76 %
IR: ν(CO) ($CH_2Cl_2$) : 1975 $cm^{-1}$
$^1H$ NMR ($CDCl_3$): δ 7.63 (m, 4H), 7.06 (m, 6H), 5.31 (s, 1H), 1.95 (s, 3H), 1.80 (s, 3H), 1.63 (s, 3H)
$^{31}P\{^1H\}$: 33.91 (d, $J_{Rh-P}$ = 170 Hz)
$^{13}C$ NMR (101 MHz, $CDCl_3$) δ 189.16 (dd, *J* = 76.3, 25.5 Hz), 187.65 (s), 185.43 (s), 134.84 (d, *J* = 51.2 Hz), 132.75 (d, *J* = 11.4 Hz), 130.19 (s), 128.26 (d, *J* = 10.3 Hz), 100.72 (s), 27.59 (d, *J* = 5.8 Hz), 27.00 (s), 14.33 (d, *J* = 33.6 Hz).
TOF MS ES+ (m/z): 430.014193
Elemental Analysis: Analysis calculated for $C_{19}H_{20}O_3PRh$: C, 53.04: H, 4.69; Found: C, 52.14: H, 4.60

### 10.3.2.4 Synthesis of [Rh(acac)(CO)($PPhMe_2$)] (1c)

The target complex was synthesised according to the general method 1 using [Rh(acac)$(CO)_2$] (50 mg, 0.19 mmol) and $PPhMe_2$ (30 μL, 0.19 mmol).

Yield: 58 mg, 0.10 mmol, 81 %
IR: ν(CO) ($CH_2Cl_2$) : 1970 $cm^{-1}$
$^1H$ NMR ($CDCl_3$): δ 7.63 (m, 4H), 7.06 (m, 6H), 5.49 (s, 1H), 2.10 (s, 3H), 1.90 (s, 3H), 1.82 (dd, 6H *J*= 1.49, 10.31 Hz),
$^{31}P\{^1H\}$: 19.75 (d, $J_{Rh-P}$ = 167 Hz)
$^{13}C$ NMR (101 MHz, $CDCl_3$) δ 189.36 (dd, *J* = 76.5, 26.2 Hz), 187.79 (s), 185.40 (s), 100.75 (s), 27.65 (d, *J* = 5.03 Hz), 27.25 (s), 18.06 (d, *J* = 71.44 Hz), 15.37 (d, *J* = 34.21 Hz)
TOF MS ES+ (m/z): (M+) 582 (M+) 554 (M+ - CO)

### 10.3.2.5 Synthesis of [Rh(acac)(CO)($PMe_3$)] (1d)

$PMe_3.HBF_4$, (32 mg, 0.19 mmol) was dissolved in $CH_2Cl_2$ (2 mL) with one drop of $Et_3N$. [Rh(acac)$(CO)_2$], (50 mg, 0.19 mmol) was added to the solution causing a rapid evolution of gas. The solvent was removed in vacuo and the complex was taken up in $Et_2O$ and filtered to remove any remaining $Et_3N.HBF_4$. The $Et_2O$ was removed to yield the target complex as a red powder.

Yield: 42 mg, 0.14 mmol, 70.6 %
IR: ν(CO) ($CH_2Cl_2$) : 1967 $cm^{-1}$
$^1H$ NMR ($CDCl_3$): δ 5.47 (s, 1H), 2.07 (s, 3H), 1.93 (s, 3H), 1.56 (d, 9H $J$ = 12 Hz)
$^{31}P\{^1H\}$ NMR ($CDCl_3$): δ 10.1 (d, $^1J_{Rh\text{-}P}$ = 160 Hz).
$^{13}C$ NMR (101 MHz, $CD_2Cl_2$) δ 190.22 (dd, $J$ = 77.4, 26.3 Hz), 187.73 (s), 185.41 (s), 100.21 (d, $J$ = 1.9 Hz), 27.41 (d, $J$ = 5.4 Hz), 26.93 (s), 16.27 (dd, $J$ = 34.3, 1.5 Hz).
TOF MS ES+ (m/z): 305.989770

### 10.3.2.6 Synthesis of [Rh(acac)(CO)($PPh_2Et$)] (1e)

The target complex was synthesised according to the general method 1 using [Rh(acac)$(CO)_2$] (80 mg, 0.31 mmol) and P(4-$CF_3$-$C_6H_4)_3$ (60 μL, 0.31 mmol).

Yield: 95 mg, 0.21 mmol, 67 %
IR: ν(CO) ($CH_2Cl_2$) : 1973 $cm^{-1}$
$^1H$ NMR ($CDCl_3$): δ 7.72 (m, 6H), 7.41 (m, 9H), 5.48 (s, 1H), 2.44 (m, 2H), 2.09 (s, 3H), 1.87 (s, 3H), 1.14 (dt, 3H, $J$ = 18.2, 7.5 Hz)
$^{31}P\{^1H\}$: 46.16 (d, $J_{Rh\text{-}P}$ = 171 Hz)
$^{13}C$ NMR (101 MHz, $CDCl_3$) δ 189.29 (dd, $J$ = 75.9, 24.9 Hz), 187.68 (s), 185.31 (s), 133.69 (s, $J$ = 25.0 Hz), 133.23 (d, $J$ = 10.5 Hz), 130.11 (d, $J$ = 2.1 Hz), 128.18 (d, $J$ = 10.1 Hz), 100.69 (d, $J$ = 1.9 Hz), 27.62 (d, $J$ = 5.3 Hz), 27.01 (s), 20.81 (s), 20.49 (s), 8.71 (s).
TOF MS ES+ (m/z): 444.028641
Elemental Analysis: Analysis calculated for $C_{20}H_{22}O_3PRh$: C, 54.07: H, 4.99; Found: C, 54.53: H, 5.00

### 10.3.2.7 Synthesis of [Rh(acac)(CO)(PPhEt$_2$)](1f)

The target complex was synthesised according to the general method 1 using [Rh(acac)(CO)$_2$] (60 mg, 0.23 mmol) and PPhEt$_2$ (40 μL, 0.23 mmol).

Yield: 74 mg, 0.19 mmol, 84 %
IR: ν(CO) ($CH_2Cl_2$) : 1968 cm$^{-1}$
$^1$H NMR ($CDCl_3$): δ 7.83 (m, 2H), 7.43 (m, 3H), 5.49 (s, 1H), 2.10 (s, 3H), 1.88 (s, 3H), 1.16 (td, 6H, *J* = 17.1, 7.6 Hz)
$^{31}$P{$^1$H}: 44.25 (d, $J_{Rh-P}$ = 169 Hz)
$^{13}$C NMR (101 MHz, $CD_2Cl_2$) δ 189.89 (dd, *J* = 76.4, 25.1 Hz), 187.71 (s), 185.33 (s), 132.44 (d, *J* = 10.1 Hz), 130.03 (d, *J* = 2.2 Hz), 128.16 (d, *J* = 9.7 Hz), 100.21 (s), 27.35 (d, *J* = 5.1 Hz), 26.77 (s), 18.90 (d, *J* = 31.7 Hz), 8.14 (s).
TOF MS ES+ (m/z): 396 (M+) 368 (M+ - CO) 340 (M+ - CO – acac)
Elemental Analysis: Analysis calculated for $C_{16}H_{22}O_3PRh$: C, 48.50: H, 5.60; Found: C, 46.87: H, 5.55

### 10.3.2.8 Synthesis of [Rh(acac)(CO)(PEt$_3$)] (1g)

$PEt_3.HBF_4$, (20 mg, 0.097 mmol) was dissolved in $CH_2Cl_2$ (2 mL) with one drop of $Et_3N$. [Rh(acac)(CO)$_2$], (25 mg, 0.097 mmol) was added to the solution causing a rapid evolution of gas. The solvent was removed in vacuo and the complex was taken up in $Et_2O$ and filtered to remove any remaining $Et_3N.HBF_4$. The $Et_2O$ was removed to yield the target complex as a yellow powder.

Yield: 34 mg, 0.10 mmol, 76 %
IR: ν(CO) ($CH_2Cl_2$) : 1963 cm$^{-1}$
$^1$H NMR ($C_7D_8$): δ 5.31 (s, 1H), 1.91 (s, 3H), 1.77 (s, 3H), 1.51 (m, 6H) 0.99 (m, 9H).
$^{31}$P{$^1$H} NMR ($C_7D_8$): δ 43.6 (d, $^1J_{Rh-P}$ = 166 Hz).
$^{13}$C NMR (101 MHz, $CD_2Cl_2$) δ 190.24 (dd, *J* = 76.8, 25.0 Hz), 187.67 (s), 185.25 (s), 100.12 (d, *J* = 1.9 Hz), 27.43 (d, *J* = 5.0 Hz), 26.84 (s), 17.25 (d, *J* = 30.9 Hz), 7.98 (s).
TOF MS ES+ (m/z): 348.035704
Elemental Analysis: Analysis calculated for $C_{12}H_{22}O_3PRh$: C, 41.39: H, 6.37; Found: C, 38.96: H, 6.57

### 10.3.2.9 Synthesis of [Rh(acac)(CO)(P*o*-tol$_3$)] (1h)

Synthesized from [Rh(acac)(CO)$_2$] (50 mg, 0.19 mmol) and free phosphine, P*o*-tol$_3$, (58 mg, 0.19 mmol) following general method 2 to yield the target complex.

Yield: 83 mg, 0.15 mmol, 80 %

IR: ν(CO) ($CH_2Cl_2$) : 1973 cm$^{-1}$

$^1$H NMR ($CDCl_3$): δ 7.75 (m, 3H) 7.27 (m, 3H), 7.11 (m, 6H), 5.28 (s, 1H), 2.22 (s, 9H), 1.96 (s, 3H), 1.38 (s, 3H)

$^{31}$P{$^1$H}: 44.92 (d, $J_{Rh-P}$ = 173 Hz)

$^{13}$C NMR (101 MHz, $CDCl_3$) δ 187.26 (s), 185.41 (s), 142.99 (d, *J* = 9.06 Hz), 135.27 (s), 131.61 (d, J = 7.04 Hz), 130.45 (s), 128.83 (d, *J* = 49.3 Hz), 125.42 (d, *J* = 7.0 Hz), 100.29 (s), 27.53 (d, *J* = 6.04 Hz), 26.51 (s), 23.60 (s).

TOF MS ES+ (m/z): 534 (M+) 506 (M+ - CO) 406 (M+ - CO – acac)

Elemental analysis: Analysis calculated for $C_{27}H_{28}O_3PRh$ : C, 60.68: H, 5.28

Found: C,58.29; H, 5.01

### 10.3.2.10 Synthesis of [Rh(acac)(CO)(P*p*-tol$_3$)] (1i)

The target complex was synthesised according to the general method 2 using [Rh(acac)(CO)$_2$] (35 mg, 0.14 mmol) and P*p*tol$_3$ (42 mg, 0.14 mmol).

Yield: 56 mg, 0.10 mmol, 76 %

IR: ν(CO) ($CH_2Cl_2$) : 1976 cm$^{-1}$

$^1$H NMR ($CDCl_3$): δ 7.57 (m, 6H) 7.20 (m, 6H), 5.44 (s, 1H), 2.39 (s, 9H), 2.11 (s, 3H), 1.66 (s, 3H)

$^{31}$P{$^1$H}: 46.1 (d, $J_{Rh-P}$ = 175 Hz)

$^{13}$C NMR (101 MHz, $CDCl_3$) δ 189.33 (dd, *J* = 76.0, 24.8 Hz), 187.40 (s, *J* = 12.4 Hz), 185.47 (s, *J* = 8.4 Hz), 140.33 (d, *J* = 2.2 Hz), 134.41 (d, *J* = 11.7 Hz), 129.76 (s), 128.74 (d, *J* = 10.9 Hz), 100.67 (s), 27.56 (d, *J* = 5.2 Hz), 26.72 (s), 21.50 (d, *J* = 19.9 Hz), 9.28 (s).

TOF MS ES+ (m/z): 534.085128

Elemental Analysis: Analysis calculated for $C_{27}H_{28}O_3PRh$: C, 60.68: H, 5.28. Found: C, 60.53: H, 5.30.

### 10.3.2.11 Synthesis of [Rh(acac)(CO)(P(*4-F*-$C_6H_4$)$_3$)] (1j)

The target complex was synthesised according to the general method 2 using [Rh(acac)$(CO)_2$] (27 mg, 0.1 mmol) and P(4-F-$C_6H_4$)$_3$ (33 mg, 0.1 mmol).

Yield: 35 mg, 0.06 mmol, 61 %

IR: ν(CO) ($CH_2Cl_2$) : 1980 $cm^{-1}$

$^1$H NMR ($CDCl_3$): δ 7.64 (m, 6H), 7.12 (td, 6H, *J* = 8.7, 1.5 Hz), 5.47 (s, 1H), 2.12 (s, 3H), 1.66 (s, 3H),

$^{31}P\{^1H\}$: 46.62 (d, $J_{Rh-P}$ = 175 Hz)

$^{13}$C NMR (101 MHz, $CDCl_3$) δ 188.69 (dd, *J* = 75.2, 24.9 Hz), 187.75 (s), 185.32 (s), 137.29 (d, *J* = 2.4 Hz), 135.53 (d, *J* = 12.6 Hz), 128.60 (d, *J* = 11.2 Hz), 100.88 (s), 27.53 (d, *J* = 5.6 Hz), 26.83 (s).

$^{19}$F NMR (235 MHz, $CDCl_3$) δ -109.12 (dqd, *J* = 11.0, 5.5, 2.5 Hz).

TOF MS ES+ (m/z): 546.010518.

Elemental Analysis: Analysis calculated for $C_{24}H_{19}F_3O_3PRh$: C, 52.77: H, 3.51; Found: C, 52.41: H, 3.33.

### 10.3.2.12 Synthesis of [Rh(acac)(CO)(P(*4-Cl*-$C_6H_4$)$_3$)] (1k)

The target complex was synthesised according to the general method 2 using [Rh(acac)$(CO)_2$] (35 mg, 0.14 mmol) and P(4-Cl-$C_6H_4$)$_3$ (33 mg, 0.14 mmol).

Yield: 61 mg, 0.01 mmol, 81 %

IR: ν(CO) ($CH_2Cl_2$) : 1982 $cm^{-1}$

$^1$H NMR ($CDCl_3$): δ 7.58 (dd, 6H, *J* = 10.8, 11.5 Hz), 5.47 (s, 1H), 2.13 (s, 3H), 1.67 (s, 3H)

$^{31}P\{^1H\}$: 47.55 (d, $J_{Rh-P}$ = 178 Hz)

$^{13}$C NMR (101 MHz, $CDCl_3$) δ 189.36 (s), 189.11 (s), 188.61 (s), 188.36 (s), 187.77 (s), 185.32 (s), 165.42 (s), 162.91 (s), 136.43 (dd, *J* = 13.2, 8.4 Hz), 134.79 – 134.00 (m), 128.24 (s), 127.71 (s), 116.51 – 115.52 (m), 115.43 (d, *J* = 11.7 Hz), 100.86 (s), 27.53 (d, *J* = 5.7 Hz), 26.75 (s).

TOF MS ES+ (m/z): 593.918925

Elemental Analysis: Analysis calculated for $C_{24}H_{19}Cl_3O_3PRh$: C, 48.39: H, 3.22: Cl, 17.86; Found: C, 48.61: H, 3.22: Cl, 16.52

### 10.3.2.13 Synthesis of [Rh(acac)(CO)(P(*4-OMe*-$C_6H_4$)$_3$)] (1l)

The target complex was synthesised according to the general method 2 using [Rh(acac)$(CO)_2$] (40 mg, 0.16 mmol) and P(4-OMe-$C_6H_4$)$_3$ (55 mg, 0.16 mmol).

Yield: 78 mg, 0.13 mmol, 86 %

IR: ν(CO) ($CH_2Cl_2$) : 1973 $cm^{-1}$

$^1$H NMR: δ 7.59 (m, 6H), 6.29 (m, 6H), 5.44 (s, 1H), 3.84 (s, 9H), 2.22 (s, 3H), 1.66 (s, 3H),

$^{31}P\{^1H\}$ NMR ($CHCl_3$): δ 44.14 (d, $^1J_{Rh-P}$ = 175 Hz).

$^{13}$C NMR (101 MHz, $CDCl_3$) δ 189.38 (dd, *J* = 76.3, 24.9 Hz), 187.51 (s), 185.45 (s, *J* = 14.7 Hz), 161.11 (d, *J* = 2.0 Hz), 135.90 (d, *J* = 12.8 Hz), 124.26 (d, *J* = 55.9 Hz), 113.54 (d, *J* = 11.5 Hz), 100.71 (s), 77.29 (d, *J* = 11.4 Hz), 55.27 (s), 27.58 (d, *J* = 5.5 Hz), 26.72 (s).

TOF MS ES+ (m/z): 582 (M+) 554 (M+ - CO) 454 (M+ - acac)

Elemental Analysis: Analysis calculated $C_{27}H_{29}O_6PRh$ C, 55.59: H, 5.01. Found: C, 55.89: H, 4.73

### 10.3.2.14 Synthesis of [Rh(acac)(CO)(P(*4-CF$_3$*-$C_6H_4$)$_3$)] (1m)

The target complex was synthesised according to the general method 2 using [Rh(acac)$(CO)_2$] (50 mg, 0.19 mmol) and P(4-$CF_3$-$C_6H_4$)$_3$ (90 mg, 0.19 mmol).

Yield: 112 mg, 0.16 mmol, 83 %

IR: ν(CO) ($CH_2Cl_2$) : 1985 $cm^{-1}$

$^1$H NMR (400 MHz, $CDCl_3$) δ 7.88 – 7.75 (m, 1H), 7.72 (d, *J* = 7.6 Hz, 1H), 5.51 (s, 1H), 2.14 (s, 3H), 1.63 (s, 3H).

$^{31}P\{^1H\}$: 50.08 (d, $J_{Rh-P}$ = 179 Hz)

$^{19}$F NMR (235 MHz, $CDCl_3$) δ 63.12

$^{13}$C NMR (101 MHz, $CDCl_3$) δ 187.90 (s, *J* = 23.7 Hz), 185.26 (s), 135.68 (d, *J* = 48.5 Hz), 134.69 (d, *J* = 12.2 Hz), 132.87 (d, *J* = 30.8 Hz), 125.26 (dd, *J* = 10.7, 3.6 Hz), 100.98 (s), 27.52 (d, *J* = 5.1 Hz), 26.75 (s).

TOF MS ES+ (m/z): 679.0151

Elemental Analysis: Analysis calculated for $C_{27}H_{19}F_9O_3PRh$: C, 46.57: H, 2.75: Found: C, 46.25: H, 2.67

### 10.3.2.15 Synthesis of [Rh(acac)(CO)(P(*oOMe*-$C_6H_4$)$_3$)] (1n)

The target complex was synthesised according to the general method 2 using [Rh(acac)$(CO)_2$] (80 mg, 0.31 mmol) and P(2-OMe-$C_6H_4$)$_3$ (110 mg, 0.31 mmol).

Yield: 160 mg, 0.27 mmol, 88 %

IR: ν(CO) ($CH_2Cl_2$) : 1968 $cm^{-1}$

$^1$H NMR ($CD_2Cl_2$): δ 7.7-6.8 (m, 12H), 5.4 (s, 1H), 3.6 (s, 9H), 2.1 (s, 3H), 1.6 (s, 3H)

$^{31}P\{^1H\}$ NMR ($CDCl_3$): δ 33.1 (d, $^1J_{Rh-P}$ = 180 Hz).

TOF MS ES+ (m/z): 582.065722

Elemental Analysis: Analysis calculated for $C_{27}H_{28}O_6PRh$ C, 55.68: H, 4.85. Found: C, 56.14: H, 4.81

.

### 10.3.2.16 Synthesis of [Rh(acac)(CO)(PPh(*oOMe*-$C_6H_4$)$_2$)] (1o)

The target complex was synthesised according to the general method 2 using [Rh(acac)$(CO)_2$] (40 mg, 0.15 mmol) and PPh(2-OMe-$C_6H_4$)$_2$ (46 mg, 0.15 mmol).

Yield: 71 mg, 0.13 mmol, 83 %

IR: ν(CO) ($CH_2Cl_2$) : 1972 $cm^{-1}$

$^1$H NMR ($CD_2Cl_2$): δ 7.8-6.8 (m, 13H), 5.5 (s, 1H), 3.6 (s, 6H), 2.1 (s, 3H), 1.6 (s, 3H)

$^{31}P\{^1H\}$ NMR ($CDCl_3$): δ 36.7 (d, $^1J_{Rh-P}$ = 179 Hz).

$^{13}$C NMR (101 MHz, $CD_2Cl_2$) δ 190.22 (dd, *J* = 77.1, 25.1 Hz), 187.16 (s), 185.21 (s), 160.70 (s), 135.40 (d, *J* = 9.9 Hz), 134.07 (d, *J* = 11.9 Hz), 132.90 (s), 132.24 (d, *J* = 26.1 Hz), 132.09 (s), 129.30 (s), 127.27 (d, *J* = 10.9 Hz), 120.64 (s), 120.21 (d, *J* = 10.6 Hz), 111.25 (d, *J* = 4.4 Hz), 99.93 (s), 55.08 (s), 27.24 (d, *J* = 5.7 Hz), 26.41 (s)

TOF MS ES+ (m/z): 553.0646

Elemental Analysis: Analysis calculated for $C_{26}H_{26}O_5PRh$ C, 56.54: H, 4.74; Found: C, 55.82: H, 4.73

### 10.3.2.17 Synthesis of [Rh(acac)(CO)($PPh_2$(*oOMe*-$C_6H_4$) )] (1p)

The target complex was synthesised according to the general method 2 using [Rh(acac)$(CO)_2$] (40 mg, 0.15 mmol) and $PPh_2$(2-OMe-$C_6H_4$) (50 mg, 0.15 mmol).

Yield: 67 mg, 0.13 mmol, 88 %

IR: ν(CO) ($CH_2Cl_2$) : 1974 $cm^{-1}$

$^1$H NMR ($CD_2Cl_2$): δ 7.8-6.9 (m, 12H), 5.4 (s, 1H), 3.6 (s, 9H), 2.1 (s, 3H), 1.7 (s, 3H)

$^{31}P\{^1H\}$ NMR ($CDCl_3$): δ 41.2 (d, $^1J_{Rh-P}$ = 178 Hz).

$^{13}$C NMR (101 MHz, $CD_2Cl_2$) δ 187.39 (s), 185.28 (s), 160.82 (s), 134.32 (t, *J* = 10.0 Hz), 133.02 (s), 132.48 (d, *J* = 6.3 Hz), 129.91 (s), 127.84 (d, *J* = 10.7 Hz), 120.43 (d, *J* = 9.8 Hz), 111.16 (d, *J* = 4.5 Hz), 100.13 (s), 55.11 (s), 27.26 (d, *J* = 5.8 Hz), 26.45 (s).

TOF MS ES+ (m/z): 523.0529

Elemental Analysis: Analysis calculated for $C_{25}H_{24}O_4PRh$ C, 57.5: H,4.63; Found: C, 57.25: H, 4.50

### 10.3.2.18 Synthesis of [Rh(acac)(CO)($P^tBu_3$)] (1r)

The target complex was synthesised according to the general method 1 using [Rh(acac)$(CO)_2$] (50 mg, 0.19 mmol) and $P^tBu_3$ (0.25 mL, 0.19 mmol).

Yield: 76 mg, 0.17 mmol, 90.6 %

IR: ν(CO) ($CH_2Cl_2$) : 1960 $cm^{-1}$

$^1$H NMR (400 MHz, Tol) δ 5.35 (s, 1H), 1.89 (s, *J* = 6.8 Hz, 7H), 1.76 (s, 6H), 1.44 (d, *J* = 11.9 Hz, 66H).

$^{31}P\{^1H\}$ NMR ($C_7D_8$): δ 100.2 (d, $^1J_{Rh-P}$ = 179.0 Hz).

$^{13}$C NMR (101 MHz, $CD_2Cl_2$) δ 192.98 (dd, *J* = 76.5, 20.5 Hz), 187.81 (s), 184.28 (s), 100.41 (s), 39.78 (d, *J* = 12.7 Hz), 32.73 (d, *J* = 2.9 Hz), 27.29 (d, *J* = 4.8 Hz), 26.36 (s).

TOF MS ES+ (m/z): 431.129077

Elemental Analysis: Analysis calculated $C_{18}H_{34}O_3PRh$ C, 50.01: H, 7.93. Found: C, 49.16: H, 7.86

### 10.3.2.19 Synthesis of [Rh($^t$Bu-acac)(CO)(P*p*-tol$_3$)]

The target complex was synthesised according to the general method 2 using [Rh($^t$Bu-acac)(CO)$_2$] (20 mg, 0.058 mmol) and P*p*tol$_3$ (19 mg, 0.058 mmol)

Yield: 27 mg, 0.04 mmol, 89 %
IR: ν(CO) ($CH_2Cl_2$) : 1974 cm$^{-1}$
$^1$H NMR: 0.73 (s, 9H), 1.22 (s, 9H), 2.37 (s, 9H), 5.79 (s, 1H), 7.17 (dd, 6H), 7.55
$^{31}$P{$^1$H}: 45.04 (d, $J_{Rh-P}$ = 174.6 Hz)
$^{13}$C NMR (101 MHz, $CDCl_3$) δ 140.10 (s), 134.64 (s), 134.23 (d, *J* = 11.8 Hz), 128.79 (d, *J* = 10.7 Hz), 90.67 (s), 28.69 (s), 28.14 (s), 21.37 (d, *J* = 5.1 Hz).
TOF MS ES+ (m/z): 618.176528
Elemental analysis: Analysis calculated for $C_{33}H_{40}O_3Rh$: C, 62.50 H, 5.94; Found: C,61.71; H, 5.92

### 10.3.2.20 Synthesis of [Rh($^t$Bu-acac)(CO)(PPh$_3$)] (1u)

The target complex was synthesised according to the general procedure using [Rh($^t$Bu-acac)(CO)$_2$] (35 mg, 0.1 mmol) and $PPh_3$ (27 mg, 0.1 mmol).

Yield: 48 mg, 0.08 mmol, 81 %
IR: ν(CO) ($CH_2Cl_2$) : 1974 cm$^{-1}$
$^1$H NMR: 0.73 (s, 9H), 1.24 (s, 9H), 2.37 (s, 9H), 5.81 (s, 1H), 7.4 (m, 6H), 7.67 (m, 9H)
$^{31}$P{$^1$H}: 47.33 (d, $J_{Rh-P}$ = 177 Hz)
$^{13}$C NMR (101 MHz, $CDCl_3$) δ 197.09 (s), 194.13 (d, *J* = 21.0 Hz), 189.74 (dd, *J* = 76.2, 24.3 Hz), 134.34 (d, *J* = 11.6 Hz), 133.15 (d, *J* = 49.8 Hz), 130.12 (d, *J* = 2.0 Hz), 128.12 (d, *J* = 10.4 Hz), 90.75 (s),
TOF MS ES+ (m/z): 576.129731
Elemental analysis: Analysis calculated for $C_{30}H_{34}O_3PRh$: C, 64.08: H, 6.52; Found: C,63.10; H, 6.30

### 10.3.2.21 Synthesis of [Rh($CF_3$-acac)(CO)($PPh_3$)] (1v)

To a stirring solution of [RhCl(CO)($PPh_3$)]$_2$ (100 mg, 1.17 mmol) in $CH_2Cl_2$ (10 mL), hexafluoroacetylacetone (30 μL, 2.34 mmol) and NaOEt (18 mg) were added. The solution was stirred for 2 hours before the solvent was removed in vacuo and the residue was taken up in ether. Filtration of the compound through silica afforded the target complex.

Yield: 61 mg, 0.11 mmol, 45 %
IR: ν(CO) ($CH_2Cl_2$) : 1997 cm$^{-1}$
$^1$H NMR ($CDCl_3$): δ 7.4-7.69 (aromatic region - 15H), 6.25 (s, 1H)
$^{31}$P{$^1$H}: 47.78 (d, $J_{Rh-P}$ = 178.2 Hz)
$^{19}$F NMR (377 MHz, $CDCl_3$) δ -74.91 (s, 3F). -75.12 (s, 3F)
$^{13}$C NMR (400 MHz, $CDCl_3$) δ 187.26 (s), 185.41 (s), 142.99 (d, $J$ = 9.06 Hz),
TOF MS ES+ (m/z): 600.9847
Elemental analysis: Analysis calculated for $C_{24}H_{16}F_6O_3PRh$: C, 48.02: H, 2.69
Found: C,47.55; H, 2.23

## 10.3.3 Synthesis of Rh(III) complexes

### 10.3.3.1 Synthesis of [Rh(acac)(CO)I(Me)($PMe_3$)] (2d)

[Rh(acac)(CO)$PMe_3$], (20 mg, 0.065 mmol) was dissolved in $CH_2Cl_2$ (1 mL) and MeI (1 mL) and stirred for three hours before the solvent was removed in vacuo to yield the target complex as red crystals.

Yield: 27 mg, 0.059 mmol, 93 %
IR: ν(CO) ($CH_2Cl_2$) : 2063 cm$^{-1}$
$^1$H NMR ($CDCl_3$): δ 5.46 (s, 1H), 2.07 (s, 3H), 1.99 (s, 3H), 1.79 (dd, 9H $J$ = 11.9, 0.7 Hz), 1.39 (dd, 3H, $J$= 1.9 Hz)
$^{31}$P{$^1$H}: 16.44 (d, $J_{(Rh-P)}$ = 117 Hz)
$^{13}$C NMR (101 MHz, $CDCl_3$) δ 187.40 (s), 185.61 (dd, $J$ = 64.1, 20.0 Hz), 184.34 (s, $J$ = 30.3 Hz), 100.13 (s), 27.94 (d, $J$ = 8.3 Hz), 27.58 (s), 16.49 (d, $J$ = 39.0 Hz), 14.91 (dd, $J$ = 20.3, 4.3 Hz).

TOF MS ES+ (m/z): 447.915092

Elemental Analysis: Analysis calculated for $C_{10}H_{19}IO_3PRh$: C, 26.81: H, 4.27; Found: C, 27.02: H, 4.34

Crystals suitable for X-ray analysis were grown from slow evaporation of diethylether into a concentrated DCM solution.

### 10.3.3.2 Synthesis of [Rh(acac)(CO)I(Me)($PEt_3$)] (2g)

[Rh(acac)(CO)$PEt_3$] (20 mg, 0.06 mmol) was dissolved in $CH_2Cl_2$ (1 mL) and MeI (1 mL) and stirred for 3 hours before the solvent removed to yield the target complex as a yellow orange powder.

Yield: 25 mg, 0.05 mmol, 88 %

IR: ν(CO) ($CH_2Cl_2$) : 2060 $cm^{-1}$

$^1$H NMR ($CDCl_3$): δ 5.28 (s, 1H), 1.89 (s, 3H), 1.78 (s, 3H), 1.73 (m, 6H), 1.36 (dd, 3H *J* = 1.7 Hz), 0.84 (dt, 9H, *J* = 16.4, 7.6 Hz),

$^{31}$P{$^1$H} NMR ($CDCl_3$): δ 41.42 (d, $^1J_{Rh\text{-}P}$ = 116 Hz).

$^{13}$C NMR (101 MHz, $CDCl_3$) δ 187.29 (s), 186.11 (dd, *J* = 63.5, 19.0 Hz), 184.10 (s), 100.07 (s), 28.02 (d, *J* = 7.8 Hz), 27.36 (s), 17.77 (d, *J* = 33.3 Hz), 13.59 (dd, *J* = 20.2, 4.6 Hz), 7.83 (d, *J* = 5.1 Hz).

TOF MS ES+ (m/z): 489.965465

Elemental Analysis: Analysis calculated for $C_{13}H_{25}IO_3PRh$: C, 31.86: H, 5.14 Found: C, 31.70: H, 5.40

### 10.3.3.3 Synthesis of [Rh($CF_3$-acac)(I)(Me)(CO)($PPh_3$)] (4v)

[Rh($CF_3$-acac)(CO)$PPh_3$], (25 mg, 0.042 mmol) was dissolved in $CH_2Cl_2$ (2 mL) and MeI (2 mL) and stirred overnight before the solvent was removed in vacuo to yield the target complex as a brown orange powder.

Yield: 24 mg, 0.03 mmol, 77 %

IR: ν(CO) ($CH_2Cl_2$) : 2070 $cm^{-1}$

$^{1}$H NMR ($CDCl_3$): δ 7.64-7.40 (15H, aromatic protons), 5.53(s, 1H), 1.98 (dd, 3H *J* = 1.9, 4 Hz)
$^{13}$C NMR (101 MHz, $CDCl_3$) δ 182.3 (dd, *J* = 66.4, 10.06 Hz), 175.55 (dq *J* = 202.3, 35.22 Hz), 133.99 (d, *J* = 9.6 Hz), 132.12 (s), 129.15 (d, *J* = 10.9 Hz), 126.05 (s), 125.55 (s), 115.4 (q, *J* = 286.80 Hz), 90.44 (s), 6.27 (dd, *J* = 2.01, 18.11 Hz)
$^{19}$F NMR (162 MHz, $CDCl_3$) δ 27.11 (s), 26.43 (s).
$^{31}$P{$^{1}$H} NMR ($CDCl_3$): δ 26.58 (d, $^{1}J_{Rh\text{-}P}$ = 111 Hz).
Elemental Analysis: Analysis calculated for $C_{25}H_{19}F_6IO_3PRh$: C, 40.46: H, 2.58
Found: C, 38.37: H, 2.76

Crystals suitable for X-ray analysis were grown from slow evaporation of diethylether into a concentrated DCM solution.

## 10.4 Experimental details relating to chapter 8

The following section contains experimental details relating to complexes discussed in **Chapter 8**. The naming system outlined in that chapter is used herein.

### 10.4.1 Synthesis of ligands and ligand precursors

#### 10.4.1.1 Synthesis of 4,5-Dibromo-9,9-dimethylxanthene

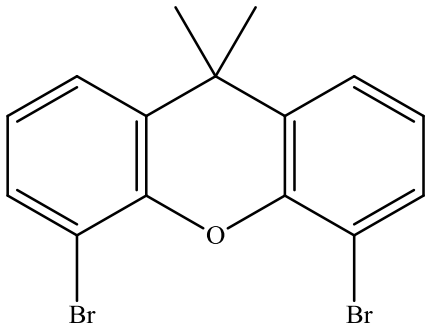


This was prepared by a method described by Buhling.[21] 9,9-dimethylxanthene, (670 mg, 3.2 mmol) was dissolved in degassed diethyl ether (25 mL) and TMEDA (1 mL) in a flame dried Schlenk tube. $^{n}$BuLi (3.2 mL, 2.5 M in cyclohexane) was added drop wise over 10 minutes at -78 °C. Once added, the solution was allowed to warm up to room temperature at which point it gradually turned bright red. The solution was stirred for

24 hours. Bromine, (0.53 mL, 10.3 mmol) was added gradually at -78 °C and the solution left to stir overnight.

The solution was quenched with a sodium bisulphite solution (20 %) and the organic phase separated. The aqueous phase was washed twice with diethyl ether and the organic phases combined and dried with $MgSO_4$. The orange oil generated on removing the solvent was purified via flash chromatography resulting in a yellow oil.

Yield: 660 mg, 1.8 mmol, 56 %

$^1$H NMR ($CDCl_3$) : δ (ppm) 7.50 (dd, 2H, *J* = 9.3, 1.4Hz), 7.35 (dd, 2H, *J* ), 7.00 (t, 2H, *J* = 7.8 Hz), 1.63 (s, 6H).

TOF MS ES+ (m/z): 368 (M+), 353 (M+ - $CH_3$), 273 (M+ -$CH_3$, -Br).

$^{13}$C NMR ($CDCl_3$): δ 149.19, 131.58, 130.58, 129.07, 118.27, 115.66, 77.37, 77.05, 76.74, 34.46, 32.29.

### 10.4.1.2 Synthesis of 2,7-dibromo-9,9-dimethyl-xanthene

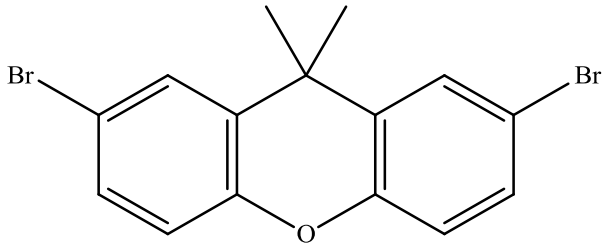


Bromine, (2 mL, 38.99 mmol) was added dropwise over 10 minutes to a cooled solution of 9,9-dimethylxanthene (3.3 g, 15.69 mmol) in acetic anhydride (10 mL) and stirred for three hours during which time the solution turned yellow. The reaction solution was poured onto cold water and the white precipitate thus formed was collected by filtration and washed with 2 portions of cold water and a 10% sodium bisulfite solution.

Yield: 5.62 g, 15.40 mmol, 98 %

$^1$H NMR ($CDCl_3$) : δ (ppm) 7.51 (2H, d, *J* = 2.34 Hz), 7.32 (2H, dd, *J* = 8.6 Hz), 6.94 (2H, d, *J* = 8.6 Hz) 1.624 (s, 6H)

$^{13}$C NMR ($CDCl_3$) : δ (ppm) 149.2, 131.5, 130.6, 129.4, 118.3, 115.7, 34.5, 32.3

TOF MS ES+ (m/z): 365.925487

Elemental Analysis: Analysis calculated for $C_{15}H_{12}OBr_2$: C, 48.95: H, 3.29; Found: C, 48.56: H, 2.80.

### 10.4.1.3 Synthesis of 2,7,9,9-tetramethylxanthene

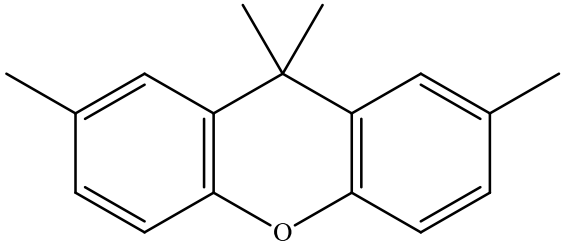


2,7-dibromo-9,9-dimethyl-xanthene (3.1 g, 8.5 mmol) was dissolved in 20 mL of degassed diethylether in a flame dried flask. $^{n}$BuLi, (7.1 mL, 17.8 mmol – 2.5 M in hexanes) was added dropwise at -78 °C over half hour. The mixture was further stirred for one hour at -78 °C before being warmed to room temperature and stirred for a further three hours forming a white cloudy solution. The solution was again cooled to -78 °C and iodomethane, (1.1 mL, 17.8 mmol) was added slowly over half hour. The solution was allowed to warm to room temperature and stirred overnight yielding a yellow solution.

The solvent was removed in vacuo and the yellow / white paste redissolved in DCM and washed with water. The combined organic layers were dried with $MgSO_4$ and filtered. The yellow solution was dried in vacuo yielding the target compound as a yellow oil.

Yield: 910 mg, 3.82 mmol, 45 %

$^{1}$H NMR ($CDCl_3$) : δ (ppm) 7.25 (br, d $J$ = 1.4 Hz), 7.05 (dd, $J$ = 8.2, 1.7 Hz), 6.99 (d, $J$ = 8.2 Hz), 2.40 (s, 6H), 1.68 (s, 6H)

$^{13}$C NMR ($CDCl_3$) : δ (ppm) 148.39, 132.01, 129.66, 127.99, 126.52, 116.05, 33.96, 32.48, 21.03

TOF MS ES+ (m/z): 238.136394

### 10.4.1.4 Synthesis of 4,5-dibromo-2,7,9,9-tetramethylxanthene

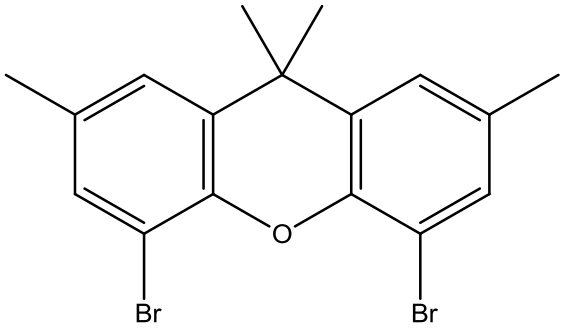


2,7,9,9-tetramethylxanthene (900 mg, 3.78 mmol) was dissolved in 20 mL acetic anhydride and cooled to 0 °C. Bromine, (0.4 mL, 7.8 mmol) was added dropwise over ten minutes and the resulting red / brown solution stirred over three days. The resulting green solution was poured onto cold water and a precipitate was observed forming. The solid was collected by filtration and washed with water and sodium bisulfite (10 %) to yield a beige / brown solid.

Yield: 1.36 g, 3.45 mmol, 90.8 %

$^{1}$H NMR ($CDCl_3$) : δ (ppm) 7.32, (2H, d, $J$ = 1.44 Hz), 7.14 (2H, d, $J$ = 1.28 Hz), 2.34 (s, 6H), 1.61 (s, 6H)

$^{13}$C NMR ($CDCl_3$) : δ (ppm) 145.3, 133.7, 131.7, 131.4, 125.4, 35.3, 31.9, 20.8,

TOF MS ES+ (m/z): 393.958459

Elemental Analysis: Analysis calculated for $C_{17}H_{16}Br_2O$: C, 51.55: H, 4.07: Found: C, 50.58: H,3.89

### 10.4.1.5 Synthesis of 4,5-di-*o*-tolphosphino-2,7,9,9-tetramethylxanthene

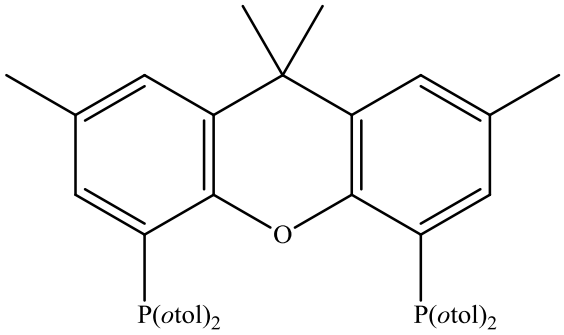


4,5-dibromo-2,7,9,9-tetramethylxanthene (440 mg, 1.19 mmol) was dissolved in diethylether (20 mL) in a flame dried flask.[22] $^{n}$BuLi (1 mL, 2.5 M in cyclohexanes) was added over ten minutes at -78 °C and stirred for one hour before being warmed and stirred for a further three hours. The solution was recooled to -78 °C and Cl$P(o\text{-tol})_2$ (660 mg, 2.65 mmol) was added slowly in THF (5 mL) to the stirring solution before being left to warm up gradually and stirred overnight.

The now cream solution was evaporated to dryness and the foamy solid was dissolved in minimum hot methanol. Upon cooling in the freezer, a white powder precipitated. The pale yellow liquid layer was decanted off under nitrogen and the white powder dried under vacuum to yield the target ligand.

Yield: 489 mg, 0.74 mmol, 73 %

$^{1}$H NMR ($CDCl_3$) : δ (ppm) 1.67 (s, 6H), 2.16 (s, 6H), 2.26 (s, 9H), 6.26 (d, 2H), 6.69 (d, 4H), 6.97 (td, 4H)

$^{31}P\{^{1}H\}$: -32.53 (s)

TOF MS ES+ (m/z): 662.283977

## 10.4.2 Synthesis of Iridium complexes

### 10.4.2.1 Synthesis of [IrI(CO)$_2$(xantphos)]

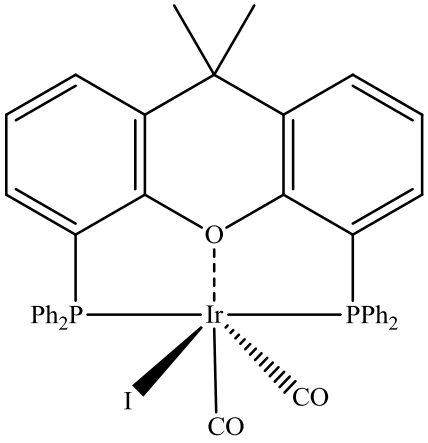


This was prepared according to a method by Fox et al.. [23] [IrI$_2$(CO)$_2$][Bu$_4$N] (200 mg, 0.27 mmol) and xantphos, (156 mg, 0.27 mmol) were dissolved in THF (40 mL) and heated to reflux for three hours. The solution was concentrated under vacuum causing precipitation of the product as an orange powder.

Yield: 210 mg, 0.22 mmol, 82 %

IR: ν(CO) ($CH_2Cl_2$) : 2044, 2023, 1970, 1954 $cm^{-1}$

$^{31}P\{^1H\}$ NMR ($CDCl_3$) : δ(ppm) -18.88 (s)

TOF MS ES+ (m/z): 799 (M+ - CO – I)

### 10.4.2.2 Reaction of $[IrI_2(CO)_2][Bu_4N]$ and *o*-tolxantphos (4a)

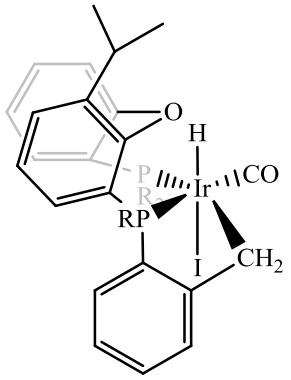


R = *o*-tol

An analogous procedure used to synthesise $[IrI(CO)_2(xantphos)]$ was employed to synthesise the target complex using $[IrI_2(CO)_2][Bu_4N]$ (50 mg, 0.067 mmol) and *o*-tolxantphos (43 mg, 0.067 mmol) dissolved in THF (20 mL). After three hours, the solution was concentrated under vacuum and 5 mL hexane was added to the solution to induce precipitation of the complex as a beige powder. The $[NBu_4I]$ byproduct could not be removed from the product mixture.

Yield: 50 mg, 0.051 mmol, 76 %

IR: ν(CO) ($CH_2Cl_2$) : 2024, 2040 (shoulder) $cm^{-1}$

IR: ν(Ir-H) ($CH_2Cl_2$) : 2253 $cm^{-1}$

$^{31}P\{^1H\}$ NMR ($CDCl_3$) : δ(ppm) Major: 4.4 (d, *J* = 18.9 Hz), -18.5 (d, *J* = 16.5 Hz)
Minor: 3.7 (d, *J* = 16.6 Hz), -28.2 (d, *J* = 19.0 Hz)

$^1H$ NMR ($CDCl_3$) : δ (ppm) Major: -16.13 (dd, *J* = 23.9, 9.6 Hz)
Minor: -15.97 (dd, *J* = 21.7, 10.6 Hz)
8.68 (dd, *J* = 15.9, 7.5 Hz, 1H), 4.53 (td, *J* = 16.5, 5.9 Hz), 3.94 (dd, *J* = 16.2, 4.8 Hz), 3.85 (d, *J* = 16.5 Hz).

TOF MS ES+ (m/z): 855.2 (M+ - I)

Crystals suitable for X-ray analysis were grown by slow evaporation of diethyl ether into a concentrated DCM solution.

### 10.4.2.3 Reaction of $[IrI_2(CO)_2][Ph_4As]$ and *o*-tol-xantphos' (5a)

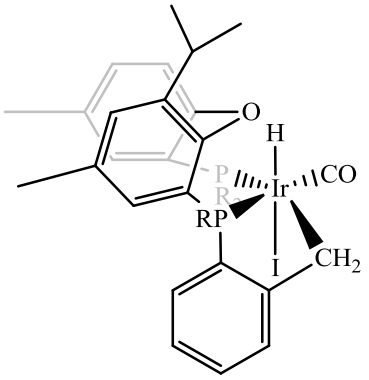


R = *o*-tol

An analogous procedure used to synthesise $[IrI(CO)_2(xantphos)]$ was employed to synthesise the target complex using $[IrI_2(CO)_2][Ph_4As]$ (160 mg, 0.18 mmol) and *o*-tol-xantphos' (120 mg, 0.18 mmol) dissolved in THF (20 mL). After three hours, the solution was concentrated under vacuum to around 5 m L at which point a beige powder begun to precipitate. The solution was left in the freezer overnight to crystallise before being collected via filtration and washed with cold hexanes.

Yield: 175 mg, 0.17 mmol, 92 %

$^{31}P\{^{1}H\}$ NMR ($CDCl_3$) : δ(ppm) Major: 3.2 (d, $J$ = 16.7 Hz), -19.4 (d, $J$ = 16.7 Hz)

Minor: 3.9 (d, $J$ = 19.0 Hz), -28.5 (d, $J$ = 19.0 Hz)

$^{1}H$ NMR ($CDCl_3$) : δ (ppm) Major: -16.13 (dd, $J$ = 23.6, 9.7 Hz)

Minor: -15.97 (dd, $J$ = 21.6, 10.5 Hz)

IR: ν(CO) ($CH_2Cl_2$) : 2024, 2040 (shoulder) $cm^{-1}$

IR: ν(Ir-H) ($CH_2Cl_2$) : 2253 $cm^{-1}$

TOF MS ES+ (m/z): 1011.1573

### 10.4.2.4 Synthesis of [Ir(CO)($^t$Bu-xantphos)]I (7a)

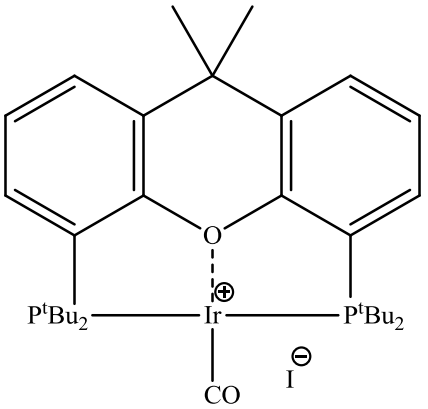


$[IrI_2(CO)_2][Bu_4N]$ (100 mg, 0.1344 mmol) and $^t$Bu-xantphos, (66.9 mg, 0.1344 mmol) were dissolved in THF (20 mL) and heated to reflux overnight. The solution was concentrated under vacuum causing precipitation of the product as a bright yellow powder. The powder was washed with cold ethanol and diethyl ether.

Yield: 70 mg, 0.08 mmol, 62 %

IR: ν(CO) ($CH_2Cl_2$) : 1981 $cm^{-1}$

$^1$H NMR ($CDCl_3$) : δ(ppm) 7.9-8.1 (m, 4H aromatics), 7.7 (t, 2H aromatics), 1.8 (s, 6H, C(C***H*****$_3$**)$_2$ ), 1.6 (m, 36H PC(C***H*****$_3$**)$_3$ )

$^{31}$P{$^1$H} NMR ($CDCl_3$) : δ(ppm) 73.95 (s)

TOF MS ES+ (m/z): 719.2772

Elemental Analysis. Analysis calculated for $C_{32}H_{48}IIrO_2P_2$: C, 45.44: H, 5.72: I, 15.00; Found: C,43.32 ; H, 6.00: I, 15.7

Crystals suitable for X-ray analysis were grown by slow evaporation of diethyl ether into a concentrated $CH_2Cl_2$ solution.

## 10.5 References


(1) Sheffield-WRGRID *http://www.shef.ac.uk/wrgrid/iceberg/specs*, **2014**.

(2) Gaussian 09, R. D.; M. J. Frisch; G. W. Trucks; H. B. Schlegel; G. E. Scuseria; M. A. Robb; J. R. Cheeseman; G. Scalmani; V. Barone; B. Mennucci; G. A. Petersson; H. Nakatsuji; M. Caricato; X. Li; H. P. Hratchian; A. F. Izmaylov; J. Bloino; G. Zheng; J. L. Sonnenberg; M. Hada; M. Ehara; K. Toyota; R. Fukuda; J. Hasegawa; M. Ishida; T. Nakajima; Y. Honda; O. Kitao; H. Nakai; T. Vreven; J. A. Montgomery, J.; J. E. Peralta; F. Ogliaro; M. Bearpark; J. J. Heyd, E. B.; K. N. Kudin; V. N. Staroverov; T. Keith; R. Kobayashi; J. Normand; K. Raghavachari; A. Rendell; J. C. Burant; S. S. Iyengar; J. Tomasi; M. Cossi; N. Rega; J. M. Millam; M. Klene; J. E. Knox; J. B. Cross; V. Bakken; C. Adamo; J. Jaramillo; R. Gomperts; R. E. Stratmann; O. Yazyev; A. J. Austin; R. Cammi; C. Pomelli; J. W. Ochterski; R. L. Martin; K. Morokuma; V. G. Zakrzewski; G. A. Voth; P. Salvador; J. J. Dannenberg; S. Dapprich; A. D. Daniels; O. Farkas; J. B. Foresman; J. V. Ortiz; J. Cioslowski; D. J. Fox *Gaussian, Inc., Wallingford CT,* **2013**.

(3) Becke, A. D. *Phys. Rev. A.,* **1988**, *38*, 3098.

(4) Lee, C.; Yang, W.; Parr, R. G. *Phys. Rev. B.,* **1988**, *32*, 785.

(5) Perdew, P.; Chevary, J. A.; Vosko, S. H.; Jackson, K. A.; Pederson, M. R.; Singh, D. J.; Fiolhais, C. *phys. Rev. B.,* **1992**, *46*, 6671.

(6) Dolg, M. *Theor. Comput. Chem.,* **2002**, *11*, 793.

(7) McLean, A. D.; Chandler, G. S. *J. Chem. Phys.,* **1980**, *72*, 5639.

(8) Krishnan, R.; Binkley, J. S.; Seeger, R.; Pople, J. A. *J. Chem. Phys.,* **1980**, *72*, 650.

(9) Dunning Jr., T. H. *J. Chem. Phys.,* **1989**, 90, 1007.

(10) Cances, M. T.; Mennuci, B.; Tomasi, J. *J. Chem. Phys.,* **1997**, *107*, 3032.

(11) Peng, C.; Schlegel, H. B. *Israel J. of Chem.,* **1993**, *33*, 449.

(12) Fukui, K. *Acc. Chem. Res.,* **1981**, *14*, 363.

(13) Cossi, M.; Barone, V.; Mennucci, B.; Tomasi, J. *Chem. Phys. Lett.,* **1998**, *286*. 253

(14) Pangborn, A. B.; Giardello, M. A.; Grubbs, R. H.; Rosen, R. K.; Timmers, F. J. *Organometallics,* **1996**, *15*, 1518.

(15) McCleverty, J. A.; Wilkinson, G. *Inorg. Synth.,* **1966**, *8*, 214.

(16) Haynes, A.; Maitlis, P. M.; Stanbridge, I. A.; Haak, S.; Pearson, J. M.; Adams, H.; Bailey, N. A. *Inorg. Chim. Acta,* **2004**, *357*, 3027.

(17) Steele, D. G.; Stephenson, T. A. *J. Chem. Soc. Dalton Trans.* **1972**, 2161.

(18) Pearson, J. M., PhD Thesis, University of Sheffield, 1994.

(19) Vickers, P. W., PhD Thesis, University of Sheffield, 1997.

(20) Otto, S.; Roodt, A.; Erasmus, J. J. C.; Swarts, J. C. *Polyhedron,* **1998**, *17*, 2447.

(21) Buhling, A.; Kamer, P. C. J.; van Leeuwen, P. W. N. M. *Organometallics,* **1997**, *16*, 3027.

(22) Hamann, B. C.; Hartwig, J. F. *J. Am. Chem. Soc.,* **1998**, *120*, 3694.

(23) Fox, D. J.; Duckett, S. B.; Flaschenriem, C.; Brennessel, W. W.; Schneider, J.; Gunay, A.; Eisenberg, R. *Inorg. Chem.,* **2006**, *45*, 7197.

# Appendix

## Cystallographic Data

**Table A1 -** Crystal data and structure refinement for ($o$-tol)$_2$P(=O)P($o$-tol)$_2$

**Table A2 -** Crystal data and structure refinement for [IrI$_2$(CO)(Me)(xantphos)]

**Table A3 -** Crystal data and structure refinement for [Rh(acac)(CO)(P$o$-tol$_3$)]

**Table A4 -** Crystal data and structure refinement for[Rh(acac)(CO)(PMe$_3$)].

**Table A5 -** Crystal data and structure refinement for
[Rh(CF$_3$-acac)(CO)(I)(Me)(PPh$_3$)]

**Table A6 -** Crystal data and structure refinement for activated Ir(I) complex

**Table A7 -** Crystal data and structure refinement for
[Ir(CO)($^t$Bu-xantphos)]I

**Table A8 -** Crystal data and structure refinement for
[IrI(Me)(CO)(xantphos)]SbF$_6$

## Kinetic Data

**Table A9 –** Kinetic data for reactions of [Rh(acac)(CO)(L)] with MeI

## NMR studies

**Figure A1** – $^{31}$P{$^1$H}-NMR spectra recorded during the reaction of complex **[Rh(acac)(CO)PPh$_3$]** with MeI [MeI] = 0.16 M.

**Figure A2** – $^{31}$P{$^1$H}-NMR spectra recorded during the reaction of complex **[Rh(acac)(CO)P(4-FC$_6$H$_4$)$_3$]** with MeI [MeI] = 0.16 M.

**Figure A3** – $^{31}$P{$^1$H}-NMR spectra recorded during the reaction of complex **[Rh(acac)(CO)P(4-ClC$_6$H$_4$)$_3$]** with MeI [MeI] = 0.16 M.

**Figure A4** – $^{31}$P{$^1$H}-NMR spectra recorded during the reaction of complex **[Rh(acac)(CO)Pptol$_3$]** with MeI [MeI] = 0.16 M.

**Figure A5** -$^{31}$P{$^1$H}-NMR spectra recorded during the reaction of complex **[Rh(acac)(CO)P(4-MeOC$_6$H$_4$)$_3$]** with MeI [MeI] = 0.16 M.

**Table A1. Crystal data and structure refinement for ($o$tol)$_2$P(=O)P($o$tol)$_2$**

| | | |
|---|---|---|
| Identification code | iah682_0m | |
| Empirical formula | C28 H28 O P2 | |
| Formula weight | 442.44 | |
| Temperature | 100(2) K | |
| Wavelength | 0.71073 Å | |
| Crystal system | Orthorhombic | |
| Space group | P2(1)2(1)2(1) | |
| Unit cell dimensions | a = 7.9005(2) Å | α= 90°. |
| | b = 16.5360(4) Å | β= 90°. |
| | c = 18.1234(5) Å | γ = 90°. |
| Volume | 2367.69(11) Å$^3$ | |
| Z | 4 | |
| Density (calculated) | 1.241 Mg/m$^3$ | |
| Absorption coefficient | 0.201 mm$^{-1}$ | |
| F(000) | 936 | |
| Crystal size | 0.43 x 0.23 x 0.18 mm$^3$ | |
| Theta range for data collection | 2.25 to 27.61°. | |
| Index ranges | -10<=h<=10, -20<=k<=21, -23<=l<=21 | |
| Reflections collected | 17728 | |
| Independent reflections | 5472 [R(int) = 0.0383] | |
| Completeness to theta = 27.61° | 99.9 % | |
| Absorption correction | Semi-empirical from equivalents | |
| Max. and min. transmission | 0.9647 and 0.9184 | |
| Refinement method | Full-matrix least-squares on F$^2$ | |
| Data / restraints / parameters | 5472 / 0 / 284 | |
| Goodness-of-fit on F$^2$ | 1.080 | |
| Final R indices [I>2sigma(I)] | R1 = 0.0603, wR2 = 0.1530 | |
| R indices (all data) | R1 = 0.0669, wR2 = 0.1568 | |
| Absolute structure parameter | 0.07(14) | |
| Largest diff. peak and hole | 0.964 and -0.411 e.Å$^{-3}$ | |

**Table A2. Crystal data and structure refinement for [IrI$_2$(CO)(Me)(xantphos)]**

| | | |
|---|---|---|
| Identification code | iahcp2qredo | |
| Empirical formula | C41 H35 I2 Ir O2 P2 | |
| Formula weight | 1067.63 | |
| Temperature | 100(2) K | |
| Wavelength | 0.71073 Å | |
| Crystal system | Orthorhombic | |
| Space group | Pca2(1) | |
| Unit cell dimensions | a = 17.7309(5) Å | α= 90°. |
| | b = 14.2112(4) Å | β= 90°. |
| | c = 14.9887(4) Å | γ = 90°. |
| Volume | 3776.81(18) Å$^3$ | |
| Z | 4 | |
| Density (calculated) | 1.878 Mg/m$^3$ | |
| Absorption coefficient | 5.289 mm$^{-1}$ | |
| F(000) | 2040 | |
| Crystal size | 0.28 x 0.21 x 0.10 mm$^3$ | |
| Theta range for data collection | 1.43 to 27.53°. | |
| Index ranges | -22<=h<=23, -18<=k<=18, -14<=l<=19 | |
| Reflections collected | 46493 | |
| Independent reflections | 7999 [R(int) = 0.0425] | |
| Completeness to theta = 25.00° | 100.0 % | |
| Absorption correction | Semi-empirical from equivalents | |
| Max. and min. transmission | 0.6198 and 0.3190 | |
| Refinement method | Full-matrix least-squares on F$^2$ | |
| Data / restraints / parameters | 7999 / 325 / 429 | |
| Goodness-of-fit on F$^2$ | 1.050 | |
| Final R indices [I>2sigma(I)] | R1 = 0.0274, wR2 = 0.0662 | |
| R indices (all data) | R1 = 0.0311, wR2 = 0.0694 | |
| Absolute structure parameter | -0.002(5) | |
| Largest diff. peak and hole | 2.012 and -1.562 e.Å$^{-3}$ | |

**Table A3. Crystal data and structure refinement for [Rh(acac)(CO)(P*o*tol$_3$)]**

| | | |
|---|---|---|
| Identification code | perksredo2xp21c | |
| Empirical formula | C27 H28 O3 P Rh | |
| Formula weight | 534.37 | |
| Temperature | 97(2) K | |
| Wavelength | 0.71073 Å | |
| Crystal system | Monoclinic | |
| Space group | P2(1)/c | |
| Unit cell dimensions | a = 36.603(4) Å | α= 90°. |
| | b = 8.8150(11) Å | β= 101.718(4)°. |
| | c = 15.0359(17) Å | γ = 90°. |
| Volume | 4750.4(10) Å$^3$ | |
| Z | 8 | |
| Density (calculated) | 1.494 Mg/m$^3$ | |
| Absorption coefficient | 0.813 mm$^{-1}$ | |
| F(000) | 2192 | |
| Crystal size | 0.12 x 0.04 x 0.04 mm$^3$ | |
| Theta range for data collection | 1.14 to 27.67°. | |
| Index ranges | -47<=h<=46, -11<=k<=11, -19<=l<=18 | |
| Reflections collected | 33957 | |
| Independent reflections | 33957 [R(int) = 0.0000] | |
| Completeness to theta = 25.00° | 99.5 % | |
| Absorption correction | Semi-empirical from equivalents | |
| Max. and min. transmission | 0.9682 and 0.9088 | |
| Refinement method | Full-matrix least-squares on F$^2$ | |
| Data / restraints / parameters | 33957 / 0 / 588 | |
| Goodness-of-fit on F$^2$ | 0.976 | |
| Final R indices [I>2sigma(I)] | R1 = 0.0766, wR2 = 0.1739 | |
| R indices (all data) | R1 = 0.1534, wR2 = 0.2179 | |
| Largest diff. peak and hole | 3.410 and -1.734 e.Å$^{-3}$ | |

**Table A4. Crystal data and structure refinement for[Rh(acac)(CO)(PMe$_3$)].**

| | | |
|---|---|---|
| Identification code | iah685cc | |
| Empirical formula | C10 H19 I O3 P Rh | |
| Formula weight | 448.03 | |
| Temperature | 100(2) K | |
| Wavelength | 0.71073 Å | |
| Crystal system | Monoclinic | |
| Space group | Cc | |
| Unit cell dimensions | a = 7.8782(8) Å | α= 90°. |
| | b = 12.9104(8) Å | β= 6.299(5)°. |
| | c = 15.4181(15) Å | γ = 90°. |
| Volume | 1558.7(2) Å$^3$ | |
| Z | 4 | |
| Density (calculated) | 1.909 Mg/m$^3$ | |
| Absorption coefficient | 3.170 mm$^{-1}$ | |
| F(000) | 864 | |
| Crystal size | 0.32 x 0.21 x 0.12 mm$^3$ | |
| Theta range for data collection | 2.66 to 27.63°. | |
| Index ranges | -10<=h<=10, -15<=k<=16, -19<=l<=20 | |
| Reflections collected | 12575 | |
| Independent reflections | 3412 [R(int) = 0.0644] | |
| Completeness to theta = 27.63° | 99.0 % | |
| Absorption correction | Semi-empirical from equivalents | |
| Max. and min. transmission | 0.7022 and 0.4302 | |
| Refinement method | Full-matrix least-squares on F$^2$ | |
| Data / restraints / parameters | 3412 / 2 / 151 | |
| Goodness-of-fit on F$^2$ | 1.037 | |
| Final R indices [I>2sigma(I)] | R1 = 0.0346, wR2 = 0.0694 | |
| R indices (all data) | R1 = 0.0382, wR2 = 0.0713 | |
| Absolute structure parameter | -0.07(2) | |
| Largest diff. peak and hole | 0.643 and -0.819 e.Å$^{-3}$ | |

**Table A5. Crystal data and structure refinement for [Rh($CF_3$-acac)(CO)(I)(Me)($PPh_3$)]**

| | |
|---|---|
| Identification code | iah686_0m |
| Empirical formula | C50 H38 F12 I2 O6 P2 Rh2 |
| Formula weight | 1484.36 |
| Temperature | 100(2) K |
| Wavelength | 0.71073 Å |
| Crystal system | Monoclinic |
| Space group | P2(1)/n |
| Unit cell dimensions | a = 15.9300(9) Å α= 90°.<br>b = 18.0019(11) Å β= 0.724(3)°.<br>c = 18.5469(11) Å γ = 90°. |
| Volume | 5318.3(5) $Å^3$ |
| Z | 4 |
| Density (calculated) | 1.854 $Mg/m^3$ |
| Absorption coefficient | 1.931 $mm^{-1}$ |
| F(000) | 2880 |
| Crystal size | 0.29 x 0.27 x 0.19 $mm^3$ |
| Theta range for data collection | 1.58 to 27.53°. |
| Index ranges | -20<=h<=20, -23<=k<=23, -24<=l<=24 |
| Reflections collected | 87252 |
| Independent reflections | 12167 [R(int) = 0.1341] |
| Completeness to theta = 25.00° | 100.0 % |
| Absorption correction | Semi-empirical from equivalents |
| Max. and min. transmission | 0.7105 and 0.6044 |
| Refinement method | Full-matrix least-squares on $F^2$ |
| Data / restraints / parameters | 12167 / 369 / 688 |
| Goodness-of-fit on $F^2$ | 0.937 |
| Final R indices [I>2sigma(I)] | R1 = 0.0472, wR2 = 0.0970 |
| R indices (all data) | R1 = 0.0836, wR2 = 0.1064 |
| Largest diff. peak and hole | 1.645 and -1.193 e.$Å^{-3}$ |

**Table A6. Crystal data and structure refinement for activated Ir(I) complex**

| | |
|---|---|
| Identification code | iahredo2_0m |
| Empirical formula | C44 H39 I Ir O2 P2 |
| Formula weight | 980.79 |
| Temperature | 117(2) K |
| Wavelength | 0.71073 Å |
| Crystal system | Monoclinic |
| Space group | P2(1)/n |
| Unit cell dimensions | a = 17.747(2) Å a= 90°.<br>b = 10.9743(13) Å b= 95.718(8)°.<br>c = 19.066(3) Å g = 90°. |
| Volume | 3694.9(8) $Å^3$ |
| Z | 4 |
| Density (calculated) | 1.763 $Mg/m^3$ |
| Absorption coefficient | 4.573 $mm^{-1}$ |
| F(000) | 1916 |
| Crystal size | 0.21 x 0.10 x 0.10 $mm^3$ |
| Theta range for data collection | 1.50 to 27.75°. |
| Index ranges | -22<=h<=23, -14<=k<=14, -24<=l<=24 |
| Reflections collected | 76276 |
| Independent reflections | 8595 [R(int) = 0.1085] |
| Completeness to theta = 27.75° | 98.8 % |
| Absorption correction | Semi-empirical from equivalents |
| Max. and min. transmission | 0.6577 and 0.4468 |
| Refinement method | Full-matrix least-squares on $F^2$ |
| Data / restraints / parameters | 8595 / 389 / 485 |
| Goodness-of-fit on $F^2$ | 1.091 |
| Final R indices [I>2sigma(I)] | R1 = 0.0726, wR2 = 0.1375 |
| R indices (all data) | R1 = 0.1160, wR2 = 0.1526 |
| Largest diff. peak and hole | 1.597 and -3.060 e.$Å^{-3}$ |

**Table A7. Crystal data and structure refinement for [Ir(CO)($^t$Bu-xantphos)]I**

| | |
|---|---|
| Identification code | iah674p-1 |
| Empirical formula | C34 H52 Cl4 I Ir O2 P2 |
| Formula weight | 1015.60 |
| Temperature | 150(2) K |
| Wavelength | 0.71073 Å |
| Crystal system | Triclinic |
| Space group | P-1 |
| Unit cell dimensions | a = 11.3249(9) Å α= 106.071(6)°.<br>b = 13.5484(19) Å β= 108.894(4)°.<br>c = 14.6939(10) Å γ = 99.489(7)°. |
| Volume | 1967.8(3) Å$^3$ |
| Z | 2 |
| Density (calculated) | 1.714 Mg/m$^3$ |
| Absorption coefficient | 4.559 mm$^{-1}$ |
| F(000) | 1000 |
| Crystal size | 0.38 x 0.12 x 0.06 mm$^3$ |
| Theta range for data collection | 2.57 to 27.81°. |
| Index ranges | -14<=h<=14, -17<=k<=17, -19<=l<=19 |
| Reflections collected | 42536 |
| Independent reflections | 9153 [R(int) = 0.1050] |
| Completeness to theta = 25.00° | 99.8 % |
| Absorption correction | Semi-empirical from equivalents |
| Max. and min. transmission | 0.7716 and 0.2762 |
| Refinement method | Full-matrix least-squares on F$^2$ |
| Data / restraints / parameters | 9153 / 249 / 417 |
| Goodness-of-fit on F$^2$ | 1.103 |
| Final R indices [I>2sigma(I)] | R1 = 0.0805, wR2 = 0.2002 |
| R indices (all data) | R1 = 0.1142, wR2 = 0.2229 |
| Largest diff. peak and hole | 4.390 and -5.428 e.Å$^{-3}$ |

**Table A8. Crystal data and structure refinement for [IrI(Me)(CO)(xantphos)]SbF$_6$**

| | |
|---|---|
| Identification code | chris1_0m |
| Empirical formula | C42 H37 Cl2 F6 I Ir O2 P2 Sb |
| Formula weight | 1261.41 |
| Temperature | 100(2) K |
| Wavelength | 0.71073 A |
| Crystal system | Monoclinic, |
| Space group | P2(1)/c |
| Unit cell dimensions | a = 12.0099(3) A α = 90 deg.<br>b = 24.6243(6) A β = 92.1380(11) deg.<br>c = 14.5388(3) A γ = 90 deg. |
| Volume | 4296.64(17) A^3 |
| Z | 4 |
| Calculated density | 1.950 Mg/m^3 |
| Absorption coefficient | 4.702 mm^-1 |
| F(000) | 2416 |
| Crystal size | 0.25 x 0.11 x 0.10 mm |
| Theta range for data collection | 1.63 to 27.53 deg. |
| Limiting indices | -15<=h<=15, -32<=k<=32, -18<=l<=18 |
| Reflections collected / unique | 105019 / 9880 [R(int) = 0.0284] |
| Completeness to theta = 27.53 | 99.8 % |
| Absorption correction | Semi-empirical from equivalents |
| Max. and min. transmission | 0.6507 and 0.3861 |
| Refinement method | Full-matrix least-squares on F^2 |
| Data / restraints / parameters | 9880 / 0 / 517 |
| Goodness-of-fit on F^2 | 1.661 |
| Final R indices [I>2sigma(I)] | R1 = 0.0200, wR2 = 0.0569 |
| R indices (all data) | R1 = 0.0215, wR2 = 0.0574 |
| Largest diff. peak and hole | 1.102 and -1.043 e.A$^{-3}$ |

The following section contains pseudo first order rate constants ($k_{obs}$) for the reaction of [Rh(acac)(CO)L] complexes with MeI. All kinetic experiments were conducted in dichloromethane. Experimental errors are expected to be less than 5 % in each case.

**Table A9 –** Kinetic data for the reaction of [Rh(acac)(CO)(L)] complexes with MeI.

| Complex | [MeI] / M | T / °C | $10^3.k_{obs}$ / $s^{-1}$ |
|---|---|---|---|
| [Rh(acac)(CO)($PPh_3$)] | 0.032 | 23 | 1.10±0.004 |
| | 0.064 | 23 | 2.12±0.008 |
| | 0.16 | 23 | 4.89±0.02 |
| [Rh(acac)(CO)($PCy_3$)] | 0.02 | 23 | 0.721±0.003 |
| | 0.04 | 23 | 1.44±0.004 |
| | 0.064 | 23 | 1.99±0.004 |
| | 0.08 | 23 | 2.44±0.003 |
| [Rh(acac)(CO)(P*p*$tol_3$)] | 0.008 | 23 | 0.401±0.003 |
| | 0.016 | 23 | 0.999±0.006 |
| | 0.04 | 23 | 2.56±0.012 |
| | 0.08 | 23 | 5.03±0.026 |
| | 0.16 | 23 | 11.1±0.022 |
| | 0.08 | 18 | 4.16±0.013 |
| | 0.08 | 28 | 6.34±0.009 |
| | 0.08 | 33 | 7.94±0.01 |
| [Rh(acac)(CO)(P(4-Cl-$C_6H_4)_3$)] | 0.04 | 23 | 0.298±0.0006 |
| | 0.08 | 23 | 0.506±0.002 |
| | 0.16 | 23 | 1.70±0.013 |
| | 0.32 | 23 | 2.40±0.001 |
| | 0.64 | 23 | 4.45±0.15 |
| | 0.16 | 28 | 1.67±0.003 |
| | 0.16 | 18 | 0.675±0.002 |
| | 0.16 | 13 | 0.517±0.002 |
| [Rh(acac)(CO)(P(4-F-$C_6H_4)_3$)] | 0.04 | 23 | 0.388±0.0009 |
| | 0.08 | 23 | 0.790±0.0008 |
| | 0.16 | 23 | 1.48±0.005 |
| | 0.32 | 23 | 2.17±0.002 |
| | 0.32 | 22 | 2.03±0.003 |
| | 0.32 | 28 | 2.92±0.01 |
| | 0.32 | 33 | 3.91±0.006 |

| | | | |
|---|---|---|---|
| [Rh(acac)(CO)(P(4-$CF_3$-$C_6H_4$)$_3$)] | 0.64 | 23 | 0.851±0.0005 |
| | 1.6 | 23 | 1.94±0.001 |
| | 3.2 | 23 | 2.32±0.003 |
| | 6.4 | 23 | 3.68±0.007 |
| | 1.6 | 28 | 2.25±0.003 |
| | 1.6 | 33 | 2.65±0.004 |
| | 1.6 | 37 | 4.24±0.005 |
| [Rh(acac)(CO)($PPh_2Me$)] | 0.01 | 23 | 1.09±0.005 |
| | 0.02 | 23 | 1.97±0.007 |
| | 0.04 | 23 | 3.97±0.005 |
| | 0.08 | 23 | 7.92±0.008 |
| | 0.02 | 18 | 1.73±0.004 |
| | 0.02 | 27 | 2.40±0.001 |
| | 0.02 | 33 | 3.65±0.005 |
| [Rh(acac)(CO)($PPhMe_2$)] | 0.01 | 23 | 1.36±0.009 |
| | 0.02 | 23 | 3.96±0.009 |
| | 0.04 | 23 | 6.61±0.02 |
| | 0.06 | 23 | 11.3±0.02 |
| | 0.04 | 13 | 3.99±0.02 |
| | 0.04 | 18 | 5.51±0.013 |
| [Rh(acac)(CO)($PMe_3$)] | 0.0048 | 23 | 1.06±0.006 |
| | 0.008 | 23 | 2.80±0.011 |
| | 0.016 | 23 | 6.61±0.012 |
| | 0.02 | 23 | 7.45±0.020 |
| [Rh(acac)(CO)($PPh_2Et$)] | 0.01 | 23 | 0.471±0.003 |
| | 0.02 | 23 | 1.43±0.006 |
| | 0.04 | 23 | 3.40±0.007 |
| | 0.08 | 23 | 7.00±0.02 |
| | 0.02 | 13 | 1.01±0.005 |
| | 0.02 | 18 | 1.18±0.005 |
| | 0.02 | 28 | 2.03±0.003 |
| [Rh(acac)(CO)($PPhEt_2$)] | 0.01 | 23 | 0.976±0.005 |
| | 0.02 | 23 | 1.83±0.007 |
| | 0.04 | 23 | 4.38±0.016 |
| | 0.08 | 23 | 10.1±0.041 |
| | 0.02 | 22 | 1.77±0.008 |
| | 0.02 | 28 | 2.23±0.007 |
| | 0.02 | 33 | 2.78±0.008 |

| | | | |
|---|---|---|---|
| [Rh(acac)(CO)($PEt_3$)] | 0.01 | 23 | 1.44±0.008 |
| | 0.02 | 23 | 2.64±0.0111 |
| | 0.04 | 23 | 4.81±0.014 |
| | 0.06 | 23 | 8.33±0.013 |
| | 0.08 | 23 | 11.1±0.027 |
| | 0.01 | 13 | 0.872±0.002 |
| | 0.01 | 18 | 1.05±0.002 |
| | 0.01 | 26 | 1.42±0.005 |
| | 0.01 | 32 | 1.86±0.005 |
| [Rh(acac)(CO)(P*o*anisyl$_3$)] | 0.1284 | 25 | 34.6 |
| | 0.963 | 25 | 24.0 |
| | 0.0642 | 25 | 18.8 |
| | 0.0321 | 25 | 10.4 |
| | 0.0161 | 25 | 5.59 |
| [Rh(acac)(CO)(PPh*o*anisyl$_2$)] | 0.01605 | 25 | 21.9 |
| | 0.01284 | 25 | 18.3 |
| | 0.00963 | 25 | 12.6 |
| | 0.00642 | 25 | 9.55 |
| | 0.0321 | 25 | 6.50 |
| [Rh(acac)(CO)($PPh_2$*o*anisyl)] | 0.01605 | 25 | 8.91 |
| | 0.01284 | 25 | 7.12 |
| | 0.00963 | 25 | 6.12 |
| | 0.00642 | 25 | 4.15 |
| | 0.00321 | 25 | 2.61 |
| [Rh(acac)(CO)(P*o*tol$_3$)] | 1.6 | 23 | 0.175±0.0005 |
| | 3.2 | 23 | 0.371±0.0008 |
| | 4.8 | 23 | 0.490±0.0002 |
| | 6.4 | 23 | 0.563±0.0007 |
| | 8.0 | 23 | 0.687±0.0005 |
| [Rh($^t$Bu-acac)(CO)(P*p*tol$_3$)] | 0.04 | 23 | 3.61±0.06 |
| | 0.064 | 23 | 5.70±0.12 |
| | 0.08 | 23 | 7.18±0.22 |
| | 0.16 | 23 | 13.9±0.39 |
| [Rh($^t$Bu-acac)(CO)($PPh_3$)] | 0.04 | 23 | 2.08±0.002 |
| | 0.068 | 23 | 2.66±0.002 |
| | 0.08 | 23 | 3.45±0.006 |
| | 0.01 | 23 | 4.55±0.009 |
| | 0.16 | 23 | 6.59±0.018 |

| | | | |
|---|---|---|---|
| | 0.068 | 23 | 2.24±0.004 |
| | 0.068 | 23 | 3.60±0.005 |
| | 0.068 | 23 | 4.08±0.008 |

The following section contains $^{31}P\{^{1}H\}$-NMR spectra for the reactions of various [Rh(acac)(CO)L] complexes with 0.16 M MeI (in $CDCl_3$) at 25 °C.

**Figure A1**: **[Rh(acac)(CO)($PPh_3$)]**

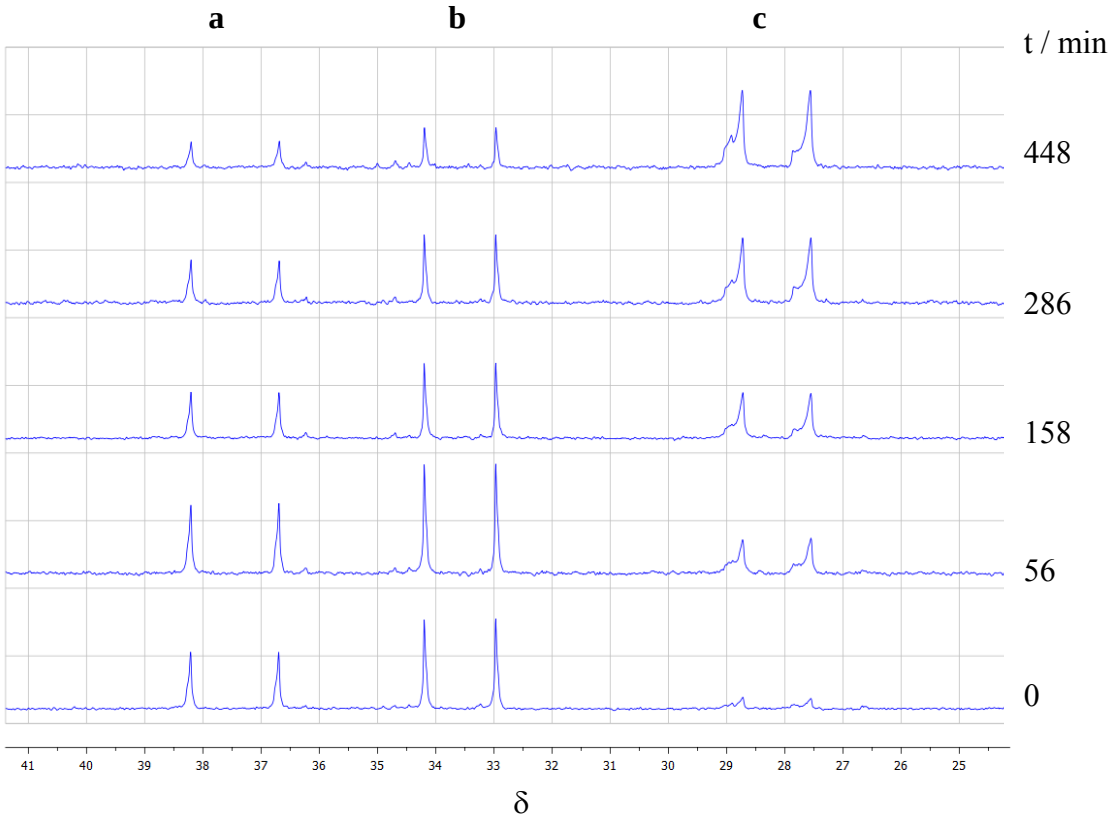


a – 37.44 (d, $J$ = 153.3 Hz) c – 28.15 (d, $J$ = 118.2 Hz)

b – 33.58 (d, $J$ = 124.3 Hz)

**Figure A2**: **[Rh(acac)(CO)P(4-FC$_6$H$_4$)$_3$]**

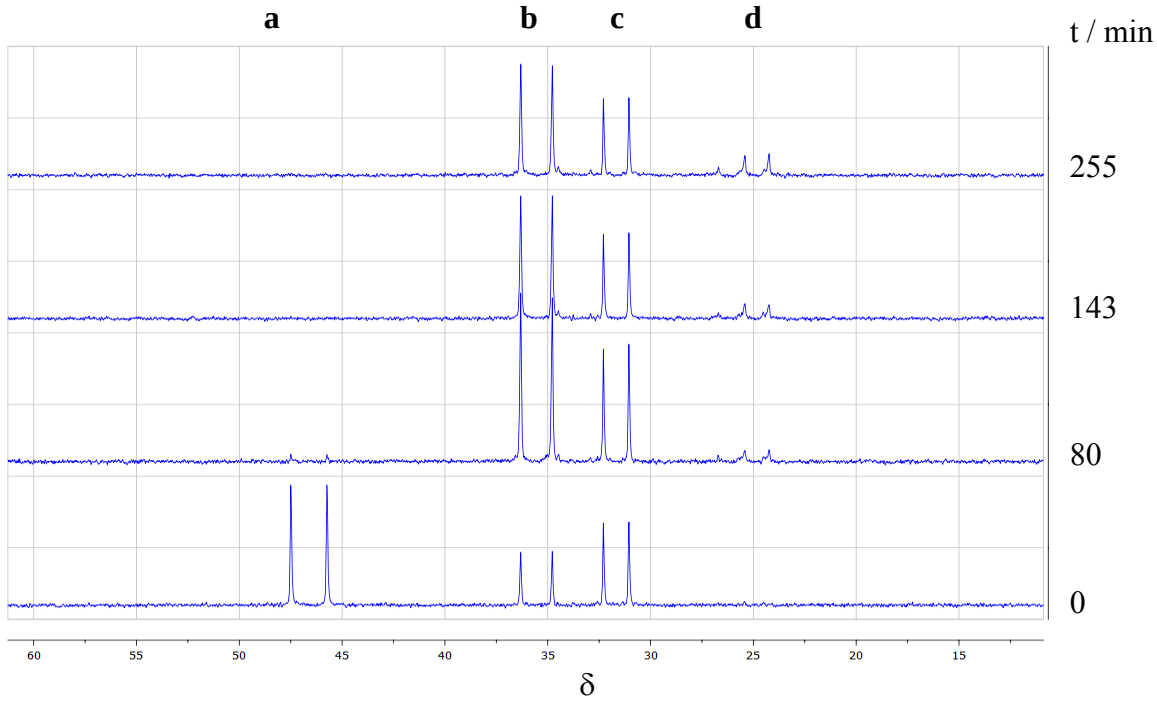


a – 46.62 (d, $J$ = 177.5 Hz) c – 31.67 (d, $J$ = 125.5 Hz)

b – 35.55 (d, $J$ = 155.2 Hz) d – 24.82 (d, $J$ = 118.8 Hz)

**Figure A3: [Rh(acac)(CO)P(4-ClC$_6$H$_4$)$_3$]**

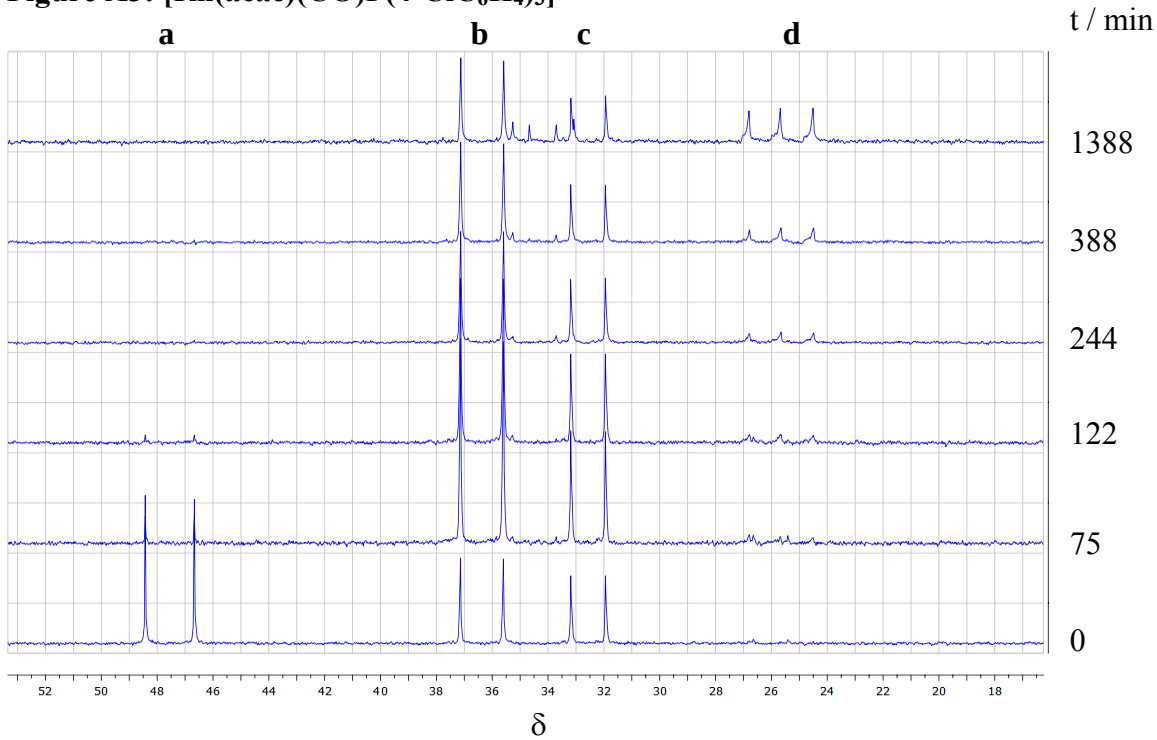


a – 47.55 (d, $J$ = 177.6 Hz) c – 32.57 (d, $J$ = 125.6 Hz)

b – 36.36 (d, $J$ = 155.7 Hz) d – 25.09 (d, $J$ = 120.2 Hz)

**Figure A4: [Rh(acac)(CO)P*p*tol$_3$]**

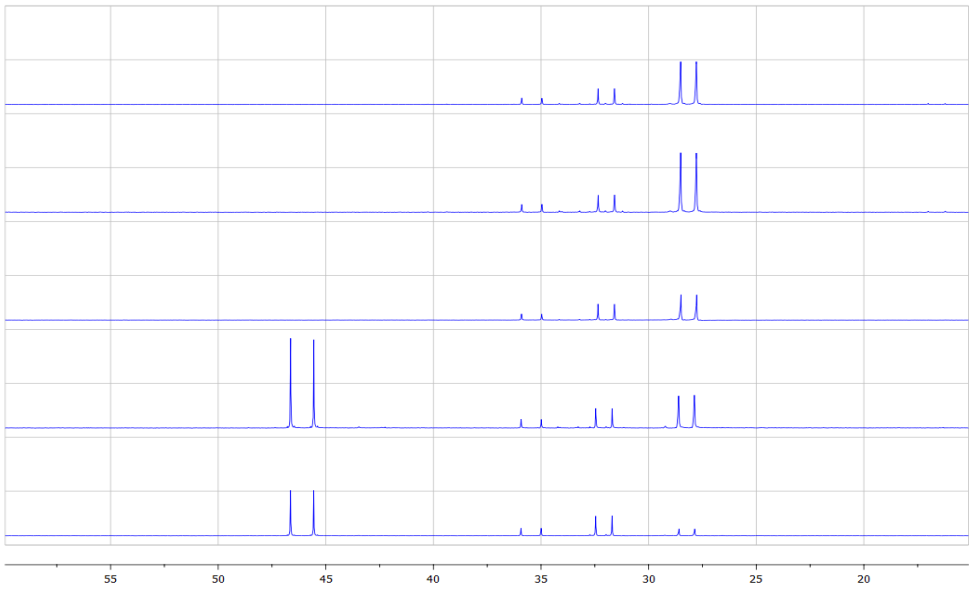


a – 46.10 (d, $J$ = 174.4 Hz) c – 32.08 (d, $J$ = 123.4 Hz)

b – 35.46 (d, $J$ = 151.8 Hz) d – 28.24 (d, $J$ = 118.3 Hz)

**Figure A5: [Rh(acac)(CO)P(4-MeOC$_6$H$_4$)$_3$]**

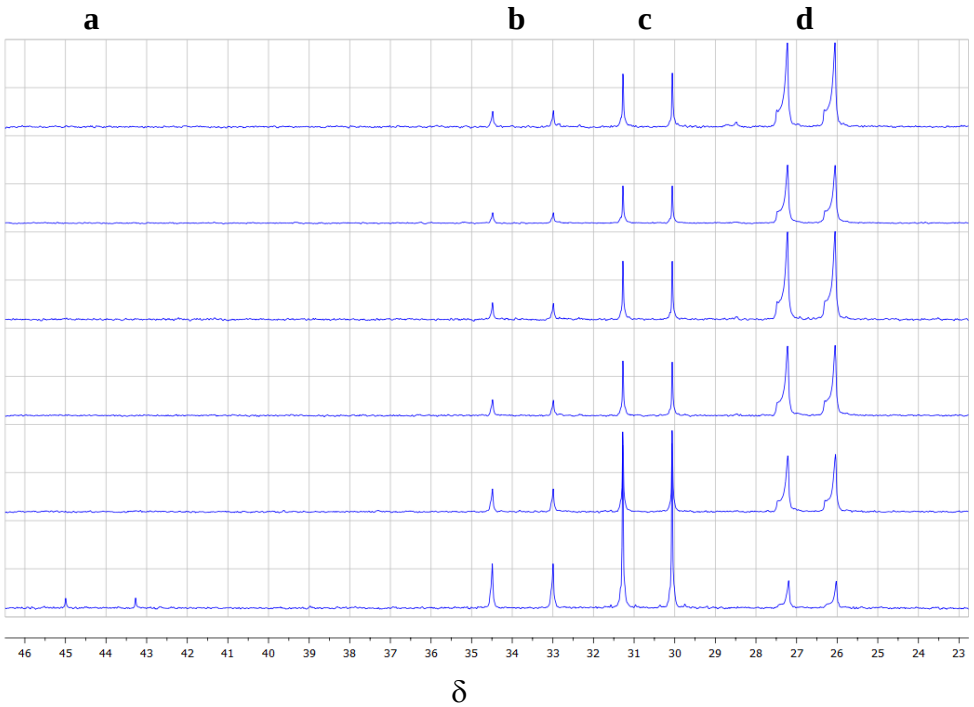


a – 44.13 (d, $J$ = 174.1 Hz) c – 30.67 (d, $J$ = 122.8 Hz)

b – 33.74 (d, $J$ = 151.3 Hz) d – 30.67 (d, $J$ = 122.8 Hz)

**Figure A6:** $^{13}C$ / $^{1}H$ correlation NMR from the reaction of $[IrI_2(CO)_2]Ph_4As$ and *o*tol-xantphos.